CENTRO INTERNACIONAL DE ESTUDOS
DE DOUTORAMENTO E AVANZADOS
DA USC (CIEDUS)

TESE DE DOUTORAMENTO

LOW-ENERGY CALIBRATION, RECONSTRUCTION SOFTWARE AND LIGHT-COLLECTION EFFICIENCY PARAMETRIZATION OF THE NEXT-WHITE DETECTOR

Gonzalo Martínez Lema

ESCOLA DE DOUTORAMENTO INTERNACIONAL

PROGRAMA DE DOUTORAMENTO EN FÍSICA NUCLEAR E DE PARTÍCULAS

SANTIAGO DE COMPOSTELA

2018

USC
UNIVERSIDADE
DE SANTIAGO
DE COMPOSTELA

Declaración do Autor da Tese

Low-energy calibration, reconstruction software and light-collection efficiency parametrization of the NEXT-White detector

D. Gonzalo Martínez Lema

Presento a miña tese, seguindo o procedemento axeitado ao Regulamento, e declaro que:

1. A tese abarca os resultados da elaboración do meu traballo.
2. De selo caso, na tese faise referencia ás colaboracións que tivo este traballo.
3. A tese é a versión definitiva presentada para a súa defensa e coincide coa versión enviada en formato electrónico.
4. Confirmo que a tese non incorre en ningún tipo de plaxio doutros autores nin de traballos presentados por min para a obtención doutros títulos.

En Santiago de Compostela, 24 de xullo de 2018

Asdo.
Gonzalo Marínez Lema

USC
UNIVERSIDADE
DE SANTIAGO
DE COMPOSTELA

Autorización do Director/Titor da Tese

Low-energy calibration, reconstruction software and light-collection efficiency parametrization of the NEXT-White detector

D. José Ángel Hernando Morata

INFORMA:

Que a presente tese, correspóndese co traballo realizado por D. Gonzalo Martínez Lema, baixo a nosa dirección, e autorizamos a súa presentación, considerando que reúne os requisitos esixidos no Regulamento de Estudos de Doutoramento da USC, e que como directores desta non incorre nas causas de abstención establecidas na Lei 40/2015.

En Santiago de Compostela, 24 de xullo de 2018

Asdo.
José Ángel Hernando Morata

USC
UNIVERSIDADE
DE SANTIAGO
DE COMPOSTELA

A Bolbi, a Sofi e aos pulpiños,
por facerme feliz.

USC
UNIVERSIDADE
DE SANTIAGO
DE COMPOSTELA

Acknowledgments

This thesis is the end of a long journey. I would not be here without the help of many people to which I am deeply grateful.

First, I want to express my gratitude to my supervisor **José Ángel Hernando Morata**, who not only taught me and guided me since the last stages of my degree, but introduced me to the NEXT collaboration. I would also like to thank **J. J. Gómez Cadenas**, who has also inspired me a lot and dedicated long hours to discuss the results with me. Academics aside, you let me live in your home during some of my stays in Valencia and helped me go to Geneva in multiple occasions, for which I am very grateful. We still owe each other a chess match. I would like to thank the whole NEXT collaboration for welcoming me and making me feel like part of the family.

Quiero agradecer en particular a todo el grupo de NEXT del IFIC. Primero, al grupo del *zulo* de aquel año 2013: **Javi, Vicente, Alberto, Sara, Marc, Francesc** y **Ander**. Con vosotros tuve el primer contacto y me recibisteis con los brazos abiertos. Al final, subía tanto al segundo piso que acabé instalándome allí durante mis viajes a Valencia. Mi gratitud se extiende a **Paola, Andrew, Justo, Pau, Neus, Josh** y **José María** por siempre haber tenido un rato para hacerme caso. Gracias también a **Michel**, por sus comentarios, sugerencias y críticas constructivas a mi trabajo. Una mención especial a **Andrew**, quien siempre está dispuesto a ayudar en lo que haga falta y más. En concreto, mil gracias por todas las veces que has corregido mi mediocre inglés, por ejemplo el de esta tesis. También a **Paola**, con la que he desarrollado gran parte de mi trabajo y quien siempre ha estado disponible al otro lado de la pantalla. En el último año **Ander** ha sido otro gran apoyo, tanto para tratar con el detector y sus excentricidades, como para lidiar con otros menesteres. Gracias, *nexters*.

No sé en que idioma agrader a **Jacek Generowicz**. Siempre tengo la duda de si hablarte en español o inglés. Sea como sea, quiero darte las gracias por tener la paciencia y la voluntad de enseñarme *the ways of the force*. Por supuesto, parte de esta tesis no hubiese sido posible sin tu esfuerzo y tu dedicación al desarrollo de IC.

Quero agradecer a **meus pais** o seu contínuo e incondicional apoio durante todas as etapas da miña vida. Sen a súa inestimable axuda e perseverancia, definitivamente non estaría hoxe aquí.

Por suposto, non pode faltar unha mención a **Brais, Antía, Miriam, Cris, Miguel** e **Martino** (p. italiano). Grazas por tódolas risas e os cafés onde contamos as nosas cosis, *jeiteamos* a máis non poder e pasamos os bos e os malos momentos. Reformulando algo que me dixeron recentemente, esta é a última proba da *escape room* da academia.

Por último, grazas a **Sofi** por estar sempre aí, por aturarme e por facerme ver o mundo doutro xeito. Se non fora porque cando estou contigo a física non existe, probablemente non me tivese mantido cordo.

USC
UNIVERSIDADE
DE SANTIAGO
DE COMPOSTELA

Resumo

Introdución

O Modelo Estándar de física de partículas (SM) é a teoría física máis exitosa e precisa desenvolvida ata agora. Segundo este modelo, os neutrinos son partículas sen carga e sen masa. Non obstante, nas últimas décadas, unha serie de experimentos de oscilación de neutrinos observaron transicións de sabor nestas partículas, algo que só pode ocorrer se a súa masa é distinta de cero. Esta observación indica que o SM está incompleto, e polo tanto debe estenderse para acomodar esta propiedade dos neutrinos. Máis aló diso, a masa dos neutrinos, aínda que non foi medida, está acoutada a valores por debaixo do eV, varias ordes de magnitude máis pequena que a do resto de fermións.

Existen distintas maneiras de incorporar neutrinos masivos no Modelo Estándar. A máis sinxela consiste en considerar os neutrinos como partículas de Dirac, é dicir, similar ao resto dos leptóns. Neste caso, a extraordinaria masa dos neutrinos sería dun certo xeito arbitraria. Por outra banda, o neutrino é o único fermión elemental sen carga. Isto abre a porta a que poida ser a súa propia antipartícula, é dicir, unha partícula de Majorana.

A posibilidade de que os neutrinos sexan partículas de Majorana podería explicar varios fenómenos da natureza. Por unha banda, a ínfima masa dos neutrinos podería estar conectada coa existencia de partículas moi masivas (moito máis que a masa do bosón Z) mediante o que se coñece como mecanismo de *see-saw*. A maiores, a violación do número leptónico que introduciría esta propiedade é unha das condicións necesarias para que se dea a *leptoxénese* primordial, un dos mecanismos propostos para explicar a asimetría materia-antimateria observada no universo.

Debido a isto, a investigación en física de neutrinos centrouse recentemente na determinación da natureza dos neutrinos. Se ben existen distintos xeitos de establecer experimentalmente a natureza dos neutrinos, a máis prometedora actualmente é a busca da desintegración dobre beta sen neutrinos ($\beta\beta^{0\nu}$). Este é un proceso nuclear teorizado que, de ser observado, indicaría inequívocamente que os neutrinos son partículas de Majorana.

A desintegración dobre beta

A desintegración dobre beta *con* emisión de neutrinos ($\beta\beta^{2\nu}$) é un proceso nuclear extremadamente lento que está considerado no Modelo Estándar. Malia que a vida media deste proceso é varias ordes de magnitude maior que a idade do universo, xa foi observado experimentalmente en varios isótopos. Por outra banda, o modo *sen* emisión de neutrinos non sería posible dentro do Modelo Estándar actual. Ata o momento non se atopou ningunha evidencia experimental contundente desta desintegración.

No relativo ao marco teórico do proceso, existe un importante teorema, coñecido como *teorema da caixa negra*, que demostra a conexión entre a existencia da $\beta\beta^{0\nu}$ e a natureza Majorana dos neutrinos. Ademáis, pódense considerar procesos análogos teóricamente á $\beta\beta^{0\nu}$, tales como a $\beta^+\beta^{+0\nu}$, a $\beta^+\varepsilon^{0\nu}$ e $\varepsilon\varepsilon^{0\nu}$. Non obstante, estos resultan experimentalmente menos prácticos.

Experimentalmente, o parámetro que define a busca é o período de semidesintegración do proceso, que vén dado por

$$\left(T^{0\nu}_{1/2}\right)^{-1} = G^{0\nu} \ \left|M^{0\nu}\right|^2 \ \left(\frac{m_{\beta\beta}}{m_e}\right)^2 .$$

onde $G^{0\nu}$ é o factor de espacio de fase, $\left|M^{0\nu}\right|$ é o factor de matriz nuclear (NME) do proceso, m_e é a masa do electrón e $m_{\beta\beta}$ é a chamada masa de Majorana efectiva do neutrino. Esta defínese como

$$m_{\beta\beta} = \left|\sum_i U^2_{ei} m_i\right| .$$

onde U_{ei} son os elementos da primeira fila da matriz Pontecorvo-Maki-Nakagawa-Sakata (PMNS), que establece a mestura de autoestados de sabor e autoestados de masa. Os elementos desta matriz están actualmente acoutados polas observacións dos experimentos de oscilación de neutrinos. Destas dúas ecuacións, dedúcese a conexión entre a magnitude observable empíricamente (o período de semidesintegración) e a escala de masa dos neutrinos.

Observar a desintegración dobre beta sen neutrinos non é unha tarefa sinxela. A técnica consiste en medir a suma ad enerxía dos electróns emitidos pola radiación. Mentres que o modo emisor de neutrinos ten un espectro contínuo, o modo sen neutrinos produce un sinal de enerxía fixa. Debido ao longo período de desintegración deste proceso ($\gtrsim 10^{26}$ anos), precísanse grandes cantidades do isótopo emisor e longos períodos de exposición. As habitualmente baixas abundancias naturais e o custo de enriquecemento son un factor relevante á hora de escoller a fonte da desintegración. Outro destos factores é o valor da enerxía da desintegración, $Q_{\beta\beta}$. Os elementos radioactivos naturais atópanse prácticamente en tódolos materiais. A radiación emitida por estos poboa a rexión de enerxía por debaixo dos 3 MeV, polo que interesa atopar un isótopo cun valor de $Q_{\beta\beta}$ alto para minimizar a interferencia destos sucesos no experimento. Non obstante, a presenza de trazas de elementos radiactivos nos materiais que compoñen o detector constitúe sempre nunha fonte contínua de fondo. Os experimentos procuran evitar isto mediante a utilización de materiais radiopuros, a blindaxe do detector con materiais densos e co uso de técnicas de diferenciación de fondo. Finalmente, a medida desta desintegración ten un fondo intrínseco irreducible: aquel do modo emisor de neutrinos. A única diferenza observable entre os dous modos é a enerxía dos electróns saíntes, polo que se precisa unha resolución enerxética excelente para poder distinguilos.

A busca da desintegración dobre beta sen neutrinos comezou a finais dos 90 cunha serie de experimentos a pequena escala. Entre eles, un grupo reducido de científicos do experimento Heidelberg-Moscow anunciou o descubrimento da desintegración, aínda que foi máis tarde refutada por experimentos con maior sensitividade.

Existen na actualidade varios experimentos buscando a desintegración dobre beta sen

neutrinos. EXO e KamLAND-Zen e GERDA lideran na actualidade a busca con sensitividades ao período de semidesintegración da orde de 10^{26} anos. Actualmente o mellor límite á masa de Majorana efectiva está imposta por KamLAND-Zen. A medida dun período de semidesintegración

$$T^{0\nu}_{1/2} > 1.1 \cdot 10^{26}, \qquad 90\%\ \text{CL}$$

establece un límite na masa de Majorana efectiva de

$$m_{\beta\beta} < 61 - 165, \qquad 90\%\ \text{CL},$$

dependendo do modelo usado para o cálculo do factor de matriz nuclear.

Non obstante, existen alternativas en desenvolvemento que implementan diferentes técnicas e usan diferentes isótopos para buscar esta desintegración. Entre elas atópanse CUORE, SNO+, SuperNEMO e NEXT.

NEXT

NEXT (**N**eutrino **E**xperiment with a **X**enon **T**PC) buscará a desintegración dobre beta sen neutrinos en ^{136}Xe cunha cámara de proxección temporal (TPC) de xenon a alta presión. O detector NEXT-100, co que a colaboración comezará a buscar a desintegración, consiste nunha TPC electroluminiscente con $\mathcal{O}$(100 kg) de xenon enriquecido ao 91 % en ^{136}Xe a 15 bar. O detector está instrumentado cun plano de PMTs (tubos fotomultiplicadores) nun extremo para realizar a medida enerxética dos eventos e cun plano de SiPMs (fotomultiplicadores de silicio) no outro extremo para realizar a reconstrución espacial dos eventos. A tecnoloxía céntrase en conseguir unha resolución en enerxía excelente ($<$ 1 % FWHM na $Q_{\beta\beta}$) e en reducir o fondo de contaminación mediante a análise da topoloxía dos eventos.

O uso de xenon gasoso permite reducir a resolución enerxética intrínseca do detector ao Factor de Fano. En xenon, a resolución intrínseca na $Q_{\beta\beta}$ é $\sim$0.3 % FWHM. Non obstante, as técnicas de amplificación por recoleción de carga non permiten achegarse a este valor debido ás altas flutuacións no proceso de avalancha. Consecuentemente, a amplificación do sinal realízase mediante electroluminiscencia, un proceso polo cal a carga se utiliza para emitir luz mediante a ionización do medio. Este proceso presenta flutuacións moito menores. Isto permite acadar resolucións enerxéticas próximas á intrínseca, dados os valores adecuados da configuración do detector.

Por outra banda, o sinal medido nos SiPMs pode producir unha reconstrución espacial completa do evento. O sinal característico dun electrón nas condicións desta cámara consiste nunha fina traza onde o electrón deposita unha pequena cantidade de enerxía por unidade de lonxitude que remata nunha gran deposición de enerxía ou *blob*. Posto que os eventos de sinal están compostos por dous electróns, estes estarán caracterizados por ter dous *blobs*. Os eventos de fondo, polo contrario, están xerados por un único electrón e producirá un só *blob*. O número de *blobs* identificados en cada evento permite, polo tanto, caracterizalo como sinal ou como fondo e reducir a cantidade destos últimos.

NEXT é unha colaboración internacional con gran presenza de grupos españois. O proxecto comezou en 2009 cunha fase de I+D para demostrar o concepto do detector e as posibilidades que ofrece esta tecnoloxía. Durante este período, construíronse dous prototipos (NEXT-DEMO and NEXT-DBDM) que operaron dende 2009 a 2014. NEXT-DBDM dedicouse a demostrar a excelente resolución enerxética do detector a diferentes presións. O detector obtivo unha resolución de 1.1 % FWHM para unha enerxía de 662 keV a 10 bar. O estudo repetíuse a 15 bar, obtendo unha resolución do 1.0 % FWHM. Ambolos dous valores extrapolan aproximadamente a 0.5 % FWHM na $Q_{\beta\beta}$. O detector NEXT-DEMO reproducíu os resultados de resolución enerxética de NEXT-DBDM usando desplazadores de lonxitude de onda e demostrou por primeira vez a posibilidade de obter información topolóxica do evento para reducir o fondo de contaminación. Neste último estudo acadou unha redución de fondo do ∼76 % cunha eficiencia de sinal do ∼67 %.

O proxecto atópase actualmente na súa primeira fase coa operación do detector NEXT-White (NEW). Construído entre 2015 e 2016 e instalado no Laboratorio Subterráneo de Canfranc, NEW é un modelo a escala ∼1:2 do detector NEXT-100 e fai uso dos mesmos materiais e aproximadamente a mesma tecnoloxía. Os principais obxectivos deste aparato son a validación das solucións tecnolóxicas propostas para NEXT-100 nun detector de grandes dimensións, a evaluación do modelo de fondo que ten o experimento nas condicións de laboratorio que terá durante a medida do sinal de dobre beta e a medida do período de semidesintegración da dobre beta *con* emisión de neutrinos.

O traballo desta tese céntrase en tres aspectos diferentes, mais relacionados, do detector NEXT-White: a simulación da resposta óptica, a implementación do software de reconstrución e a calibración de baixa enerxía do detector usando datos de $^{83}\mathrm{Kr}^{m}$.

Simulación da resposta óptica

A simulación da resposta óptica do detector fai unha contribución ao software de simulación do experimento. A propagación e seguimento de fotóns é a parte máis intensiva da simulación do detector. Para reducir esta compoñente da simulación, constrúese un modelo de probabilidade de detección de fotóns do detector, que reemplaza a propagación individual de fotóns por unha descrición estatística do número de fotóns detectador por cada sensor. Non obstante, unha descrición precisa da resposta do detector require a dispoñibilidade de grandes cantidades de datos durante a execución da simulación, o cal compromete a viabilidade do método. A parametrización do modelo de probabilidade resolve este conflicto mediante a introdución dun conxunto de funcións que reproducen o modelo de probabilidade sen necesidade de ter acceso aos datos durante a execución da simulación. Esta técnica é, ademáis, trasladable a detectores de grandes dimensións, o cal permite simular grandes cantidades de datos mediante técnicas Monte Carlo para detectores como NEXT-White e NEXT-100 que, doutro xeito, serían irrealizables.

O sinal de escintileo (S1) e o de ionización (S2) son parametrizados independentemente. Para o sinal S1 créase un modelo de probabilidade simulando a emisión de fotóns dende distintos puntos do volume activo e gravando a cantidade de fotóns recibidos por cada PMT. A parametrización deste modelo realízase mediante o uso de coordenadas cilíndricas relativas. Para reproducir o modelo de probabilidade, parametrízase primeiro a coordenada dr e, posteriormente, a súa

dependencia coa coordenada z. A parametrización está baseada en polinomios de segunda e cuarta orde, respectivamente. O modelo de probabilidade do sinal S2 xenérase mediante a simulación do proceso de electroluminiscencia dende distintso puntos no plano (x, y) e gravando a cantidade de fotóns recibidos por cada PMT e SiPM. A parametrización deste modelo faise separadamente para cada tipo de sensor. Para os PMTs, utilízanse coordenadas polares absolutas, posto que o modelo depende únicamente da coordenada r. A dependencia da recolección de luz de cada PMT con r parametrízase usando un polinomio de grao 9. Para os SiPMs utilízanse coordenadas polares relativas, xa que a recolección de luz depende fortemente da distancia transversal entre o punto de emisión e o sensor. Esta dependencia reprodúcese adecuadamente usando un polinomio de grao 9. Todos estes modelos son verificados comprobando que a predición nos puntos simulados é estatísticamente compatible co resultado da simulación orixinal. Finalmente, este proceso é repetido para a xeometría de NEXT-100.

Implementación do software de reconstrución

A implementación do software de reconstrución constitúe a segunda contribución ao experimento NEXT. Esta tese contén unha descripción exhaustiva de cada unha das etapas da cadea de reconstrución do experimento, así como das estruturas lóxicas usadas para gardar a información.

Os datos producidos polo detector consiste nunha serie de sinais eléctricos que se dixitalizan mediante tarxetas ADC e se formatean con módulos FPGA para producir os chamados datos *raw* (sen procesar). Estes datos precisan ser procesados para obter a información relevante. Esta tarefa é realizada mediante unha serie de algoritmos de reconstrución: unha coleción de funcións que transforman os datos en estruturas máis elaboradas de fácil interpretación. Estas estruturas son as que serán en última instancia usadas para realizar a análise de datos e a produción de resultados físicos.

O procesado dos datos *raw* comeza mediante o uso dun programa que traduce a información producida polo detector a unha estrutura de formas de onda gardadas usando unha estrutura *hdf5*. No caso dos datos simulados con Monte Carlo, outro programa emula a electrónica do detector para producir o mesmo tipo de datos que o detector. Estas formas de onda son adicionalmente procesadas para producir o que se coñecen como `PMaps`. Este procesado dá conta de tres principais características: a distorsión introducida pola electrónica na forma de onda dos PMTs, as diferentes respostas dos sensores a un mesmo sinal e a restrición da localización do sinal a unhas pequenas seccións da forma de onda. A última etapa da reconstrución divídese en función do tipo de datos analizados. Os eventos de tamaño reducido, ou que se poden considerar puntuais, son procesados para reducir a información dos sensores a un punto no espazo asociada a unha certa deposición de enerxía. Os eventos de maior tamaño son divididos para producir unha colección de deposicións de enerxía (*hits*). Estos *hits* pódense interpretar como a representación discretizada dunha traza.

A maiores, discútese o entorno de software utilizado polo experimento (IC). IC segue unha estrutura innovadora no ámbito da comunidade de física de partículas. Está totamente escrita na linguaxe Python e usa ferramentas desenvolvidas e usadas por unha comunidade máis ampla, concretamente centrada no entorno *anaconda*. A estrutura baséase nunha certa filosofía de software fundamentada nó método de verificación contínuo e na optimización do desenvolvemento. A principal característica deste entorno é o esquema *dataflow*. Baseado nunha estrutura modular, o principal beneficio desta arquitectura vén dado pola similitude entre o diagrama de fluxo dun

determinado programa e a súa implementación dentro do paradigma de *dataflow*.

Calibración de baixa enerxía do detector NEXT-White

A calibración de baixa enerxía do detector NEXT-White usando datos de $^{83}\mathrm{Kr}^{m}$ constitúe a contribución á análise de datos do experimento. A resposta do detector depende da posición do evento no volume da cámara. En particular, pequenas concentracións de impurezas no xenon capturan unha parte dos electróns de deriva, reducindo o sinal producido. A maiores, a eficiencia de recolección de luz dos sinais depende da posición (x, y) do evento. Ámbolos dous efectos resultan nunha resposta inhomoxénea ao longo do volume activo do detector que deterioran a súa resolución enerxética. Posto que calquera análise física realizada co detector depende da precisión da medida enerxética, dita resposta debe de ser homoxeneizada.

A ecualización da resposta do detector realízase con datos producidos pola desintegración do $^{83}\mathrm{Kr}^{m}$. Este elemento é introducido no volume activo do detector a partir da desintegración de unha fonte de $^{83}\mathrm{Kr}$ introducida no sistema de gas. As desintegracións de $^{83}\mathrm{Kr}^{m}$ producen eventos extremadamente curtos, que se poden considerar puntuais, en todo o volume do detector. Estes eventos son usados para correxir tanto pola finita vida media dos electróns de deriva como polas variacións de eficiencia de recolección de luz.

A creación de mapas de vida media e resposta do detector para distintas rexións do detector permite determinar con precisión estas cantidades. No caso da vida vida media, a enerxía do evento corríxese mediante unha función exponencial, que permite recuperar o sinal orixinal. Os efectos de xeometría, por outra banda, son tidos en conta normalizando a enerxía medida a un certo punto da cámara, típicamente ao centro.

A efectividade do método é evaluada mediante a medida da resolución en enerxía do detector para estos eventos. Despois de correxir polos efectos mencionados, obtense unha resolución enerxética para deposicións de 41.5 keV de $(4.553 \pm 0.010\ (\mathrm{stat.}) \pm 0.324\ (\mathrm{sys.}))$ % FWHM en todo o volume e $(3.804 \pm 0.013\ (\mathrm{stat.}) \pm 0.112\ (\mathrm{sys.}))$ % FWHM nun volume fiducial para un período de toma de datos a 7.2 bar. Unha extrapolación $E^{-1/2}$ proporciona unha estimación da resolución para a enerxía $Q_{\beta\beta}$ de $(0.5916 \pm 0.0014\ (\mathrm{stat.}) \pm 0.0421\ (\mathrm{sys.}))$ % FWHM en todo o volume activo e de $(0.4943 \pm 0.0017\ (\mathrm{stat.}) \pm 0.0146\ (\mathrm{sys.}))$ % FWHM nun volume fiducial. O estudo realízase tamén para un período de toma de datos a 9.1 bar, para o cal se obteñen resultados semellantes.

A comparación dos resultados con predicións teóricas e simuladas con Monte Carlo demostran que se acadou unha resolución enerxética próxima á intrínseca. Finalmente, proporciónanse uns casos prácticos de aplicación deste método a outras análises físicas realizadas co detector.

Conclusións

A determinación da natureza dos neutrinos, é dicir, se son partículas de Dirac ou de Majorana, é unha das cuestións clave na física de partículas actual. Atopar a desintegración dobre beta sen neutrinos sería un sinal inequívoco de que os neutrinos son partículas de Majorana. Entre os experimentos en desenvolvemento para atopar este proceso atópase NEXT. NEXT buscará a

desintegración dobre beta sen neutrinos en ^{136}Xe usando unha cámara de proxección temporal, centrada na obtención dunha excelente resolución enerxética e na capacidade de redución do fondo de contaminación mediante a análise da información topolóxica do evento. Esta tese enfócase en tres contribucións ao proxecto NEXT: a simulación da resposta óptica dos detectores NEXT-White e NEXT-100 que permite simular grandes cantidades de eventos con técnicas Monte Carlo; a implementación do software de reconstrución do experimento, usado en calquera análise de física do experimento; e a calibración de baixa enerxía do detector, esencial para correxir a enerxía do evento debido aos diferentes efectos que introducen perdas de sinal e acadar a resolución enerxética óptima, sen a cal non se podería realizar ningunha análise física.

USC
UNIVERSIDADE
DE SANTIAGO
DE COMPOSTELA

Preface

Neutrinos are, arguably, the less understood particles in the Standard Model of particle physics. In the past decades, it has been discovered through neutrino oscillation experiments that these are massive particles, contradicting the assumptions of the theory. The possible Majorana nature of neutrinos could explain not only their seemly arbitrary low mass, but also the matter-antimatter asymmetry of the universe. Thus, the research in neutrino physics has been recently focused on the search for the neutrinoless double beta decay ($\beta\beta^{0\nu}$), a hypothetical nuclear process that would prove the Majorana nature of neutrinos.

The standard mode of the double beta decay ($\beta\beta^{2\nu}$), with two-neutrino emission and allowed within the standard model, has already been observed in a number of isotopes. The neutrinoless mode, on the other hand, can only occur if neutrinos are Majorana particles and there has not been any convicing evidence of its occurrence so far. There are multiple projects implementing different techniques to search for the decay, amonst them is the NEXT experiment.

NEXT will search for $\beta\beta^{0\nu}$ in ^{136}Xe with a High-Pressure Xenon TPC. The NEXT-100 detector consists of an electroluminiscent TPC with $\mathcal{O}(100$ kg) of xenon enriched to 91 % in ^{136}Xe at 15 bar. The detector is instrumented with PMTs to measure the event energy and with an array of SiPMs for tracking purposes. The technique is focused on achieving an excellent energy resolution (< 1 % FWHM at $Q_{\beta\beta}$) and significant background rejection using topological information.

The operation of the NEXT-White (NEW) detector constitutes the first phase of the project and is currently ongoing. Built in 2015-2016, NEW is a $\sim$1:2 scale model of the NEXT-100 detector and uses the same materials and technology. Its primary purposes are the validation of the technological solutions for NEXT-100 in a large-scale detector, the assesment of the background model and the measurement of the $\beta\beta^{2\nu}$ half life.

This work focuses on three different, yet related, aspects of NEXT-White: the simulation of the optical response, the implementation of the reconstruction software and the low-energy calibration of the detector with ^{83}Kr^{m} data.

The optical simulation of the detector contributes to the simulation software of the experiment. The photon detection probability model of the detector is parametrized to achieve an accurate description of the detector response, whilst maintaining the memory capability requirements within attainable values. The method can also be tranferred to larger detectors, hence providing a tool to simulate large-statistics Monte Carlo datasets for the NEXT-White and NEXT-100 detectors, which would be otherwise impossible.

The implementation of the reconstruction software constitutes the second contribution to NEXT. This thesis contains a through description of each stage of the reconstruction chain and the software structures created to hold the information. Furthermore, we discuss the software

framework (IC), the software philosophy behind it, and its main feature: the *dataflow* scheme.

The low-energy calibration methodology using $^{83}\mathrm{Kr}^m$ data taken with the NEXT-White detector contributes to the data analysis of the experiment. These data are used to correct for the finite electron lifetime and for the dependence of the measured energy with the event position. After producing calibration maps to correct for both effects, we measure an excellent energy resolution for 41.5 keV point-like deposits of $(4.553 \pm 0.010\ (\mathrm{stat.}) \pm 0.324\ (\mathrm{sys.}))$ % FWHM in the full volume and $(3.804 \pm 0.013\ (\mathrm{stat.}) \pm 0.112\ (\mathrm{sys.}))$ % FWHM in a restricted fiducial volume for a 7.2 bar Run. A naive $E^{-1/2}$ extrapolation yields energy resolutions at $Q_{\beta\beta}$ of $(0.5916 \pm 0.0014\ (\mathrm{stat.}) \pm 0.0421\ (\mathrm{sys.}))$ % FWHM in the full volume and $(0.4943 \pm 0.0017\ (\mathrm{stat.}) \pm 0.0146\ (\mathrm{sys.}))$ % FWHM in the fiducial volume. Similar results were obtained for a 9.1 bar Run.

This thesis is structured in seven chapters that can be grouped in two parts.

The first part (Chapters 1, 2 and 3) describes the context in which this thesis has been developed. Chapter 1 introduces the theoretical concepts related to neutrinos and the motivations to search for processes that determine their nature. Chapter 2 covers both the theoretical and the experimental aspects of the neutrinoless double beta decay. Chapter 3 contains a description of the NEXT experiment and its past, current and future detectors.

The second part (Chapters 4, 5 and 6) of the thesis focuses on the contributions made to the NEXT experiment. The simulation of the optical response of the NEXT-White and NEXT-100 detectors is discussed in Chapter 4. Chapter 5 describes the implementation of the reconstruction software of the experiment and its framework. The description of the software framework of the NEXT experiment is expected to be published in the future. Chapter 6 covers the analysis of the low-energy calibration of the NEXT-White detector using $^{83}\mathrm{Kr}^m$ decays. This chapter is based on the paper

> **NEXT Collaboration**: G. Martínez-Lema et al. *Calibration of the NEXT-White detector using* $^{83}\mathrm{Kr}^m$ *decays.* [arXiv:1804.01780]

of which I am the main author. The paper has been submitted to JINST, and is currently under review.

Chapter 7 concludes this dissertation. Following this chapter are two appendices. Appendix A gives some detail on the definition and performance of the barycenter algorithm, which is mentioned in different occasions and significant to the analysis performed in Chapter 6. Finally, Appendix B provides a lengthy display of some persistent and transient representations of the data structures described in Chapter 5.

Contents

USC
UNIVERSIDADE
DE SANTIAGO
DE COMPOSTELA

List of Figures

List of Tables

USC
UNIVERSIDADE
DE SANTIAGO
DE COMPOSTELA

1 The nature of neutrinos

1.1 Neutrinos and the Standard Model

The standard model of particle physics (SM) is the current and most successfull theory about matter and fundamental interactions. In this model, matter is divided in two groups based on their quantum properties (see Figure 1.1): bosons (integer spin) and fermions (half-integer spin). Fermions are subsequently divided into two groups based on their color charge: quarks (carry color) and leptons (do not carry color). Neutrinos are leptons with spin 1/2 and carry zero electrical charge and have negligible mass compared with other fermions. These properties make them very difficult to detect since they essentially interact only via the weak force.

Three families of light[1] *active*[2] neutrinos have been experimentally found and the possibility of a fourth family being discovered has been statistically discarded [2]. For a long time, neutrinos were thought to be massless but, relatively recently, a series of neutrino oscillation experiments [3, 4, 5, 6, 7, 8, 9] discovered that neutrinos have non-zero mass [10, 11, 12, 13, 14], albeit their values are still unknown. This finding implies that the neutrino states taking part in the weak interaction (ν_e, ν_μ, ν_τ) are not the same as the neutrino mass states (ν_1, ν_2, ν_3), which take part in the particle evolution throught time and space. The conversion between both states is usually written as

$$\nu_l = \sum_i U_{li}^* \nu_i, \tag{1.1}$$

where U is a 3×3 non-diagonal unitary complex matrix called Pontecorvo-Maki-Nakagawa-Sakata (PMNS) matrix. The PMNS matrix is often expressed in terms of three angles (θ_{12}, θ_{13}, θ_{12}) and three phases (δ, α_1 and α_2) as

[1] Light in this context means $m \ll m_Z$, where m_Z is the mass of the Z boson.

[2] A relevant part of the research in the neutrino field is dedicated to search for *sterile* (i.e. non-interacting) neutrinos.

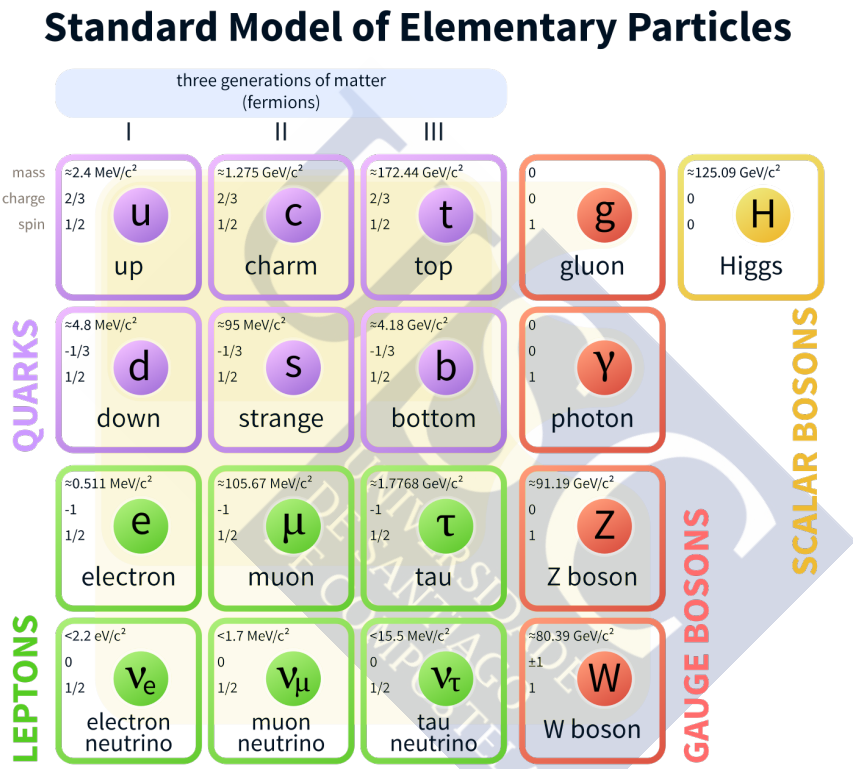

Figure 1.1: Chart with the elementary particles as described in the SM. The colors represent the three groups of particles in the theory: bosons (red and yellow), quarks (purple) and leptons (green). Image from [1].

$$U = \begin{pmatrix} c_{12}c_{13} & s_{12}c_{13} & s_{13}e^{-i\delta} \\ -s_{12}c_{23} - c_{12}s_{23}s_{13}e^{i\delta} & c_{12}c_{23} - s_{12}s_{23}s_{13}e^{i\delta} & s_{23}c_{13} \\ s_{12}s_{23} - c_{12}c_{23}s_{13}e^{i\delta} & -c_{12}s_{23} - s_{12}c_{23}s_{13}e^{i\delta} & c_{23}c_{13} \end{pmatrix} \times \begin{pmatrix} 1 & & \\ & e^{i\alpha_1} & \\ & & e^{i\alpha_2} \end{pmatrix}, \tag{1.2}$$

where

$$\begin{aligned} s_{12} \equiv \sin(\theta_{12}) &= \frac{|U_{e2}|}{\sqrt{1-|U_{e3}|^2}}, \quad c_{12} \equiv \cos(\theta_{12}) = \frac{|U_{e1}|}{\sqrt{1-|U_{e3}|^2}}, \\ s_{23} \equiv \sin(\theta_{12}) &= \frac{|U_{\mu 2}|}{\sqrt{1-|U_{e3}|^2}}, \quad c_{23} \equiv \cos(\theta_{12}) = \frac{|U_{\tau 3}|}{\sqrt{1-|U_{e3}|^2}}, \\ s_{13} \equiv \sin(\theta_{13}) &= |U_{e3}|\,. \end{aligned} \tag{1.3}$$

The angles provide a measure of the mixing of mass eigenstates in each flavor eigenstate. Their values are currently constrained to[3] [15] $\theta_{12}(^\circ) = 33.0^{+1.1}_{-1.0}$, $\theta_{13}(^\circ) = 8.43 \pm 0.14$ and $\theta_{12}(^\circ) = 40.7^{+1.2}_{-0.9}$.

If neutrinos are Dirac particles (Section 1.2), δ is the only physical phase, which accounts for the $\mathcal{CP}$ violation in the lepton sector [16, 17, 18]. The value of this phase is not completely constrained (see Table 1.1). The best fit value yields 1.38π for the normal ordering, but the 3-σ range does not disfavor any physical value. Thus, the status of the $\mathcal{CP}$-symmetry in the lepton sector is still unclear [19]. On the other hand, if neutrinos are Majorana particles (Section 1.3), $\alpha_{1,2}$ could be measured and different from zero.

The value of neutrino masses are constrained from different types of experiments. Cosmological observations [20, 21, 22] set the limit on the sum of neutrino masses. Currently,

$$\sum m_\nu < 0.12 \text{ eV}, \qquad 95\% \text{ CL}. \tag{1.4}$$

On the other hand, β-decay experiments [23, 24, 25, 26, 27] set a limit on the effective electron-antineutrino mass, defined as

$$m_\beta^2 \equiv m_{\bar{\nu}_e}^2 = \sum_i |U_{ei}|^2 m_i^2, \tag{1.5}$$

which is currently [24, 27]

$$m_\beta < 2.05 \text{ eV}, \qquad 95\% \text{ CL}. \tag{1.6}$$

[3] These values are obtained assuming the normal ordering. See text below.

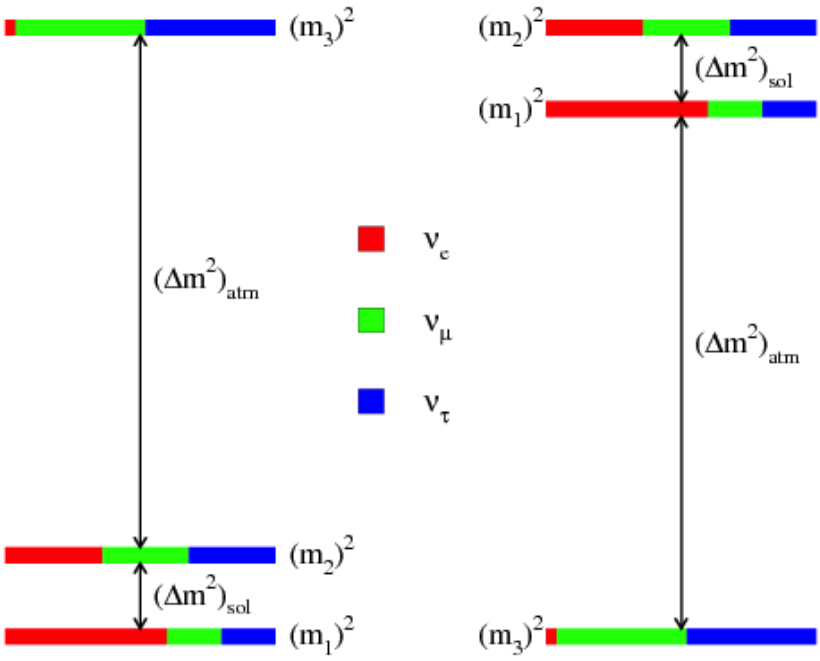

Figure 1.2: Scheme of the two possible neutrino mass hierarchies or orderings based on observations from neutrino oscillation experiments. The vertical axis represents mass and increases from bottom to top. Colors represent the flavor content of each mass eigengstate: red for electron, green for muon and blue for tau. The left and right panels show the normal and inverted hierarchies, respectively.

Neutrino oscillation experiments are not sensitive to the absolute mass scale of neutrinos, but can measure square differences between the different mass eigenstates. Accelerator- and atmospheric-based neutrino oscillation experiments have measured the so-called *atmospheric mass splitting*, which is currently [15]

$$\Delta m^2_{\text{atm}} \equiv \Delta m^2_{31} = (2.51 \pm 0.05) \cdot 10^{-3}\ \text{eV}^2 \tag{1.7}$$

Reactor- and solar-based neutrino oscillation experiments, on the other hand, have measured the *solar mass splitting* [15]

$$\Delta m^2_{\odot} \equiv \Delta m^2_{12} = (7.37 \pm 0.16) \cdot 10^{-5}\ \text{eV}^2 \tag{1.8}$$

Notice that these results do not establish the ordering the neutrino mass eigenstates, and there are two possibilities: the normal and the inverted hierarchies (orderings). This is illustrated in Figure 1.2, where the normal hierarchy represents the state where Δm_{atm} is positive and the inverted hierarchy the state in which Δm_{atm} is negative. Table 1.1 summarizes the current knowlegde of the neutrino mixing parameters from a global fit of the current neutrino oscillation data [15].

Other type of experiments may resolve the so-called *hierarchy problem*. That is the case neutrino oscillations in matter [28, 29, 30], interference in neutrino oscillations [31] and neutrinoless double beta decay (Chapter 2).

Parameter	Unit	Hierarchy	Best fit value	3-σ range
Δm^2_{21}	10^{-5} eV^2	Any	7.37	6.93 - 7.96
Δm^2_{31}	10^{-3} eV^2	NH	2.525	2.411 - 2.646
Δm^2_{23}	10^{-3} eV^2	IH	2.505	2.390 - 2.624
s^2_{12}	-	Any	0.297	0.250 - 0.354
s^2_{23}	-	NH	0.425	0.381 - 0.615
s^2_{23}	-	IH	0.589	0.384 - 0.636
s^2_{13}	-	NH	0.0215	0.0190 - 0.0240
s^2_{13}	-	IH	0.0216	0.0190 - 0.0242
δ	π rad	NH	1.38	0 - 0.17 $\oplus$ 0.76 - 2
δ	π rad	IH	1.31	0 - 0.15 $\oplus$ 0.69 - 2

Table 1.1: Current limits on the neutrino mixing parameters from a global fit to the current neutrino oscillation data [15].

1.2 Dirac neutrinos

As described in Section 1.1, neutrinos are classified as leptons. In the SM, leptons are grouped in three family flavors, organized as weak-isospin doublets:

$$L^L_\ell = \begin{pmatrix} \nu_\ell \\ \ell \end{pmatrix}_L \quad \text{with} \quad \ell = (e, \mu, \tau), \tag{1.9}$$

where L (for left-handed) references to the negative helicity component. For massless neutrinos, the chiralily and helicity eigenstates coincide, which implies the non-existence of the right-handed (R) helicity (positive chirality) component. This was supported by experimental data until the late 1960s when neutrino oscillations were observed and the mass of the neutrinos had to be different from zero. Since neutrinos are massive, the R component must be considered within the theory.

In the SM, all fermion masses arise from Yukawa couplings of the fermion fields to the Higgs doublet. For charged leptons, the lagrangian is[4] [32]:

$$-\mathcal{L}_{Yukawa} = \sum_{\alpha,\beta=e,\mu,\tau} Y^\ell_{\alpha,\beta}\ \overline{L^L_\alpha}\ \Phi\ \ell^R_\beta\ +\ h.c. \tag{1.10}$$

where $\Phi = (\Phi^+ \quad \Phi^0)^T$ is the Higgs doublet, ℓ^R is the weak-isospin singlet and Y^ℓ is a 3×3 complex matrix of Yukawa couplings. Since the *vacuum expectation value* (VEV) of the Higgs fields is not zero[5], Equation 1.10 can be rewritten in the *unitary gauge* as [32]:

[4] Here, *h.c.* stands for hermitian conjugate.
[5] This is the so-called *spontaneous electroweak symmetry breaking.*

$$-\mathcal{L}_{Yukawa} = \left(\frac{v+H}{\sqrt{2}}\right) \sum_{\alpha=e,\mu,\tau} y_\alpha^\ell \; \overline{\ell_\alpha^L} \; \ell_\alpha^R \; + \; h.c. \tag{1.11}$$

where v is the Higgs' VEV, H is the Higgs boson field and y_α^ℓ are the Yukawa couplings. From Equation 1.11, the mass of charged leptons is taken as

$$m_\alpha = \frac{v \; y_\alpha^\ell}{\sqrt{2}}. \tag{1.12}$$

The parameters y_α^ℓ cannot be extracted from the theory and therefore must be obtained from experimental data.

The same formalism can be used to give mass to neutrinos. This is known as the *Dirac mass term* and consists in introducing the positive-chirality components (ν_R) of the neutrino fields to the lagrangian from Equation 1.10:

$$\begin{aligned} -\mathcal{L}_{Yukawa} = & \sum_{\alpha,\beta=e,\mu,\tau} Y_{\alpha,\beta}^\ell \; \overline{L_\alpha^L} \; \Phi \; \ell_\beta^R \\ & + \sum_{\alpha,\beta=e,\mu,\tau} Y_{\alpha,\beta}^\ell \; \overline{L_\alpha^L} \; \Phi^C \; \nu_\beta^R \\ & + \; h.c. \end{aligned} \tag{1.13}$$

where Φ^C is the charge-conjugate of Φ. Thus, in the unitary gauge, the Dirac mass term for neutrinos is:

$$\begin{aligned} -\mathcal{L}_{\text{mass}}^D &= \sum_{\alpha=e,\mu,\tau} \frac{v \; y_\alpha^\nu}{\sqrt{2}} \; \overline{\nu_\alpha^L} \; \nu_\alpha^R + h.c. \\ &= \sum_{\alpha=e,\mu,\tau} m_\alpha^D \; \overline{\nu_\alpha} \; \nu_\alpha, \end{aligned} \tag{1.14}$$

where $\nu = \nu_L + \nu_R$ and $m_\alpha^D = v\, y_\alpha^\nu/\sqrt{2}$. In order to match these theoretical expressions with experimental data, the Yukawa couplings must be of the order of 10^{-12}. This value contrasts with the values found for other leptons, which go from 10^{-6} (e) to 10^{0} (τ). The unusual gap between neutrino couplings and the electron coupling (see Figure 1.3) raises the question of whether the neutrinos are *the same type of particle* as the other leptons or they have some property that makes them have such small masses. Since these couplings cannot be predicted by the theory, there is no real reason to consider them incorrect, but at the theoretical level, they are somewhat unsatisfactory [32, 33, 34, 35].

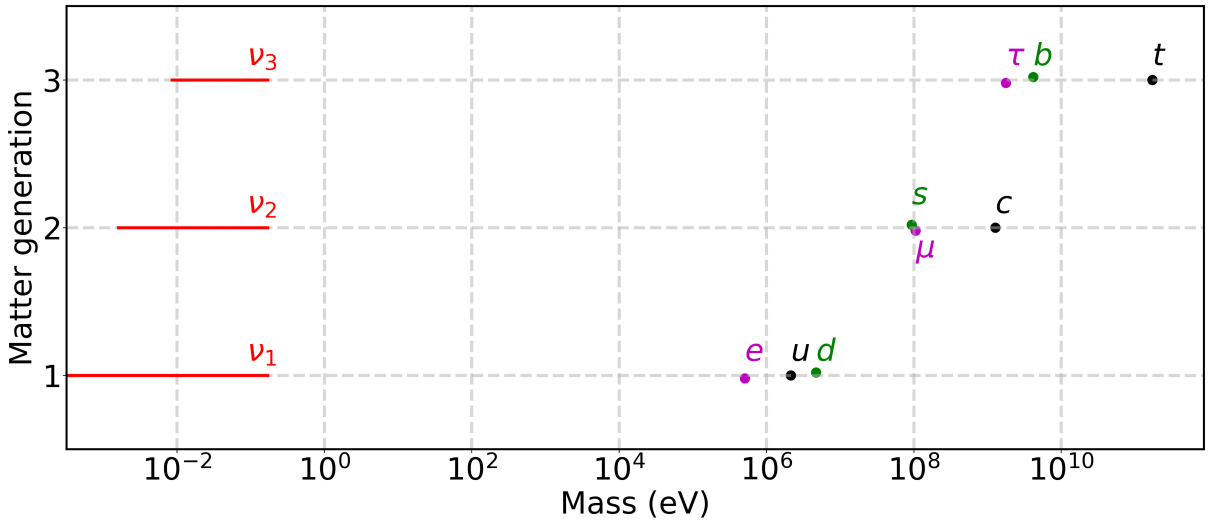

Figure 1.3: Graph of the masses of the SM fermions illustrating the hierarchical structure found in nature. This representation illustrates the enormous gap between neutrino masses and the rest of fermions. This figure assumes normally-ordered neutrinos, but a similar one is found for the inverted hierarchy. Mass values are taken from [19].

1.3 Majorana neutrinos

In 1937, Ettore Majorana realized that two of the four degrees of freedom in the spinor field of a massive neutral particle could be reduced by imposing the following condition [36]:

$$\nu^C = \nu \tag{1.15}$$

where ν^C is the charge-conjugate of ν. This condition implies the equivalence of the particle and its antiparticle, which can only be achieved in neutral leptons and that is the case of neutrinos. Only one state (either ν or ν^C) is needed to describe both neutrino and antineutrino states. Decomposing the neutrino field into its chiral components and applying Equation 1.15 yields the relation those components must satisfy:

$$\nu_R = {\nu_L}^C \tag{1.16}$$

The *Majorana mass term* for the Lagrangian can be constructed by applying Equation 1.16 to Equation 1.14:

$$-\mathcal{L}^{M,L}_{\text{mass}} = \frac{1}{2}\, m_L\, \overline{{\nu_L}^C}\, \nu_L \;+\; h.c., \tag{1.17}$$

where $m_L = v\, y^\nu/\sqrt{2}$ is a free parameter of the theory related to the Higgs VEV. This is the mass term associated to negative-chirality neutrino fields, but the one for the positive-chirality counterpart can also be contructed as:

$$-\mathcal{L}^{M,R}_{\text{mass}} = \frac{1}{2}\, m_R\, \overline{\nu_R^C}\, \nu_R \;+\; h.c. \tag{1.18}$$

The difference between Equation 1.17 and Equation 1.18 is that the former contains the weak-isospin doublets that interact with the Higgs while the latter is a singlet and is not coupled to that field. Thus, the parameter m_R is independent from the Higgs coupling and can take a more sensible value than m_L. This is the base of the *seesaw mechanism* (Section 1.3.1), which may be responsible for the small values of the neutrino masses.

The mass terms Equation 1.14, Equation 1.17 and Equation 1.18 transform negative-(positive-) chirality states into their positive (negative) counterparts. On top of that, Equation 1.17 and Equation 1.18 also turn particles into antiparticles, resulting in a violation of the *total lepton number* (LNV) of two units ($|\Delta L| = 2$).

1.3.1 The seesaw mechanism

As discussed in Section 1.1, the SM does not consider neutrinos as massive particles, which clashes with the findings about neutrino oscillations. Thus, the SM must be extended to include right-handed neutrinos. The most general mass term within the SM is the addition of the positive-chirality mass term from Equation 1.18:

$$\mathcal{L}^{D+M}_{\text{mass}} = \mathcal{L}^{D}_{\text{mass}} + \mathcal{L}^{M,R}_{\text{mass}}. \tag{1.19}$$

It is convinient to reformulate Equation 1.19 as:

$$-\mathcal{L}^{D+M}_{\text{mass}} = \frac{1}{2}\, \overline{\mathcal{N}_L^C}\, M\, \mathcal{N}_L \;+\; h.c., \tag{1.20}$$

where $\mathcal{N}_L$is the negative-chirality doublet

$$\mathcal{N}_L = \begin{pmatrix} \nu_L \\ \nu_R^C \end{pmatrix}, \tag{1.21}$$

and M is a matrix of masses which takes the following value:

$$M = \begin{pmatrix} 0 & m_D \\ m_D & m_R \end{pmatrix} \tag{1.22}$$

This non-diagonal matrix indicates that the chiral fields lack of a definite mass. In order to get the mass eigenstates, M must be diagonalized by finding the matrix U such that

$$U^T\, M\, U = \begin{pmatrix} m_1 & 0 \\ 0 & m_2 \end{pmatrix}, \tag{1.23}$$

where $\mathcal{N}_L = U n_L$ with $n_L = (\nu_L \quad N_L)^T$. The eigenvalues $m_1$and m_2 are:

$$m_{1,2} = \frac{1}{2}\left(m_R \mp \sqrt{m_R^2 + 4m_D^2}\right) \tag{1.24}$$

These new fields are still negative-chirality ones because they came from purely negative-chirality ones, but they also have a definite mass. Now Equation 1.20 reads:

$$-\mathcal{L}_{\text{mass}}^{D+M} = \frac{1}{2}\left(m_1\ \overline{\nu_L^C}\ \nu_L + m_2\ \overline{N_L^C}\ N_L\right) + h.c. \tag{1.25}$$

Comparing Equation 1.25 with Equation 1.17 we see they share the same structure. From here, we can deduce that ν_L and N_L satisfy Equation 1.15 and are, therefore, Majorana particles.

The so-called *seesaw mechanism* is based on this lagrangian. As mentioned in Section 1.3, the positive-chirality fields do not acquire mass via the coupling to the Higgs field. This condition is key for the *seesaw mechanism* as the value of m_R can take any value while m_D remains in the same range as the other leptons' masses[6]. Within this premise we can assume a Yukawa coupling of the same order as the correspondent charged lepton ($m_D \sim m_\ell$) and a value for $m_R \gg m_D$ of the order of the electroweak scale. Using these values in Equation 1.24, we can deduce

$$m_1 \simeq \frac{m_D^2}{m_R} \qquad \text{and} \qquad m_2 \simeq m_R. \tag{1.26}$$

Hence, we obtain two extremely assymmetric states in terms of mass. By using some indicative values $m_D \sim 1$ MeV and $m_R \sim 10^6$ MeV, we obtain that m_1 could be in the order of meV while m_2 would be approximately 1 TeV. This mechanism would explain why neutrinos are so light, but introduces a new neutrino state N, which can be a hint of new-physics at a much larger energy scale.

The see-saw mechanism presented here is the simplest version. It can be easily generalized [32] to the three neutrino families to complete what is known as *type I see-saw*. In this case, each light neutrino (ν_i) is associated to a heavy neutrino (N_i). The mass matrix from Equation 1.22 is now a 6×6 mass matrix that reads

$$M = \begin{pmatrix} 0 & M_D^T \\ M_D & M_R \end{pmatrix} \tag{1.27}$$

where M_D and M_R are 3×3 complex matrices. The neutrino field in Equation 1.21 keeps the same form, but the $\nu_L$and ν_R^Ccomponents are redefined to give

$$\nu^L = \begin{pmatrix} \nu_e^L \\ \nu_\mu^L \\ \nu_\tau^L \end{pmatrix} \quad \text{and} \quad \nu_R^C = \begin{pmatrix} \nu_{s_1}^{R\,C} \\ \nu_{s_2}^{R\,C} \\ \nu_{s_3}^{R\,C} \end{pmatrix}, \tag{1.28}$$

[6]This is often described [32, 34, 35] as a more *natural* or *plausible* solution to the neutrino mass problem than a coupling that is significantly different than the others for no aparent reason.

where e, μ and τ represent the active lepton flavors and s_1, s_2 and s_3 label the sterile neutrino states. This mass matrix can be diagonalized to produce analogous results as before with three heavy neutrino fields, instead of just one.

It is interesting to consider the see-saw limit, in which the eigenvalues of M_R are much larger than those of M_D. In this scenario, the light and heavy neutrino mass matrices are decoupled and form a block-diagonal matrix $M \simeq \text{diag}\,(M_{\text{light}},\ M_{\text{heavy}})$. Analogously to Equation 1.26, these matrices are given by

$$M_{\text{light}} \simeq -{M_D}^T {M_R}^{-1} M_D \quad \text{and} \quad M_{\text{heavy}} \simeq M_R. \tag{1.29}$$

M_{light} is usually referred to as the *neutrino mass matrix*, which, when diagonalized, provides the value of the mass eigenstates in Equation 1.1 as

$$U^T M_{\text{light}} U = \text{diag}\,(m_1, m_2, m_3) \tag{1.30}$$

where U is the PMNS matrix.

Furthermore, there are more ellaborate variations of this formalism in the literature. In particular, the so-called *type II seesaw mechanism* [32] assumes equal proportion of left- and right-handed components for the neutrino field. In this case, the mass term associated to the left-handed component is no longer zero and the eigenvalues are slightly different. Notwithstanding, the seesaw mechanism in all its variations offers an elegant solution to the neutrino mass problem and creates a portal to new physics beyond the SM.

1.4 What if neutrinos were Majorana particles?

The implications of Equation 1.15 are profound. It could for example explain why our universe is made enterely of matter. Our current understanding of the universe is based on inflationary models, which predict a matter-antimatter symmetry as the inflation phase would dilute any initial deviation from equal abundance [37]. Within these models, the baryon assymmetry, i.e. the difference between the number densities of baryons and antibaryons relative to the number of photons (η) would be negligible [38]. However, the measurements of baryon asymmetry from the *Big Bang nucleosynthesis* (BBN) and the *cosmic microwave background* (CMB) observations reveal consistent results with a matter-only universe [38]:

BBN: $\quad 5.8 \cdot 10^{-10} \leq \eta \leq 6.6 \cdot 10^{-10}, \qquad 95\ \%\ \text{CL}\ [19]$

CMB: $\qquad \eta = (6.09 \pm 0.06) \cdot 10^{-10}\ [19]$

Thus, there is concluding evidence that the asymmetry between matter and antimatter is not caused by the initial condition of the universe but rather by some dynamic process(es) that introduces the asymmetry. These processes are collectively called *baryogenesis*.

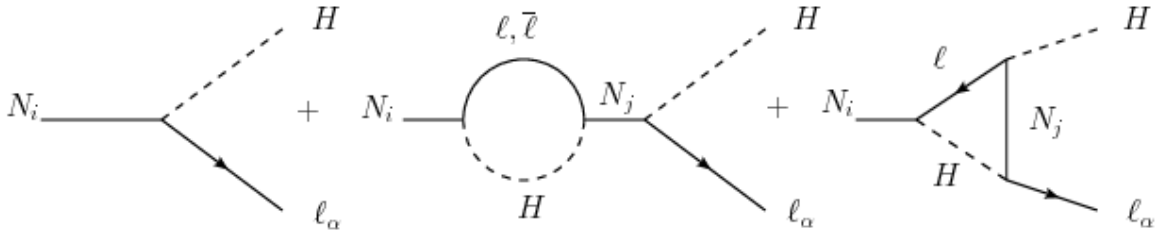

Figure 1.4: Feynman diagrams describing the decay of the heavy Majorana neutrino N_i into the Higgs boson (H) and a lepton (ℓ_α). The three main contributions to this process of leptogenesis are the tree-level diagram (left), the one-loop self-energy correction (center) and the one-loop vertex diagram (right). Figure from [42].

The conditions that any baryon-generating process must satisfy in order to produce the asymmetry observed today were proposed by Andrei Sakharov in 1966 [39]. Those conditions are:

1. Violation of the baryon number.
2. Violation of both $\mathcal{C}$ and $\mathcal{CP}$ symmetries.
3. The universe went through a stage of non-equilibrium.

Whilst these constrains are known to be considered within the SM, the baryon asymmetry observed is much higher than the one the $\mathcal{CP}$ violation in the quark sector can produce. Consequently, some other process or processes must account for the difference.

Among the multiple mechanisms to produce baryogenesis [40], it is particularly interesting for this work to discuss *leptogenesis* [37, 41]. This process, analogous to baryogenesis, produces an asymmetry in the leptonic sector and it is only possible if neutrinos are Majorana particles. It is based on the decay of the heavy neutrinos predicted by the see-saw mechanism described in Section 1.3.1, which could, in principle, produce regular leptons (ℓ_α) and Higgs bosons (H) as shown in Figure 1.4.

The aforementioned conditions are satisfied in this mechanism:

1. Since they are Majorana particles, they are their own antiparticle and can decay to both $\ell_\alpha\phi$ and $\bar{\ell_\alpha}\bar{\phi}$. An asymmetry in the decay rate of these two channels would produce a lepton asymmetry, which can be converted to a baryon asymmetry via the *sphaleron process* [37]. This is an mechanism that can efficiently convert antileptons to barions, provided the sphaleron density was high enough at some stage of the universe evolution.
2. $\mathcal{C}$- and $\mathcal{CP}$-symmetries are potentially violated in these processes as long as there is more than one heavy neutrino field.
3. A non-equilibrium stage can be produced if the decay rate was slower than the expansion rate of the universe when the temperature of the universe was of the order of the mass of the heavy neutrino.

The asymmetry in lepton flavor is defined as

$$\epsilon_{\alpha\alpha} = \frac{\Gamma\left(N_1 \to \phi\ell_\alpha\right) - \Gamma\left(N_1 \to \bar{\phi}\bar{\ell_\alpha}\right)}{\Gamma\left(N_1 \to \phi\ell_\alpha\right) + \Gamma\left(N_1 \to \bar{\phi}\bar{\ell_\alpha}\right)}, \tag{1.31}$$

where Γ stands for decay rate of the corresponding channel. For this process to describe the baryon asymmetry observed in the universe, $|\epsilon_{\alpha\alpha}| > 10^{-7}$ [37]. While Majorana neutrinos would not neccesarily imply the existence this mechanism, it would make it very feasible, especially if we take into account the findings of neutrino oscillations, which imply violation of the $\mathcal{CP}$ symmetry in the leptonic sector.

1.5 Discerning between Dirac and Majorana neutrinos

The nature of neutrinos (whether they are Dirac or Majorana particles) is still unknown, but there are multiple experimental efforts trying to solve this mistery in the field of neutrino research. As discussed in Section 1.3, the existence of Majorana neutrinos can lead to physical processes that violate lepton number conservation in two units. There are multiple proposals to determine the nature of neutrinos and they are all based on the observation of a $|\Delta L| = 2$ process.

The observation of the channel discussed in Section 1.4 is not suitable for a laboratory-based experiment as the energy scale to be explored is far beyond our current capabilities. However, the existance of neutrino mass mixing provides a prolific phenomenology that can be tested in the laboratory. The simplest lepton number violating process is mediated by

$$W^- W^- \to \ell_\alpha^- \ell_\beta^-, \tag{1.32}$$

with $\alpha, \beta = e, \mu, \tau$. If the exchange of light Majorana neutrinos is the only lepton flavor violating mechanism contributing to this process, the matrix element for Equation 1.32 is

$$M_{\alpha\beta}^{\text{light}} = \left[U^* \text{diag}\left(m_1, m_2, m_3\right) U^\dagger\right]_{\alpha\beta} = \sum_{i=1}^{3} U_{\alpha i}^* U_{\beta i}^* m_i, \tag{1.33}$$

where m_i are the light neutrino mass eigenstates, U is the PMNS matrix and M^{light} is the mass matrix from Equation 1.29. This is the so-called effective neutrino mass of a given process and is handy to compare different $|\Delta L| = 2$ processes. The most fruitful searches for LNV processes are summarized in Table 1.2. Neutrinoless double beta decay (Chapter 2) searches are the most succesful observations in terms of imposing limits to effective masses.

There are also some efforts in trying to observe channels mediated by heavy Majorana neutrinos in accelerator-based experiments [43, 44, 45] and in measuring the light-heavy components of the extended version of the PMNS matrix [46].

Flavors	Exp. technique	Exp. bound	Mass bound (eV)
(e,e)	$\beta\beta0\nu$	$T_{1/2}(^{136}\mathrm{Xe} \to {}^{136}\mathrm{Ba} + 2e^-) > 1.07 \times 10^{26}$ yr	$\lvert m_{ee}\rvert < 0.165$
(e,μ)	$\mu^- \to e^+$ conversion	$\Gamma(\mathrm{Ti} + \mu^- \to e^+ + \mathrm{Ca_{gs}})$ / $\Gamma(\mathrm{Ti} + \mu^-\mathrm{capture}) < 1.7 \times 10^{-12}$	$\lvert m_{e\mu}\rvert < 1.7 \times 10^{7}$
(e,τ)	Rare τ decays	$\Gamma(\tau^- \to e^+\pi^-\pi^-)/\Gamma_{\mathrm{tot}} < 8.8 \times 10^{-8}$	$\lvert m_{e\tau}\rvert < 2.6 \times 10^{12}$
(μ,μ)	Rare kaon decays	$\Gamma(K^+ \to \pi^-\mu^+\mu^+)/\Gamma_{\mathrm{tot}} < 1.1 \times 10^{-9}$	$\lvert m_{\mu\mu}\rvert < 2.9 \times 10^{8}$
(μ,τ)	Rare τ decays	$\Gamma(\tau^- \to \mu^+\pi^-\pi^-)/\Gamma_{\mathrm{tot}} < 3.7 \times 10^{-8}$	$\lvert m_{e\tau}\rvert < 2.1 \times 10^{12}$
(τ,τ)	—	—	—

Table 1.2: Current limits on the effective neutrino masses from the most competitive total lepton number violating processes. The values are displayed according to the flavors involved. Numbers taken (or derived) from [19, 47].

USC
UNIVERSIDADE
DE SANTIAGO
DE COMPOSTELA

2 The double beta decay for Majorana neutrinos

2.1 Decay modes

The double beta decay ($\beta\beta$) is a nuclear process in which two neutrons β-decay simultaneously within the same nucleus. In the ordinary decay mode ($\beta\beta^{2\nu}$), a nucleos with atomic number Z is transformed into its isobar with atomic number Z + 2 emitting two electrons and two electron antineutrinos without going through the intermediate Z + 1 isotope:

$$ {}^{A}_{Z}\mathrm{X} \rightarrow {}^{A}_{Z+2}\mathrm{Y} + 2\ e^{-} + 2\ \bar{\nu}_{e} \tag{2.1} $$

This second-order process was first considered by Maria Goeppert-Mayer in 1935 [48]. Albeit there has been geochemical evidence of its existance since 1950 [49], a direct measurement of the decay was not performed until 1987 when the half-life of ^{82}Se was measured to be $T_{1/2}(^{82}\mathrm{Se}) = \left(1.1^{+0.8}_{-0.3}\right) \cdot 10^{20}$ y [50]. Multiple observations in different isotopes have been reported ever since with half-lives in the range 10^{17} to 10^{21} years. These are the longest radioactive decay half-lives ever measured. In Table 2.1 a summary of the current best $\beta\beta^{2\nu}$ half-life measurements is presented.

For this process process to be measurable, the single β decay must be energetically forbidden or, at the very least, very highly suppressed as the former is much slower. This is depicted in Figure 2.1, where the $A = 136$ mass parabola is shown. In this example, ^{136}Xe cannot undergo β-decay to ^{136}Cs because it is less bound. Instead, ^{136}Xe can decay via $\beta\beta$ to ^{136}Ba, which is more stable.

The $\beta\beta$ decay is theoretically predicted for 35 isotopes due to the nuclear pairing force, which makes even-even nuclides more bound than their odd-odd isobars (see Figure 2.1). In the scenario of neutrinos being Majorana particles there is an open door for a different decay mode without the emission of neutrinos ($\beta\beta^{0\nu}$), the so-called neutrinoless double beta becay:

Isotope	Mode	Transition	$T_{1/2}$ (y)	Method
^{48}Ca	$\beta^-\beta^-$		$(6.4\ ^{+0.7}_{-0.6}\ ^{+1.2}_{-0.9}) \cdot 10^{19}$	NEMO-3 [51]
^{76}Ge	$\beta^-\beta^-$		$(1.926 \pm 0.094) \cdot 10^{21}$	GERDA [52]
^{78}Kr	$\varepsilon\varepsilon$		$(9.2^{+5.5}_{-2.6} \pm 1.3) \cdot 10^{21}$	BAKSAN [53]
^{82}Se	$\beta^-\beta^-$		$(9.6 \pm 0.3 \pm 1.0) \cdot 10^{19}$	NEMO-3 [54]
^{96}Zr	$\beta^-\beta^-$		$(23.5 \pm 1.4 \pm 1.6) \cdot 10^{18}$	NEMO-3 [55]
^{100}Mo	$\beta^-\beta^-$		$(69.0 \pm 1.5 \pm 3.7) \cdot 10^{17}$	CUPID [56]
^{100}Mo	$\beta^-\beta^-$		$(69.3 \pm 0.4) \cdot 10^{17}$	NEMO-3 [57]
^{100}Mo	$\beta^-\beta^-$	$0^+ \to 0^+_1$	$(6.9^{+1.0}_{-0.8} \pm 0.7) \cdot 10^{20}$	Ge coincidence [58]
^{100}Mo	$\beta^-\beta^-$	$0^+ \to 0^+_1$	$(5.7^{+1.3}_{-0.9} \pm 0.8) \cdot 10^{20}$	NEMO-3 [59]
^{116}Cd	$\beta^-\beta^-$		$(27.4 \pm 0.4 \pm 1.8) \cdot 10^{18}$	NEMO-3 [60]
^{116}Cd	$\beta^-\beta^-$		$(29^{+4}_{-3}) \cdot 10^{18}$	$^{116}CdWO_4$ scint. [61]
^{130}Te	$\beta^-\beta^-$		$(8.2 \pm 0.2 \pm 0.6) \cdot 10^{20}$	CUORE-0 [62]
^{130}Te	$\beta^-\beta^-$		$(7.0 \pm 0.9 \pm 1.1) \cdot 10^{20}$	NEMO-3 [63]
^{136}Xe	$\beta^-\beta^-$		$(2.165 \pm 0.016 \pm 0.059) \cdot 10^{21}$	EXO-200 [64]
^{136}Xe	$\beta^-\beta^-$		$(2.38 \pm 0.02 \pm 0.14) \cdot 10^{21}$	KamLAND-Zen [65]
^{150}Nd	$\beta^-\beta^-$		$(93.4 \pm 2.2^{+6.2}_{-6.0}) \cdot 10^{17}$	NEMO-3 [66]

Table 2.1: Half-lives of the $\beta\beta$-emitting isotopes that have been measured so far. Only the measurements with the smallest or comparable uncertainty for each transition are listed. In the cases where multiple uncertainties are specified, the former corresponds to the statistical and the latter to the systematic.

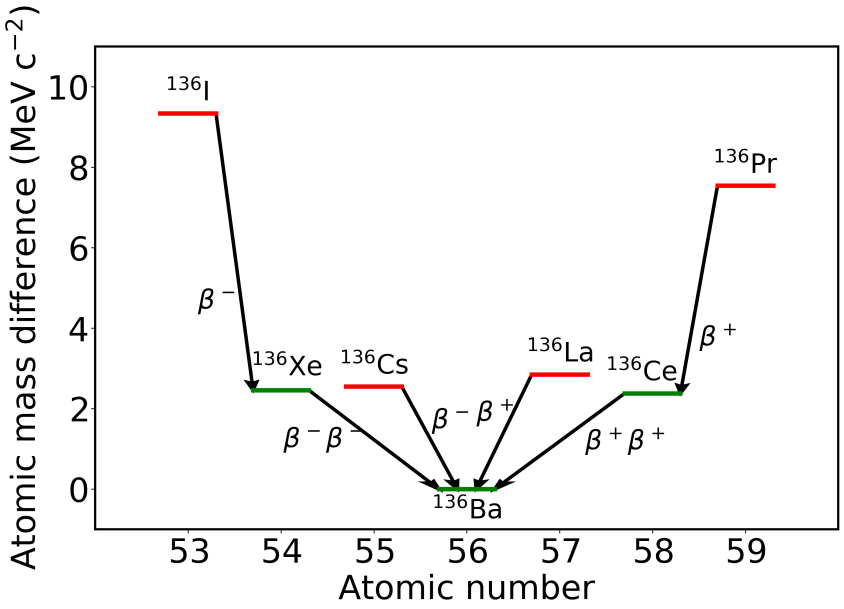

Figure 2.1: Atomic masses of isotopes with $A = 136$ relative to the most bound isotope, ^{136}Ba. Green lines label the pair-pair isotopes, which are in general more bound than the odd-odd ones, represented by red lines. The transition each nucleus can undergo is indicated by the black arrows. While the odd-odd nuclei can β-decay to the correspondent pair-pair ones, $\beta\beta$ decay to ^{136}Ba is the only possibility for ^{136}Xe and ^{136}Ce as the transition to the odd-odd isotope is energetically forbidden.

$$ {}^{A}_{Z}\mathrm{X} \rightarrow {}^{A}_{Z+2}\mathrm{Y} + 2\, e^{-}. \tag{2.2} $$

First proposed in 1939 by Wendell H. Furry [67], the $\beta\beta^{0\nu}$ is a $|\Delta L| = 2$ process useful to probe the nature of neutrinos. In spite of the experimental effort, there has not been any accepted experimental evidence to support the existence of this decay mode (see Section 2.6.1 for a discussion on previous searches).

There are both similarities and differences between the two decay modes. In both transitions the nuclear recoil is negligible and the emitted leptons carry virtually all energy. In all isotopes, the transition begins in a 0^+ ground state and in most of the isotopes the transition goes to a 0^+ ground state independently of the mode[1]. The involvement of two weak processes (see Figure 2.4), makes both modes intrinsically slow, as the decay rate is proportional to G_F^4.

On the other hand, unlike $\beta\beta^{2\nu}$, the neutrinoless double beta decay is a process forbidden in the SM. In the SM-allowed mode the neutrons are considered to be uncoupled, but in the $\beta\beta^{0\nu}$ mode they are necessarily correlated (see Section 2.3). Phase space availability makes the neutrinoless mode more favorable. However, its decay rate is suppresed by a proportionality to the tiny neutrino masses which nullifies this effect and makes the rate even slower.

The biggest discrepancy comes from the spectrum of the sum of kinetic energies of the emitted electrons. The lack of neutrinos in the $\beta\beta^{0\nu}$ mode makes its energy spectrum a mono-enertetic

[1]In some cases the transition to an excited 0^+ or 2^+ state is possible, yet highly suppressed due to the reduced phase space available.

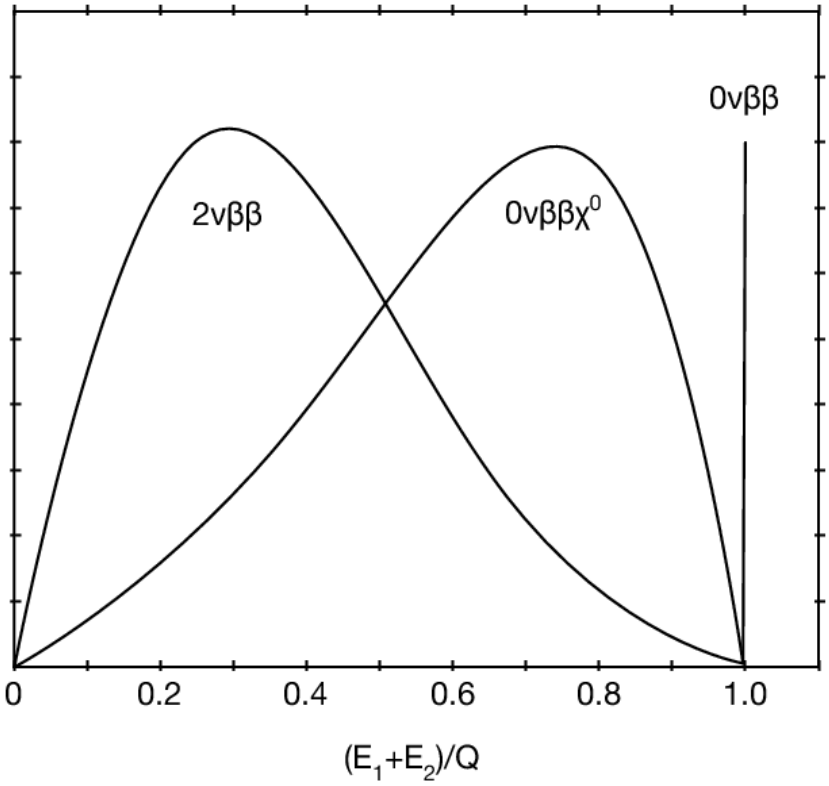

Figure 2.2: Spectra for the sum of the kinetic energies of the outcoming electrons in three different modes of the $\beta\beta$ decay: $\beta\beta^{2\nu}$, $\beta\beta^{0\nu}$ and $\beta\beta^{0\nu}$ with Majoron emission (see Section 2.4). The amplitudes are not representative of the actual decay rates.

line at $Q_{\beta\beta}$, the Q-value of the reaction, defined as:

$$Q_{\beta\beta} = M({}^{A}_{Z}\mathrm{X}) - M({}^{A}_{Z+2}\mathrm{Y}). \tag{2.3}$$

On the other hand, in the $\beta\beta^{2\nu}$ case the energy is shared among electrons and neutrinos. Thus, the spectrum goes from 0 to $Q_{\beta\beta}$ and is continuous, peaking below $Q_{\beta\beta}$ / 2.

Furthermore, Majorana neutrinos open the door to some other closely related LNV nuclear processes, listed in Table 2.2. From the theoretical point of view, these processes are identical to the $\beta\beta^{0\nu}$ one. Notwithstanding, from the experimental point of view, they are not as suitable as those undergoing the regular $\beta\beta$ decay. The lack of phase space for the $\beta^{+}\beta^{+0\nu}$ and $\beta^{+}\varepsilon^{0\nu}$ decays [68, 69, 70] and the underdevelopment of the experimental technique in the $\varepsilon\varepsilon^{0\nu}$ field makes an experiment of this type less convenient. Having said that, the research in those directions should also be explored. It would help understand and improve nuclear models and reinforce the experimental evidence of Majorana neutrinos (if that is the case) by observing its multiple manifestations.

Name	Symbol	Diagram
Double positron emission	$\beta^+\beta^{+0\nu}$	${}^{A}_{Z}\mathrm{X} \rightarrow {}^{A}_{Z-2}\mathrm{Y}$
Positron emission plus electon capture	$\beta^+\varepsilon^{0\nu}$	${}^{A}_{Z}\mathrm{X} + e^- \rightarrow {}^{A}_{Z-2}\mathrm{Y} + e^+$
Double electron capture	$\varepsilon\varepsilon^{0\nu}$	${}^{A}_{Z}\mathrm{X} + 2\,e^- \rightarrow {}^{A}_{Z-2}\mathrm{Y}^*$

Table 2.2: LNV nuclear processes analogous to the neutrinoless double beta becay. These processes become possible if neutrinos are Majorana particles.

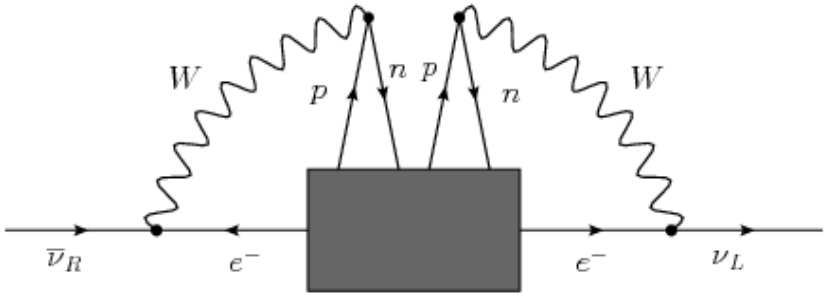

Figure 2.3: Diagram of the *black box theorem* demonstrating how any neutrinoless double beta decay mechanism induces a transition from $\bar{\nu}$ to ν. This translates into an effective Majorana mass term. See text for details.

2.2 The black box theorem

There are multiple beyond-SM theories predicting $|\Delta L| = 2$ processes in the literature and all of them can lead to neutrinoless double beta decay. Besides, regardless of the mechanism, the existence of $\beta\beta^{0\nu}$ implies that neutrinos are Majorana particles. This was proved by Schechter and Valle in 1982 [71]. They realized that any LNV diagram contributing to the decay would also make a contribution to $(m_\nu)_{ee}$ in the neutrino mass matrix (Equation 1.33). This is the so-called *black box theorem* and is illustrated in the diagram of Figure 2.3. In this representation, a $\bar{\nu_e} \rightarrow \nu_e$ transition is induced via any LNV operator responsible for the neutrinoless double beta decay. Such transition implies a non-zero value for $(m_\nu)_{ee}$.

Notwithstanding, the small mass generated at four-loop level cannot explain the mass splittings observed in neutrino oscillations [72, 73]. Thus, other still unkwown Dirac or Majorana mass contributions must exist. Besides, the theorem can either clarify which mechanism is the dominant contribution to $\beta\beta^{0\nu}$ and it could, therefore, be directly or inderectly connected to neutrino oscillations or not connected at all [72]. The standard mechanism discussed in Section 2.3 is a case of direct connection.

2.3 The standard neutrinoless double beta mechanism

The simplest version of a neutrinoless double beta decay is depicted in the diagram of Figure 2.4. Here, two d quarks from different neutrons emit a pair of virtual W bosons, which exchange a light Majorana neutrino to produce the outcoming electrons. As mentioned before, this diagram

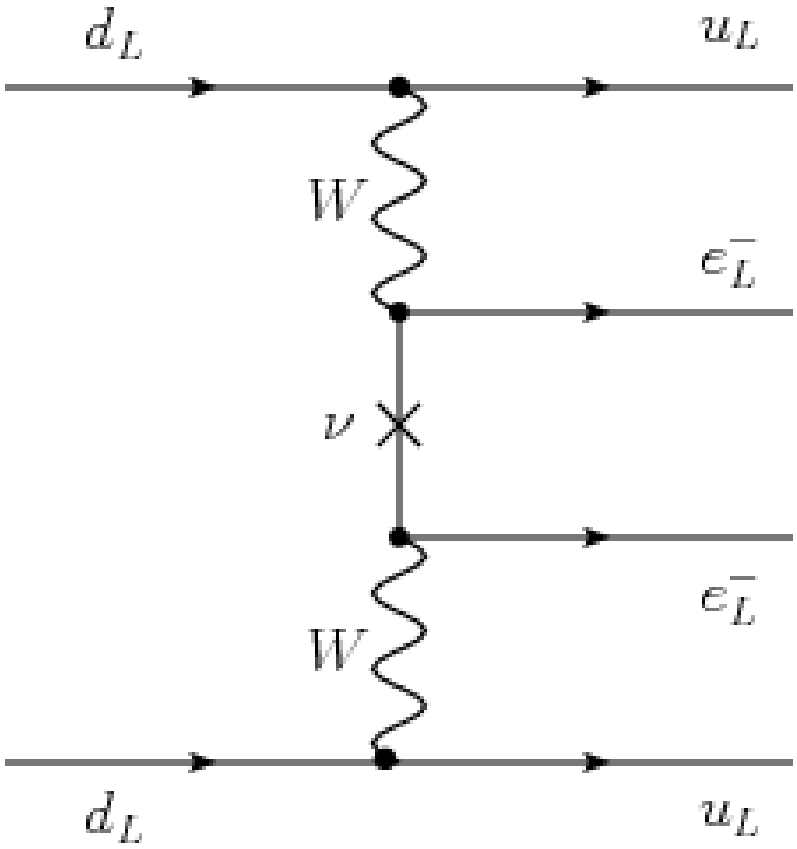

Figure 2.4: Feynman diagram of the standard mechanism of the neutrinoless double beta decay. Two neutrons within the same nucleus emit a W boson each, which exchange a light Majorana neutrino and produce two electrons.

is only possible in the case of massive Majorana neutrinos.

We can interpret this neutrino exchange as one W boson producing an antineutrino with almost complete positive helicity, yet a tiny $\mathcal{O}(m_\nu/E)$ fraction of negative helicity, which is absorbed at the other W boson vertex. Since there are three light neutrino mass states (ν_i), the total contribution to this diagram would be a sum over these states. Besides, the double vertex introduces a weight factor U_{ei}^2. Thus, the modulus of the amplitude of the $\beta\beta^{0\nu}$ decay must be proportional to the so-called *effective neutrino Majorana mass* defined as:

$$m_{\beta\beta} = \left| \sum_i U_{ei}^2 m_i \right| . \tag{2.4}$$

This effective mass is simply $m_{\beta\beta} \equiv |(m_\nu)_{ee}|$, i.e. the modulus of the electron-electron flavor of the neutrino mass matrix.

For the light Majorana neutrino exchange to dominate the decay, the masses of neutrinos contributing to the process must be below $\sqrt{Q} \sim 10^8$ eV. In this scenario, the half-life of the process can be written as [74]:

$$\left(T^{0\nu}_{1/2}\right)^{-1} = G^{0\nu} \left|M^{0\nu}\right|^2 \left(\frac{m_{\beta\beta}}{m_e}\right)^2. \tag{2.5}$$

Here, $G^{0\nu}(Q, Z)$ is a phase space factor and $\left|M^{0\nu}\right|$ is the nuclear matrix element (NME). While the former can be compute precisely ($\sim 0.1\%$ uncertainty), the NME depends on nuclear models, which are difficult to calibrate for the heavy nuclei that can undergo this decay. Despite the uncertainties, Equation 2.5 provides a method to infer $m_{\beta\beta}$ from the decay half-life. Even if no measurement of the decay half-life is achieved, we can set a lower bound to its value, which translates into an upper bound to $m_{\beta\beta}$.

In this mechanism, the decay is directly connected to neutrino oscillation phenomenology, provided light Majorana neutrino exchange is the dominant contribution to $\beta\beta^{0\nu}$. From 2.4 we can establish a connection between the observable value $m_{\beta\beta}$ and the neutrino masses. Hence, $\beta\beta^{0\nu}$ experiments can probe the absolute mass scale of neutrinos complementarily to cosmological observations. The individual neutrino mass eigenvalues can also be inferred. Despite being affected by the uncertainties in the oscillation parameters, the unknown phases of the mixing matrix and the ambiguity on the neutrino mass hierarchy, the relation between $m_{\beta\beta}$ and the lightes neutrino mass eigenstate (m_{light}) can be predicted with certain accuracy as shown in Figure 2.5. This graphical representation was first proposed by F. Vissani [75] and has become one of the most widely used schemes to measure the sensitivity of $\beta\beta$ experiments to the neutrinoless decay. The two bands in Figure 2.5 represent the inverted (green) and normal (red) neutrino hierarchies and their widths come from the 3-σ intervals around the best fit values of the oscillation and phase parameters. The grey area indicates the overall current limit on $m_{\beta\beta}$ and the right panel shows the best limits for the different isotopes under study by various $\beta\beta^{0\nu}$ experiments [57, 76, 77, 78].

The current generation of $\beta\beta^{0\nu}$ experiments have already reached the limit imposed by cosmological observations and the next generation will be able to explore the inverted hierarchy region. However, the latest results from neutrino oscillation experiments [79] and cosmological observations [80] tend to favor the normal ordering meaning that the experimental techniques need to be improved and larger scales achieved for the forthcoming generation.

Positive results for neutrino mass scale observables can shed some light on neutrino properties. For instance, the determination of the effective mass, m_β, in single beta decay experiments [27] in association with that of neutrinoless double beta decay can constrain the Majorana phases $\alpha_{1,2}$ in Equation 1.2 [81]. Inconsistent results among the different type of observations can also provide some understanding of the nature of neutrinos. For example, neutrinos would be proved to be Dirac particles if m_β and m_{cosmo} are in disagreement with $m_{\beta\beta}$. On the other hand, a value of $m_{\beta\beta}$ differing from theoretical predictions would point towards alternative mechanism for $\beta\beta^{0\nu}$ decay.

2.4 Alternative $\beta\beta^{0\nu}$ mechanisms

A number of non-standard $\beta\beta^{0\nu}$ mechanisms have been proposed by different authors [72]. These proposals differ from the standard mechanism discussed in Section 2.3 in one of more of the following features:

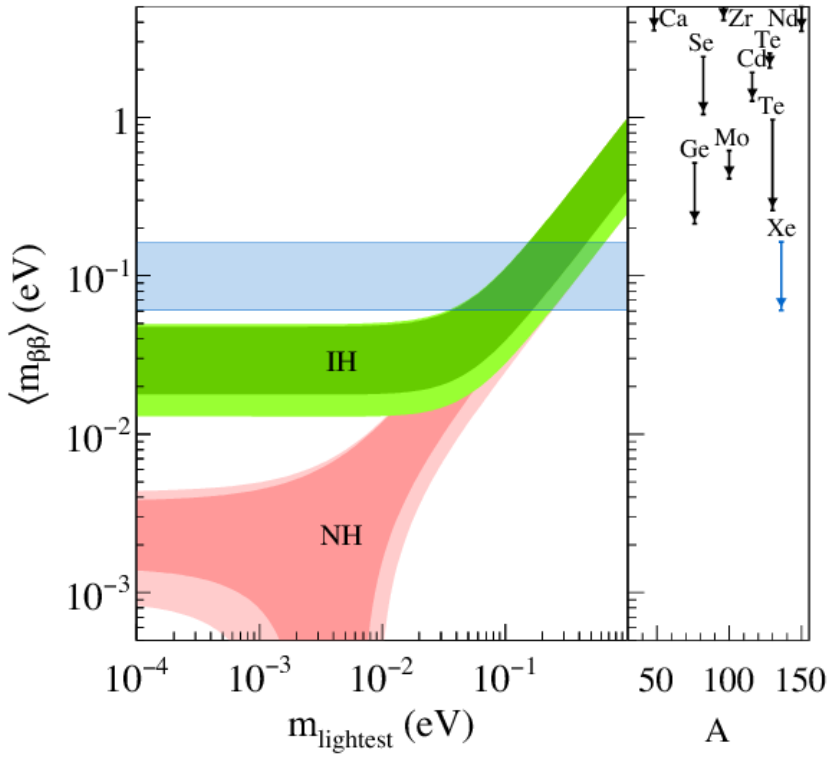

Figure 2.5: The effective Majorana mass, $m_{\beta\beta}$, as a function of the lighest neutrino mass m_{light}. The dark (light) green band represents the available values within a 1-σ (3-σ) range. The equivalent depiction is shown for the normal ordering in red. The horizontal shaded region marks the probed region from the latest KamLAND-Zen result [76]. The best experimental limits on $m_{\beta\beta}$ measured at a 90% CL for different nuclei are also shown in the side panel. Figure from [76].

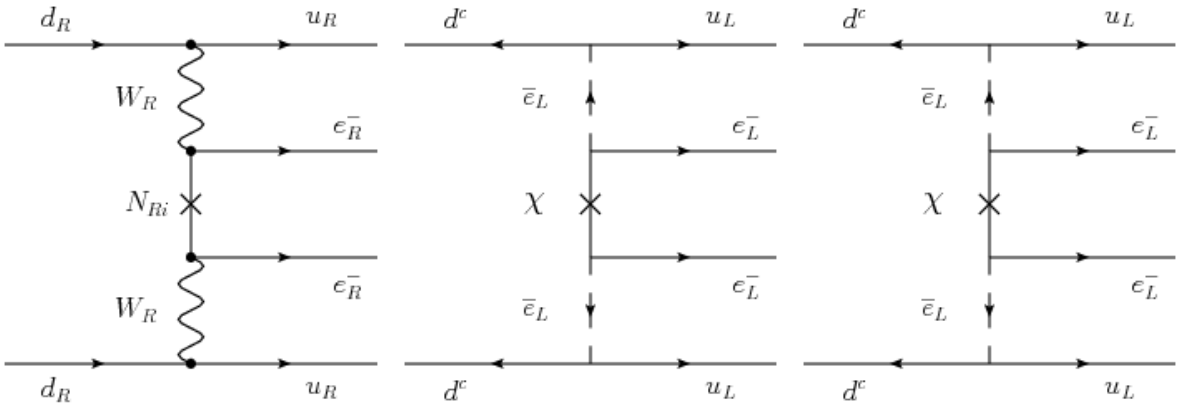

Figure 2.6: Feynman diagrams for the most common non-standard mechanisms for $\beta\beta^{0\nu}$ decay: (a) Heavy Majorana neutrino exchange with positive-chirality currents [82]; (b) Neutralino exchange in supersymmetry theories with R-parity violation [83]; (c) Majoron emission [84].

- The Lorentz structure of charged and neutral currents. For instance, in left-right symmetric theories we may have a W_R-mediated current. Heavy Majorana neutrinos can be the exchanged particle in this framework, as shown in Figure 2.6a.
- The energy scale of the exchanged virtual particles. There are two examples to this aspect: heavy Majorana neutrinos can replace the light Majorana neutrino in the diagram of Figure 2.4, and heavy supersymmetric neutral particles (e.g. the neutralino (χ)) can also be the exchanged of the decay in R-parity violating theories. This is depicted in Figure 2.6b.
- The number of outgoing particles. The most popular theory involves the emission of a Majoron, a very light (or massless) particle that can couple to neutrinos and be a subproduct of the neutrino exchange. This is displayed in Figure 2.6c.

The latter case is of special relevance for $\beta\beta^{0\nu}$ experiments. The Majoron emission would have an impact in the energy spectrum of the outcoming electrons as shown in Figure 2.2, provided their coupling to neutrinos is large enough. The resulting spectrum is continous and peaks above $Q_{\beta\beta}/2$. The first case can also be observable, in principle. The right-handness of the emitted electrons would be manifest in their angular and energy correlations.

2.5 The recipe for a $\beta\beta^{0\nu}$ experiment

The observation of the neutrinoless double beta decay would be a major breakthrough in particle physics. As discussed in Section 2.2, it would unequivovally certify the Majorana nature of neutrinos, the only kwown elementary particles of this kind. However, the rareness of the decay presents a major challenge to experimental searches. From Equation 2.5, we can predict that, in order to explore values of $m_{\beta\beta}$ of the order of 50 meV, an experiment needs to be sensible to half-lives of the order of 10^{26} years, depending on the NME and the isotope of choice. These such long half-lives have never been measured and, thus, the experimental techniques need to pushed to the limit.

The radioactive decay law can reveal a more tangible number to sense the impact of the half-life to the experimental challenge. For a given observation time t, the expected number of $\beta\beta^{0\nu}$ decays can be expressed as[2]:

$$N^{0\nu}_{\beta\beta} = \log 2 \cdot \frac{N_A}{W_{\beta\beta}} \cdot \epsilon \cdot \frac{M_{\beta\beta} \cdot t}{T^{0\nu}_{1/2}}, \tag{2.6}$$

where N_A is the Avogadro number, ϵ is the detection efficiency, and $W_{\beta\beta}$ and $M_{\beta\beta}$ are the molar mass and mass of the $\beta\beta$ emitter isotope. It is also useful to define the exposure as $M_{\beta\beta} \cdot t$. This comes in hand when comparing different experiments with different active masses and different observation times. From Equation 2.6, it follows that an experiment with 100 kg of emitter would observe one decay per year, assuming perfect detection efficiency and $m_{\beta\beta} \sim 50$ meV.

This scenario is, of course, unrealistic. In real-life experiments, the detection efficiency is far from perfect and background events reduce significantly the sensitivity to the $\beta\beta^{0\nu}$ decay. Thus, in order to provide a reference for the sensitivity of a $\beta\beta^{0\nu}$ experiment to $m_{\beta\beta}$ in a null-observation scenario, it is useful to define the figure of merit as the upper limit imposed to $m_{\beta\beta}$. For a background-free experiment with no observations, the combination of Equation 2.5 and Equation 2.6 yields:

$$\mathcal{S}(m_{\beta\beta}) = K_1 \sqrt{\frac{1}{\epsilon \cdot M_{\beta\beta} \cdot t}}, \tag{2.7}$$

where K_1 is an isotope-dependent constant[3]. The current generation of $\beta\beta^{0\nu}$ experiments is not background free and, consequently, the limit to $m_{\beta\beta}$ is not optimal. The number of background events (b) is integrated in Equation 2.7 as:

$$\mathcal{S}(m_{\beta\beta}) = K_2 \sqrt{\frac{\sqrt{b}}{\epsilon \cdot M_{\beta\beta} \cdot t}}, \tag{2.8}$$

where K_2 factors in K_1 and the proportionality of $\mathcal{S}(m_{\beta\beta})$ with the background. The background level is usually proportional to the exposure and to the energy window ΔE defined by the energy resolution of the detector:

$$b = c \cdot M_{\beta\beta} \cdot t \cdot \Delta E, \tag{2.9}$$

where c is the background rate. We will usually measure this number in ckky, i.e. counts per keV per kg and per year. Again, this facilitates the comparison among the different $\beta\beta^{0\nu}$ experiments[4]. Applying Equation 2.9, Equation 2.8 reads:

[2] Actually this equation is an approximation for $t \ll T_{1/2}$ Since the experiments are expected to run for a few years and the half-lives are $\sim 10^{17}$ times longer than the age of the universe, I think this is a safe approximation.

[3] The exact value of K_1 is $K_1^2 = \frac{W_{\beta\beta}}{N_A \cdot \log 2} \frac{m_e^2}{G^{0\nu} \cdot |M^{0\nu}|}$

[4] There are multiple techniques in the field with completely different mass scales and energy resolutions. As discussed in Section 2.6.2, KamLand-Zen is beginning his tonne-scale program with a resolution of ∼10 % FWHM while GERDA has ∼ 80 kg of mass and an energy resolution of 0.15 % FWHM.

$$\mathcal{S}(m_{\beta\beta}) = K_2 \epsilon^{-1/2} \sqrt[4]{\frac{c \cdot \Delta E}{M_{\beta\beta} \cdot t}}. \tag{2.10}$$

Since the aim of every experiment is to minimize $m_{\beta\beta}$ to explore the inverted (and eventually the normal) hierarchy in Figure 2.5, c and ΔE need to be minimized and the exposure and the detector efficiency, maximized. These quantities depend mainly on the isotope of choice and the experimental technique. In the following sections we will discuss how each variable can be optimized.

2.5.1 Exposure

As discussed in Section 2.5, in order to reduce the observation time to feasible values (i.e. $\mathcal{O}$(years)), large masses ($\sim 10^2$ kg)) of $\beta\beta$-emitting isotopes are needed. Besides, the latest results in cosmology and neutrino oscillations favor the normal hierarchy, pointing toward even larger masses ($\sim 10^{3-4}$ kg) for the next generation of experiments, along with a reduction of the background rate. The experimental technique is key here, as not all approachs are economically or technically feasible to scale. The scalability of the current-generation experiments and their current performance will determine their evaluation for a large-scale project.

For such large masses of $\beta\beta$ emitter, the cost of acquisition is a significant fraction of the experimental budget. The most interesting $\beta\beta$-emitting isotopes are rather rare, their production being limited to a few tons per year. For most $\beta\beta$ candidates, the isotopic abundance is around 10 %, meaning that enrichment techniques must be applied to aggregate a reasonable amount of emitter within a small volume. ^{48}Ca and ^{130}Te are the worst and best choices in this regard, respectively (see Table 2.3). On the other hand, ^{136}Xe turns out to be a good compromise for a ton-scale experiment as it has an average isotopic abundance and it is cheap to enrich.

2.5.2 $\beta\beta$-emitting isotopes

The choice of the $\beta\beta$ emitter is focused on four points: maximization of exposure (already examined in Section 2.5.1), background reduction and phase space and NME maximization:

1. The nature of the decay introduces an unavoidable background: the two-neutrino mode. An isotope with a slow $\beta\beta^{2\nu}$ mode is desired in order to reduce the backgroud in the $Q_{\beta\beta}$ energy region. This is a strong requirement for those experimental techniques with moderate energy resolution.

2. In first approximation, the phase space factor, $G^{0\nu}$, is proportional to $Q^5_{\beta\beta}$, strongly favoring isotopes with high Q-values. For this reason, only the candidates with $Q_{\beta\beta} > 2$ MeV have been historically considered for $\beta\beta^{0\nu}$ searches. This argument is strengthened by the fact that natural backgrounds populate the 0 - 3 MeV energy range and are less and less frequent the higher the energy. Hence, the intrinsic need for an ultra-low-background environment makes isotopes with high Q-values overly desirable. Figure 2.7 provides a visualization the phase factor for the most common $\beta\beta$-emitting isotopes. Remarkabily, most of the phase space factors are distributed in a short range.

Isotope	$W(\mathrm{g}\cdot\mathrm{mol}^{-1})$	IA (%)	$Q_{\beta\beta}$ (keV)	$G^{0\nu}$ $(10^{-15}$ year$^{-1})$	$\left\vert M^{0\nu}\right\vert$
^{48}Ca	47.95	0.19	4263	24.81	0.541 - 2.23
^{76}Ge	75.92	7.73	2039	2.36	2.81 - 5.55
^{82}Se	81.92	8.73	2998	10.16	2.64 - 4.67
^{96}Zr	95.91	2.80	3346	20.58	2.53 - 6.50
^{100}Mo	99.91	9.82	3034	15.92	3.73 - 6.59
^{110}Pd	109.91	11.72	2018	4.82	3.62 - 5.726
^{116}Cd	115.90	7.49	2814	16.70	2.78 - 5.35
^{124}Sn	123.91	5.79	2287	9.04	2.558 - 5.79
^{130}Te	129.91	34.08	2528	14.22	2.65 - 6.41
^{136}Xe	135.91	8.86	2458	14.58	2.177 - 4.77
^{150}Nd	149.92	5.64	3371	63.04	2.19 - 2.32

Table 2.3: Property summary of the main $\beta\beta$-emitting isotopes with $Q_{\beta\beta} > 2$MeV: atomic weight, W; natural isotopic abundance, IA; Q-value for the $\beta\beta$ process, $Q_{\beta\beta}$; phase space factor, $G^{0\nu}$; and range of NME values considering the ISM [85], QRPA Jy [86], QRPA T [87], IBM-2 [88], and EDF [89] models. $Q_{\beta\beta}$ values were extracted from [90, 91, 92, 93, 94, 95], $G^{0\nu}$ values from [68] and $\left\vert M^{0\nu}\right\vert$ values from [85, 86, 87, 88, 89].

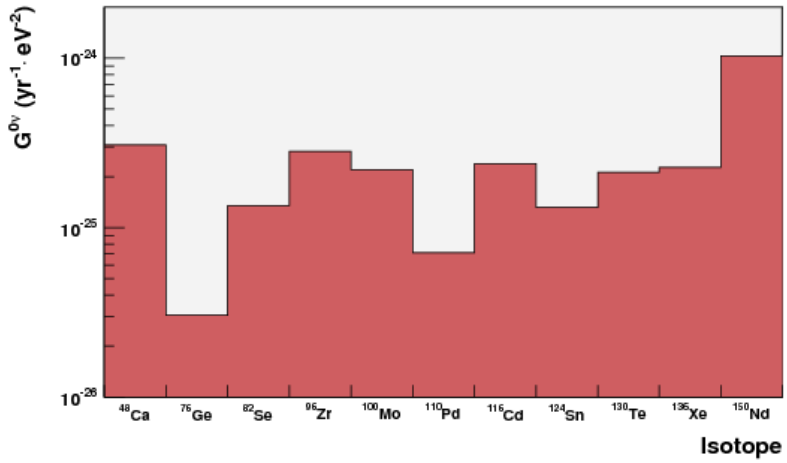

Figure 2.7: Phase space factors ($\times m_e^{-2}$) for those $\beta\beta^{0\nu}$ candidates with $Q_{\beta\beta} > 2$ MeV. All values with the exception of ^{76}Ge and ^{150}Nd are contained within a factor of 3, approximately.

3. The NME values of the different isotopes are all comprised within a factor of five of each other (see Figure 2.8), equalizing the field in that respect. Besides, the uncertainties in the nuclear models and the discrepancies among them are of the same order as, if not larger than, the differences found among the isotopes. Thus, no isotope is favored in this regard. Figure 2.8 displays the current predictions of the most common NME calculation techniques for the most relevant isotopes.

All these aspects can be factored in the constant K_1 described before. The outcome, shown in Figure 2.9, is that all isotopes are roughly equally favored, within a factor of 2 of each other.

In conclusion, there is not a clear favorite isotope for $\beta\beta^{0\nu}$ searches. Since the factors discussed in this section can be a second-order contribution, the choice of isotope will be either determined by the cost of acquisition and/or enrichment discussed in Section 2.5.1, or by its suitability for a given experimental technique.

2.5.3 Detection efficiency

Due to the rareness of the neutrinoless double beta decay, high detection efficiencies are a must. From Equation 2.10, it follows that in order to improve $\mathcal{S}(m_{\beta\beta})$ by a given factor, ξ, we can either improve the efficiency by ξ^2 or the exposure by ξ^4. Thus, achieving higher efficiencies are preferable to scaling the detector. Simpler detectors usually yield better detection efficiencies. Calorimeters such as germanium diodes and bolometers have efficiencies over 80 %, while tracking-based detectors are closer to the 30-40 % region.

Some techniques use the source material (i.e. the $\beta\beta$ emitter) as the detection medium. This method is more efficient than a separate-source approach, but it is also usually counterbalanced by the fact that part of the mass is needed to self-shield against external backgrounds.

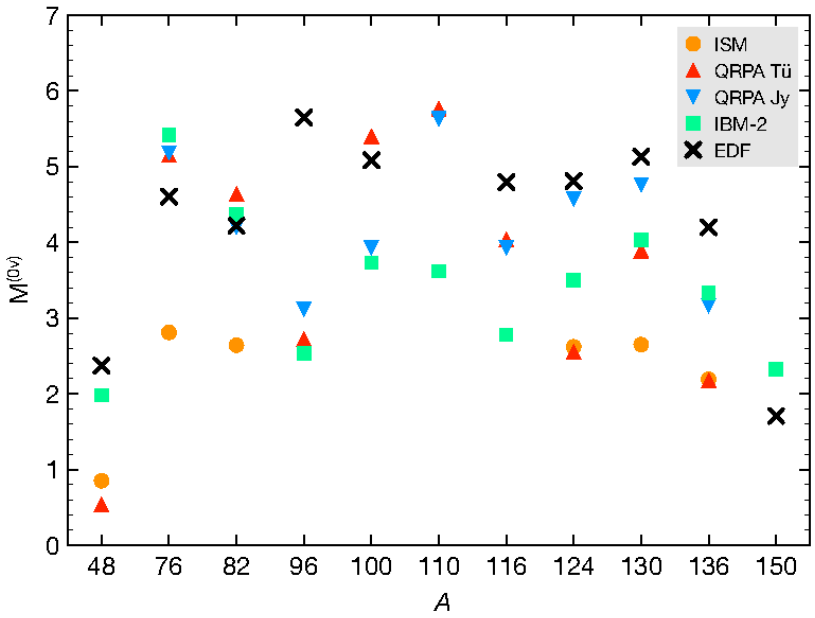

Figure 2.8: Nuclear matrix elements, $|M^{0\nu}|$, for different $\beta\beta^{0\nu}$ decay candidates computed using different theoretical frameworks: *interacting shell model* (ISM) [85], *quasiparticle random-phase approximation* by the Jyvskyl (QRPA Jy) [86] and the Tbingen (QRPA T) [87] groups, *interacting boson model* (IBM-2) [88], and *energy density functional* method (EDF) [89]. See references for the details. A factor of 5 covers the differences between the different candidates for a given model. However the uncertainties within each model and the discrepancies among them make the identification of the best $\beta\beta^{0\nu}$ candidate a hard task.

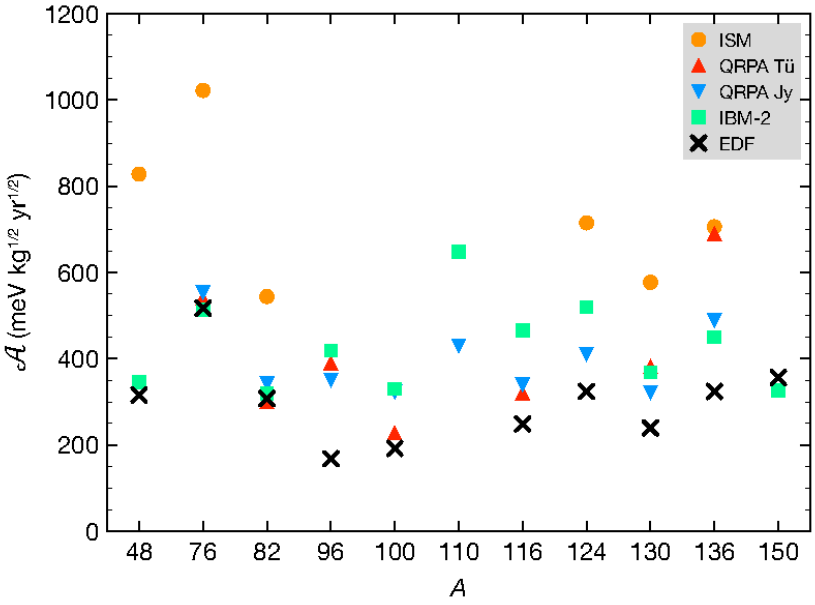

Figure 2.9: Isotopic constant $\mathcal{A} = K_1$ of the $\beta\beta$-emitting isotopes with $Q_{\beta\beta} > 2$ MeV [96].

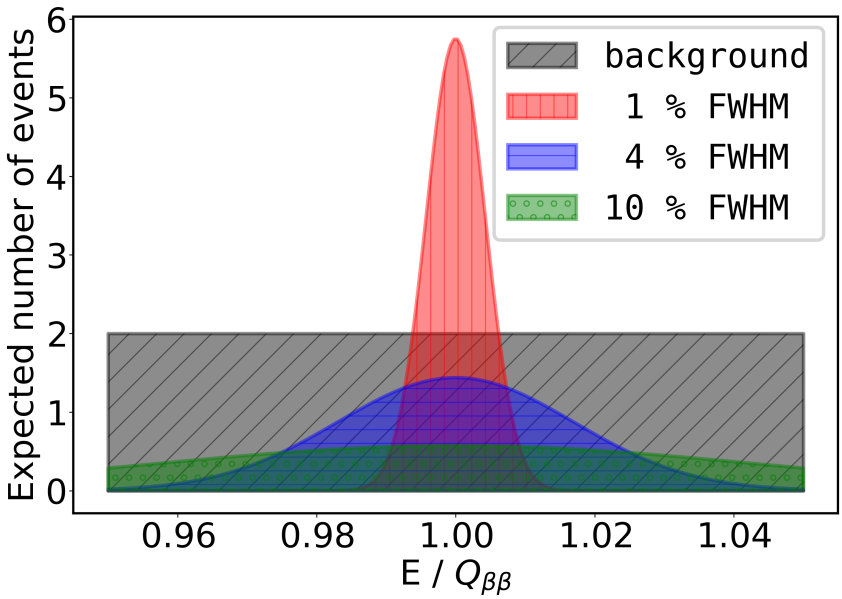

Figure 2.10: Simulation of a gaussian signal and a flat background (black) energy spectra for three different energy resolutions at FWHM: 1 % (red), 4 % (blue) and 10 % (green). A background rate of 10^{-4} ckky and a $T^{0\nu}_{1/2}$ of 10^{27} y for ^{136}Xe are assumed.

2.5.4 Energy resolution

As mentioned before, the two-neutrino mode is an intrinsic background to $\beta\beta^{0\nu}$ searches. An outstanding energy resulution is essential to any double beta decay experiment aiming to probe low values of $m_{\beta\beta}$, as it is the only manner to reduce the number of $\beta\beta^{2\nu}$ events in the energy window surrounding $Q_{\beta\beta}$. This characteristic of the experimental technique is also helpful to reduce external backgrounds.

This is schematized in Figure 2.10, where three hypothetical experiments observe the same number of background and signal events with different energy resolutions. While in the 10 % resolution experiment signal and background are essentially indistinguishable, we can hint the existance of a signal in the 5 % case and practilly claim a discovery in the 1 % scenario.

In short, the prospect for the neutrinoless double beta decay field is based in background-free ton-scale experiments. In this scenario, energy resolution is mandatory to reject the intrinsic two-neutrino mode.

2.5.5 Background reduction

The presence of background events in the $Q_{\beta\beta}$ region, deteriorates remarkably the sensitivity of an experiment to $m_{\beta\beta}$. From Equation 2.7, we see that a background-free experiment improves its sensitivity as $\sqrt{\text{exposure}}$, whilst even with a reduced background rate, the rate of improvement is much slower: $\sqrt[4]{\text{exposure}}$ (Equation 2.10). Ergo, background reduction is paramount to any $\beta\beta^{0\nu}$ experiment.

In Figure 2.11 the sensitivity to $m_{\beta\beta}$ as a function of the exposure is shown for different values

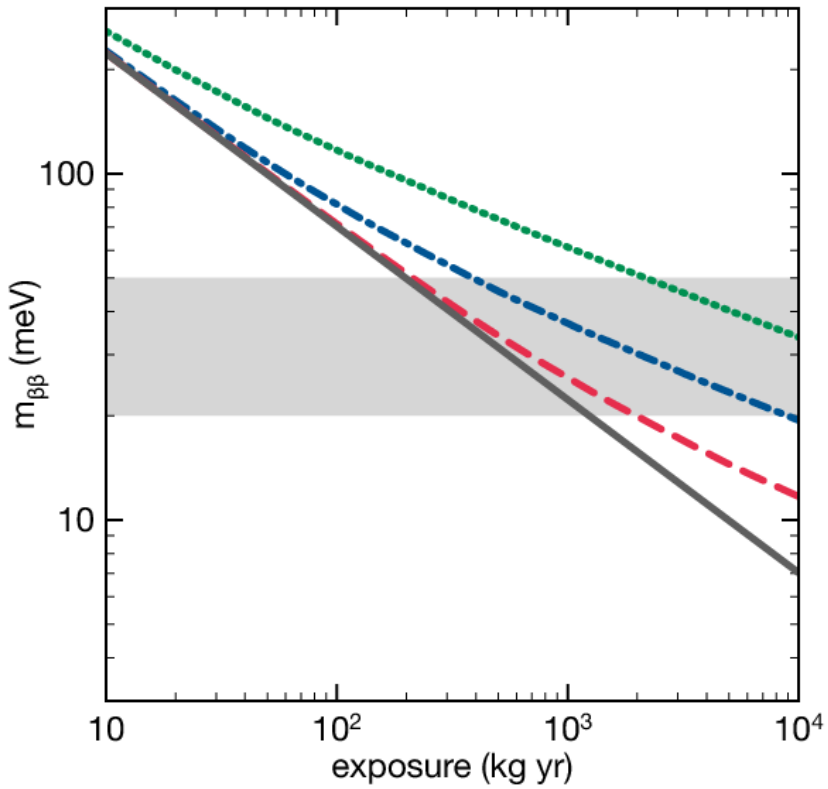

Figure 2.11: Sensitivity to $m_{\beta\beta}$ (at 90% CL) of a Xe-based experiment with perfect signal detection efficiency and four different assumptions for the background rate within the energy region of interest around $Q_{\beta\beta}$: 0.1 ckky (green, dotted line); 0.01 ckky (blue, dash-dot line); 0.001 ckky (red, dashed line) and background-free (grey, solid line). The IBM-2 nuclear matrix element [97] has been used to convert the half-life limits to $m_{\beta\beta}$. The grey band represents the inverted-hierarchy region of neutrino masses. [96].

of the background rate for a ^{136}Xe-based experiment with perfect detection efficiency. For the current generation of experiments, with accumulated exposures of $\mathcal{O}(100)$ kg year, background rates of $10^{-2} - 10^{-1}$ ckky were sufficient as there is not a vast difference to the background-free case. The same is not true, however, when considering exploring smaller values of $m_{\beta\beta}$. For an exposure of 10^3 kg y (i.e. that of a next-generation experiment), the impact of the background rate to the sensitivity is considerable and those experiments aiming to completely explore the inverted hierarchy region must achieve rates below 10^{-4} ckky. Finally, if the inverted hierarchy is explored and no signal is found, the $\beta\beta^{0\nu}$ field will consider probing the normal hierarchy. Those values of $m_{\beta\beta}$ (below 20 meV) will only be accesible with enourmous quantities of $\beta\beta$ emitter, high efficiencies and negligible ($< 10^{-5}$ ckky) backgrounds.

Background contributions

Unavoidabily, any detector we can build will be made of matter, which contains small quantities of naturally radioactive isotopes. These well known radioactive chains can be present in any material and produce gamma and beta radiation with energies close to the $Q_{\beta\beta}$ region. This

will significantly reduce the sensitivity of the experiment, as discussed before. The selection of *radiopure* materials is, therefore, of the utmost importance for a $\beta\beta^{0\nu}$ experiment. Still, this constitutes the main source of background for the current generation of experiments.

Radon is also a concern for many experiments. Its noble gas condition makes it very troublesome, as it diffuses through many materials reaching the active region of the detector. The decay products of radon can also produce background events, as they adhere to surfaces due to they are usually charged and are also radioactive. This background source can be prevent by flushing the detector components with nitrogen and placing the detector in a radon-free environment. This background is not dominant for the ongoing experiments, but it is a concern for the future ones.

External background contributions are dominated by cosmic rays. This background is reduced by placing the detector underground, as all experiments do. The second order contribution are gammas coming from the aforementioned natural radioactive chains present in all matter surrounding the experiment (e.g. the laboratory walls). The experimental area is usually shielded with dense and radiopure materials, such as lead[5] or copper, to impede the arrival of those photons to the detector. Inner shieldings are also used in this case to prevent gammas from the detector and from the outer shielding to reach the active region.

Larger-scale experiments have to consider some additional external backgrounds: muons and neutrinos. Muons can still reach the experimental area despite the large amount of mass they have to go through. Muon interactions can produce electromagnetic showers and neutrons. While the former is easily vetoed, the latter can activate detector components and generate backgrounds.

On top of all these passive background reduction systems, some experiments are developing techniques for signal/background discrimination, such as topological event reconstruction, pulse-shape discrimination and decay-product identification [98, 99].

2.6 Past, present and future of $\beta\beta^{0\nu}$ searches

2.6.1 Past experiments and their observations

Since the proposal of the existence of the neutrinoless double beta decay by Wendell H. Furry [67], many experiments have been developed, trying to observe this extremely rare process. As for $\beta\beta^{2\nu}$, they measure the kinetic energy of the outcoming electrons, the sum of which results in the energy spectrum of Figure 2.2. A number of isotopes have been investigated so far, the most relevant ones being summarized in Table 2.4.

The Heidelberg-Moscow (H-M) experiment [106] held for a long time the best limits on $T^{0\nu}_{1/2}$. They used high-purity Ge semiconductor detectors enriched to 86 % in ^{76}Ge to search for the

[5]Regular lead is not suitable for this purpose, as it is *activated* due to cosmic rays. Collisions with these particles create, via nuclear reactions, unstable isotopes that decay over time, making them too radioactive for the requirements of the experiment. Instead, ancient roman lead is used because, contrarily to recently-mined lead, it is barely radioactive. This variety is found in shipwreck sites and has spent hundreds of years underseas shielded from cosmic sources and, thus, remains unactivated. The small amounts of unstable isotopes it may have contained are already negligible as they have alredy decayed.

Isotope	Transition	Method	Half-life limit (y)
^{48}Ca		CaF_2 scint.	$> 5.8 \cdot 10^{22}$ [100]
^{76}Ge		GERDA	$> 8.0 \cdot 10^{25}$ [77]
^{82}Se		NEMO-3	$> 3.6 \cdot 10^{23}$ [101]
^{100}Mo		NEMO-3	$> 1.1 \cdot 10^{24}$ [57]
^{100}Mo	$0^+ \to 0_1^+$	NEMO-3	$> 8.9 \cdot 10^{22}$ [59]
^{100}Mo	$0^+ \to 2^+$	NEMO-3	$> 1.6 \cdot 10^{23}$ [59]
^{116}Cd		$^{116}CdWO_4$ scint.	$> 1.7 \cdot 10^{23}$ [61]
^{130}Te		CUORE	$> 1.5 \cdot 10^{25}$ [102]
^{130}Te	$0^+ \to 0_1^+$	CUORICINO	$> 9.4 \cdot 10^{23}$ [103]
^{134}Xe		EXO-200	$> 1.1 \cdot 10^{23}$ [104]
^{136}Xe		KamLAND-Zen	$> 1.07 \cdot 10^{26}$ [76]
^{136}Xe	$g.s. \to 2_1^+$	KamLAND-Zen	$> 2.6 \cdot 10^{25}$ [105]
^{136}Xe	$g.s. \to 2_2^+$	KamLAND-Zen	$> 2.6 \cdot 10^{25}$ [105]
^{136}Xe	$g.s. \to 0_1^+$	KamLAND-Zen	$> 2.4 \cdot 10^{25}$ [105]

Table 2.4: Best limits on the neutrinoless double beta decay half-life, $T_{1/2}^{0\nu}$, for different isotopes at 90 % CL.

$\beta\beta^{0\nu}$ decay. Placed in Laboratori Nazionali del Gran Sasso, the experiment accumulated a total exposure of 71.1 kg year from 1990 to 2003 and set a lower limit of $T^{0\nu}_{1/2}(^{76}\text{Ge}) \geq 1.9 \cdot 10^{25}$ y at 90 % CL ($m_{\beta\beta} \leq 320$ meV) [106]. Notoriously, a scission of the collaboration re-analyzed the data to claim the observation of the neutrinoless double beta decay, with a half-life of $T^{0\nu}_{1/2}{}^{*}(^{76}\text{Ge}) = \left(2.23^{+0.44}_{-0.31}\right) \cdot 10^{25}$ y [107]. This claim was controversial and received with sceptisim from the scientific community, which questioned the result. More recent observations have discarded such large value of $m_{\beta\beta}$ at 90 % CL [77, 76, 108, 109, 110], some using the same isotope.

The Cuoricino experiment [111], first stage of the CUORE experiment, ran from 2003 to 2008. It consisted of 11 kg of ^{130}Te arranged in 62 TeO_2 bolometric crystals and was capable of reach a sensitivity to $m_{\beta\beta}$ comparable to that of the H-M experiment, but could not disprove their claim due to the uncertainties in the NME. Their latest result establishes a lower limit $T^{0\nu}_{1/2}(^{130}\text{Te}) \geq 1.8 \cdot 10^{24}$ y at 90 % CL ($m_{\beta\beta} \leq 200 - 1100$ meV).

Held at the Laboratoire Souterrain de Modane (LSM), the NEMO-3 experiment was the first (and only) experiment to use multiple $\beta\beta$ emitters. It ran from 2003 to 2010 and has provided many measurements of the $T^{2\nu}_{1/2}$ as well as various limits of the $T^{0\nu}_{1/2}$ (see Table 2.1 and Table 2.4, respectively). In this experiment, the source material is arranged in thin foils surrounded by a tracking calorimeter. This technique allows signal/background discrimination, enhancing the sensitivity of the experiment. The precise determination of the $\beta\beta^{2\nu}$ spectra for multiple isotopes is not only extremely advantageous for improving the nuclear models and reduce the uncertainties in the NME, but can also be used to parametrize the intrinsic $\beta\beta^{2\nu}$ background.

2.6.2 Current generation of experiments

Four are the experiments currently taking data or being upgraded for a more sensitive search. They all are aiming to explorer regions of $m_{\beta\beta} \sim 50 - 100$ meV in three different isotopes: ^{76}Ge, ^{130}Te and ^{136}Xe.

KamLAND-Zen

Located at the Kamioka Obsertavory in Japan, the *KamLAND-Zen*[6] experiment searches for neutrinoless double beta decay in ^{136}Xe [76]. Their experimental technique consists in dissolving the $\beta\beta$ emitter in liquid scintillator (LS), a technique first proposed by R. Raghavan [112]. By taking advantage of the previous equipment of the KamLAND detector, the collaboration introduced a spherical inner balloon (IB) concentric to the already-existing outer balloon (OB) (see Figure 2.12). The OB, 13 meters in diameter, holds 1 ktonne of LS, used to shield the IB from external gamma radiations and as a detector for the radiation comming from the IB. The IB, 3.08 m in diameter and made of transparent nylon film, contains 13 tonnes of Xe-loaded LS. The OB is separated by a buffer oil from a stainless-steel containment tank instrumented with 1879 PMTs, which, at the same time, is surrounded by a 3.2-kt water-Cherenkov detector.

This detector took date in two phases with slightly different masses of $\beta\beta$ emitter (345 kg and 383 kg for the first and second phase, respectively). However, despite their ability to achieve large exposures, their results are compromised by the poor energy resolution of the detector.

[6] For **KAM**ioka **L**iquid scintillator **A**nti**N**eutrino **D**etector **- ZE**ro **N**eutrino.

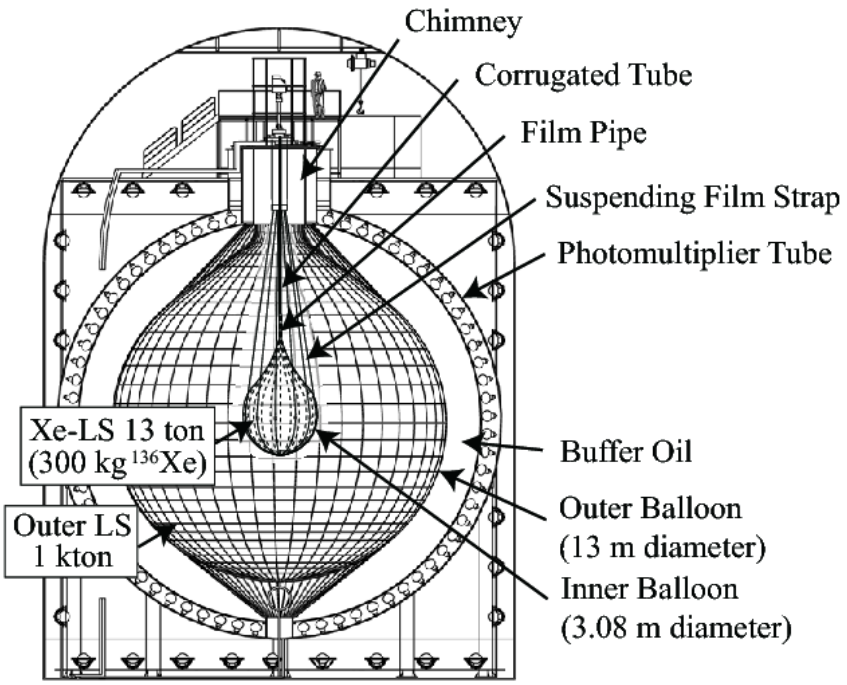

Figure 2.12: Schematic drawing of the KamLAND-Zen detector [65].

An overall background rate of 0.01 ckky was achieved [113] by Bi-Po tagging ^{214}Bi events and a tight selection cut in the fiducial volume [114]. In spite of that, their background level is an order of magnitude higher than that of EXO-200 (Section 2.6.2).

During the first phase of the experiment, which began in late 2011, they accumulated a total exposure of 89.5 kg year with an energy resolution of 9.89 % FWHM at $Q_{\beta\beta}$ establishing a lower limit $T^{0\nu}_{1/2}(^{136}\text{Xe}) > 1.9 \cdot 10^{25}$ y at 90 % CL [110]. Moreover, they measured the half-life of the two-neutrino mode to be $T^{2\nu}_{1/2}(^{136}\text{Xe}) = (2.38 \pm 0.02\ (\text{stat.}) \pm 0.13\ (\text{sys.})) \cdot 10^{21}$ y.

For the second phase of the experiment (December 2013 to October 2015), a limit of $T^{0\nu}_{1/2}(^{136}\text{Xe}) > 9.6 \cdot 10^{25}$ y was achieved, in spite of their slightly poorer resolution: 10.94 % FWHM at $Q_{\beta\beta}$ (see Figure 2.13). The combination of the results from both fases yields an improved limit of $T^{0\nu}_{1/2}(^{136}\text{Xe}) > 1.07 \cdot 10^{26}$ y, which translates into an effective majorana mass of 61 - 165 meV, depending on the NME [76].

EXO

EXO, for **E**nriched **X**enon **O**bservatory, is the other leading ^{136}Xe $\beta\beta^{0\nu}$ experiment. The detector, a liquid xenon (LXe) Time Projection Chamber (TPC), is located at the Waste Isolation Pilot Plant (WIPP), in New Mexico, USA since May 2011. During the first phase of the experiment, 200 kg of xenon enriched to ∼80 % in ^{136}Xe were deployed. Of those, 175 kg are in liquid phase, which leaves 110 kg of LXe in the active volume of the detector. The collaboration has produced $\beta\beta^{2\nu}$ half-life measurements [64] and some of the most competitive limits on the effective Majorana mass [115, 116].

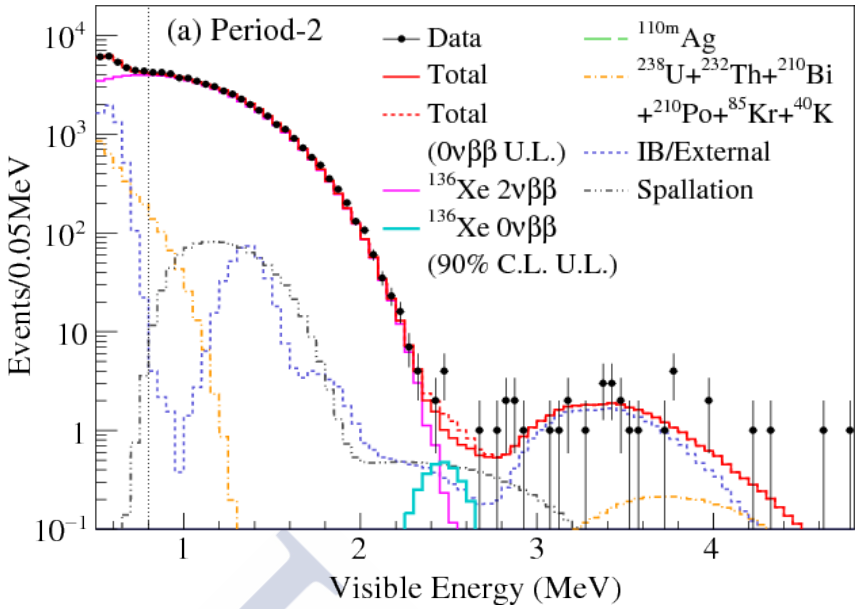

Figure 2.13: Energy spectrum of selected $\beta\beta$ candidates within a 1-m-radius spherical volume in KamLAND-Zen's Period-2 drawn together with best-fit backgrounds, the $\beta\beta^{2\nu}$ decay spectrum, and the 90 % CL upper limit for $\beta\beta^{0\nu}$ decay. [76]

The configuration of the detector, depicted in Figure 2.14, consists of a symmetric cylindrical TPC with a central transparent cathode. It is instrumented with large-area avalanche photodiodes (LAAPDs) to measure the scintillation light and with two crossed planes of parallel wires used to collect the charge of the ionization signal. Teflon sheets cover the sides of the chamber to reflect scintillation photons and improve overall light collection. LXe is contained in a thin copper vessel immersed in cryofluid held at $\sim$ 167 K inside a double-walled copper cryostat. While the cryofluid acts itself as shielding for the TPC, additional lead blocks surround the cryostat in all directions. The entire assembly is housed in a clean room at WIPP with four sides covered by plastic scintillator panels, used to veto cosmic muons.

Electrons produced in LXe do not travel more than a few mm due to the high density of the medium. Thus, $\beta\beta$ events are tipically single-site (SS) events, while gamma backgrounds produce multiple-site (MS) events. This, combined with their mm-accurate cluster reconstruction, allows the experiment to perform some background rejection, although not as efficiently as others.

The energy resolution of LXe is not as good as that of gaseous xenon (see Figure 3.3). However, by measuring both scintillation and ionization signals, anti-correlation corrections can be performed [117] , achieving an energy resolution at $Q_{\beta\beta}$ of 3.6 % FWHM for SS events and 3.88 % FWHM for MS events [115].

The experiment achieved a background rate of $1.7 \cdot 10^{-3}$ ckky, which, combined with a moderately large exposure of $\sim$ 100 kg year, results in a very competitive $m_{\beta\beta}$ sensitivity. The collaboration produced a number of salient results:

- The measurement of the half-life for the two-neutrino mode was performed using an exposure of 23.14 kg year. They achieved a detector efficiency for $\beta\beta^{2\nu}$ decays of 87.4 % within a fiducial region and obtained $T^{2\nu}_{1/2}(^{136}\text{Xe}) = (2.165 \pm 0.016(\text{stat.}) \pm 0.059(\text{sys.})) \cdot 10^{21}$ y [64].

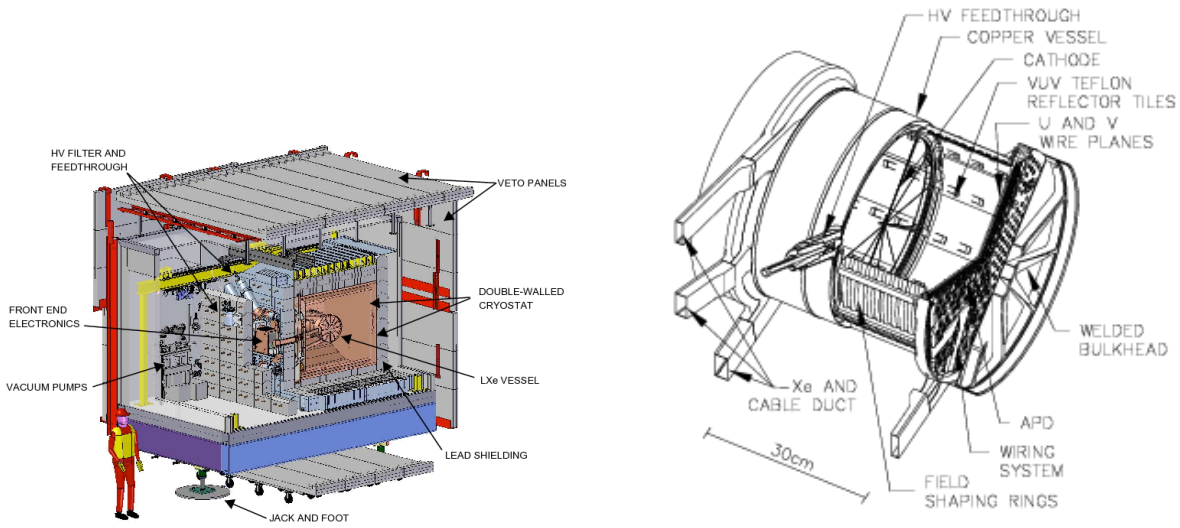

Figure 2.14: Schematic drawings of the EXO-200 clean room (left) and TPC (right) [118].

- For the zero-neutrino analysis, they accumulated an exposure of 100 kg year and measured an efficiency of 84.6 %. The collaboration reports a lower limit at 90 % CL of $T^{0\nu}_{1/2}(^{136}\text{Xe}) > 1.1{\cdot}10^{25}$ y (see Figure 2.15), which corresponds to values of $m_{\beta\beta}$ of 190 - 450 meV, depending on the NME [115].
- An additional analysis searched for the double electron capture of ^{134}Xe. Albeit not yet observed, they report lower limits on both the two-neutrino and the neutrinoless modes at 90 % CL: $T^{2\nu}_{1/2}(^{134}\text{Xe}) > 8.7 \cdot 10^{20}$ y and $T^{0\nu}_{1/2}(^{134}\text{Xe}) > 1.1 \cdot 10^{23}$ y [104]

GERDA

Located at LNGS, the **GER**manium **D**etector **A**rray (*GERDA*) experiment searches for $\beta\beta^{0\nu}$ in ^{76}Ge using high-purity germanium (HPGe) diodes. The diodes (see Figure 2.16) are arranged in strings suspended into a vacuum-insulated stainless-steel cryostat filled with LAr [119]. The LAr serves two purposes: cooling the detector and shielding it from external radiation. The inner surface of the cryostat is covered by 6 cm of a pure copper lining in order to reduce background contributions from the vessel. The cryostat itself is placed in a PMT-instrumented water tank, used as a muon veto and as a γ and neutron shield. The experimental technique of the GERDA experiment is based on an outstanding energy resolution complemented with a strong external background supression.

The first phase of the experiment, from November 2011 to March 2013, used eight refurbished semi-coaxial HPGe detectors enriched to 86 % in ^{76}Ge from past experiments (H-M and IGEX) plus a non-enriched detector from the GENIUS-TF project [120] adding up to 17.67 kg of ^{76}Ge. In July 2012, the experiment added 5 broad-energy germanium (BEGe) diodes to the detector as a test for the second phase of the experiment, which consisted of 7 HPGe and 30 BEGe.

The BEGe outperformed the HPGe detectors notably, improving the sensitivity of the

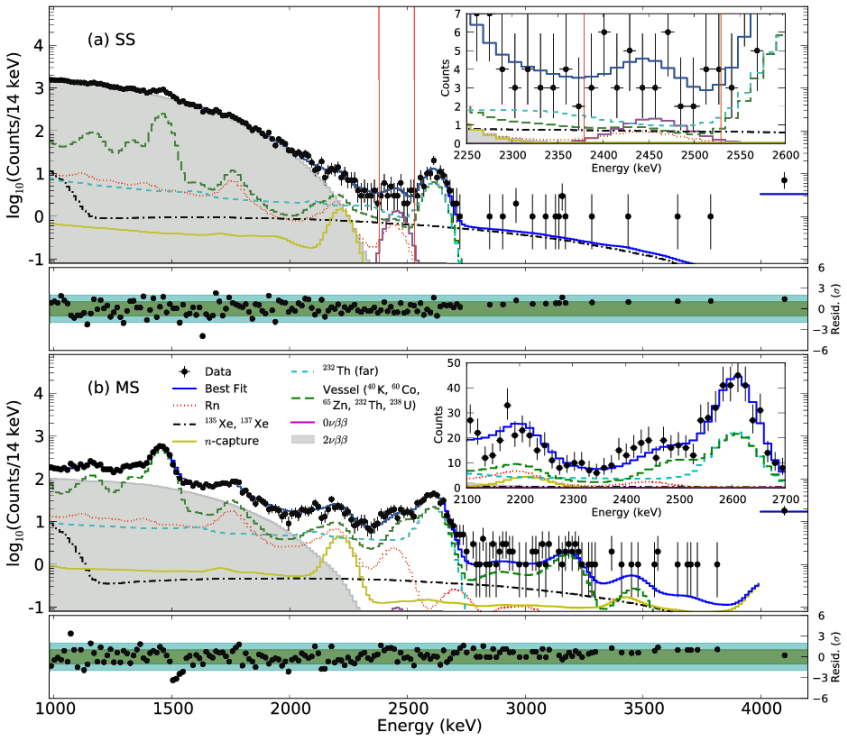

Figure 2.15: Best fit to the low background data single-site energy spectrum for Phase I (top) and Phase II (bottom) of the EXO experiment. The energy bins are 15 keV and 30 keV below and above 2800 keV, respectively. The inset shows a zoomed in view around the best-fit value for $Q_{\beta\beta}$. [115]

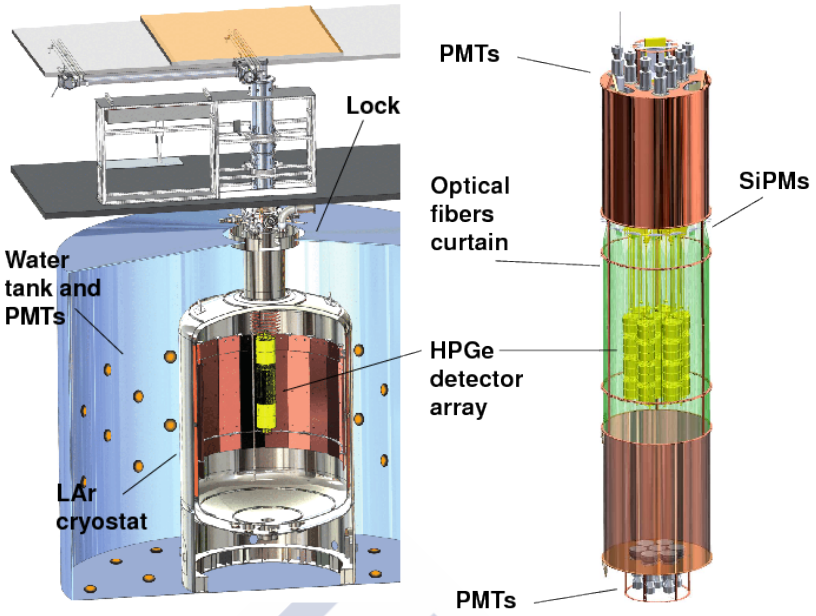

Figure 2.16: Schematic drawing of the GERDA detector [108].

experiment. The collaboration measured a resolution of (4.8 ± 0.2) keV $(0.23 \pm 0.01$ %) FWHM for the semi-coaxial detectors and (3.2 ± 0.2) keV $(0.16 \pm 0.01$ %) for the BEGe detectors at $Q_{\beta\beta}$ [109]. As for EXO, signal and background have different signatures in these detectors. Pulse shape discrimination allows the distinction of SS (signal) from MS (background) events. This improves greatly the sensitivity of the experiment to $m_{\beta\beta}$, as discussed in Section 2.5. The collaboration reported background measurements for both the first and second phases of the experiment. For Phase I, they estimate a background rate of $(11 \pm 2) \cdot 10^{-3}$ ckky [121], while for Phase II they improved it up to $\left(0.7^{+1.1}_{-0.5}\right) \cdot 10^{-3}$ ckky [109], reaching a nearly background-free regime.

The elevated cost of enriching germanium constitutes the Achilles' heel of the experiment. Notwithstanding, the compactness of solid-state detectors together with the negligible background levels compensates this fact. The collaboration leads the $\beta\beta^{0\nu}$ field in ^{76}Ge and has produced outstanding results. During Phase I, the GERDA collaboration published an analysis in which they measure the half-life of the two-neutrino mode. A value of $T^{2\nu}_{1/2}(^{76}\text{Ge}) = (1.926 \pm 0.095) \cdot 10^{21}$ y was estimated from a total exposure of 20.3 kg year[7] (17.9 kg year from semi-coaxial detectors and 2.4 kg year from BEGe detectors) [52]. The $\beta\beta^{0\nu}$ analysis was performed during both phases. In phase two, they report a limit on the half-life of $8.0 \cdot 10^{25}$ year (see Figure 2.17). The combination with the Phase I data yields a final estimate of $T^{0\nu}_{1/2}(^{76}\text{Ge}) > 5.3 \cdot 10^{25}$ y at 90 % CL [109], corresponding to an effective Majorana mass in the range 150 - 330 meV, depending on the NME. This result from the GERDA collaboration discredits strongly the claim made by part of the H-M experiment.

[7] 1.3 kg year of HPGe data were discarded due to high backgrounds

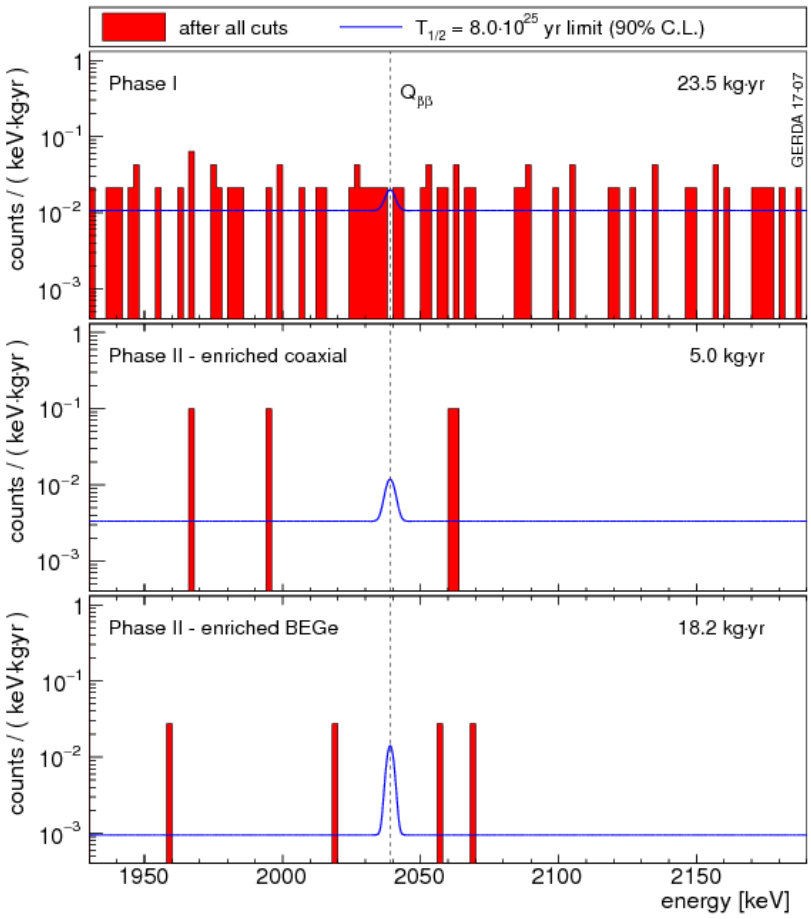

Figure 2.17: Energy spectra measured by GERDA in the analysis window for Phase I and Phase II coaxial detectors and Phase II BEGe detectors, resp., after all cuts. The binning is 2 keV. The grey vertical bands indicate the intervals excluding known γ lines. The blue lines show the hypothetical $\beta\beta^{0\nu}$ signal for $T^{0\nu}_{1/2} = 8.0 \cdot 10^{25}$ year, on top of their respective constant backgrounds. [108]

CUORE

The **C**ryogenic **U**nderground **O**bservatory for **R**are **E**vents (*CUORE*) [122] is the last $\beta\beta^{0\nu}$ experiment to run to the day. Following the steps of the MiDBD [123] and Cuoricino [111] experiments, it searches for the neutrinoless double beta decay of ^{130}Te using TeO_2 crystal bolometers[8] [124]. Located at LNGS, it began its data taking in 2016. The design of the CUORE detector, shown in Figure 2.18, consists of 988 bolometers deployed in 19 towers, for a total 206 kg of $\beta\beta$ emitter mass. Each bolometer is a TeO_2 crystal cube of 5-cm side instrumented with a temperature sensor and a resistive heater. The towers are held inside a cryostat system made of nested copper vessels were they can reach a temperature of 10 mK. Multiple layers of lead (with decreasing activity) shield the bolometers from external background sources. Moreover, a three-layer octogonal external shield protects the whole set-up from environmental gamma rays and neutrons.

The experimental technique is based on the detection of small changes of temperature in the crystals. The interaction of particles is detectable as their interactions in the crystal translates into a temperature change due to the small heat capacity at 10 mK. This technique counts with an outstanding energy resolution of 4.9 keV (0.2 %) FWHM at $Q_{\beta\beta}$ [125], comparable to that of GERDA.

The background rejection, on the other hand, is not as good as GERDA's. The CUORE collaboration reports a measurement of $(58 \pm 4) \cdot 10^{-3}$ ckky [125].

The first phase of the experiment, CUORE-0, consisted in a reduced detector, with only one tower of bolometers. With this configuration the collaboration reported both a measurement of the $\beta\beta^{2\nu}$ half life and a limit on the neutrinoless mode. With an exposure of 33.4 kg year, a half-life of $T^{2\nu}_{1/2}(^{130}\text{Te}) = (8.2 \pm 0.2(\text{stat.}) \pm 0.6(\text{sys.})) \cdot 10^{20}$ y was measured [62]. On the other hand, the limit on the $\beta\beta^{0\nu}$ was set to $T^{0\nu}_{1/2}(^{130}\text{Te}) > 2.9 \cdot 10^{24}$ y at 90 % CL. The combination of this result with the one previously obtained with the Cuoricino detector yields $T^{0\nu}_{1/2}(^{130}\text{Te}) > 4.0 \cdot 10^{24}$ y at 90 % CL.

SNO+

The *SNO+* experiment is a follow-up of the *Sudbury Neutrino Observatory* (SNO) [127]. It is a multipurpose experiment based on a vessel filled of liquid scintillator placed in SNOLAB, the deepest underground laboratory, in Ontario, Canada. The detector (see Figure 2.19) reuses multiple components of its predecessor, replacing heavy water by 780 tonnes of Te-loaded liquid scintillator, which provides a lower energy threshold. A 12-m diameter acrylic vessel is instrumented with ∼9500 photomultiplier tubes adding up to a 54 % photocathode coverage. The space between the vessel and the cavern walls is filled with ultra pure water for background reduction. Due to the lower density of the scintillation with respect the surrounding water, the acrylic vessel needs to be held down to the floor via a rope net.

Although the search for neutrinoless double beta decay in ^{130}Te is the main goal of the experiment, it is also involved in studying neutrinos from multiple sources. In the first phase, the experiment will dilute 1.3 tonnes of ^{130}Te in the scintillator for a low-background run, but this

[8] Due to the high natural abundance of ^{130}Te (see Table 2.3), the crystals are made of natural tellurium.

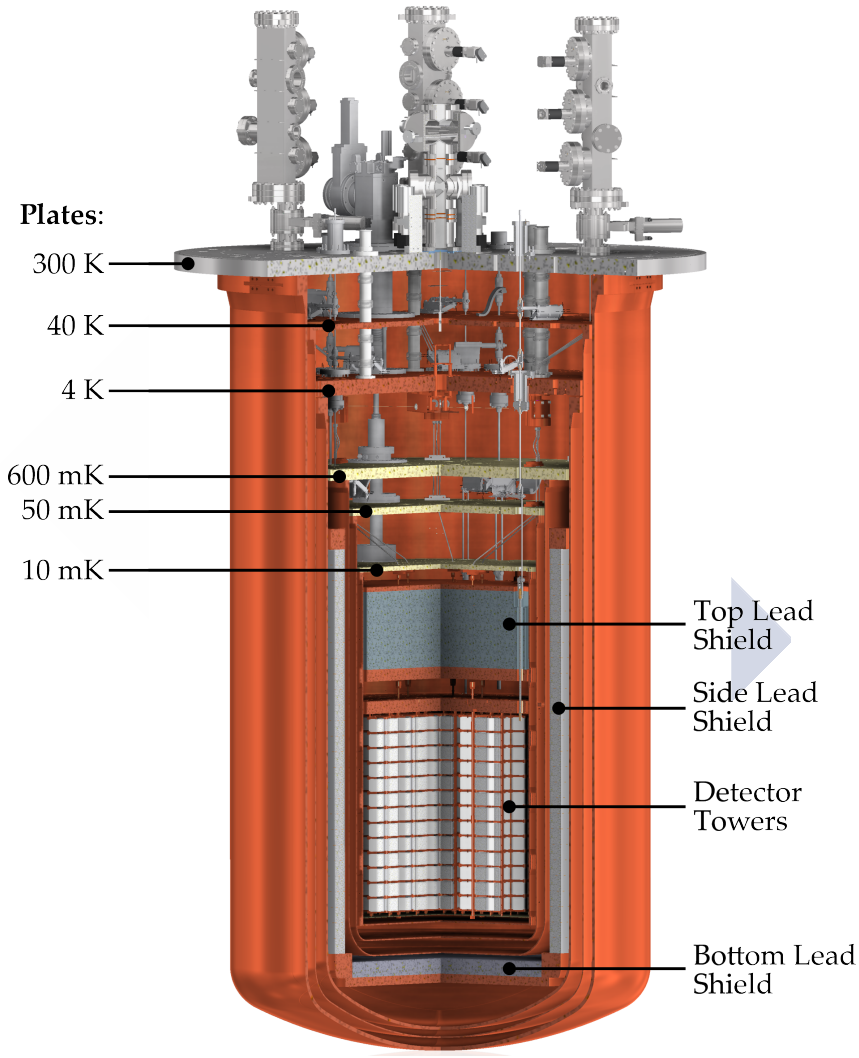

Figure 2.18: Schematic drawing of the CUORE detector [126].

quantity is foreseen to be increased in the future in order to explore the bottom of the inverted hierarchy region.

The SNO+ approach is similar to that of KamLAND-Zen (Section 2.6.2), where large $\beta\beta$ emitter masses are used to counterbalance the low energy resolution of the experimental technique (∼10.8 % FWHM at $Q_{\beta\beta}$ is expected). As discussed in Section 2.5, the $\beta\beta^{2\nu}$ will be a major source of background for the experiment. Fortunatelly, the half-life of ^{130}Te is among the highest. External backgrounds come mainly from uranium and thorium impurities in the liquid scintillator, which can be suppressed via Bi-Po α-tagging techniques [128]. A fiducial region will be also defined to reject backgrounds comming from the detector surroundings. In this experimental conditions, a sensitivity to $T^{0\nu}_{1/2}$ of $9 \cdot 10^{25}$ y at 90 % CL is expected for 5 years of data-taking.

Other experiments

There are multiple efforts to find the neutrinoless double beta decay. Those leading the field have already been summarized in Section 2.6.2. Here, we enumerate some alternative techniques that are currently in their R&D phase, with the exception of NEXT, focus of this work, that will be described in Chapter 3.

SuperNEMO This experiment will use thin foils of ^{82}Sesurrounded with tracking chambers and calorimeter walls. Low background rates are projected for the detector along with a 4 % FWHM at 3 MeV. These properties are still to be demonstrated and, as a consequence, the collaboration has started the construction of the first module, which will be used to assess the performance of the detector.

Majorana Using a modular setup composed of two ultra-pure electroformed copper cryostats to hold HPGe detectors, the MAJORANA projects plans to search for neutrinoless double beta decay in ^{76}Ge. The detector, the MAJORANA demonstrator, is under construction in Sanford Underground Research Facility (SURF) in South Dakota, USA. Their goal is to prove the expected background rate of $< 7.5 \cdot 10^{-4}$ ckky in the foreseen scenario of a world-wide collaboration with GERDA targeting a joint tonne-scale ^{76}Ge experiment.

AMoRE The AMoRE experiment will search for neutrinoless double beta decay in ^{100}Mo using calcium molybdate crystals as a cryogenic scintillation detector. With an energy resolution of 0.2 % FWHM at $Q_{\beta\beta}$, the experiment projects a sentivity to the half-life of the neutrinoless mode of $3 \cdot 10^{26}$ y for 250 kg year of exposure.

CANDLES Searching for $\beta\beta^{0\nu}$ in ^{48}Ca, the CANDLES experiment uses CaF_2 scintillation crystals. The high $Q_{\beta\beta}$ value of this isotope (4274 keV) mitigates the need for a background reduction, as the energy of gamma lines and α decays from natural sources are well below their region of interest. However, the low natural abundance and difficulty for enrichment is a clear disadvantage for this technique.

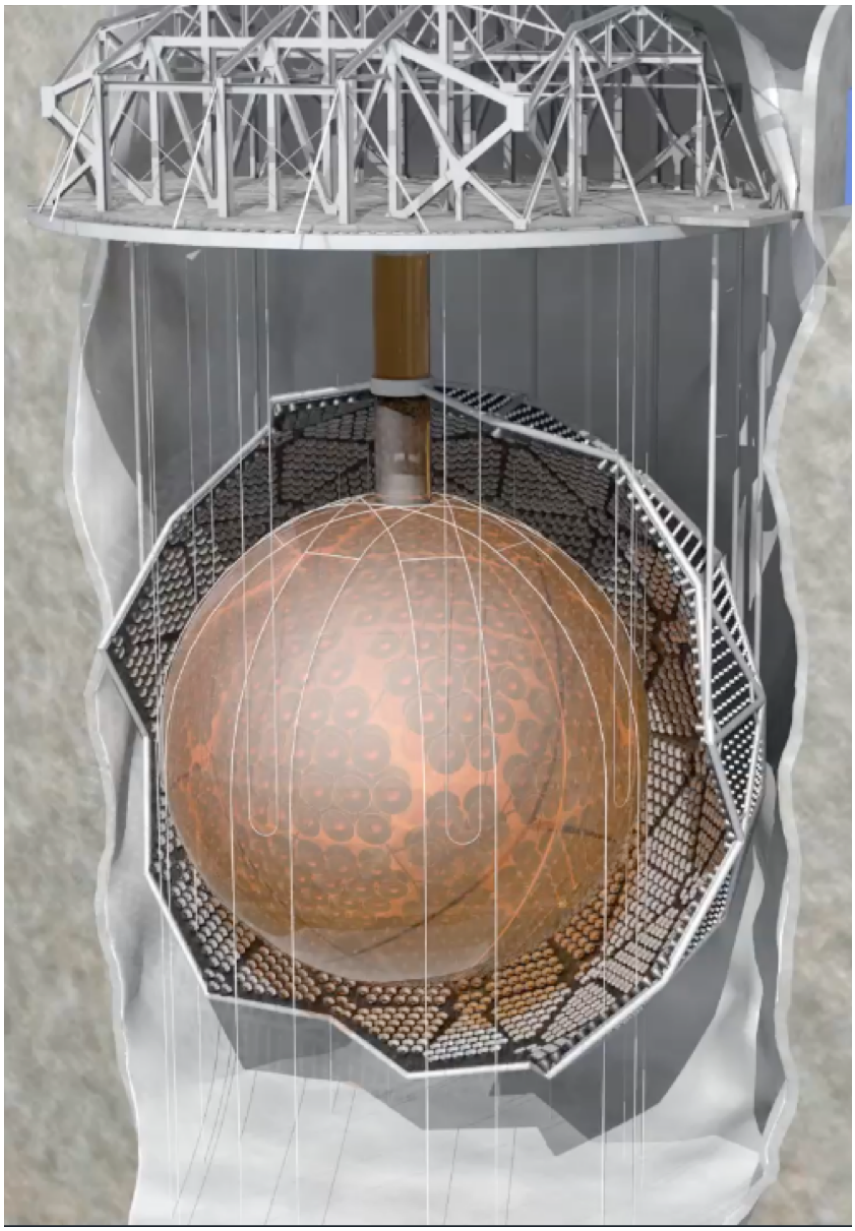

Figure 2.19: Artistic view of the SNO detector [129].

2.6.3 The future of neutrinoless double beta decay experiments

The inverted hierarchy

The current generation of experiments can already explore the top of the inverted hierarchy with masses of tens or hundreds of kg, but, in order to explore smaller values of $m_{\beta\beta}$, they will need tens or hundreds of tonnes.

The aim of the next generation of experiments (2020 - 2030) is to fully explore the inverted hierarchy region. This requires detectors with masses of the order of the tonne and not all the current techniques will be viable at these large scales. Thus, only a handful of techniques are going be retained; most likely, one for each isotope. Some of those are summarized in the following:

- GERDA and MAJORANA are already arranging a merge into a world-wide collaboration to search for $\beta\beta^{0\nu}$ in ^{76}Ge at the tonne scale. This alliance will require at least 20 times more emitter mass than they currently have and a background rate below 10^{-4} ckky.
- Bolometer-based experiments will require isotopically-enriched crystals, which can be expensive (except for those based on ^{130}Te). The ability to extract a tracking signature would also be advantageos to reduce background rates, albeit it would slightly compromise the energy resolution. The CUORE collaboration is already considering using particle identification for their tonne-scale project [130].
- KamLAND-ZEN and SNO+ are planning the exploration of the inverse hierarchy by increasing the $\beta\beta$ emitter mass, improving the energy resolution to values close to 6 % FWHM and reducing their background rate. Notwithstanding, the sensitivity of these approaches will ultimately be compromised by the intrinsic two-neutrino background.
- A tonne scale of SuperNEMO seems unfeasible due to the enormity of their current design for a 10-kg scale detector.
- nEXO is the tonne-scale programme for the EXO collaboration. It consists of a 5-tonne LXe TPC capable of fully cover the inverted hierarchy region. Self-shielding at the cost of emitter mass is a must in order to reach low levels of background, together with neutron shielding to prevent xenon activation.

The normal hierarchy

A number of neutrino oscillation and cosmological experiments have reported a mild preference of the data for the normal hierarchy. The discovery of the neutrinoless double beta decay becomes even more arduous in this scenario. Any experiment aiming to probe that region will be required to be in the background free regime. The scalability of the experiment would probably had been assessed in the tonne-scale generation, but for such large masses, modular detectors that can be split and placed in different laboratories are probably desirable. The natural abundance and enrichment cost will also play a role in the discussion, as for some $\beta\beta$ emitters, the availability is reduced.

3 The NEXT experiment

The *NEXT*[1] experiment will search for the neutrinoless double beta decay in ^{136}Xe using a High-Pressure xenon (HPXe) Time Projection Chamber (TPC). The detector will run at the *Laboratorio Subterráneo de Canfranc* (LSC) under the Spanish Pyrenees [131] and its design is based on three main features: excellent energy resolution, use of topological signature for background suppression and ease scalability. The collaboration is a world-wide project involving about 100 physicists and engineers from different institutions in Spain, Portugal, USA, Colombia, Russia and Israel. In this chapter, we describe the main features of the detector and review the results from the R&D phase along with the status of the experiment.

3.1 Detector features

3.1.1 Separated-Optimized Functions TPC (SOFT)

A neutrinoless double beta decay event occurring in gaseous xenon would leave a very distintic signature: a 30-cm ionization track (at 10 bar) produced by the tortuous multiple-scattering of the two electrons in the gas terminated with large energy depositions at both ends (see Section 3.1.4). The identification of this topology in the event can be used for background rejection as proved by the Gotthard experiment [132]. Besides, the contribution of the two-neutrino mode can only be reduced with an excellent energy resolution.

While the reconstruction of the event requires a dense distribution of sensors, achieving an optimal energy resolution requires single-photon sensitivity and large photon collection areas. These two schemes can hardly be integrated in a single readout arrangement. Consequently, the approach of the NEXT experiment is based on the use of different types of sensors for different purposes, optimizing their functionality individually. This is known as the separated-optimized functions TPC (SOFT) concept [133, 134].

[1] **N**eutrino **E**xperiment with a **X**enon **T**PC

The design of the detector consists on an asymmetric TPC instrumented with photomultiplier tubes (PMTs) on one side for energy measurement (the *energy plane*), and with an array of silicon photomultipliers (SiPMs) on the other side for topology extraction (the *tracking plane*). The signal produced in the detector is amplified via electroluminiscence (Section 3.1.3) near the tracking plane to accomplish an optimal energy resolution. On top of that, the TPC walls are coated with tetraphenyl butadiene (TPB), a wavelength shifter that converts light into a more suitable frequency for its detection.

The timeline of an event in this detector, schematized in Figure 3.1 is as follows. A primary electron produced in xenon propagates through the medium scattering very frequently with atoms, transfering some energy in the process. Part of this energy is emitted as scintillation photons in the VUV range ($\sim$ 178 nm). The remaining is spent mostly in the ionization of the gas, producing secondary ionization electrons (ie). A moderate electric field (0.3 - 0.4 kV cm^{-1}) prevents electron recombination, drifting them towards the TPC anode, near the tracking plane. At the end of the drift region, the electrons go through a small gap (the *EL region*) with a more intense electric field (2 - 3 kV cm^{-1} bar^{-1}). The higher energy of the electrons when colliding with the xenon atoms produce VUV photons that are emitted isotropically. Since the sensors used in the detector are not sensitive to VUV light, a wavelength shifter is used in order to convert the light to blue ($\sim$430 nm), where the PMTs have a higher detection efficiency.

The scintillation light (S1) is detected by the energy plane, establishing the start of the event, t_0[2]. The electroluminiscence light (S2) is measured by both planes. The energy plane acts as a signal integrator: the total number of photons detected is proportional to the event energy. On the other hand, the tracking plane is placed a few mm away from the EL region, meaning that light is highly focused in one region. This light is detected by the SiPMs, placed in a regular grid, which act as pixels. The amount of charge in each pixel is inversely proportional to the distance to the emission point. Different algorithms can use this information to reconstruct the transverse position. The time difference between the S1 and S2 signals is used to compute the third spatial dimension, achieving a full three-dimensional reconstruction.

3.1.2 Energy resolution in xenon

As discussed before, an excellent energy resolution is mandatory for $\beta\beta^{0\nu}$ searches. It is needed for reducing both external and intrinsic backgrounds.

In gaseous detectors, the number of ionization electrons (N_i) is a good measure of the energy deposited. Fixed-energy events will have, on average, an energy $E = N_\mathrm{i} \cdot W_\mathrm{i}$, where W_i is the average energy needed to produce an ionization electron. The stochastic fluctuations in N_i have been found [136] to be generally well described by

$$\sigma_\mathrm{i}^2 = F \cdot N_\mathrm{i} = F \cdot \frac{E}{W_\mathrm{i}}, \tag{3.1}$$

where the number F depends on the medium and is known as *Fano factor*. This establishes a lower limit for the energy resolution, often called *intrinsic energy resolution* (FWHM) of the detector:

[2]These are weak signals. Thus, only the PMTs have the features (low noise, high gain, large collection area) necessary to detect them

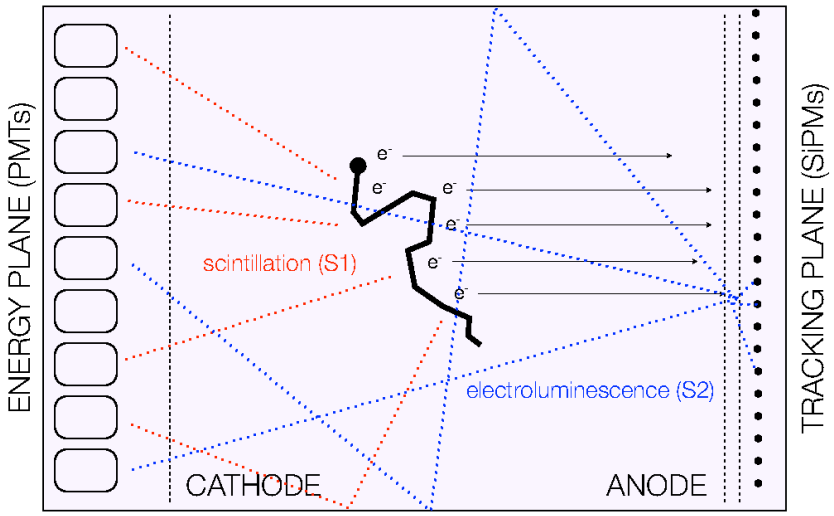

Figure 3.1: The Separated-Optimized Functions TPC (SOFT) concept [133, 134] as implemented in NEXT. The propagation of a primary electron in the gas (thick black line) produces scintillation light (red) detected by the PMTs and secondary ionization electrons. The latter are forced to drift towards the anode (thin balck lines), where they are accerelated to produce electroluminiscence photons (blue). This light is recorded by the PMTs, providing a calorimetry measurement, and by the SiPMs which, due to their proximity to the emission point, can provide a reconstruction of the event [135].

Figure 3.2: Anticorrelation between the scintillation and ionization signals for single-site events in LXe as recorded by the EXO-200 TPC using a ^{228}Th calibration source. The energy resolution improves significantly when considering both measurements [116].

$$\begin{aligned} \frac{\delta E}{E} = \frac{\delta N_\mathrm{i}}{N_\mathrm{i}} &= 2.35 \cdot \frac{W_\mathrm{i} \cdot \sigma_\mathrm{i}}{E} \\ &= 2.35 \cdot \frac{W_\mathrm{i} \cdot \sqrt{F \cdot E / W_\mathrm{i}}}{E} \\ &= 2.35 \cdot \sqrt{\frac{F \cdot W_\mathrm{i}}{E}} \end{aligned} \tag{3.2}$$

Different sources have reported Fano factors for gaseous xenon between 0.13 and 0.17 [137, 138, 139], in agreement with Monte Carlo simulations [140]. On the other hand, the energy resolution found in liquid xenon would translate to a value of the Fano factor $F > 20$ [117, 141], contradicting the theoretical estimations. There is no consensus in the causes of this discrepancy [142, 143], although the fluctuations in the recombination process at high densities seem to have a bigger impact than those in the creation of ionization electrons [133, 142]. The energy of recombination transitions is mostly emitted as scintillation light, which can be measured. An experiment in this high-recombination regime must take into account both the scintillation and ionization signals, which are strongly anti-correlated (see Figure 3.2) in order to improve the energy measurement. Nonetheless, the energy resolution is still one order of magnitude worse than that of the low-density domain.

In a paper in 1997 [144], Bolotnikov and Ramsey measured the energy resolution of ionization

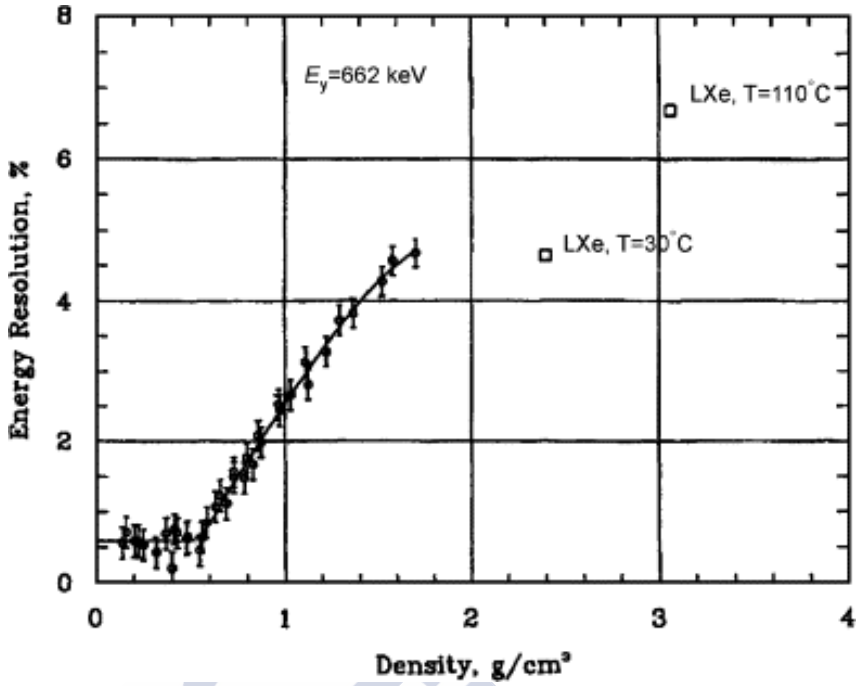

Figure 3.3: Dependence with density of the energy resolution FWHM measured in xenon using the ionization signal produced by the interaction of 662-keV gamma radiation from ^{137}Cs. [144]

signals produced by 662-keV gamma rays as a function of the xenon density. The result, shown in Figure 3.3, demonstrates clearly how the energy resolution is essentially constant for densities below $\rho_t \sim 0.55$ g/cm^3 ($P \sim 100$ bar) and deteriorates rapidly above that, approaching typical values for liquid xenon. Below the transition point and for the range of operation pressures of NEXT, the intrinsic energy resolution at 662 keV would be 0.6 % FWHM. It has been suggested [133, 142] that the contribution of globs of liquid xenon coexisting in the gas could account for this behavior. These globs would be more frequent as density increases, but practically inexistent below ρ_t.

Given the form of Equation 3.2, we can extrapolate the energy resolution to other energies as $E^{-1/2}$. At the $Q_{\beta\beta}$ value of xenon we find an energy resolution of:

$$\left.\frac{\delta E}{E}\right|_{Q_{\beta\beta}} \simeq 0.3 \text{ \% FWHM.} \tag{3.3}$$

The amount of photons and electrons in each case depend on the average energy needed to produce them, W_s and W_i, respectively. Different sources report experimental measurements for these quantities [145, 146]:

$$W_s = (76 \pm 6) \text{ eV}, \qquad W_i \simeq 22.4 \text{ eV}. \tag{3.4}$$

For ^{136}Xe, with $Q_{\beta\beta} = 2457.83$ keV, we obtain:

$$N_s = (32342 \pm 2551) \text{ photons}, \qquad N_i \simeq 109723 \text{ electrons}. \tag{3.5}$$

Since the operation pressure in NEXT is well below ρ_t, the effect of recombination discussed above can be neglected and the energy is measured purely from the ionization signal[3]. In that case, the optimal energy resolution is given by Equation 3.3. Notwithstanding, in practice, a number of effects can deteriorate this prediction. Some of those are the following:

1. Small concentrations of electronegative substances can reduce the number of ionization electrons reaching the amplification region. This process is known as attachment and can be reduced by means of a gas purification system, keeping a low level of impurities. On top of that, electron recombination, non-perfect transparency of the detector components, etc. can also have a second-order effect and reduce this number further. The less the number of ionization electrons, the higher the fluctuations, worsening the energy resolution. If ϵ is the overall electron collection efficiency, the fluctuations in N_i will be affected by a factor $L = 1 - \epsilon$.
2. The processes of signal amplification occurring within the PMTs introduce further fluctuations. For a signal amplification m, its variance is represented by G.
3. The intrinsic noise of calorimetric sensors increases slightly the variance of the output signal. For PMTs, this noise is gaussianly distributed and can be described by the standard deviation in electron units, n.

These are the main contributions to the energy resolution[4] and they are, in principle, uncorrelated. Assuming they are all gaussian processes, the total variance is the sum of variances:

$$\sigma_n^2 = (F + G + L) \cdot N_\mathrm{i} + \frac{n^2}{m}, \tag{3.6}$$

for an energy resolution of

$$\frac{\delta E}{E} = 2.35\sqrt{\frac{F + G + L + n^2/(mN_i)}{N_i \cdot \epsilon^2}}. \tag{3.7}$$

Examining Equation 3.7, it is clear that maximizing ϵ is essential. It would reduce L to a negligible value while minimizing the overall fluctuations. The Fano factor F is irreducible and the value G is usually larger than F for proportional counters involving avalanche multiplication, but that is not the case when using electroluminiscence amplification as discussed in Section 3.1.3. Finally, the last term is usually negligible for low-noise sensors, particularly for the $Q_{\beta\beta}$ energy range, but must be taken into account at lower energies.

Assuming optimal conditions (i.e. sufficiently high energies and perfect electron collection efficienty), the energy resolution can be written as:

$$\frac{\delta E}{E} = 2.35\sqrt{\frac{F + G}{N_\mathrm{i}}} = 2.35\sqrt{\frac{(F + G) \cdot W_\mathrm{i}}{E}} \tag{3.8}$$

[3]This is true as long as the density of ionization electrons is not too high, as is the case for alpha particles interacting in the medium.

[4]Some other contributions can be attributed to sensor calibration, non-linear responses, Bremsstrahlung losses, etc.

3.1.3 Electroluminiscence amplification

The impact of the amplification stage in this type of detectors is far from negligible. As discussed in Section 3.1.2, G needs to be much smaller than F in order to reach the optimal energy resolution given by the Fano Factor. To illustrate this, lets consider two amplification techniques: charge avalanche and electroluminiscence, depicted in Figure 3.4.

In charge-avalanche detectors (Figure 3.4a) the ionization electrons produced by incoming radiation are drifted towards an anode wire. In its vecinity, the electric field is suficiently strong for electrons to engage in ionizing collisions, leading to an avalanche of electrons, which is collected by the wire. This method usually amplifies an ionization signal by a factor $M \sim 10^3 - 10^4$. In this regime of amplification, space charge effects can ge neglected and the amplified signal is proportional to the original ionization signal, which is in turn proportional to the radiation energy:

$$N_{av} = M \cdot N_{\mathrm{i}} = M \cdot \frac{E}{W_{\mathrm{i}}}. \tag{3.9}$$

However, the fluctuations in M are not negligible. Their contribution to the energy resolution, $G_{av} = (\sigma_M/M)^2$, is of the order of the Fano Factor of gaseous xenon, with values ranging from 0.2 to 0.9 [148, 149] in common operation conditions.

On the other hand, in electroluminiscence detectors (Figure 3.4b), each electron is drifted towards a region with a moderately high electric field (EL region) where they are accelerated enough to excite the atoms or molecules of the medium but not to ionizing them. Excited atoms de-excite by emitting characteristic VUV light, which is collected by sensitive photosensors (typically PMTs). This intense signal is produced while the electrons drift and therefore is much more time-dilated than the scintillation signal. For some carefully chosen values of the electric field strength and EL region width the amplification gain (EL yield), Y, can be as high as a few thousands photons per ionization electron. It has been experimentally found [150] that the EL yield can be parametrized as

$$\frac{Y}{P\Delta x} = \left(136\ \frac{E}{P} - 99\right) \text{photons electron}^{-1}\ \text{cm}^{-1}\ \text{bar}^{-1}, \tag{3.10}$$

where P is the pressure, E/P the reduded EL field and Δx is the width of the EL amplification region.

The fluctuations in this optical amplification can be described by $\sigma_Y^2 = J_{CP}\ Y$, where J_{CP} is the so-called Conde-Policarpo (CP) factor. Contrary to the charge-avalanche technique, these fluctuations can be reduced to negligible values. This is shown in Figure 3.5, where the CP factor is represented as a function of the reduced electric field. The condition $J_{CP} \ll F$ is sattisfied for $E/P \in [1.6, 3.3]$ kV cm^{-1} bar^{-1}, and the fluctuations associated to this process can essentially be neglected. Notwithstanding, in contrast to the charge-avalanche technique, only a tiny fraction ($\eta \sim 0.1\%$) of the emitted light is actually detected. This is caused by a number of factors: the non-perfect material reflectivity, the finite photosensor coverage and the quantum efficiency of the photosensors, among others. In these conditions, the distribution of the number of photons converted to photoelectrons is well described by a binomial distribution with variance

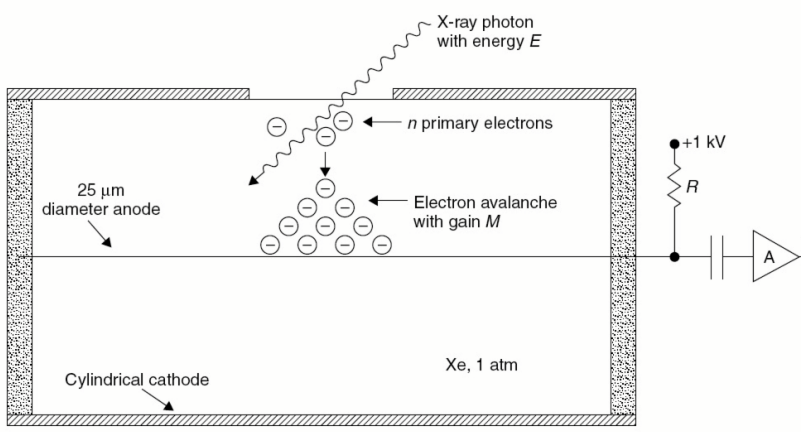

(a)

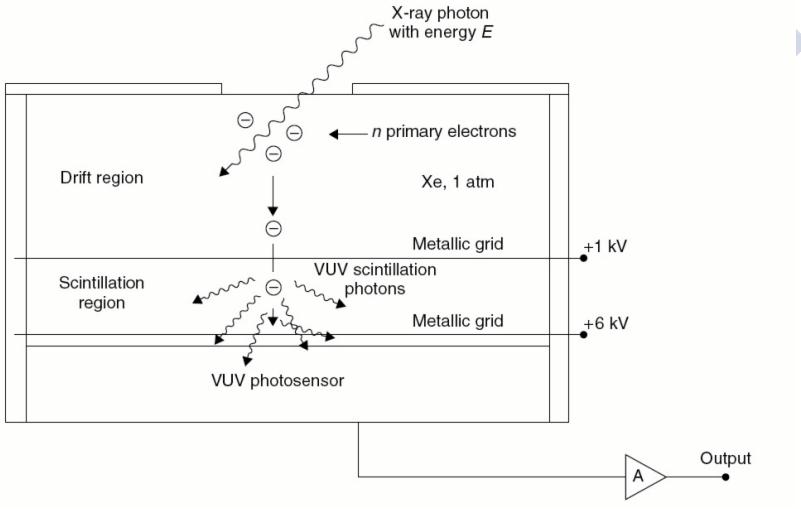

(b)

Figure 3.4: Principle of operation of a gas proportional counter with avalanche gain (a) and a gas proportional scintillation counter (b) [147].

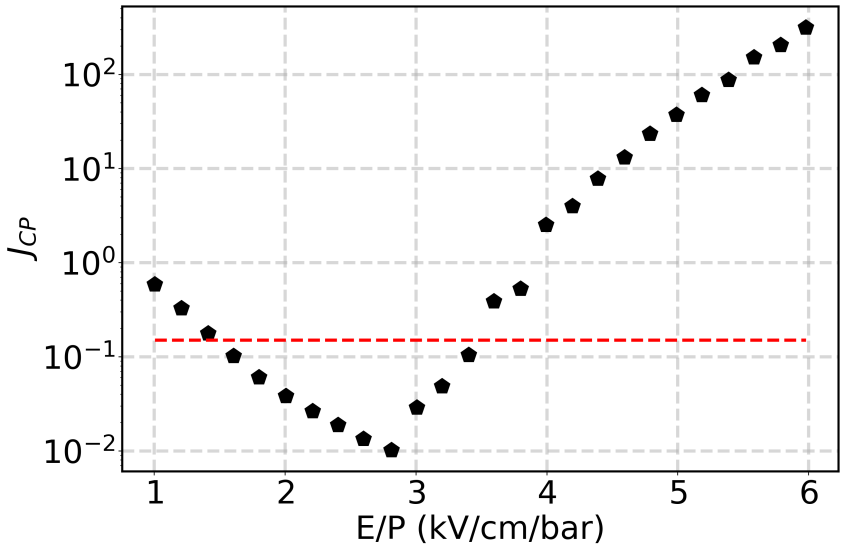

Figure 3.5: Dependence of the Conde-Policarpo factor (black dots), J_{CP}, with the reduced electric field strength for gaseous xenon. The Fano Factor in the same conditions is shown as a red dashed line. The condition $J_{CP} \ll F$ is sattisfied for $E/P \in [1.6, 3.3]$ kV cm^{-1} bar^{-1}. Figure redrawn from [150].

$\sigma_{pe}^2 = \eta(1-\eta)N_{\rm i}Y$. Finally, the amplification process occurring within the photosensor introduces another source of fluctuations that must be taken into account. The detection of a photon in this type of sensors is based on the photoelectric effect. When an electron is pluck from the active material of the sensor by an incoming photon, it engages in the charge avalanche process described above, amplifying the signal by several orders of magnitude. Hence, the fluctuations in that signal can be described by the characteristic resolution of the sensor $\sigma_{ps} = \sigma_q/q$, where q is the charge produced in the photosensor.

The contribution to the energy resolution of the entire electroluminiscence amplification process is determined by the addition of both contributions:

$$G = \frac{J_{CP} - 1}{Y} + \frac{1 + (\sigma_q/q)^2}{\eta Y}. \tag{3.11}$$

Near-intrinsic energy resolutions can be achieved if $G \ll F$. The current technology of photomultiplier tubes allows values of $\sigma_q/q \sim 0.5$ and, as mentioned before, J_{CP} can be much smaller than 1 with the appropriate conditions. Thus, the second term in Equation 3.11 dominates the contribution to the energy resolution. For this term to be smaller than the Fano Factor in xenon, $F = 0.15$, the number of photons detected per ionization electron, ηY, must be higer than 10. Under these circumstances, the energy resolution is given by

$$\frac{\delta E}{E} = 2.35\sqrt{\frac{F+G}{N_{\rm i}}} = 2.35\sqrt{\frac{F}{N_{\rm i}} + \frac{J_{CP}-1}{YN_{\rm i}} + \frac{1+(\sigma_q/q)^2}{\eta Y N_{\rm i}}}. \tag{3.12}$$

In Figure 3.6, each of the contributions to the energy resolution is disected for $P = 15$ bar, $\eta = 6 \cdot 10^{-3}$ and $\Delta x = 6$ mm. Notice that the energy resolution decreases rapidly below 1

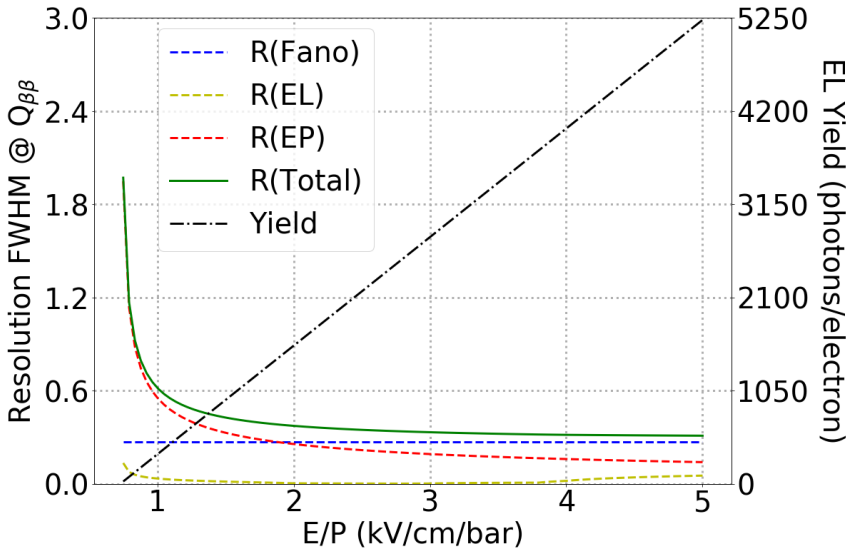

Figure 3.6: Energy resolution terms and EL yield as a function of the reduced electric field for a 6-mm-wide EL region, an overall photon collection efficienty $\eta \sim 0.006$ and a pressure $P = 15$ bar [151].

kV cm^{-1} bar^{-1} and then approaches asympotically to the Fano limit from 2 kV cm^{-1} bar^{-1} onwards. Hence, near-intrinsic energy resolutions are achievable with moderately high electric fields.

3.1.4 Event topology

As stated in Section 3.1.1, background rejection can be performed using the event topological information. A high-energy electron propagating through a high-pressure gas will lose energy in two phases. For energies of the order of 1 MeV, the electron losses energy approximately at a constant rate of $\sim$ 65 keV/cm, behaving as a minimum inonizing particle (MIP). On the other hand, for lower energies, the electron losses its energy rapidly in a very short distance at a rate inversely proportional to the electron energy. This large energy deposit is the so-called *blob*, and can only be recognized in gaseous detectors.

A $\beta\beta^{0\nu}$ event produces two electrons, the kinetic energies of which add up to que $Q_{\beta\beta}$ value. The tracks of those electrons are conected at the decay point and teminate in two *blobs*, one at each end (see Figure 3.7a). On the other hand, at the $Q_{\beta\beta}$ energy, the main background are high-energy photons comming from the natural radioactivity of the detector components. When those photons interact in the gas volume, they produce a track with about the same energy and length but, crucially, only one *blob* (see Figure 3.7b). This feature allows the differenciation of signal and background events from the three-dimensional reconstruction of the event.

The background rejection capability relies ultimately on the ability for *blob* recognition. This presents a number of challenges. The electron tracks are twisty and can overlap themselves, which makes the reconstruction more complicated but, more importantly, can create small regions with high energy depositions that can mimic a low-energy *blob*. Great spatial resolutions are needed for these cases to be resolved efficiently. Moreover, during the first stage of the electron propagation, when it is still highly energetic, it can produce delta rays or emit *bremsstrahlung*

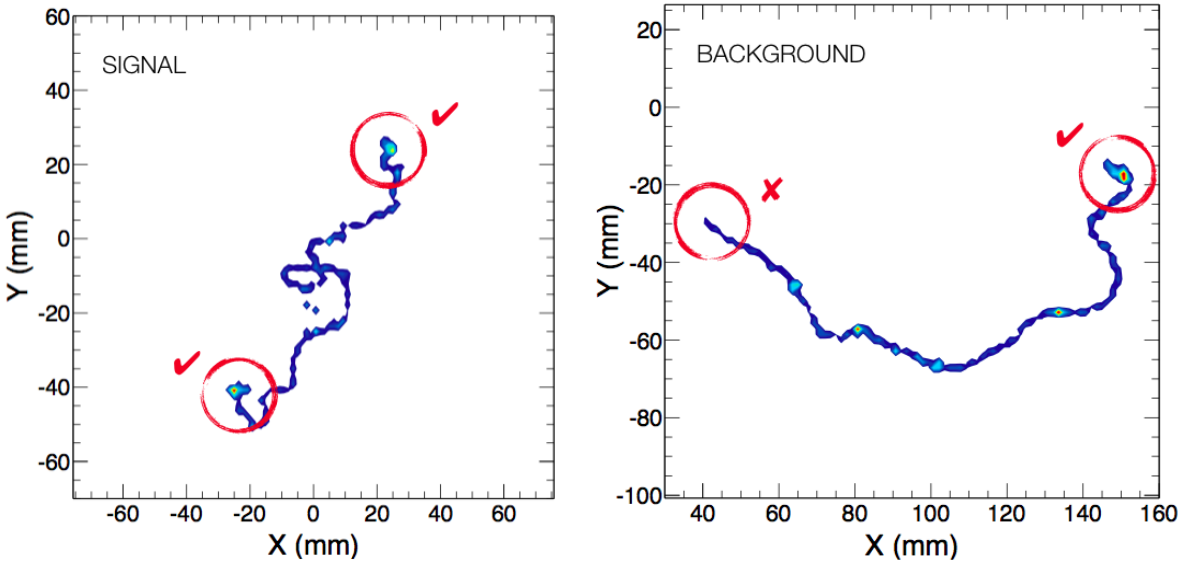

(a) Signal (b) Background

Figure 3.7: Characteristic topological signatures of signal and background events in NEXT. Both events were produced using a Monte Carlo simulation in xenon at 15 bar. The $\beta\beta^{0\nu}$ event (left panel) contains two blobs, while the single-electron background event (right panel) contains just one [152].

photons which can reconvert to electrons near the main electron track. This proximity can make the two tracks to be misidentified as a single track, which will have the same signature as that of a $\beta\beta$ event. On the other hand, the intrinsic transverse and longitudinal diffusions of the drifting electrons make both of the previous points even more difficult to address, as the tracks become blurry and two-point separation becomes inneficient.

In pure xenon, the transverse and longitudinal diffusions are, respectively, of the order of 1 mm/$\sqrt{\text{cm}}$ and 0.3 mm/$\sqrt{\text{cm}}$. With drift lengths of the order of tenths of meters, a blur of the order of 1 cm is expected. This means that tracking schemes with sensor spacings below 1 cm do not translate in a big improvement in reconstruction. Moreover, these sensors are placed a few mm from the emission plane and will eventually receive a considerable amount of light. Thus, they must be able to operate in a non-saturation regime while maintaining a reasonable gain in order to differenciate between MIP- and *blob*-like sections of the track. They must also be stable and operate at high pressure (10 - 15 bar) as they are exposed to the gas.

Silicon photomultipliers (SiPMs) are a good technological solution as they fulfill all the aforementioned requirements. Besides, these sensors are relatively unexpensive, are not greatly radioactive and can yield a good spatial resolution without extremely dense arrays. Monte Carlo simulations within the NEXT collaboration have shown [134] that a 1-cm pitch square array is the optimal compromise between background rejection ability and a reasonable number of channels at the nominal operation pressures (10 - 15 bar).

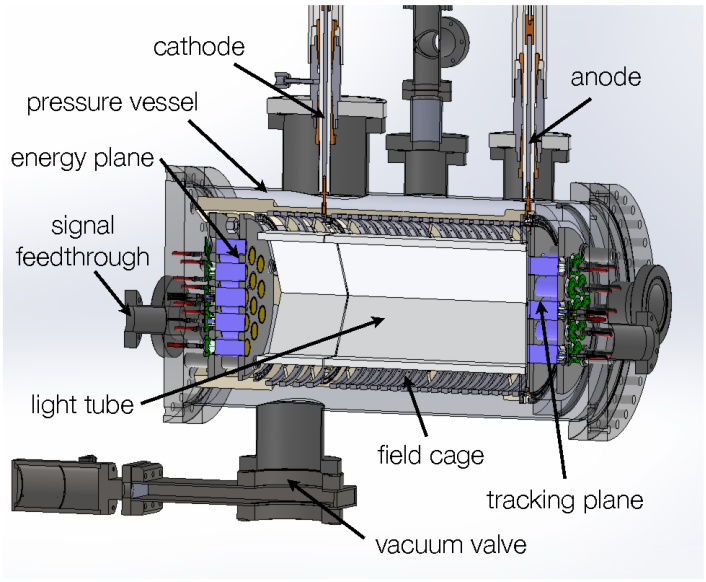

Figure 3.8: Cutaway view of the NEXT-DEMO detector with the major components labeled [153].

3.2 R & D detectors

The first phase of the NEXT project (2009 - 2014) has been largely devoted to R & D. Two small-sized prototypes were built to demonstrate the detector concept and capabilities. The collaboration also used these detectors to explore technological solutions for larger detectors while accumulating technical expertise. In this section we describe both detectors and give a summary of their major results.

3.2.1 NEXT-DEMO

Designed as a proof-of-concept prototype, the NEXT-DEMO detector (see Figure 3.8) was a HPXe electroluminiscent asymmetric TPC that operated from 2009 to 2014. A vessel capable of withstanding up to 15 bar housed a 30-cm drift length TPC with a 16-cm radius hexagonal cross section. The TPC included an EL amplification region 5 mm width and was instrumented with 19 1-inch PMTs and 256 1-mm^2 SiPMs arranged in a 1-cm-pitch square grid. Light collection was improved by introducing a PTFE tube (*the light tube*) with high-reflectivity that also defined the active volume. The xenon circulated in a closed loop through the vessel and a number of purifying systems to ensure a long electron lifetime. The detector was not made radiopure nor shielded against external backgrounds and the whole equipment was installed in a semi-clean room at *Instituto de Física Corpuscular* in Valencia, Spain.

With this prototype the collaboration aimed to validate the design for the target NEXT-

100 detector (described in Section 3.4). Specifically, the main goals of this prototype were to demonstrate the energy resolution capabilities of this technique and to proof that the event topology can be used to background rejection. Besides, on the technical side, the collaboration used this detector to understand gas circulation and purification in large volumes and to test long drift lengths, high voltages and wavelength shifters.

The TPC was operated in two stages. During the first phase, the detector was instrumented with 19 1-inch pressure-resistant Hamamatsu R7378A photomultiplier tubes on both planes. To avoid saturation, the tracking plane was operated in a low gain regime. With this configuration, the detector run with two different conditions: ultraviolet configuration (UVC) in which the light tube was not coated with a wavelength shifter and blue configuration (BC), in which the detector components were coated with TPB[5]. Due to the inefficienty of PMTs for track reconstruction, this feature of the detector could not be evaluated and only average position of the event was achieved. Notwithstanding, the energy resolution was measured in both conditions using the 511 keV back-to-back photons from the β^+ decay of a ^{22}Na source. After correcting for geometrical light collection variations, an energy resolution of 2.89 % FWHM at 511 keV for the UVC and 1.75 % FWHM for BC (see Figure 3.9) [154]. The improved energy resolution in the blue configuration is a direct consequence of the factor 3 increase in light collection produced by the wavelength shifter. A $E^{-1/2}$ extrapolation to the $Q_{\beta\beta}$ value for the BC result yields a resolution of 0.8 % FWHM, well within the target range of the NEXT experiment: 1 % FWHM at $Q_{\beta\beta}$.

For the second phase of the DEMO operation, the PMTs of the tracking plane were replaced by 256 Hamamatsu S10362-050-11P silicon photomultipliers (SiPMs), which allowed a better reconstruction. The energy resolution was again evaluated with this configuration using ^{22}Na and ^{137}Cs calibration sources [155]. For the ^{137}Cs photopeak (662 keV), the energy resolution was measured to be 1.56 % FWHM, which extrapolates $E^{-1/2}$ to 0.83 % FWHM at $Q_{\beta\beta}$ (see Figure 3.10). A slightly better result was obtained for the 511 keV photopeak of the ^{22}Na source: 1.62% FWHM at 511 keV, which extrapolates $E^{-1/2}$ to 0.74 % FWHM at $Q_{\beta\beta}$[156].

Besides measuring energy resolution, the collaboration applied some preliminary reconstruction methods using the newly installed tracking plane. The technique consist in applying a barycentre algorithm (described in Appendix A) to the time-sliced signal of the SiPMs. Each slice corresponds to one value in the drift coordinate (z) while the transverse coordinates (x and y) are provided by the barycentre algorithm. After matching the PMT signal to each point, a three-dimensional reconstruction of the event is achieved. On top of that, a cubic spline was used for a smoother result as shown in Figure 3.11, where different types events are displayed.

More thorough analyses of the background rejection capabilities of the technique were also performed with this detector [152]. In these studies, based on the contrast between blob energies, a background rejection of (75.7 ± 1.4) % with a signal efficiency of (66.7 ± 1.0) % was achieved, matching closely the results obtained from Monte Carlo simulations (see Figure 3.12).

3.2.2 NEXT-DBDM

Designed to demonstrate the excellent energy resolution capabilities of the technology, the NEXT-DBDM prototype (see Figure 3.13) was built and operated from 2009 to 2014 at Lawrence

[5]The xenon emits light in the UV wavelength range (172 nm) where the photosensors have poor detection efficiency. However, they are much better in the visible range, thus the choice of using a wavelength shifter to convert UV photons into blue ones.

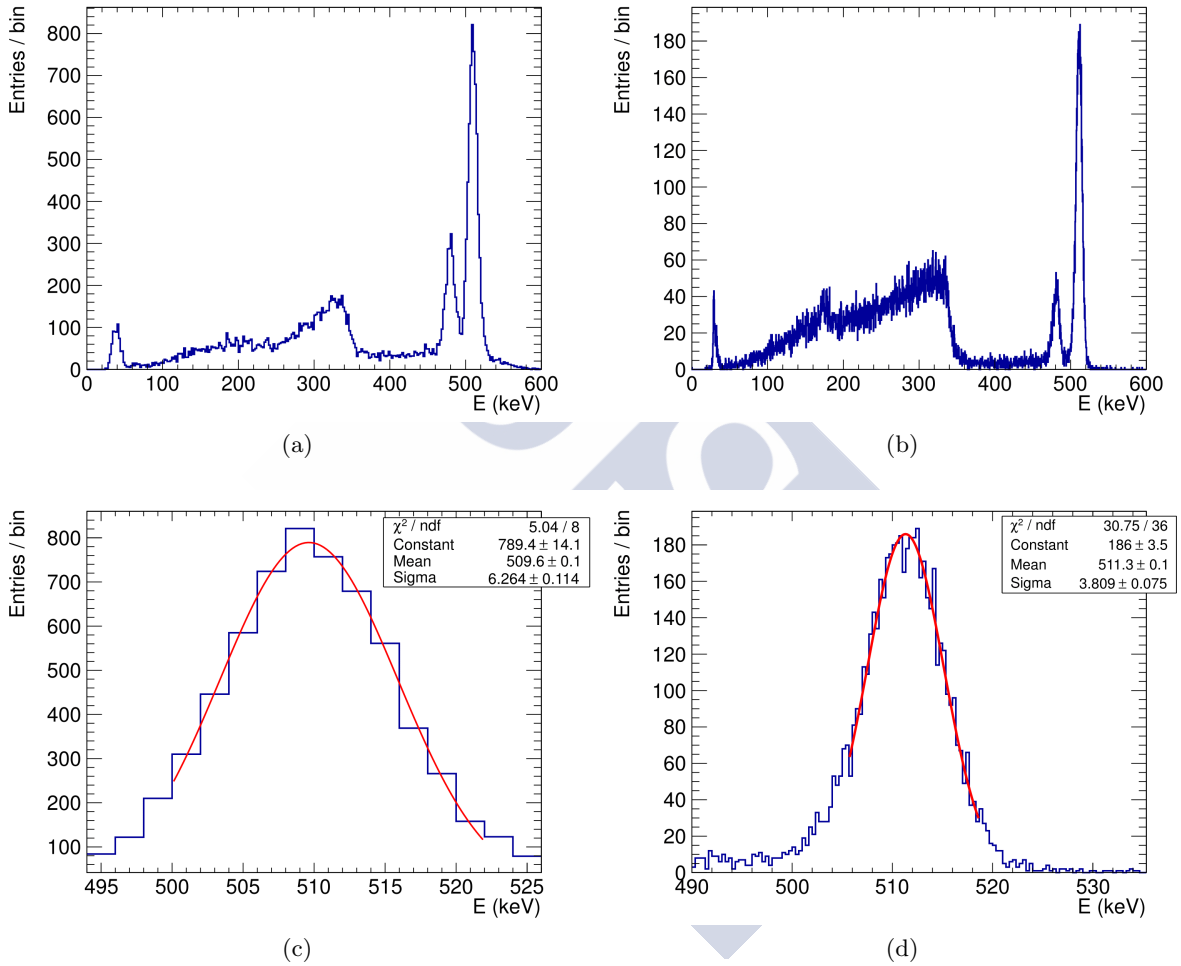

Figure 3.9: Top: Energy spectra produced by the interaction of 511-keV gammas from a ^{22}Na calibration source in the active volume of the detector after geometrical corrections for the UV configuration (left) and the blue configuration (right) of the NEXT-DEMO detector. Bottom: Gaussian fits to the photopeak of the respective spectra above. The fits yield an energy resolution of 2.89 % FWHM (left) and 1.75 % FWHM (right) with acceptable χ^2 values [154].

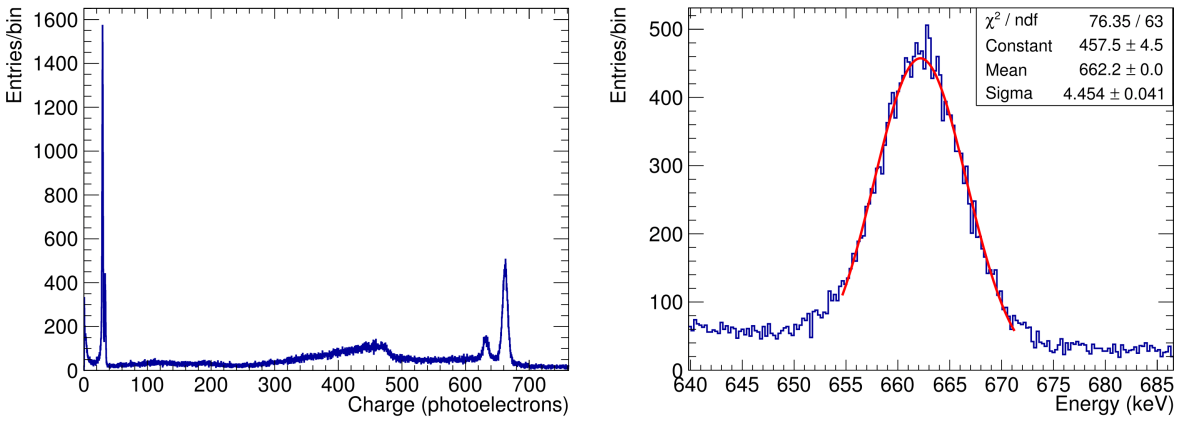

(a) (b)

Figure 3.10: Full energy spectrum of 662-keV gamma interactions from a ^{137}Cs calibration source in the active volume of the NEXT-DEMO detector after geometrical corrections (left) and detailed view of the photopeak energy region (right) with a gaussian fit to extract resolution. The fit yields a resolution of 1.56 % FWHM, which extrapolates $E^{-1/2}$ to 0.74 % FWHM at $Q_{\beta\beta}$ [156].

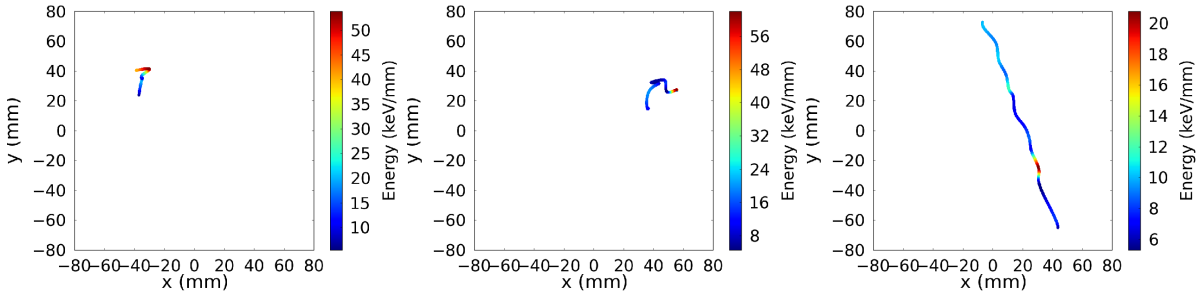

(a) ^{22}Na (b) ^{137}Cs (c) μ

Figure 3.11: x-y track projections of three different types of events as reconstructed in NEXT-DEMO. [155]

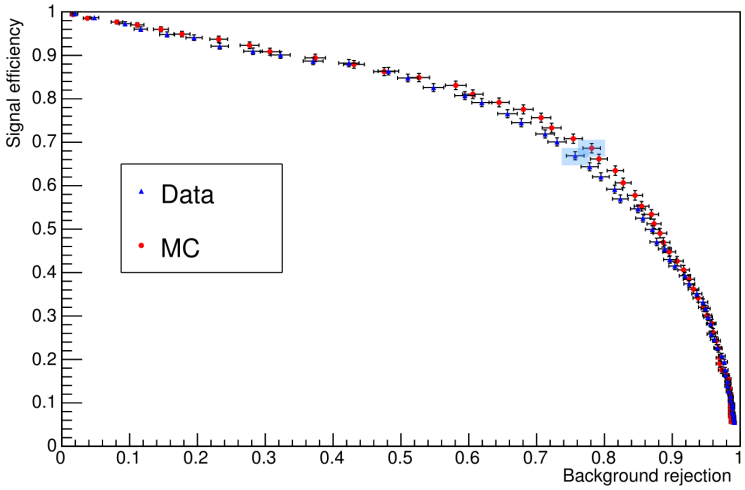

Figure 3.12: Signal efficiency as a function of background rejection obtained with the NEXT-DEMO detector when varying the required minimum energy of the lower energy blob candidate [152].

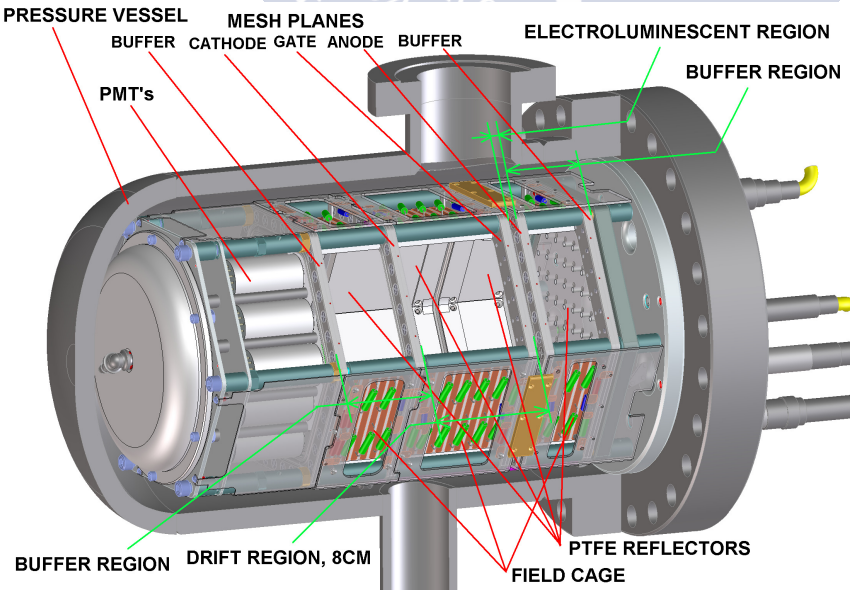

Figure 3.13: Cutaway view of the NEXT-DBDM detector with the major components labeled [153].

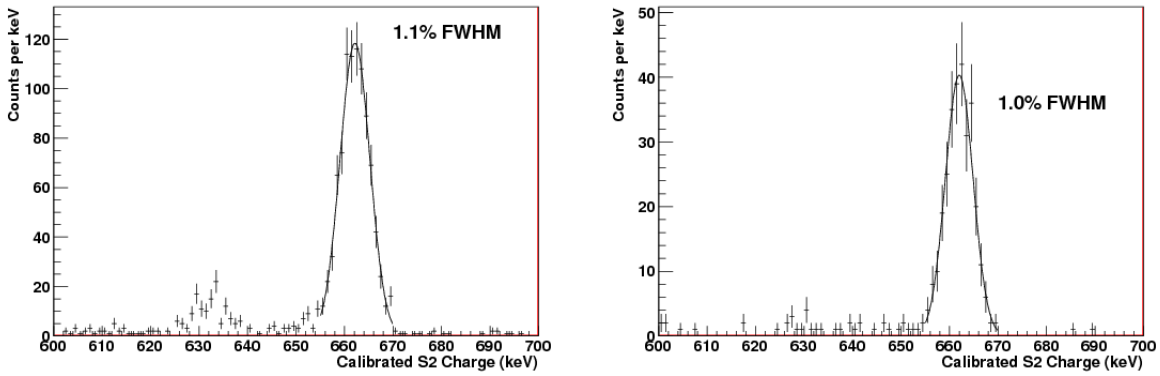

(a) (b)

Figure 3.14: Energy spectra measured with NEXT-DBDM at the 662 keV photopeak produced by a ^{137}Cs source at 10 bar (left) and 15 bar (right). Energy resolutions of 1.1 % FWHM and 1.0 % FWHM at 662 keV are found, respectively [157].

Berkeley National Laboratory (USA). As in the NEXT-DEMO design, the TPC had a hexagonal cross section with a drift length of 8 cm and a 5-mm-wide EL amplification region. It was housed in a 33.5-cm long stainless steel cylindrical pressure vessel 20 cm in diameter. The detector was instrumented with 19 1-inch PMTs in the energy plane, whilst a reflective plate was used in place of the tracking plane to improve light collection efficiency.

The most salient result from this detector is the energy resolution analysis performed using the 662 keV photopeak from a ^{137}Cs source. In this study [157], an energy resolution was measured at 10 bar and 15 bar achiving values of 1.1 % FWHM and 1.0 % FWHM, respectively, at 662 keV (see Figure 3.14). These values, extrapolated as $E^{-1/2}$ to $Q_{\beta\beta}$, produce energy resolutions of 0.57 % FWHM and 0.52 % FWHM, well within the target range of 1 % established by the collaboration.

3.3 The NEXT-White detector

After a successful R & D phase, the NEXT collaboration begins the first stage of the experiment with the construction of NEXT-White[6] (NEW): a 1:2 scale model of the NEXT-100 detector in both the radial and the longitudinal dimensions. NEW is an intermediate step in the construction of the NEXT-100 detector. Its primary purposes are the validation of the technological solutions proposed in the Technical Design Report [158] in a large-scale detector and the assessment of the background model. This detector will also provide a measurement of the energy resolution close to the $Q_{\beta\beta}$ energy and the characterization of the 2-electron topological signature, by measuring the $\beta\beta^{2\nu}$ mode. NEXT-White started operations at *Laboratorio Subterráneo de Canfranc* (LSC) in October 2016 and, after a short comissioning run (Run I), it run under estable conditions for over eight months (Run II) at a pressure of 7.2 bar and $E/P \simeq 1.7$ kV cm^{-1} bar^{-1}. After a short Run III with a technical problem, operation was resumed in May 2018 (Run IV). During the current Run, the detector will be used to measure the background in the operation conditions foreseen for the $\beta\beta^{2\nu}$ Run.

[6]Named after Prof. James White.

3.3.1 Gas system

The gas system used for the NEW detector is almost the same than the one that will be used for NEXT-100 since both detectors have the same gas requirements with the obvious exception of the volume. Thereby, once the NEXT-100 detector is ready, the only parts that we will need to be changed are the pressure vessel and the recovery tanks.

The gas system is a vital part of the detector given that the source and detection medium of the detector coincides. In addition, Its main functions are the following:

- Pressurization and depressurization of the system.
- Recirculation and cleaning of the gas.
- Evacuation of the detector.

These operations have to be completely safe and without major failures when operating with xenon due to the gas price, especially when enriched. This reliability level can not be achieved just with passive components because some decisions require active input. For this reason, the gas system has been fully automated using a *Compact RIO* (a FPGA-based PLC (Programmable Logic Controller) from *National Instruments*). The *Compact RIO*, which runs a real time *LabVIEW* variant, is connected to the different monitoring devices of the system (pressure gauges, vacuum gauges, valves, compressor, chiller, etc.) and acts accordingly by opening and closing the valves that control the gas flow. The *Compact RIO* is also connected to the slow control net so all the parameters can be used to generate the proper reports or alarms and to interact with the other elements connected to this net, explained later.

For the gas evacuation, the standard procedure consists on the liquefaction of the gas stored in the whole system using a custom cryo-recovery bottle (Figure 3.15a). This bottle is cooled carefully with liquid nitrogen so the gas is recovered slowly by the depressurization created. Then, a vacuum pump is used to recover the residual gas in the vessel and the rest of the pipes.

However, this procedure is rather slow and has to be done manually thus rendering it useless in the case of an emergency. For this reason an emergency recovery technique had to be implemented. To do this recovery an emergency tank, with a volume capable of housing the whole experiment gas at approximately 1 bar, is kept at a moderate vacuum. If an anomaly is detected and the gas on the experiment is compromised, a big *Carten* valve is automatically opened and the gas flows quickly from the vessel to the tank through a 4-inch pipe. Once there, the gas can be redirected to the cryo-recovery bottle to safely store the gas. As shown in Figure 3.15b, during the NEW phase the NEXT-100 vessel is used as recovery tank, as it has the desired volume for this function.

Gas cleaning is an absolute necessity in order to avoid signal deteriorations due to impurities. For cleaning, the gas is in constant recirculation, using a compressor built by the *SERA* company, through getters (Figure 3.16a). Two types of getters are used: the cold getters, which clean the gas from O_2, H_2O, CO, H_2, volatile acids, organics, refractory compounds and volatile bases; and the hot getter, which outlet impurity levels for O_2, H_2O, CO, CO_2, H_2, N_2 and CH_4 are reduced to low parts per billion (ppb) levels or below.

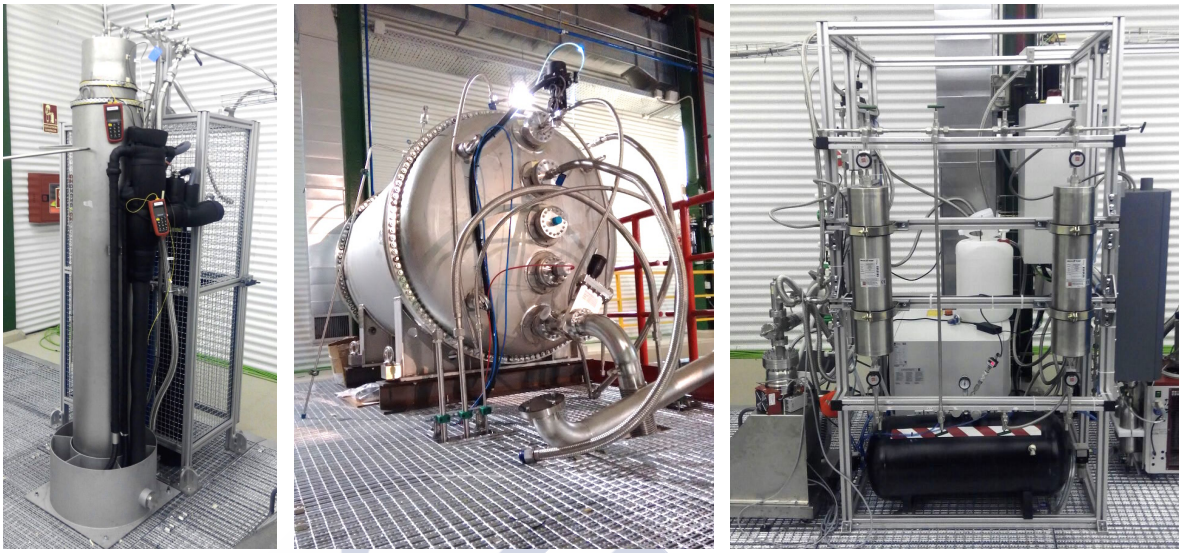

(a) Cryo-recovery bottle (b) NEXT-100 vessel used as emergency recovery tank (c) Gas system frame with the main components

Figure 3.15: Different parts of the gas system for the NEXT-White detector.

(a) Gas system frame holding the getters (b) Compressor (c) Compact RIO cabinet

Figure 3.16: Different parts of the NEXT-White gas system involved in gas recirculation.

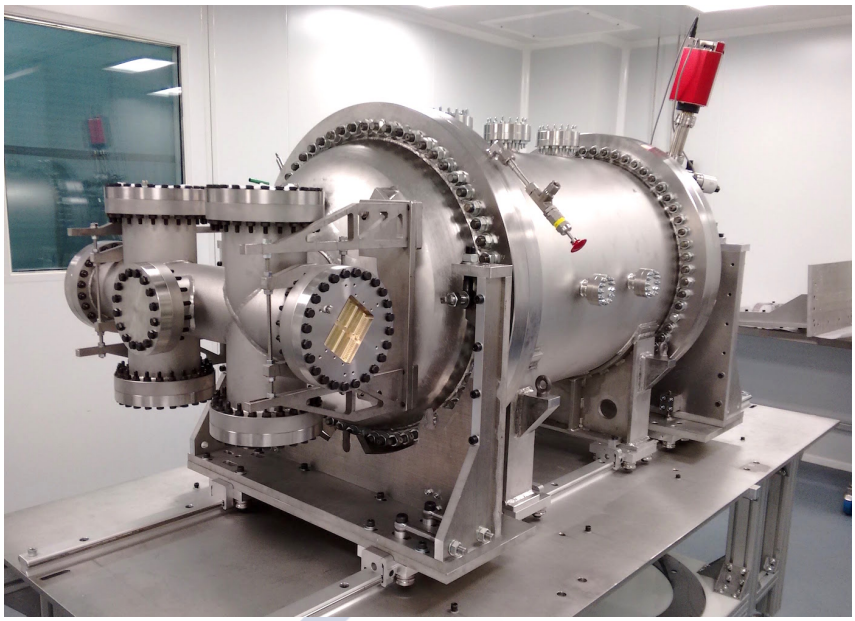

Figure 3.17: The NEXT-White detector pressure vessel before being placed in the operation platform.

3.3.2 Pressure vessel

The NEW pressure vessel (Figure 3.17) has been manufactured with the same 316Ti steel alloy selected for the NEXT-100 detector, from *Nironit* [159, 160], by the company *TRINOS*. The fabrication of the vessel was made possible thanks to a *CEDETI* grant.

With an internal diameter of 64 cm and a length of 950 cm, the dimensions of NEW are intermediate between NEXT-DEMO and NEXT-100. By design the pressure vessel can hold up to 50 bar and it is CE certified to 20 bar.

For shielding purposes, inside the vessel there are 6 cm thick copper bars, covering all the cylinder. The bars are designed with a stepped profile, so each one matches the adjacent bars while impeding the passage of outer particles into the active volume. In addition to that, both detection planes have a copper plate incorporated of 12 cm thickness. This ensures that all the active volume is properly shielded form any direction except for some openings in the copper, placed to allow the detector calibration using radioactive sources outside the vessel.

3.3.3 Lead castle

To shield NEW from the external flux of high-energy gamma rays, the pressure vessel of the detector is placed inside a lead castle (Figure 3.18), with a wall thickness of 20 cm, made of layers of staggered lead bricks held with a steel structure. The bricks have standard dimensions ($200 \times 100 \times 50$ mm^3), and an activity in uranium and thorium lower than 0.4 mBq/kg so they do not become a major background source of the experiment.

The lead castle is made of two halves mounted on a system of wheels that moves on rails and alternates between two possible positions: an open and a closed one. The former is used for

Figure 3.18: The NEXT Experiment lead castle. The NEW detector stands previously to the piping and cabling installation.

installation and service of the pressure vessel; the latter is used during normal operation. A lock system fixes the castle to the floor in both configurations to avoid accidental displacements.

Due to the mild seismic activity of the part of the Pyrenees where the LSC is located, the lead castle is mounted on a seismic structure in order to isolate it from possible ground vibrations. Thereby the lead castle is not mechanically attached to the working platform, and all the electrical and gas connections are flexible between this separate structures.

3.3.4 Time projection chamber (TPC)

Field cage

The field cage generates the electric field within the active volume of chamber to drift the ionization electrons produced in the gas. This electric field has to be enough to avoid electron recombination in gas. On the other hand, the field in the drift region should be highly uniform and homogeneous trying to avoid any radial component of the field. Those field characteristics are mandatory to ensure no charge losses in the walls during the drifting process.

The NEW field cage has an outer diameter of 500 mm and a length of 500 mm. This dimensions are approximately equal to both the longitudinal and radial dimensions expected for NEXT-100.

The design is based on a high density polyethylene (HDPE) cylindrical shell, 25 mm thick, which isolates the copper shield from the voltage inside the cage. There are copper rings uniformly

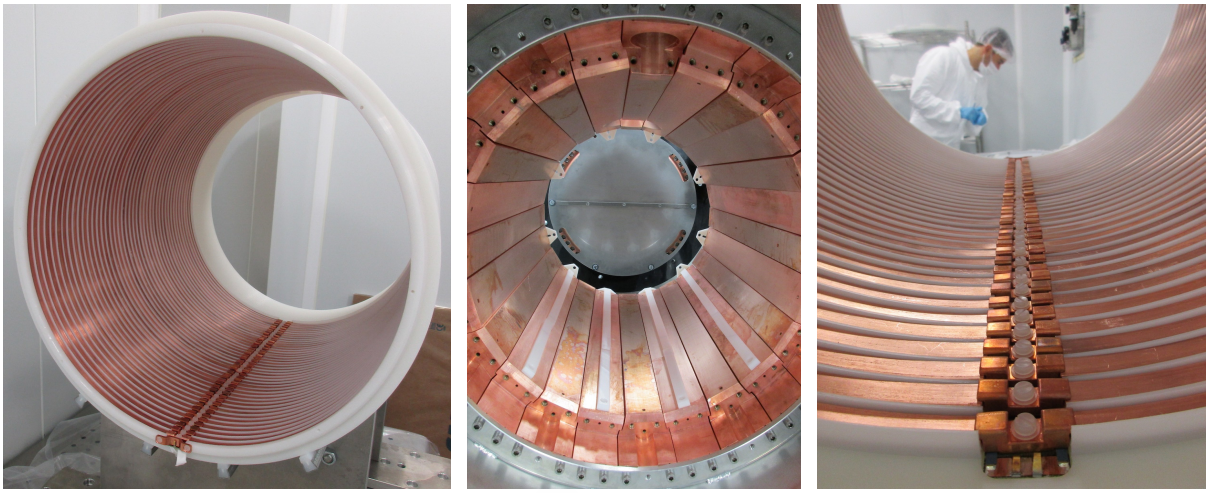

(a) Field cage before being installed

(b) HDPE supports to keep the field cage in place

(c) Detail of the copper rings attached to the resistor chain

Figure 3.19: Detail of the NEXT-White field cage during assembly.

distributed placed inside grooves in the HDPE body and connected by copper clamps to a resistor chain. This scheme allows for an homogeneous field.

These rings are made out of electrolytic copper which section is a rounded rectangle of 10×3 mm and 0.5 mm radius on the edges. The grooves for the rings are 4 mm in depth, allowing some space between the surface of the ring and the wall of the field cage that is necessary to support the light tube inside the field cage.

Cathode

In the energy plane end-side of the field cage, a transparent grid is placed to serve as the TPC cathode (Figure 3.20a). It is located at 100 mm from the PMTs. The cathode is the section with the highest voltage, which produces the electric field towards the gate, where the EL region starts.

However, an electric field is also produced in the PMTs direction. Since the cathode is at high voltages, an enormous electric potential is produced between the PMTs and the cathode. This potential has to be degraded to near zero volts at the PMT window surface so a buffer region is defined.

In this region the design of the field cage is made in such a way that it degrades the voltage without using rings, trying to avoid electric fields regions near the breakdown. The polyethylene there is also slightly thinner (15 mm) than in the drift region to give enough space to introduce the cathode inside the field cage.

The electric field that will be generated in NEW will be $\sim$0.3 kV cm^{-1} enough to avoid recombination of the ionized electrons. Therefore, a maximum voltage of 30 kV (for a drift of 500 mm) is foreseen in the cathode.

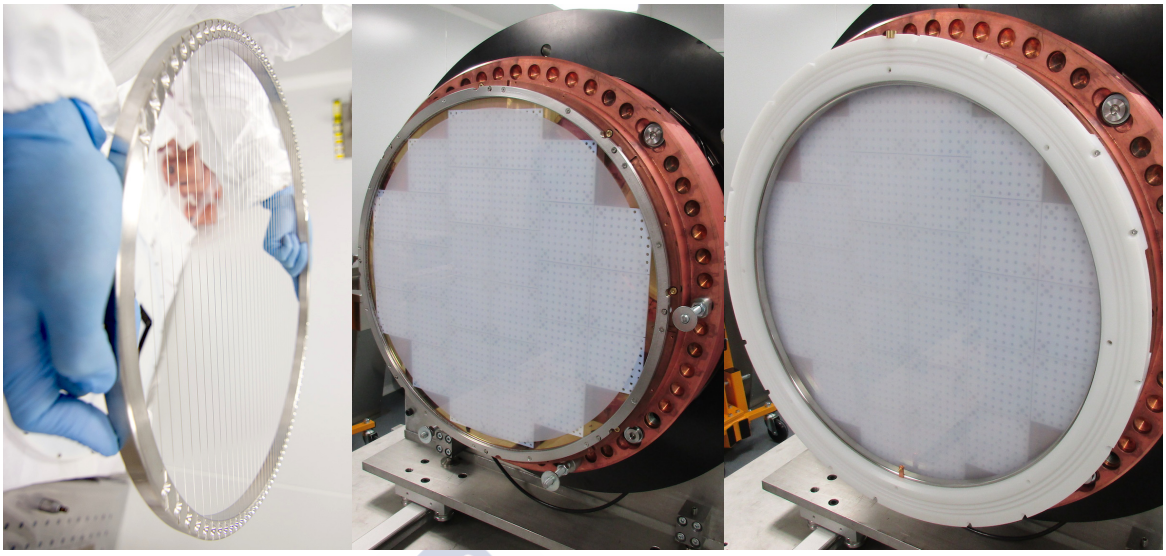

(a) Cathode grid (b) Fused silica anode (c) Gate grid mounted over the anode

Figure 3.20: The NEXT-White field cage cathode, anode and gate, during the installation on June 2016.

EL region, gate and anode

The solution for the EL region is to use a combination of a mesh, for the gate (Figure 3.20c), and a solid quartz (fused silica) plate coated with Indium-Tin Oxide (ITO) as anode (Figure 3.20b). This coating results in a ∼90% transparency conductive layer that allows to fix a voltage in the surface of the quartz plate and then creates an homogeneous field in the EL region. The quartz plate is coated with TPB to shift the VUV light of the xenon electroluminescence to blue, to be detected by the tracking plane SiPMs which are not sensitive to VUV light.

The quartz plate solution has multiple advantages. First, it protects the SiPMs from sparking and there is no need to coat the SIPMs themselves, only the quartz plate. Second, it removes the necessity for tension and strength at one side of the mesh, only a small ring surrounding the edge of the ITO coating is needed to prevent sharp edges of the conductive layer. The production of the quartz plate is simpler and cheaper than the mesh.

Both anode and gate are assembled in the tracking plane copper plate, so the distance between the anode and the SiPMs can be precisely adjusted between 4 and 6 mm. Then a spring contact in the gate connects it electrically to the field cage.

The anode is set at 0 kV while the gate voltage values will vary depending on the pressure of the detector and the width of the EL region. When operating at 15 bar and EL region width of 5 mm, 15 kV will be needed at the gate for an E/p of 2 kV cm^{-1} bar^{-1}.

Resistor chain

The resistor chain has two purposes: to hold together the two sides of the different rings, and to connect the rings by resistors. Thereby a voltage divider is created and the potential is uniformly

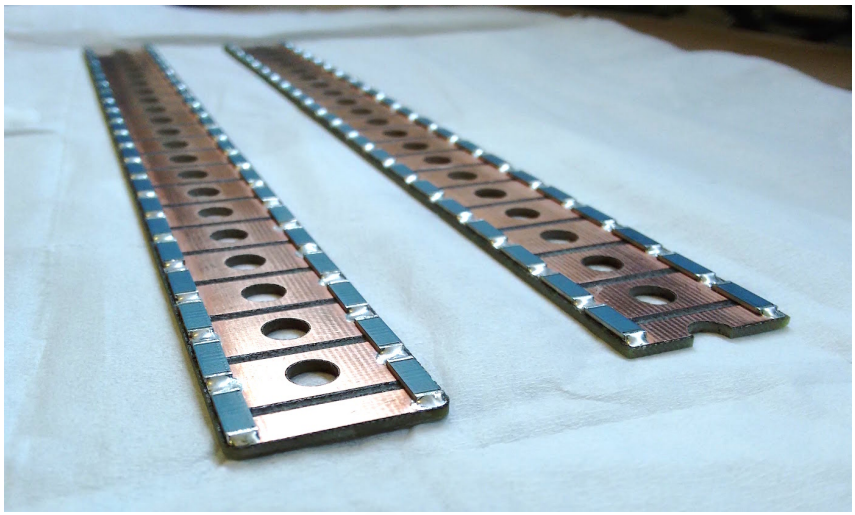

Figure 3.21: The NEXT-White resistor chain in two pieces before the assembly on the field. The chain shown is the first FR4 prototype, made to test the field cage performance before the final one is produced.

degraded.

The NEXT-White resistor chain (Figure 3.21) is mounted on a *CuFlon* board connecting every ring to the next one and also the cathode and the gate to their closest rings. The resistors need to hold high voltage and their tolerance needs to be minimum to guarantee homogeneity in the electric field. Instead of using just one resistor between rings two parallel 10 GΩ resistors have been mounted to safeguard a possible resistor failure.

High voltage feedthroughs

The voltages needed for the operation of NEXT-White are similar to the NEXT-DEMO requirements. The design has been slightly modified for a better connection with the cathode and gate of this detector.

The feedthroughs have been completely redesigned to ensure that they hold easily the 50 kV considered as the maximum requirement for normal operation. The design is based on an original idea by H. Wang [161].

Light tube

The most internal part of the detector, the light tube (Figure 3.23), consists of a hollow PTFE cylinder, placed inside the field cage. As explained and to increase light collection, the inner side of the light tube has been coated with TPB. Due to the big size of the pieces, the coating was made at the *Darkside* [162] facilities of the *Laboratori Nazionali del Gran Sasso* (LNGS).

The light tube has an inner diameter of 416 mm, and a wall of just 10 mm. Due to the delicate design parameters, a preliminary version (shown in Figure 3.23) made by several rings attached together was first used. A new one will be produced in just one piece and installed in a

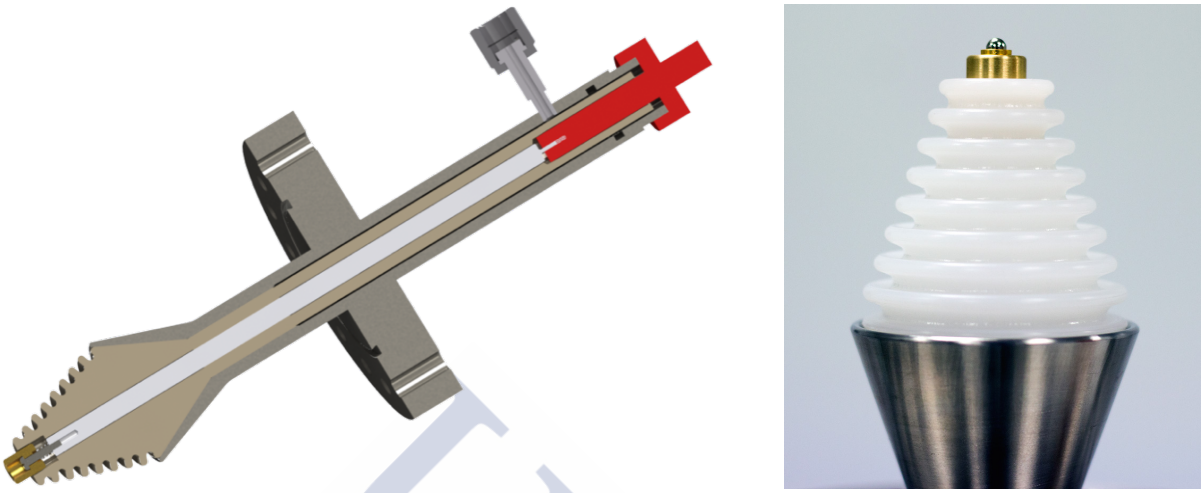

(a) HV feedthrough design cross section

(b) HV feedthrough tip detail

Figure 3.22: High voltage feedthroughs designed for NEXT-White.

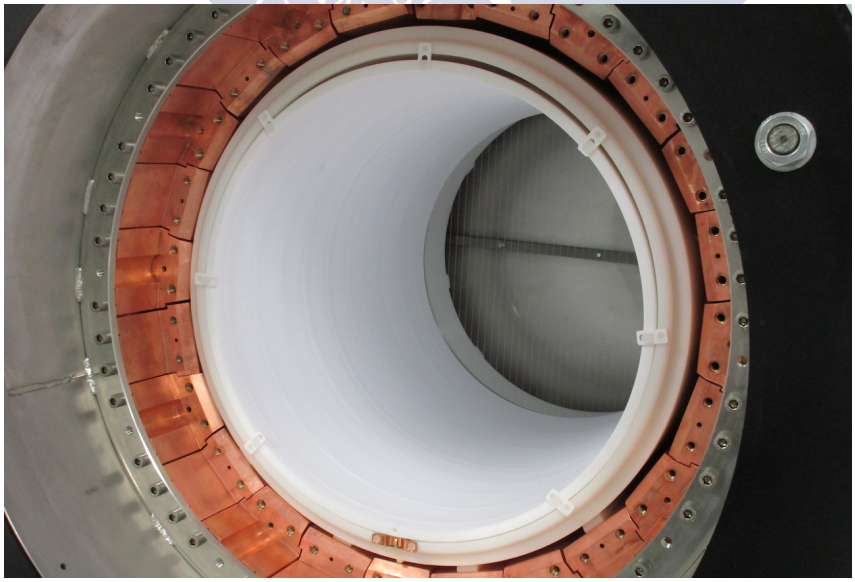

Figure 3.23: The NEXT-White light tube, made of PTFE.

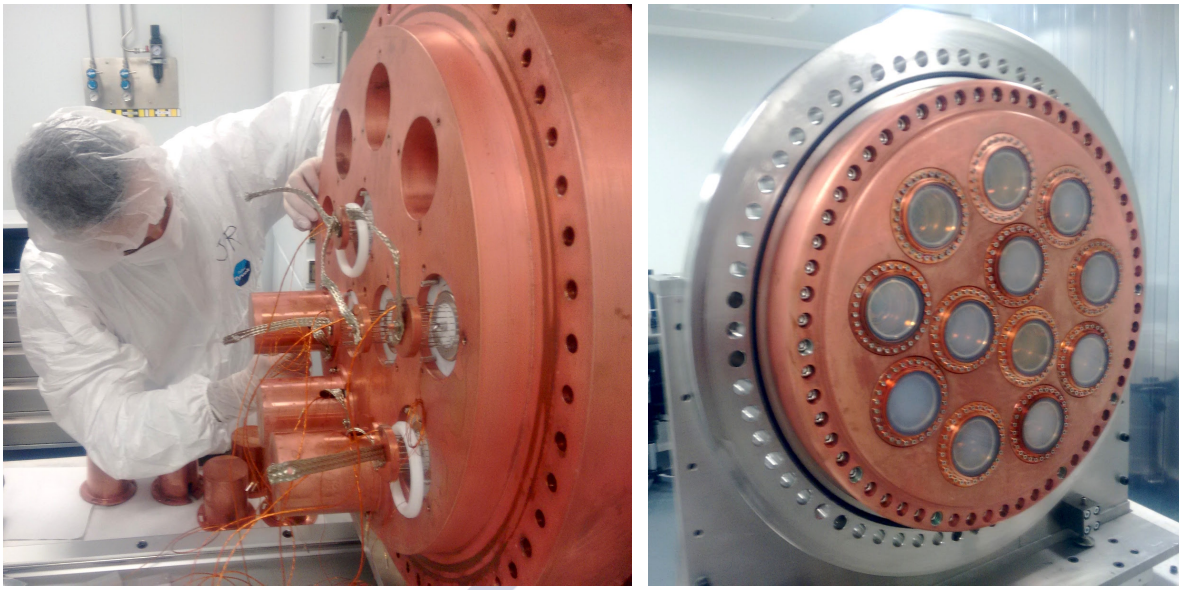

(a) Back side of the energy plane being installed. The PMTs are placed inside the holes, and covered with a 12 cm copper "hat"

(b) Front side of the energy plane. The sapphire windows isolate the vacuum from the pressure

Figure 3.24: The NEXT-White energy plane during installation on July 2015.

detector upgrade.

Near the cathode there is a small support that prevents it from touching the cathode wires. The light tube does not need any fixing to the field cage, it is supported by friction to it.

3.3.5 Energy plane

The NEXT-White energy plane is composed by 12 *Hamamatsu R11410-10* PMTs [163]. These PMTs, which will also be used in NEXT-100, are characterized by their low radioactivity and are ideal for low-background experiments. The design of the energy plane (shown in Figure 3.24) consists of a 12 cm thick copper support plate with 12 copper window surrounds with brazed sapphire windows fixed to the front of the plate and covering the 12 apertures through which the PMTs are fed. The set-up as a whole seals the pressure vessel from the torispherical head which is held at vacuum levels of $\sim 10^{-4}$ mbar.

Additional copper shielding (Figure 3.24a) are fixed to the vacuum side of the apertures to guard against gammas traversing the PMTs and entering in the detector volume. The PMTs are optically coupled to the sapphire window using *NyoGel OCK-451* and held in place by a HDPE brace and spring.

In order to improve the light collection, the sapphire windows are coated with TPB. To protect the PMTs from the electric field inside the TPC, the windows were also coated with a conductive layer of ITO, the same used for the fused silica plate on the field cage.

The PMTs are supplied with high voltage and have their signal extracted via a shielded twisted pair cable connected to a custom feedthrough in the torispherical head. The distribution

(a) One of the Hamamatsu R11410-10 PMTs

(b) Kapton base potted with thermal epoxy

Figure 3.25: One of the PMTs and its polarization base used in the NEXT-White detector.

of signal and supply at each individual PMT is controlled using a *Kapton* circuit board (base) which has the resistor divider to properly fed the PMT dynodes. Then the base is covered with a copper cap filled with epoxy which is connected by a braid to the support plate, to allow generated heat to be dissipated in the vacuum conditions.

3.3.6 Tracking plane

The NEXT-White tracking plane is made of 28 *Kapton* boards, known as DICE-boards within the collaboration (KDB). Each KDB has an 8×8 SiPM array placed with 1 cm pitch for a total of 64 SiPMs, a NTC temperature sensor and four LEDs for PMT calibration. The KDBs over-cover the fiducial region with 1792 SiPMs, ensuring that there are no blind spots. The connector is located at the end of a long tail, and is separated from the gas, in the fiducial volume, by a 120 mm thick copper plate shield.

The choice of material for the board was driven by the radioactivity budget of the experiment. To reduce the background contribution of the tracking plane *Kapton* was chosen as its activity (upper limit) is, at least, one order of magnitude less than the DICE-boards used in NEXT-DEMO.

To improve the reflectivity of the tracking plane and be able to collect more light on the energy plane the DICE-Boards are covered by PTFE masks, as shown in Figure 3.26b.

3.3.7 Electronics and DAQ

From the beginning of the NEXT Experiment, the electronics were devised to be easily scalable and compatible with all the detector stages. So almost all the electronics are evolved versions from the early stages of NEXT-DEMO.

The energy plane front-end have been upgraded to accommodate the new differential cable scheme intended to reduce the coupled noise due to the long cables. Also, as the PMTs are biased with positive voltage, a coupling capacitor is needed in order to isolate the high voltage

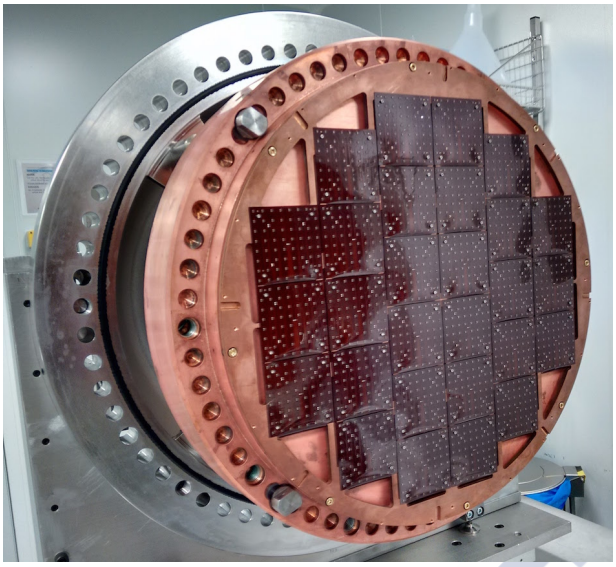

(a) Tracking plane installation on November 2015

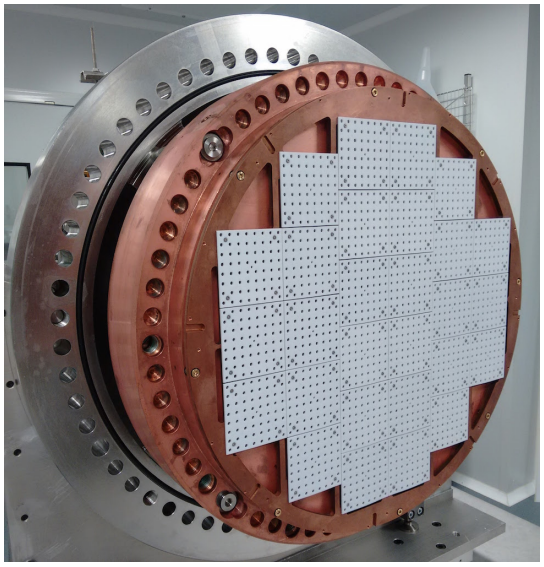

(b) Tracking plane upgrade with PTFE masks on April 2016

Figure 3.26: The NEXT-White tracking plane.

from the input analog stage, but allowing the smalls signals to pass through. This produces a known effect that distorts the signal, so a further signal reconstruction that deconvolves this effect is needed to keep the energy resolution [164]. This deconvolution can be made online so the trigger is not affected by the distortion but also offline as the raw signal and the deconvolved one are sent to the ADC cards via HDMI cable. There the signals are digitized, and then processed.

Concerning the digital stage, each front-end board has a *Virtex-6 XC6VLX130T* FPGA which reads out data from up to 64 1-MHz ADCs, formats data, time-stamps and stores them in a reconfigurable-length dual-event circular buffer to avoid dead time. When a trigger is received, zero-suppressed data are read out and sent to the upper stage. The circular buffer is implemented with the internal resources of the FPGA and is able to store two complete events in raw mode, whose maximum size corresponds to several times the maximum detector drift time (up to 3.2 ms).

Baseline adjustment and zero-suppression parameters (baseline reference, value over the baseline, pre- and post-samples, minimum number of samples to consider a pulse) are configurable through a set of commands. In zero-suppression mode, the system triggers when the signal exceeds the value over the baseline fixed during at least the minimum number of samples to consider a pulse. Then, this signal is sent with its pre- and post-samples. Raw data mode of operation, where no zero suppression occurs, is also supported for testing purposes.

Both tracking plane and energy plane front-end cards interface the Scalable Readout System's (SRS) DAQ interface modules [165] (tested on both FECv3 and the new FECv6) through the SRS' DTCC (Data, Trigger, Clock and Control) link specification over copper [166]. In this link, data, trigger, clock and slow controls flow on the same RJ-45 or HDMI connector over 4 LVDS pairs. *ALICE's DATE* is used as DAQ software environment. As a result, the front-end electronics are fully compatible with CERN RD-51 SRS electronics. The DTCC configuration used is the basic one. The link has been fully tested up to 250 Mbps over the two data pairs using 1-m-long SFTP 6A copper cables.

Figure 3.27: The NEXT-White electronics cabinets. From the left, the computers and servers, the energy plane, and the tracking plane cabinet. At each side of the cabinets there is a big UPS, capable of supply the whole system up to 40 minutes in case of power failure.

3.3.8 Slow control

The complexity of the NEXT-White detector demands an advanced control system. This system is the so-called the slow control (SC). With the slow control an internal network which connects all the subsystems and devices involved in the experiment has been created. In addition, it adds an intelligence that keeps the system safe and acts to prevent and solve problems immediately. In Figure 3.28 the control displays are shown.

An especialized slow control for each of several systems of NEW has been developed to a total number of six:

- **High Voltage:** Monitors and controls the voltage on the field cage cathode and gate. Detects the sparks and recovers or shuts down the system according to the parameters set.
- **Gas System:** Monitors all the parameters involving the gas system: valves, pressure, vacuum, compressor, chiller, vacuum pumps, RGA. It allows for manual activation of an emergency stop.
- **Power Supplies:** Monitors and controls all the power supplies that power the electronics in the experiment.
- **PMT High Voltage:** Monitors and controls the PMTs power supply, detects overcurrents and controls the vacuum pump connected to the energy plane volume.
- **Sensors:** Monitors the temperatures and other important parameters of the electronics and DAQ computers. It also controls the contactors that power almost all the equipment and electronics.

Figure 3.28: The Slow Control for the NEXT-White detector.

- **Main:** This slow control receives the main parameters and warnings from the other ones and summarizes them so shifters know if everything is working properly just looking at this one. It also has an emergency button, that stops everything to prevent damage, and can remotely switch on the other slow control computers.

All the slow controls are interconnected since their behavior may affect other subsystems. All of them also generates reports, including all the events registered for each subsystem and the main parameters measured. Also emails are sent to shifters, with warnings or alarms produced, so intervention can be done as soon as possible.

3.4 The NEXT-100 detector

The NEXT experiment was formally proposed to the *Laboratorio Subterráneo de Canfranc* in 2009 in a *Letter of Intent* [167] that outlined the physics case and basic design concepts. The detector design was narrowed down in a Conceptual Design Report [134] published in 2011, and fixed a year later in a Technical Design Report (TDR) [158]. Given this timeline, the configuration of the prototypes from the R & D phase was consequently favored as it had been thoroughfully tested.

As mentioned before, the NEXT-White detector is a ∼1:2 version of the NEXT-100 detector. Thus, only some minor differences need to be stipulated:

Pressure vessel and inner shielding

The NEXT-100 pressure vessel Figure 3.29 is made of a cylindrical central section of 160 cm length, 136 cm inner diameter and 1 cm wall thickness, and two identical torispherical heads of 35 cm height, 136 cm inner diameter and 1 cm wall thickness. As for the NEXT-White detector, it has been fabricated with stainless steel type 316Ti due to its low levels of natural radioactive

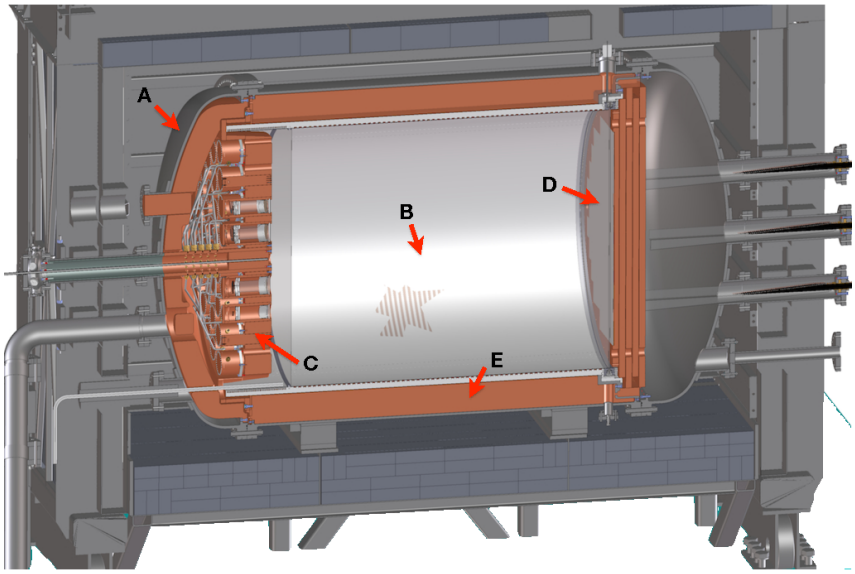

Figure 3.29: Cross-section view of the NEXT-100 detector inside its lead castle shield. A stainless-steel pressure vessel (A) houses the electric-field cage (B) and the two sensor planes (energy plane, C; tracking plane, D) located at opposite ends of the chamber. The active volume is shielded from external radiation by at least 12 cm of copper (E) in all directions.

contaminants. The vessel has been built by a specialized company based in Madrid and designed almost entirely by the Collaboration following the ASME Pressure Vessel Code.

The radioactivity from the vessel is stopped from entering the active volume by an inner copper shield of 12 cm thickness. This reduces the γ contamination from the vessel by three orders of magnitude.

Field cage and light tube

The main body of the field cage is an open-ended high-density polyethylene (HDPE) hollow cylinder of 148 cm length, 107.5 cm inner diameter and 2.5 cm wall thickness that provides structural stiffness and electric insulation. A series of copper rings for electric field shaping are fixed to the inner surface of the cylinder, soldered to a resistor chain that fixes the voltage of each ring. The rings are covered by highly-reflective PTFE tiles coated with TPB to shift the xenon VUV light to blue and improve the light collection efficiency. One of the ends of the HDPE cylinder is closed by a fused-silica window 1 cm thick. The inner surface of the window functions as the TPC anode thanks to a transparent, conductive of Indium-Tin Oxide (ITO) and is also TPB-coated. The two other electrodes of the TPC, the EL gate and the cathode, are positioned 5 mm and 106.5 cm away from the anode, respectively and are built with highly-transparent stainless steel wire mesh stretched over circular frames. The high voltage is supplied to the electrodes via custom-made feed-throughs.

Energy plane

The energy plane of the NEXT-100 detector will be composed of 60 3-inch Hamamatsu R11410-10 PMTs [163] located behind the cathode of the TPC for a coverage of ∼30 %. The copper plate and mechanical elements of the energy plane have the same structure as NEXT-White, adapted to the bigger size of the detector.

Tracking plane

The structure of tracking plane will be a scaled replica of the one made for the NEXT-White detector. The number of DICE-Boards is increased to 112 for a total of 7168 SiPMs. Due to the larger amount of SiPMs, the feed-through is being improved and optimized, to allow higher connector density. Also the front-ends used will be the future revision of the board, the FEB64v3.

Electronics

The design of the electronics subsystem will remain untouched, aside from an overall scaling. It will need a larger number of electronic boards (roughly five times more front-end cards) with the subsequential DAQ system scale.

Gas system

The gas system components used for the NEXT-White detector are already those planned for NEXT-100 and therefore only minor modifications need to be implemented for this detector. The most noticeable difference is the emergency recovery tank, which is ten times bigger as the factor-of-two increase in detector dimensions translates into a much higher gas volume.

4 Simulation of an optical TPC

The simulation of the detector response is an essential tool for any physics experiment. For NEXT, it has guided the design of the NEXT-100 detector as well as its prototypes in different manners. For instance, it has been used to estimate the performance of the detector in various configurations (for example, different pitch sizes of the tracking plane), to predict the background levels under specific conditions and to develop the reconstruction and selection algorithms used in NEXT-White (Chapter 5). Besides, the comparison of real data results with those obtained with a Monte Carlo simulation reflects the understanding of the detector.

In this chapter, a Monte Carlo study of the response of the NEXT-White detector is presented. A map of the light collection of the detector along the three spatial coordinates is performed to produce the so-called *light tables*. This tables can be used to substitute the light-propagation stage of Monte Carlo simulations, which is extremely computationally intensive. The use of the light tables allows the generation of large-statistics Monte Carlo datasets, which would be otherwise impossible to create due to the long computation times. However, a fine description of the detector requires enormous tables and the technique becomes unfeasible for large detectors, such as NEXT-White or NEXT-100. Therefore, the response maps are parametrized to generate a set of functions that reproduce the detector response in all of the active volume. Finally, this methodology is repeated for the NEXT-100 detector.

This technique has allowed the collaboration to simulate a background spectrum based on radioactivity measurements made to the different components. These data will be crucial to understand the different background contributions of the experiment, which ultimately determines its the sensitivity to the $\beta\beta$ decay. Moreover, the simulation of $^{83}\mathrm{Kr}^{m}$ data has helped to demonstrate the quality of the results of the analysis presented in Chapter 6.

4.1 The NEXT simulation software

The software for simulation is divided into different modules to perform very specific tasks. The first module, NEXUS(Section 4.1.1), uses the Geant4 package [168] to simulate the interactions of the electrons in the gas. Then comes DETSIM (Section 4.1.2), a C++ module that simulates the light propagation within the detector. Finally the *diomira* (Section 5.1.2) programme emulates the electronics of the detector.

4.1.1 Nexus

In the case of NEXT, the complexity of the particle propagation within the chamber requires the use of numerical techniques to simulate the signal produced in each sensor. This is done in NEXUS[1], a Geant4-based [168] programme to simulate the NEXT detectors. NEXUS was developed by the Collaboration in the beginning of the project and refined ever since. A detailed description of the software can be found in [169] and only a brief overview is offered here.

As a Geant4-based programme, the NEXUS software follows its same structure. The detector simulation is divided into four main modules: the detector geometry, where the dimensions and characteristics of every component are specified; the physics lists, where the physical process to be taken into account are enumerated; the event generation, where the initial conditions of any event are described; and the user actions, where the data operations are designated. All these parameters are set in plain-text configuration files with a specific format.

The programme has two main modes of operation: full simulation and fast simulation. In the fast simulation mode, a number of primary particles are placed in a certain region of the detector with a certain momentum. These particles are propagated in the medium and their interactions are simulated based on physical models, which can result in the production of additional particles. The energy depositions in the active volumen of the detector are stored in the form of *track hits* and written to the output file.

In the full simulation mode, the programme carries on with the emission of scintillation (S1) photons and the drift of secondary electrons. The scintillation photons produced during the passage of charged particles through the medium are individually tracked along their trajectories. The trajectory information can be recorded in disk for further analysis. Those photons reaching a PMT or a SiPM add entries to the zero-suppressed time histogram that constitutes the sensor waveform[2] The sampling (time bin) of this histogram is a configurable parameter. The secondary electrons are subjected to the electric field which forces them to drift towards the anode while diffusing both in the tranverse and the longitudinal directions. Finally, the emission of EL photons (S2) is simulated. Each photon is individually tracked, following the same procedure as for the S1 light.

[1] Acronym for **NEX**T **U**tility for **S**imulation

[2] A sensor waveform is the digitized signal produced by the sensor for a given time interval. See Section 5.1.1 for a more detailed description.

4.1.2 Detsim

The tracking of photon trajectories is the most computational-intensive task of the simulation. For low-energy electrons (41.5 keV) a fully-simulated event takes about two minutes, but this becomes unfeasible for events in the $Q_{\beta\beta}$ energy range as it takes multiple hours to generate an event. However, the generation of the *track hits* is fairly rapid, taking only a few ms per event. Moreover, the physical processes simulated in the full mode depend only on certain parameters. For instance, it is well known that the diffusion of drift electrons can be statistically modeled as a gaussian distribution which standard deviation is the diffusion coefficient. In the case of light emission, the amount of light detected for a given point in space depends only on the geometry and materials of the detector, which are generally fixed. This leads to the division of the simulation process into two stages: *track hits* simulation and *detector response* simulation.

The simulation of track hits is the aforementioned fast simulation mode of the Nexus programme. The simulation of the *detector response*, on the other hand, is a separate programme: Detsim[3]. In this software, the *track hits* produced by Nexus are read to produce sensor waveforms. As stated before, Detsim uses numerical models of the physical processes in order to generate the result more rapidly. The main tasks performed by Detsim are the following:

- Create ionization electrons. The energy despositions in the active volume can be translated to an average number of ionization electrons as $N_i = E/W_i$ (see Section 3.1.2). The actual number of ionization electrons created by a particular energy deposition comes from sampling a Poisson distribution with $\lambda = N_i$. These electrons are placed at the same point as the originating energy deposition, which are created for every mm traveled by the originating particle.

- Simulate the electron transport to the EL region. The drift of electrons occurs purely on the z coordinate, but their diffusion along both the tranverse and longitudinal coordinates blurs its position in the three-dimensional space. This is modeled as a gaussian distribution centered at the originating point and with a standard deviation corresponding to the diffussion coefficient. The diffusion coefficients for the transverse and longitudinal coordines have been recently measured in NEXT-White [170]. The values obtained were (1279 $\pm$ 3 (stat.) $\pm$ 40 (sys.)) $\mu\text{m}/\sqrt{\text{cm}}$ for the transverse diffusion coefficient and (318.9 $\pm$ 1.8 (stat.) $\pm$ 20.1 (sys.))$\mu\text{m}/\sqrt{\text{cm}}$ for the longitudinal coordinate at 7.2 bar. Each electron (x, y)-position and time-of-arrival is individually computed by sampling these gaussian distributions.

- Simulate the light emission and detection in each sensor. Given a certain detector description, the (x, y)-position of the electron fully determines the photon detection probability for each sensor. These probabilities can be computed beforehand, building a detection probability model for the detector. The average number of photons in each sensor is then given by $N_{av} = G_{EL} \cdot P(x, y)$, where G_{EL} is the EL amplification gain, i.e. the average number of photons emitted per ionization electron; and $P(x, y)$ the probability model for a given sensor. Finally, the actual number of photons detected by each sensor is sampled from a poisson distrubution with mean N_{av}.

These operations are performed on an event-by-event basis. For each event, a zero-suppressed

[3] Detsim stands for **DET**ector **SIM**ulation

time histogram is recorded for each sensor, producing an output equivalent to that of the full simulation mode.

4.2 The light detection probability model for NEXT-White

Building a detection probability model is an exhaustive task, but fairly simple. Essentially, the process consists in measuring the light received by each sensor for each emission point in the chamber. Due to the random nature of the light emission process, only its statistical properties can be estimated. By using these properties, the light emission process can be replicated (in statistical terms) without actually propagating the photons. In the following, the methodology for building the S1 and S2 probability models are described.

4.2.1 S1 probability model

The S1 light can be emitted from anywhere in the active volume. Hence, the probability model must describe the whole active volume of the detector. This is accomplished by registering the amount of light detected by each PMT[4] when the light is emitted from different points on a three-dimensional grid (the so-called S1 light table). For each point point in the grid, a large number of fixed-energy photons (N_{emitted}) are isotropically emitted. These photons are then tracked using the same physics as in the full simulation mode described in Section 4.1.1 to produce a waveform for each PMT. Finally, each sensor waveform is summed to obtain the total number of photons (N_{detected}), which is translated to a detection probability as $P = N_{\text{detected}}/N_{\text{emitted}}$.

For the S1 probability model of the NEXT-White detector, three million photons were emitted from every point on a 1-cm-pitch cubic grid overcovering the active region. This configuration ensures a fine description of the light detection efficiency while maintaining the computing time within reasonable values[5]. The energy of these photons was set to 7.20625 eV (172.051 nm), which corresponds to the middle of the emission scintillation spectrum (see Figure 4.1).

The large volume covered by the model translates into substantial variations in solid angle coverage. This is manifest in Figure 4.2 where the detection probability of a PMT close to the center (top) and close to the edge (bottom) is shown as a function of (x, y) for two different values of the longitudinal coordinate: z = 530 mm (left) and z = 10 mm (right).

4.2.2 S2 probability model

The light emission process associated to the S2 signal is more complex than that of the S1 signal. The electroluminiscence yield of an electron takes place along its path while traversing the EL region. Albeit small, the width of the EL region cannot be neglected due to its proximity to the tracking plane.

[4]The SiPMs detection probabilities are not considered for the S1 model as this signal is too weak to be distinguished from the intrinsic dark noise of this type of sensors.

[5]The simulation of the S1 light table took approximately one week on a $\mathcal{O}(200)$-core computer grid under the conditions mentioned in the text.

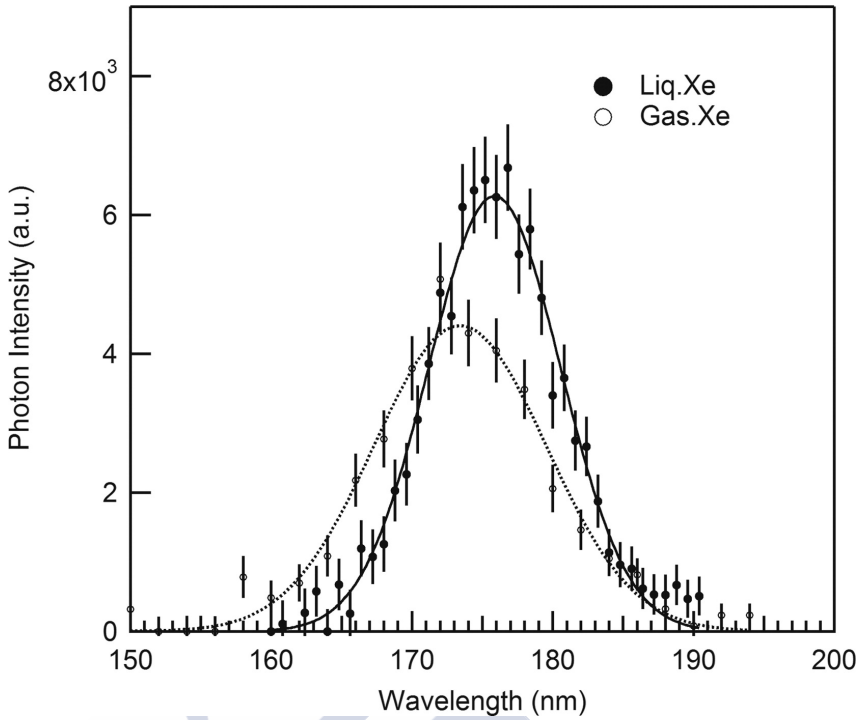

Figure 4.1: Typical scintillation spectrum of liquid and gaseous xenon [171]

On the other hand, the accuracy of the estimation of the light detection probability is of the uttermost importance due to its role in the energy resolution of the detector (Section 3.1.2). Hence, the S2 probability model is built using a 1-mm-pitch square grid overcovering the EL region (the S2 light table). At each of these points, a large number of electrons (N_{electron}) are placed at the boundary of the EL region. The electrons will accelerate according to the electric field applied while emitting a large number of photons (N_{emitted}) along its trajectory. The randomness of the trajectory is averaged among the multiple electrons while the fluctuations in the number of photons emitted are kept reasonably low. In this manner, the statistical properties of the light yield are best reproduced.

In this case, both PMT and SiPM waveforms are extracted from the simulation. Besides, because the S2 light is emitted during a relatively long time[6] ($\sim$2 μs), the output waveforms are not summed over time. Thus, a three-dimensional table (for the x, y and t coordinates) is extracted from the simulation with the probability of photon detection in a given time bin given by: $P = N^{\text{bin}}_{\text{detected}}/(N_{\text{electron}}\ N_{\text{emitted}})$. The table for the PMTs are slightly different due to its different sampling time: 100 ns for PMTs and 1 μs for SiPMs. A common time window of 2 μs was chosen for both types of sensor.

The probability tables of PMTs and SiPMs are vastly different (Figure 4.3). In Figure 4.3a the time-integrated probability of one of the PMTs close to the center is represented as a function of the (x, y) coordinate of the emission point. The remoteness of the emission plane to the PMT plane makes manifest the cylindrical symmetry of the chamber. The central region of the chamber yields a fairly homogeous light collection efficiency. The response drops rapidly for larger radii, but the minimum value is roughly half of its maximum.

[6]The time it takes for an electron to cross the EL gap depends on the width of this region and on the reduced electric field applied. In order to mimic the operating conditions of NEXT-White, the simulation was run with a 6-mm EL gap and a reduced electric field of 2 kV cm^{-1} bar^{-1}.

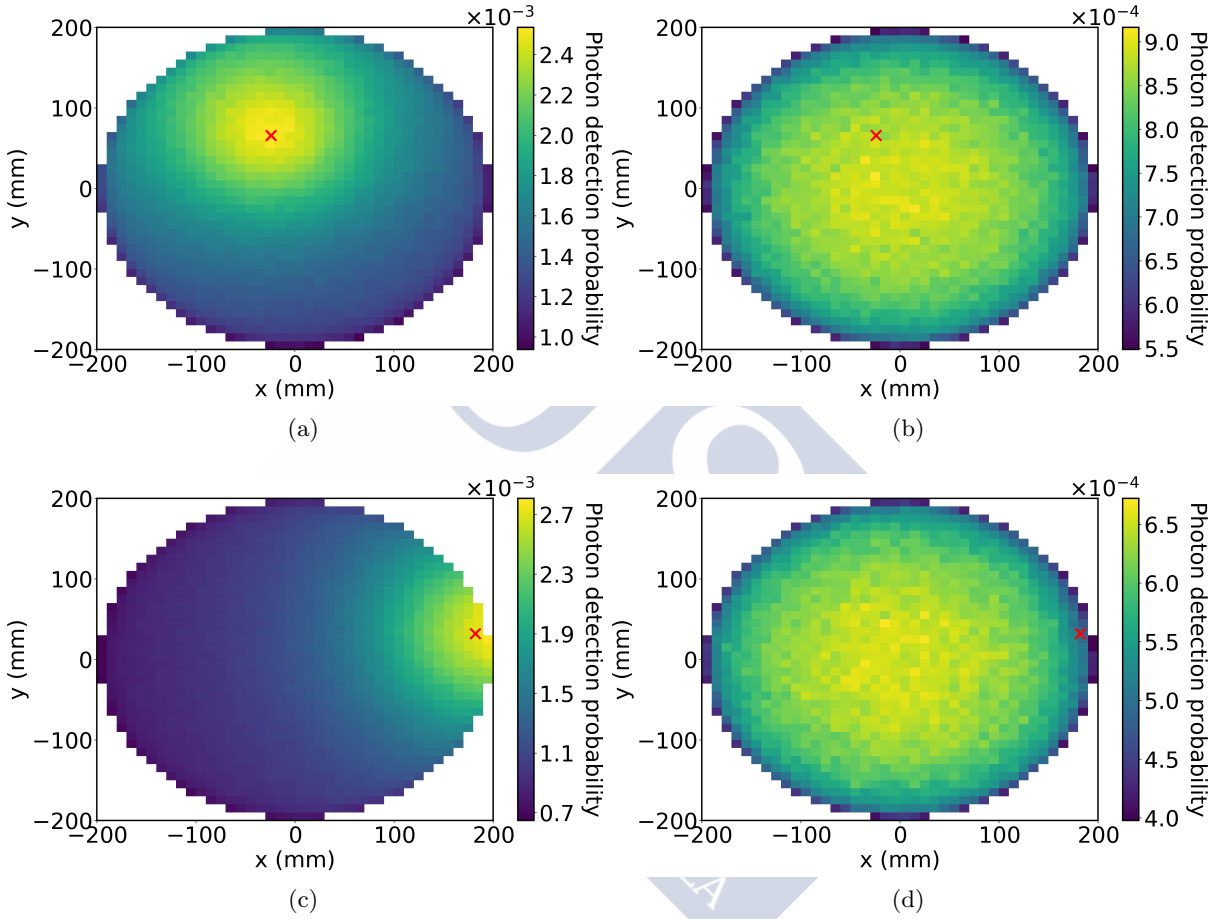

Figure 4.2: S1 photon detection probability in the NEXT-White detector as a function of the (x, y) coordinate of the emission point for a PMT close to the center (top) and a PMT close to the edge (bottom) for two different values of the longitudinal coordinate of the emission point: z = 530 mm (left) and z = 10 mm (right). The increase in detection probability for (x, y) points neighboring the PMT in consideration gains relevance at higher values of z. This is a direct consequence of the increase in solid angle coverage.

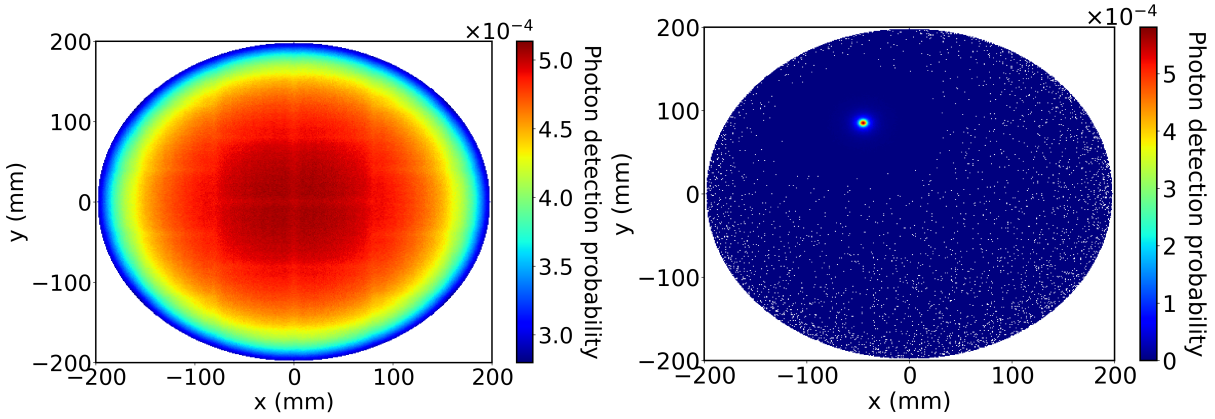

Figure 4.3: Photon detection probability as a function of the (x, y) coordinate of the emission point for a PMT close to the center (left) and for a SiPM at x = −45 mm, y = 85 mm (right).

Figure 4.3b shows the time-integrated probability of the SiPM at x = −45 mm, y = 85 mm as a function of the (x, y) coordinate of the emission point. The proximity of the tracking plane to the EL region is reflected in the focused spot of the light detection probability around the SiPM in question. This contrasts with the structure found for the PMTs, where light is essentially received from anywhere in the EL region.

4.3 Parametrization of the probability model

The probability model of the detector is a powerful tool to reduce the computing time in the simulations. A $\beta\beta^{0\nu}$ event, which takes multiple hours to fully simulate on a given machine, can be produced in a matter of seconds using the probability tables. Notwithstanding, this speed improvement is paid with memory allocation. The dimensions of the NEXT-White detector, 200 mm in radius and 530 mm in drift length, translate into enormous probability tables. Naturally, the tables become even larger for bigger detectors. This causes two major concerns: the RAM allocation is limited to a few GB and the time spent loading the tables into memory becomes a bottleneck in the simulation.

The S1 table is objectively small, as it consists of approximate 66600 grid points[7] for which we need to store the (x, y, z) position and the probability of each of the twelve PMTs. Storing these numbers as double-precision floats leads to a RAM allocation of 8 MB.

On the other hand, the S2 table is fairly large. The grid consists of ∼ 125 000 points[8]. For each grid point, the probability of each time bin of each sensor must be stored as well as the emission point (x, y) coordinates. That is 20 probabilities for each of the 12 PMTs and 2 probabilities for each of the 1792 SiPMs. Adding all contributions, we end up with a final

[7]Both the x and y coordinates cover a range of 400 mm at a pitch of 10 mm. However, only a factor $\pi/4$ is contained in the active region. The z coordinate covers 530 mm at the same pitch. This results in $n = 53 \cdot 40 \cdot 40 \cdot \frac{\pi}{4} \simeq 66600$ grid points.

[8]Similarly to the calculation for the S1 table, the x and y coordinates cover a range of 400 mm at a pitch of 1 mm, but only a factor $\pi/4$ is contained in the active region. This results in $n = 400 \cdot 400 \cdot \frac{\pi}{4} \simeq 125000$ grid points.

estitation of 7.5 GB of RAM allocation.

When extrapolating these values to NEXT-100 under the same conditions we find unmanageable sizes of ∼250 MB for the S1 table and ∼120 GB for the S2 table.

Furthermore, from Figure 4.3, it is particularly obvious that the S2 probability model contains unexploited symmetries. Although not so easily seen, the same can be said of the S1 model. Making use of these symmetries can drastically reduce the amount of data in the model. In addition, the tables are a measurement of the probability at certain points of the chamber, but a continuous model is needed for an accurate simulation. This limitation is naturally minimized by reducing the pitch of the simulation grid and can be further optimized using interpolation algorithms. Nonetheless, the increase in the computational requirements for the simulation makes this option unsuitable. Finally, the probability model is just one snapshot of the light detection efficiency of the detector. The statistical deviations from the model will be reproduced in any subsequent simulation and can still slightly bias the generation of Monte Carlo events. This is more noticiable were light detection probabilities are small, such as the boundary of the active region or a few cm away from a SiPM.

In order to minimize these effects, the probability model has been parametrized. As described in the following subsections, the data are summarized in a set of functions that reproduce the probabilty model at the simulation points. The parametrized model is a natural extension of the table model to any point in the active region. Besides, these functions take advantage of the symmetries, which allows a more accurate determination of the probability for a given position while minimizing any possible statistical deviations of the probability measurements. Lastly, the functions eliminate the need for large memory allocation, while keeping the number of CPU operations low.

4.3.1 Parametrization of the S1 model

The S1 probability model describes the full active volume. Thus, the variations in light collection efficiency are fairly large. The strongest dependence comes from the z coordinate, as shown in Figure 4.4, where the PMT-summed light collection efficiency is represented as a function of z. However, the relative proximity of the emission point to the sensor, generates another dependence on the transverse coordinate as shown in Figure 4.2a.

For parametrizing the model, we exploit the symmetries found in the simulated data, which come naturally from the geometry. In order to make use of these symmetries we define the following relative cylindrical coordinates (see Figure 4.5):

$$\begin{aligned} \mathrm{d}r^2 &= (\mathrm{x}_{\mathrm{emission}} - \mathrm{x}_{\mathrm{pmt}})^2 + (\mathrm{y}_{\mathrm{emission}} - \mathrm{y}_{\mathrm{pmt}})^2 \\ \mathrm{d}\phi &= \phi_{\mathrm{emission}} - \phi_{\mathrm{pmt}}, \qquad \mathrm{d}\phi \in [-\pi, \pi). \end{aligned} \tag{4.1}$$

With this coordinate system, the rotational symmetry of the data becomes evident. We exploit this symmetry by using the absolute value of $\mathrm{d}\phi$, rather than $\mathrm{d}\phi$. Nonetheless, not all PMTs are equivalent. Their light collection efficiencies depend on their radial position in the energy plane. Thus, the PMTs are grouped according to their disposition in two concentric

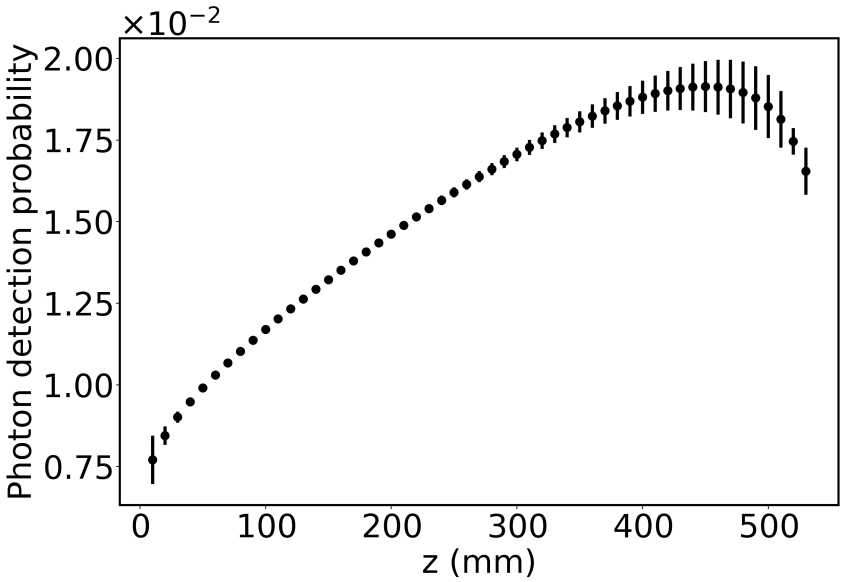

Figure 4.4: PMT-summed S1 light collection efficiency of the NEXT-White detector as a function of the longitudinal coordinate, z.

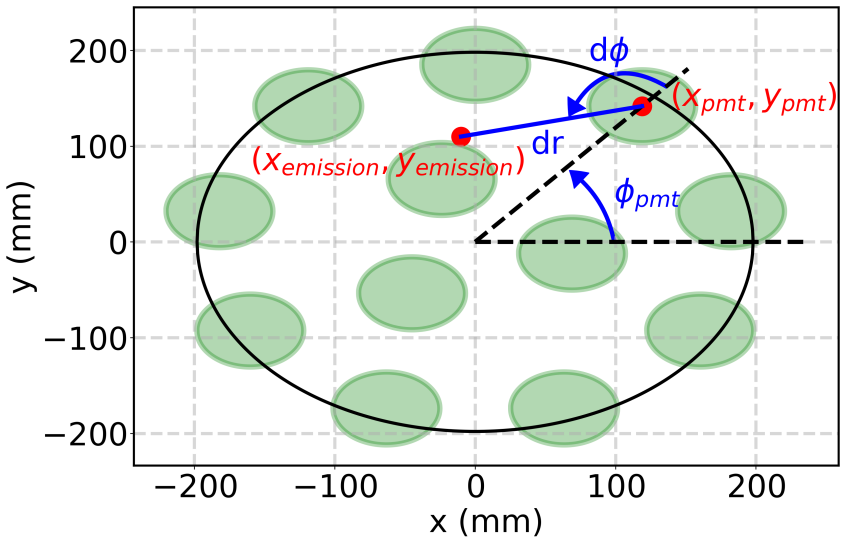

Figure 4.5: Schematic representation of the coordinate system defined for the S1 parametrization in the NEXT-White detector.

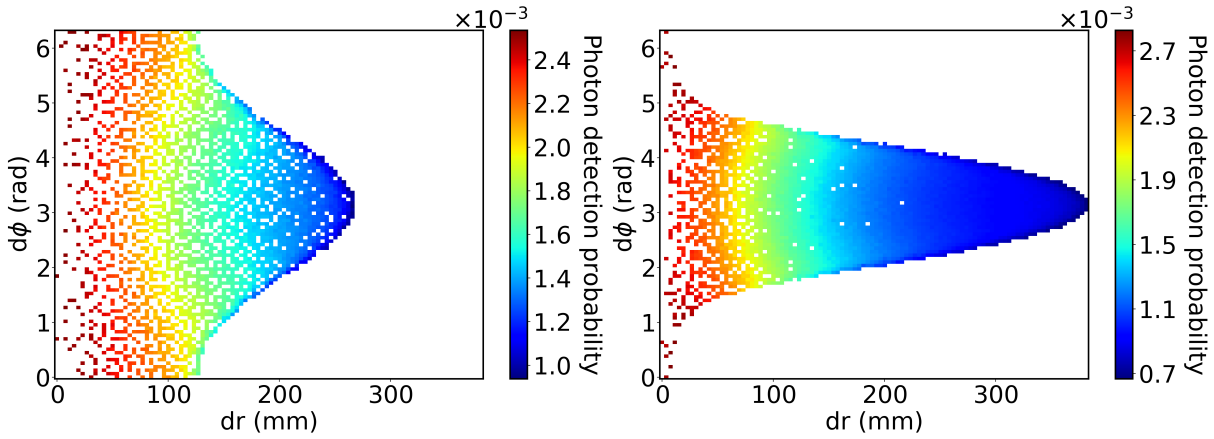

(a) (b)

Figure 4.6: Photon detection probability (color) as a function of the dr and dϕ coordinates of the emission point for the inner PMTs (left) and for the outer ones (right) for $z_{emission} = 530$ mm in the NEXT-White detector.

circles: three around the center of the chamber at radius[9] $r_{pmt} \approx 60$ mm (inner PMTs) and the remaining nine at $r_{pmt} \approx 185$ mm (outer PMTs),. Each group of PMTs is separately treated, but within each set, the simulation data can be merged, hence increasing the statistical significance of the probability measurements. In Figure 4.6 the detection probability (color scale) is shown as a function of dr and dϕ for the inner PMTs (left panel) and for the outer ones (right panel) for $z_{emission} = 530$.

The dependence of the light detection with dr is coupled to dϕ. Thus, the light collection efficiency is first parametrized for different slices of the dϕ coordinate and each value of z indepedently. Nine slices were chosen for the NEXT-White detector, as it optimizes the description of the probability model while keeping a reasonable amount of data in each slice. For each dϕ slice, we analyze the detection probability as a function of dr. The correlation between these magnitudes varies significantly among the different dϕ slices. Nonetheless, the trend can be reproduced by means of a second-degree polynomial:

$$f(\mathrm{dr}) = p_0 + p_1 \cdot \mathrm{dr} + p_2 \cdot \mathrm{dr}^2. \tag{4.2}$$

Figure 4.7a shows the dependendence of the probability with dr for z = 480 mm (black dots) and the best fit curve (red solid line) for all dϕ sectors for the inner PMTs. All fits result in a good χ^2/ndof value. The equivalent display for the outer PMTs is shown in Figure 4.7b.

The previous parametrization is repeated for each value of z and then, the variation of the coefficients p_i in Equation 4.2 along z is analyzed. A smooth evolution is found for all coefficients, which can be parametrized using a fourth-degree polynomial:

$$p_i(\mathrm{z}) = p_{i0} + p_{i1} \cdot \mathrm{z} + p_{i2} \cdot \mathrm{z}^2 + p_{i3} \cdot \mathrm{z}^3 + p_{i4} \cdot \mathrm{z}^4. \tag{4.3}$$

[9] $r_{pmt} = \sqrt{x_{pmt}^2 + y_{pmt}^2}$

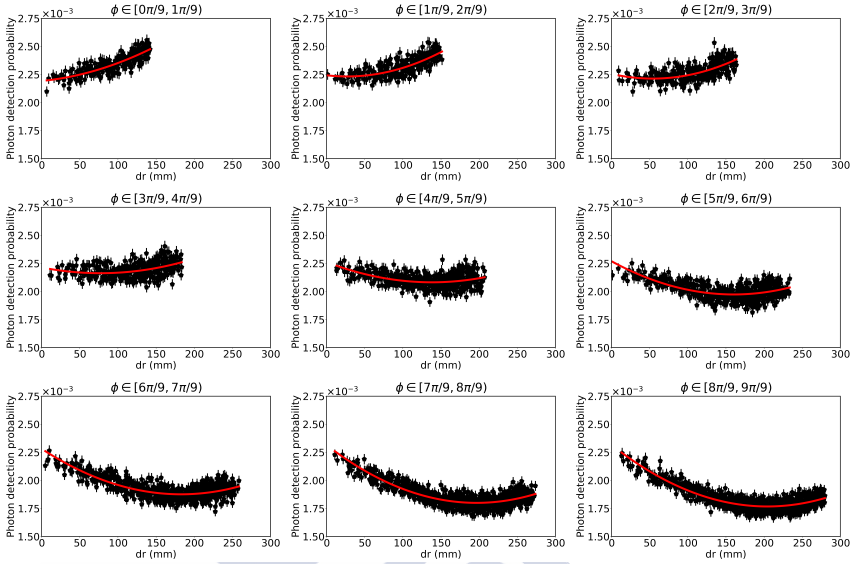

(a)

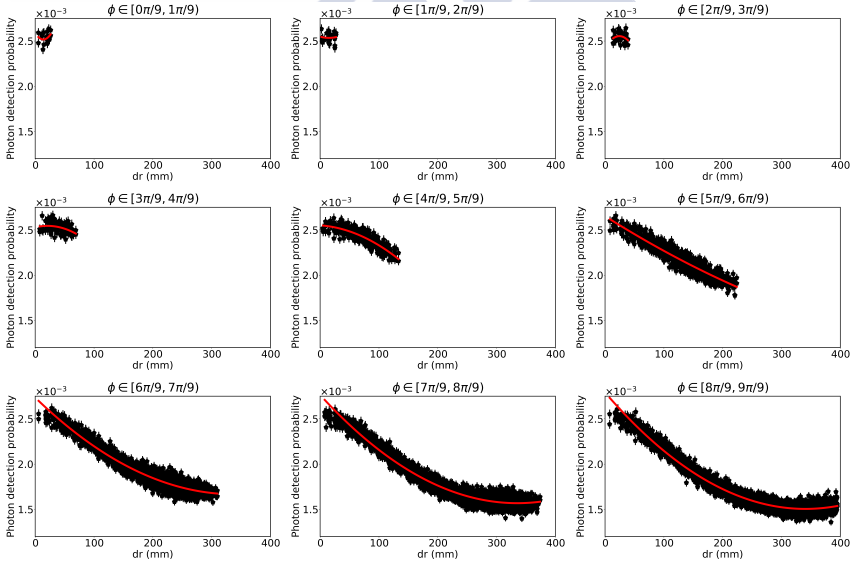

(b)

Figure 4.7: S1 photon detection probability as a function of dr (black dots) and best fit (solid red line) to a second-degree polynomial for different dϕ ranges of the NEXT-White detector. The top panel corresponds to the inner PMTs and the bottom panel to the outer ones. Both sets correspond to the grid points at z = 480 mm.

In Figure 4.8a the value of the three coefficients in Equation 4.2 (black dots) is presented as a function of z along with the best fit curve (red line) for the inner PMTs and the 4th dϕ sector (corresponding to the range $[4\pi/9, 5\pi/9)$). All fits reproduce well the data, with a value of χ^2/ndof close to 1. This procedure is repeated for all parameters in all dϕ sectors for both the inner and outer PMTs.

Finally, the parametrization is wrapped in a function of three variables: the coordinates of the emission point x, y and z. This function will convert the cartesian coordinates into those suitable for the parametrization: dr, dϕ and z. Following this, a set of coefficients p is choson according to the value of dϕ. The photon detection probability is computed by evaluating

$$p_i(\mathrm{z}) = \sum_{i=0}^{2} \sum_{j=0}^{4} p_{ij} z^j r^i, \tag{4.4}$$

for each PMT.

Validation

The first requirement the parametrized model must satisfy is the reproducibility of the data from which it was created. This is achieved by comparing the probabilities in the tables and the prediction of the parametrized model at the same grid points. Naturally, statistical fluctuations must be taken into account. Thus, the data comparison is performed using the following statistically-robust figure-of-merit (the so-called *pull* statistics).

$$g = \frac{\text{observation} - \text{prediction}}{\sigma(\text{observation})} \tag{4.5}$$

which, applied to this case becomes

$$g = \frac{N_{\text{parametrization}} - N_{\text{table}}}{\sigma(N_{\text{parametrization}})}, \tag{4.6}$$

where N_{table} are the number of photons detected by a given PMT when N_{emitted} photons are produced at a given point in space as recorded in the S1 table, $N_{\text{parametrization}}$ is the prediction of the parametrized model and $\sigma(N_{\text{parametrization}})$ its uncertainty. For quantities with gaussian uncertainties, the *pull* is a normally-distributed variable. In this case, $N_{\text{parametrization}}$ can be approximated as a gaussianly-behaved variable due to the large number of photons emitted in the simulation. Hence, it follows that $\sigma(N_{\text{parametrization}})$ can be approximated[10] as $\sqrt{N_{\text{parametrization}}}$.

The quantity in Equation 4.6 is computed for every grid point in the simulation. When histogrammed, a mean zero and unit sigma gaussian distribution is revealed, as shown in Figure 4.9. This constitutes a demonstration that the parametrized model is robust and can reproduce the original simulation data.

[10]To be strictly robust, the uncertainties in the coefficients of the parametrization should be taken into account. Nonetheless, they are negligible compared with the fluctuations expected from a Poisson distribution.

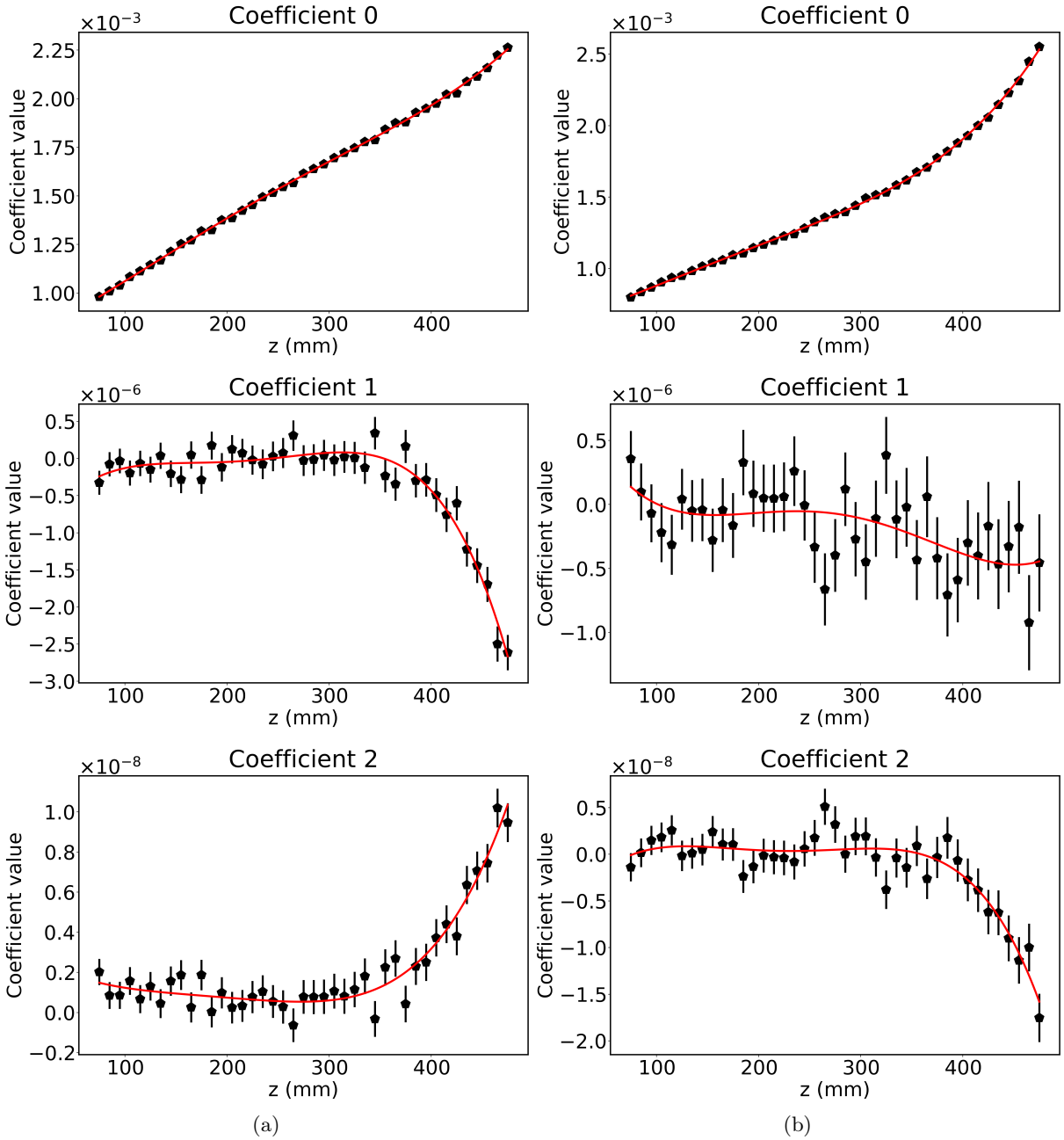

Figure 4.8: Value of the coefficients of the second-degree polynomial as a function of z (black dots) and best fit to a fourth-degree polynomial (red line). The data correspond to the 4th dϕ sector, ranging from $4\pi/9$ to $5\pi/9$. The left panel corresponds to the inner PMTs and the right panel to the outer PMTs of the NEXT-White detector.

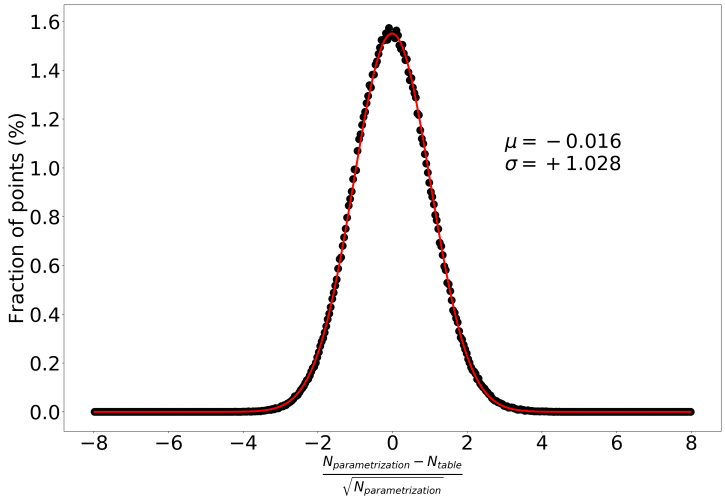

Figure 4.9: *Pull* distribution for all PMTs and all grid points in the NEXT-White S1 table simulation. The distribution is normal within statistical uncertainties.

4.3.2 Parametrization of the S2 model

Contrary to the S1 probability model, both the PMTs and the SiPMs have to be parametrized. These parametrizations are independent, as their models are completely different.

PMT model parametrization

The S2 light is emitted exclusively from the EL region, which is sufficiently far off for solid angle coverage not to vary excessively. In addition, the light tube reduces the loss of light due to reflections significantly. However, the reflectivity of the internal components of the chamber is not perfect. Thus, light collection efficiency decreases when light is emitted closer to the edge, as it suffers more reflections (see Figure 4.3a).

Moreover, the distance between the emission plane and the PMT plane minimizes the dependence of the light collection efficiency on the PMT position. This leads to a rotational symmetry that comes naturally from the geometry of the detector and can be exploited. In fact, the tables for the PMTs within each ring are equivalent within statistical fluctuations. Despite this symmetry, an individual PMT parametrization is chosen, as it yields the same results and is more convenient to implement.

The S2 signal is produced by electrons traversing the EL gap. This process is not instantaneous, but takes approximately 2 μs. In principle, the photon detection probability may vary over this time interval. However, as shown in Figure 4.10, we observe only minimal discrepancies with respect to a constant probability. Thus, for this parametrization we consider only the time-integrated response of the detector to reduce statistical fluctuations.

The parametrization takes advantage of the rotational symmetry and depends only on the

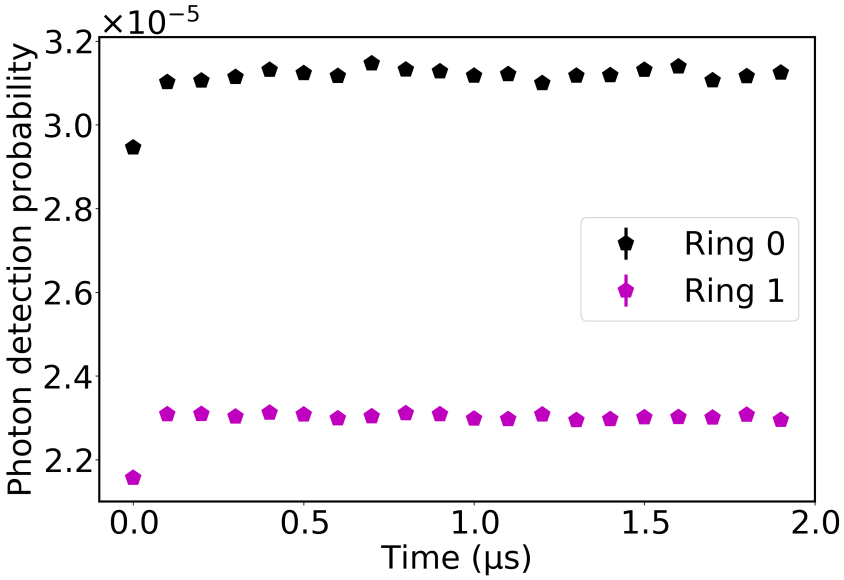

Figure 4.10: Average PMT photon detection probability as a function of time in the NEXT-White detector. The data correspond to the simulation points at $r_{emission} < 5$mm to minimize the dependence on the position.

absolute radial coordinate, $r_{emission}$ [11]. For each PMT, the time-integrated dependence of the light collection efficiency with $r_{emission}$ is studied. We find a reasonably constant efficiency for $r < 150$ mm where it starts to drop abruptly. The light collection efficiency reaches its minimum value at the boundary of the EL region, approximately 1/2 of that at the center of the chamber. The deviations around the average value are found to be consisten with a poisson statistics for the whole range of $r_{emission}$.

The probability-vs-$r_{emission}$ data are fitted to a high-degree polynomial, which reproduces well the data in the full range of the active region. For the NEXT-White detector, a 9th-degree polynomial was chosen as it yielded the best χ^2/ndof value.

In Figure 4.11a the photon detection probability is presented as a function of $r_{emission}$ (black dots) along with the best fit line (red) for one of the central PMTs. The fit yields a good χ^2/ndof value. The equivalent result is presented for an outer PMT in Figure 4.11b.

The parametrization is wrapped in a function of two variables: $x_{emission}$ and $y_{emission}$. These are used to compute $r_{emission}$ which is the argument of the aforementioned polynomials. The photon detection probability is then calculated for each PMT.

SiPM model parametrization

The proximity of the EL region to the tracking plane results in the highly focused response seen in the SiPM light tables (Figure 4.3b). Thus, for a given SiPM, most of the EL plane has nearly zero photon detection probability. It is then natural to parametrize the model using relative transverse coordinates. In this coordinate system all SiPMs are equivalent and the simulation datasets can be merged. Moreover, a rotational symmetry is found and only the

[11] $r_{emission} = \sqrt{x^2_{emission} + y^2_{emission}}$

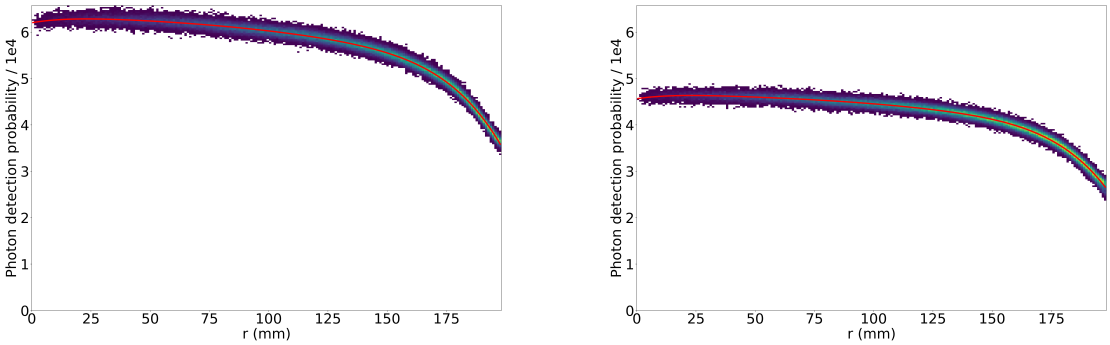

(a) (b)

Figure 4.11: S2 photon detection probability as a function of r (black dots) and best fit line (red) for a central (left) and an outer (right) PMT in the NEXT-White detector.

relative transverse distance between the emission point and the SiPM is relevant:

$$\mathrm{dr}^2 = (\mathrm{x_{emission}} - \mathrm{x_{sipm}})^2 + (\mathrm{y_{emission}} - \mathrm{y_{sipm}})^2. \tag{4.7}$$

For building this parametrized model the dependence of the photon detection probability with dr is analyzed. This is done for each time bin separately, as their response are significantly different. In both cases the efficiency drops rapidly in the first few mm. At 20 mm both distributions are two orders of magnitude smaller than their peak value. Hence, the parametrized model is restricted to a small region around the SiPM. In the case of the NEXT-White detector a 25 mm parametrization range was chosen after considering both the computational performance and the model accuracy.

The probability dependence with dr is parametrized using a high-degree polynomial. For the NEXT-White detector a 9th-degree polynomial was chosen based on the χ^2/ndof of the data fits.

In Figure 4.12 the photon detection probability for all SiPMs is presented as a function of dr (black dots) along with the best fit line (red) for the first (left) and second (right) time bin. Both fits yield good χ^2/ndof values.

The parametrization is wrapped in a function of two variables: $\mathrm{x_{emission}}$ and $\mathrm{y_{emission}}$. It then selects the SiPMs within the previously-fixed parametrization range[12] to reduce the number of calculations. For those SiPMs, $\mathrm{dr_{emission}}$ is evaluated and used to compute the photon detection probability for each time bin using the polynomials.

Validation

The parametrized model is validated by comparing its prediction for the simulation grid points with the actual simulation result, as done for the S1 model (Section 4.3.1. The same figure-of-merit in Equation 4.6 is used.

[12]Those outside the parametrization range have therefore a zero probability of photon detection.

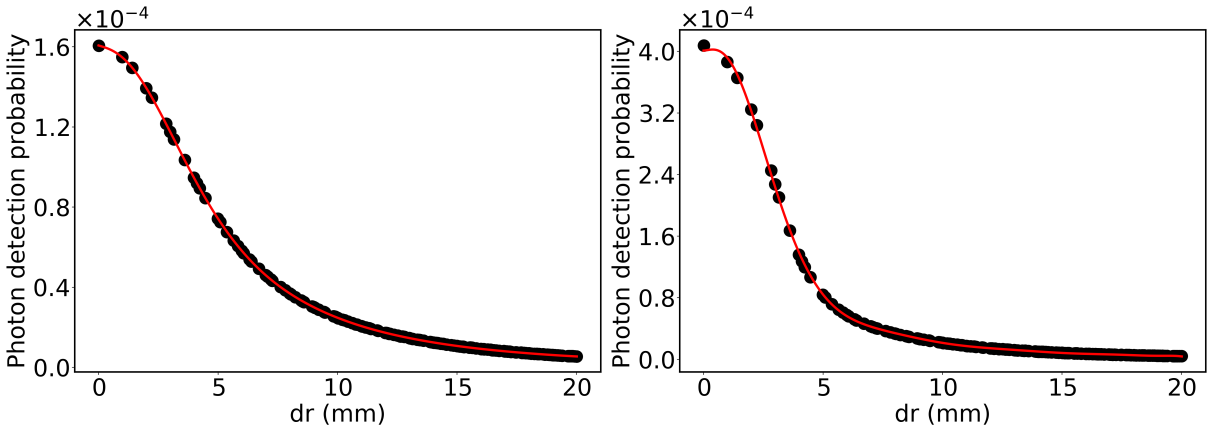

(a) (b)

Figure 4.12: S2 photon detection probability for all SiPMs as a function of dr (black dots) and best fit (red line) for the first (left) and second (right) time bins in the NEXT-White detector.

For the PMT parametrization, this quantity is computed for every grid point in the simulation, but for the SiPM parametrization, only those nodes within the parametrization range of every SiPM are considered.

In Figure 4.13 the value of g for all PMTs is histogrammed. A normal distribution is found, demonstrating that the parametrization can reproduce the S2 PMT tables without biases.

In Figure 4.14 the histograms of the *pull* for the first time bin (top panels) and the second time bin (bottom panels) is shown. Although the distributions for all SiPMs (left panels) are nearly normal, the emergence of non-gaussian tails indicate the presence of some imperfections in the parametrized model. However, when considering only those SiPMs with $r_{sipm} < 180$ mm (right panels), the tails are no longer present. Clearly, this is an effect of reflections in the light tube, which affect the photon detection efficiency for those SiPMs near the edge.

Albeit imperfect, this model satisfies the reproducibility of the light detection capabilities of the detector. This is motivated by the fact that the data near the edge of the active volume are usually discarded for fiducialization reasons.

The model can be extended by parametrizing independently the SiPMs at $r_{sipm} < 180$ mm and $r_{sipm} > 180$ mm. However, the rotational symmetry exploited in the parametrization does not hold in the second range and two coordinates must be used. In addition to the intricacy of achieving a two-dimensional parametrization, the improvement in the simulation result does not counterbalance the increase in CPU cycles that this type of model would entail.

4.4 The light detection probability model for NEXT-100

The methodology for building and parametrizing a probability model can be applied to any detector, and specifically to NEXT-100. The forthcoming building and operation of NEXT-100 program demands predictions based on Monte Carlo simulations. Background levels based on radioactivity measurements of the detector components are of utmost importance to determine

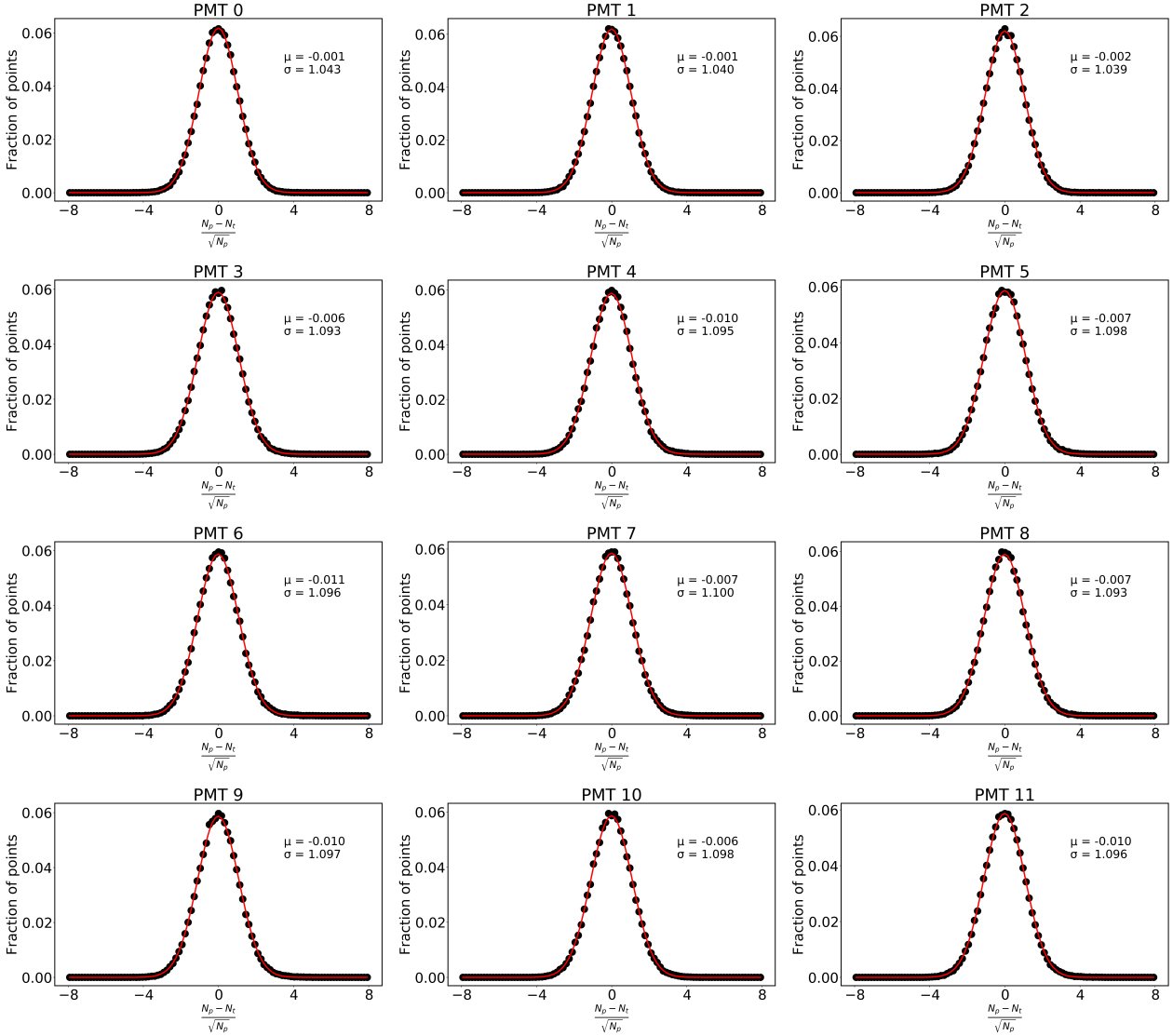

Figure 4.13: *Pull* distribution for all PMTs in the NEXT-White detector and all grid points in the simulation using a 9th-degree polynomial parametrization for each PMT. A normal distribution is observed, proving that the parametrization of the S2 PMT model is robust.

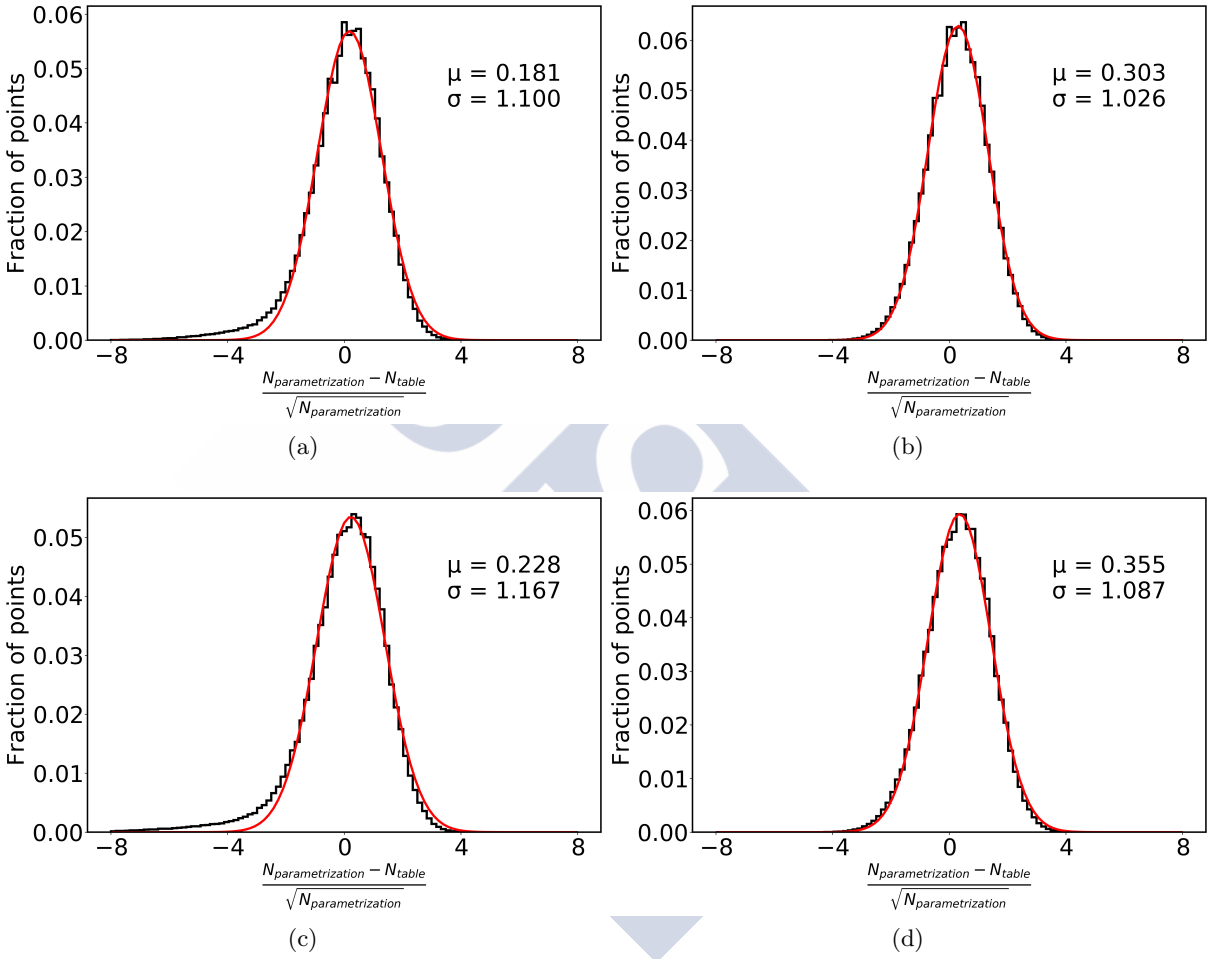

Figure 4.14: *Pull* distributions for the parametrizations of the first time bin (top) and the second time bin (bottom) data when considering all the SiPMs (left) and only those with $r_{sipm} < 180$ mm. In the left panels, non-gaussian tails contaminate an otherwise normal distribution. In the right panels, the absence of near-edge sensors reduces the contamination of light reflections in the tube and corroborates the accuracy of the parametrized model for most of the active region.

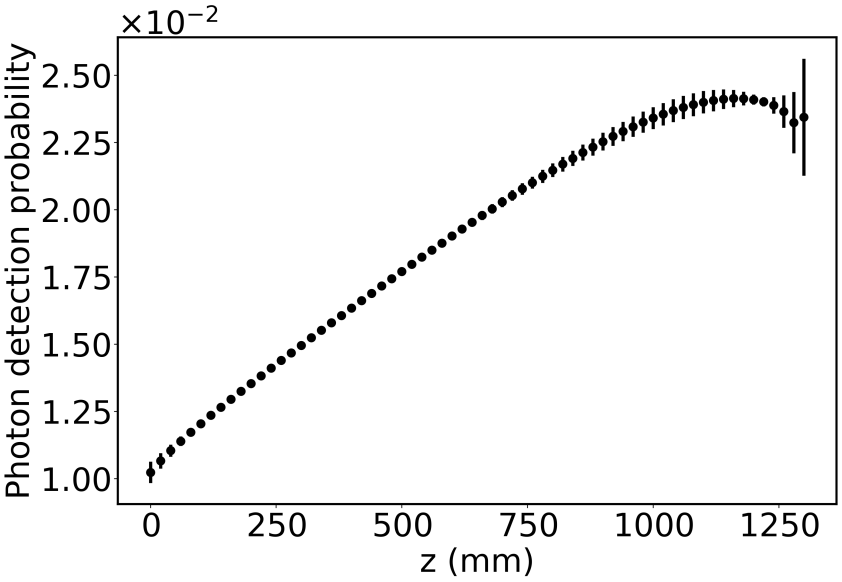

Figure 4.15: PMT-summed S1 light collection efficiency of the NEXT-100 detector as a function of the longitudinal coordinate, z.

the sensitivity of the detector to the neutrinoless double beta decay [172]. Building a probability model for the detector allows the generation of large-statistic Monte Carlo datasets to assess the detector performance.

The NEXT-100 geometry has been outlined in the TDR published in 2012 [158] and can be summarized as follows. The detector consists of a cylindrical TPC with an active region defined by a TPB-coated light tube of 535 mm radius and 1300 mm drift length. It is instrumented with 60 PMTs and with 7168 SiPMs identical to those used in the NEXT-White detector. The PMTs are arranged in four rings in a similar fashion as for NEW and the SiPMs arranged in a similar 1-cm-pitch square grid.

The probability model is first built by creating the light collection efficiency tables described in Section 4.2. However, since the detector is much larger and not yet built, a compromise between accurary and simulation cost was taken by reducing the number of grid points for both the S1 and S2 tables. The model is then parametrized in a similar manner as that described in Section 4.3 and validated using the same methods.

4.4.1 S1 probability model

A 2-cm-pitch cubic grid overcovering the active volume was chosen to generate the S1 probability model. With this configuration, the number of grid points is similar to that of NEXT-White without deteriorating significantly the description of the detector. In Figure 4.15 the PMT-summed photon detection probability is shown as a function of the drift coordinate. A trend similar to that of NEW is found. The same dependence on the PMT position is observed for NEXT-100, although it is negliglible for most of the detector, due to its bigger dimensions.

Following the procedure in Section 4.3.1, the data are transformed to relative cylindrical coordinates and grouped according to the PMT radial position. The bigger detector dimensions

translate into more complex data distributions than in the case of NEXT-White. Thus, higher-degree polynomials were used to parametrize the model of this detector. Namely, a fourth-degree polynomial for the dr coordinate and a sixth-degree polynomial for the z coordinate.

In Figures 4.16 and 4.17 the dependence of the photon detection probability with dr (black dots) is shown for each PMT ring. The data correspond to the simulation points at z = 500 mm and the best fit to the polynomial is shown in red. Figures 4.18 and 4.19 show the variation with z of the 3rd coefficient in the dr parametrization of the innermost PMTs. In both cases the fits are not as exemplary as what was obtained for the NEXT-White detector, but the χ^2/ndof values are fairly good.

The model is finally validated by histogramming the quantity g defined in Equation 4.6 and the result is shown in Figure 4.20. While a perfect normal distribution is not achieved, the deviations from this reference are not very large.

The main causes for this small deviations are that the trends are difficult to reproduce even with higher-degree polynomials, and that the stability of the fit procedure is fairly delicate. Moreover, the accuracy of the S1 model is not of the uttermost importance, as it does not take part in the main features of the detector. Hence, the parametrized model of the S1 photon detection efficiency is considered to perform reasonably well within the requirements of this task.

4.4.2 S2 probability model

The S2 probability model for NEXT-100 is generated in the same fashion as for NEXT-White. A 2-mm-pitch square grid overcovering the active region was chosen for the PMT model to maintain the size of the datasets similar to that of NEW. The SiPM model, on the other hand, was created with a fine-pitched square grid around the center of the chamber. This choice is based on the results of the NEXT-White model, for which the response was found to be approximately homogeneous in most of the chamber. Thus, we chose to accurately simulate the NEXT-100 model for short distances in the center to then extrapolate it everywhere.

The time-integrated PMT photon detection probability[13] as a function of (x, y) is presented in Figure 4.21a for one of the innermost PMTs. The structure of the table is similar to that of NEXT-White, only with a larger proportion of homogeneous response. In Figure 4.21b the table for a SiPM at x = −5 mm and y = +5 mm is shown. The same focused response around the SiPM in question is observed.

The model is parametrized for PMTs and SiPM independently as described in Section 4.3.2. The same 2-μs time window and time-binning was used for both type of sensors.

The PMT model is again parametrized using the radial dependence of the photon detection probability. The curve observed is hard to reproduce with a single polynomial, even considering higher degrees. Thus, the parametrization is done separately for two ranges of r: from 0 to 400 mm and from 400 mm to 535 mm. Fifth- and sixth-degree polynomials are used, respectively, for each range. These degrees were chosen based on grounds of the χ^2/ndof value obtained. The polynomials are also required to match within 1 % at the split point. Finally, Both polynomials are glued together to produce a single function of one variable.

[13] As discussed in Section 4.3.2, the PMT photon detection probability is approximately constant throughout the light emission time.

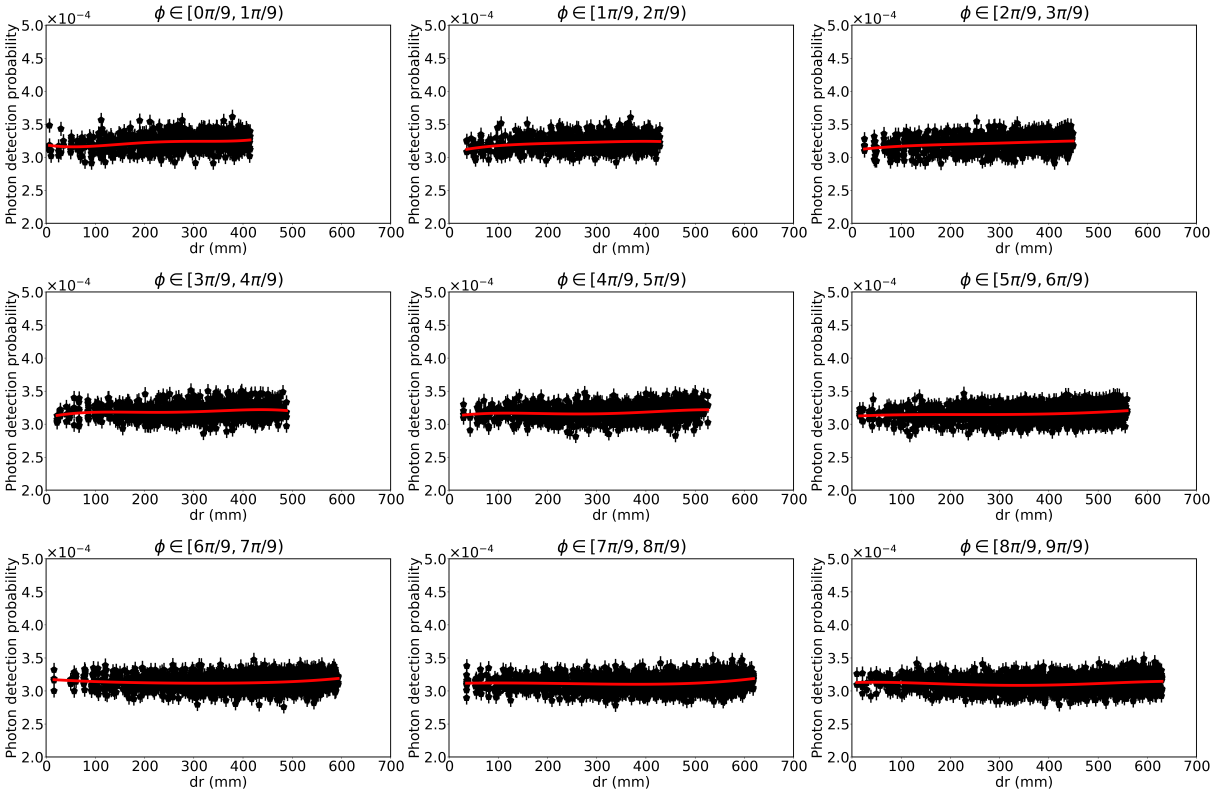

(a) Ring 0

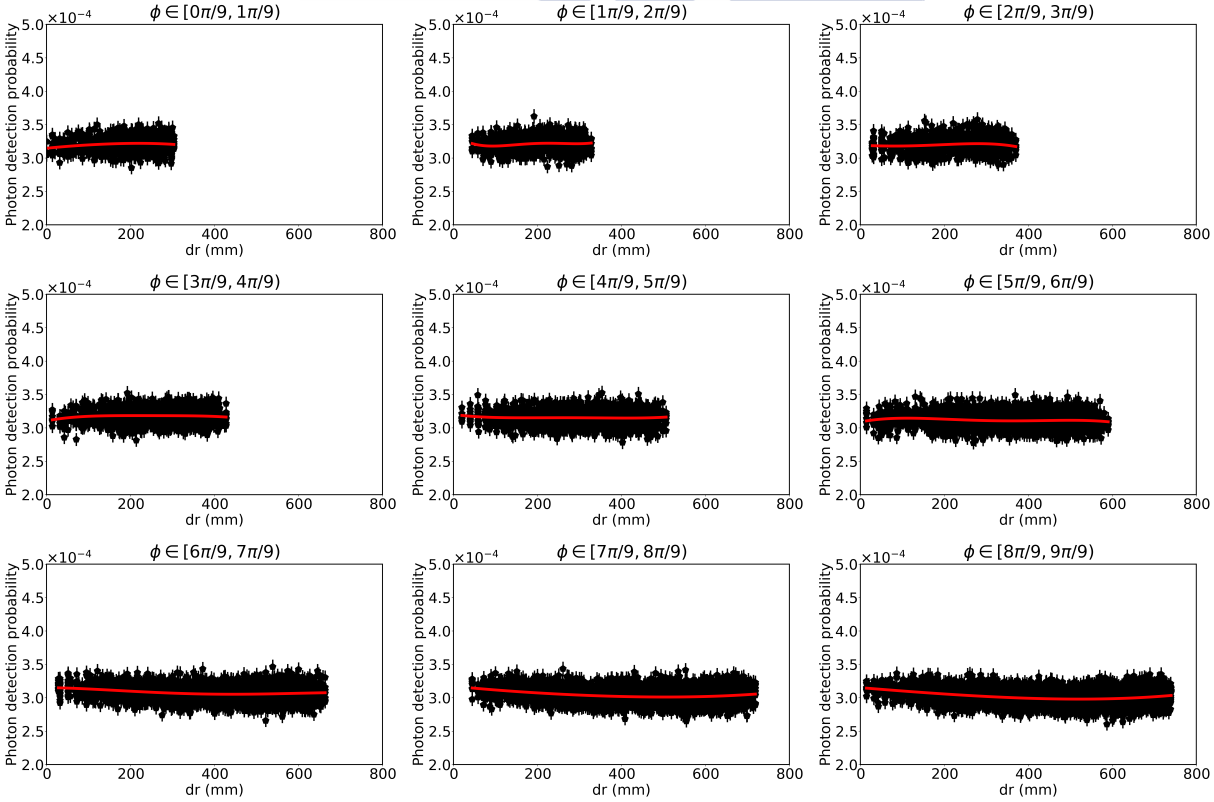

(b) Ring 1

Figure 4.16: Photon detection probability as a function of dr for the inner PMT rings (black dots) and best fit (solid red line) to a fourth-degree polynomial. The data correspond to the simulation points at z = 500 in the NEXT-100 detector.

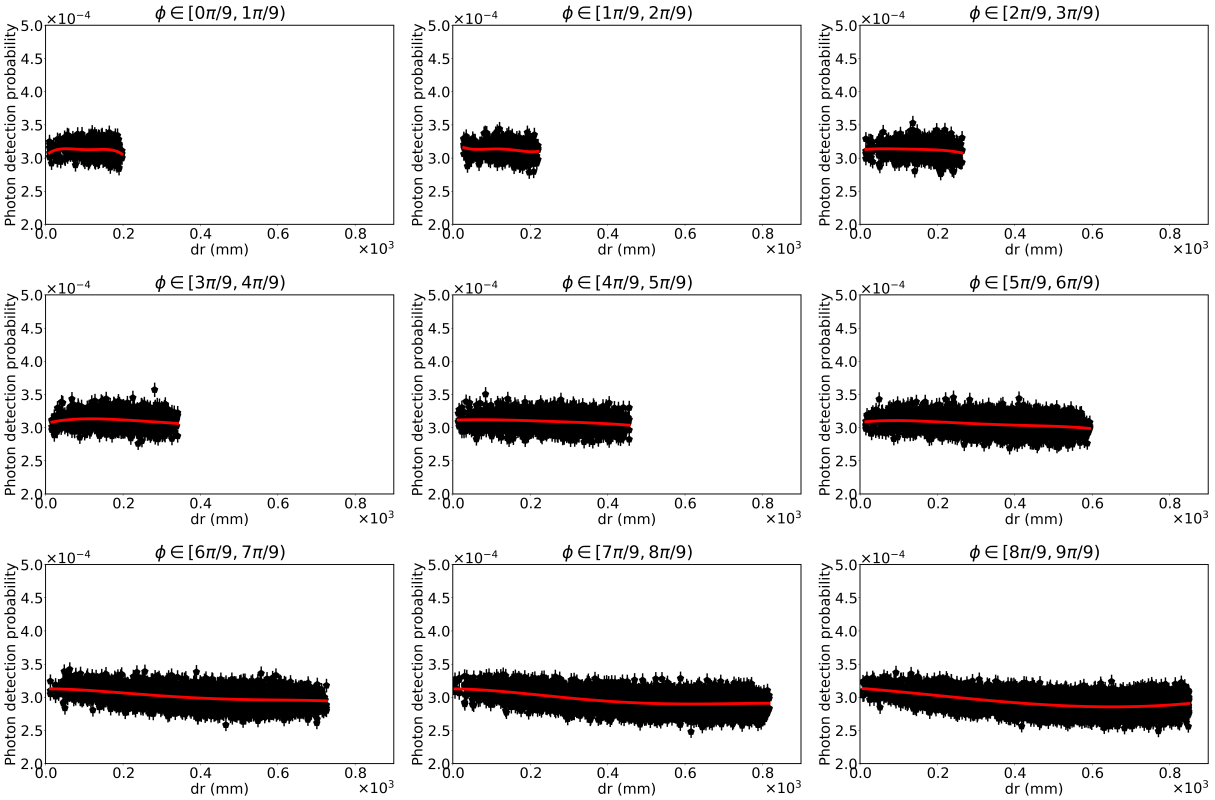

(a) Ring 2

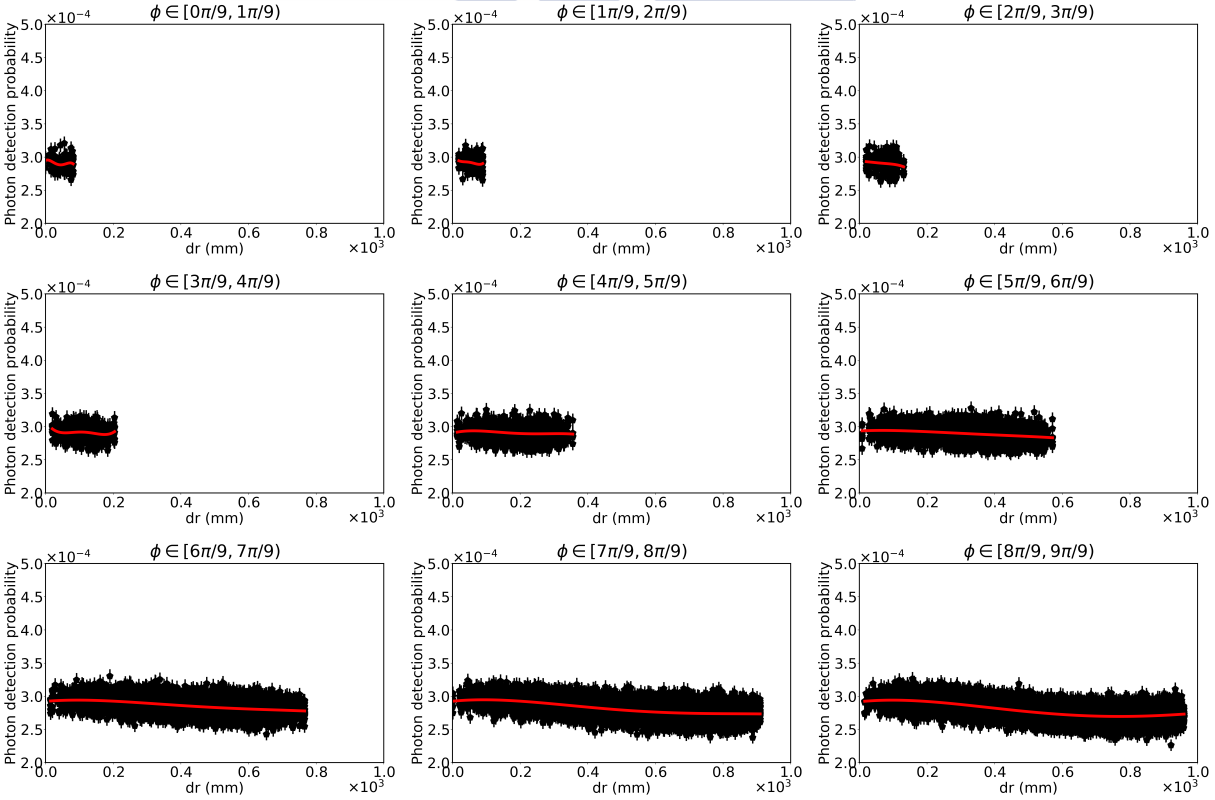

(b) Ring 3

Figure 4.17: Photon detection probability as a function of dr for the outer PMT rings (black dots) and best fit (solid red line) to a fourth-degree polynomial. The data correspond to the simulation points at z = 500 in the NEXT-100 detector.

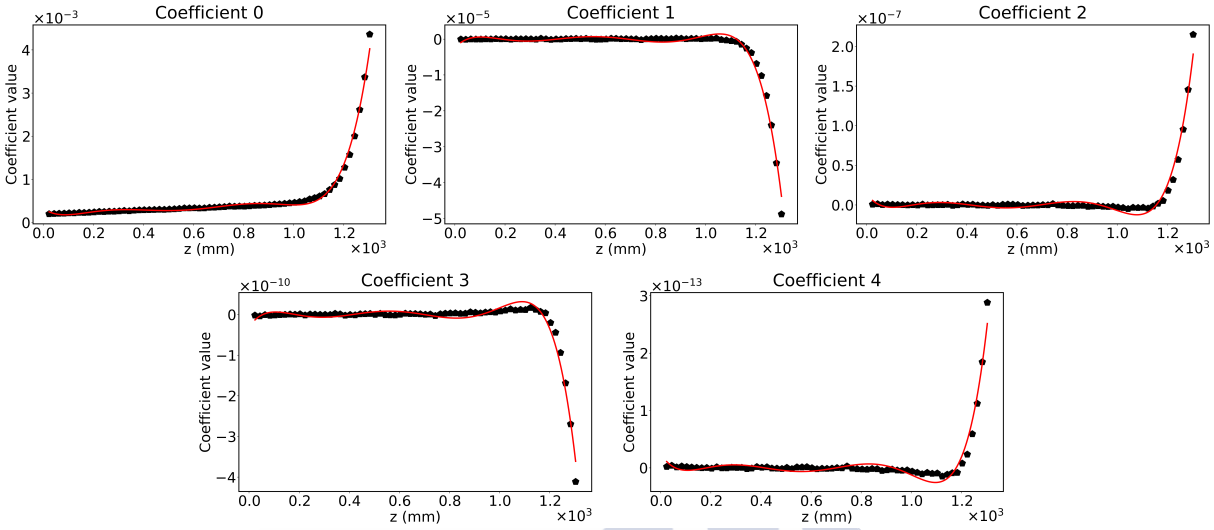

(a) Ring 0

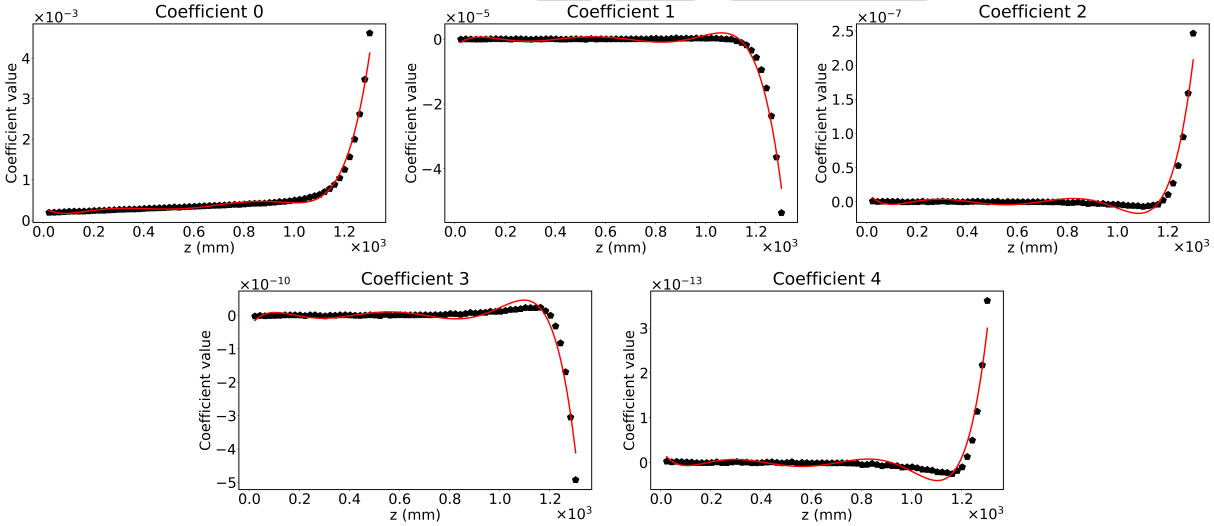

(b) Ring 1

Figure 4.18: Variation in z and best fit line to a 6th-degree polynomial of the coefficients of the S1 dr parametrization for the inner PMT rings of the NEXT-100 detector.

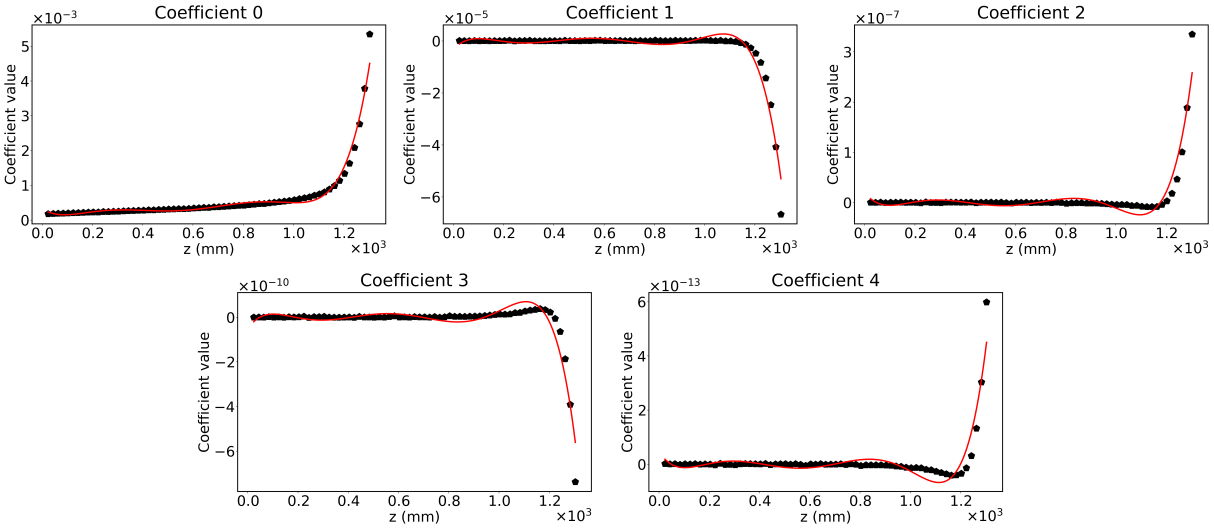

(a) Ring 2

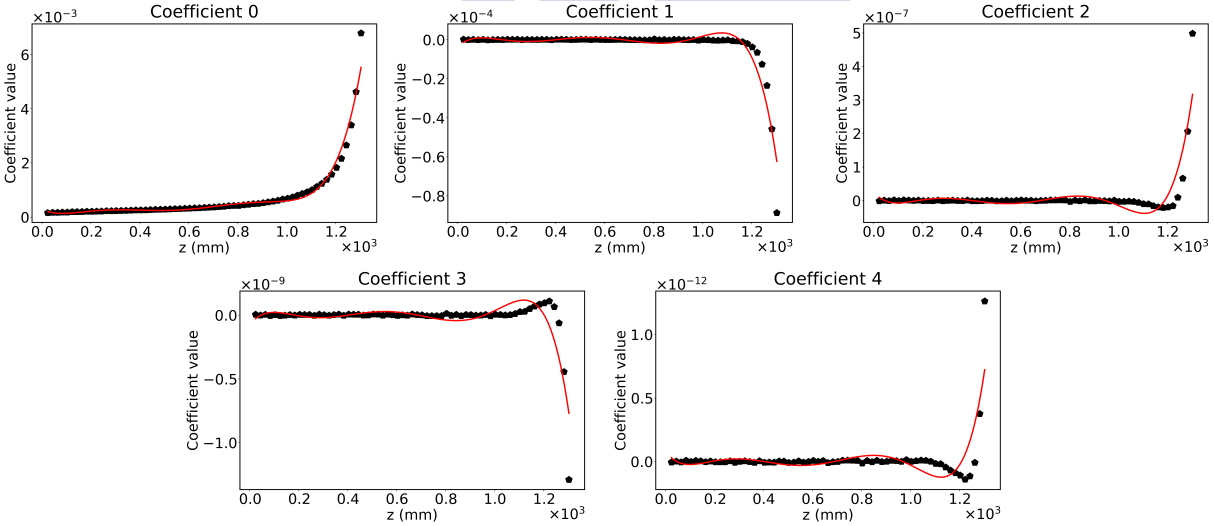

(b) Ring 3

Figure 4.19: Variation in z and best fit line to a 6th-degree polynomial of the coefficients of the S1 dr parametrization for the outer PMT rings of the NEXT-100 detector.

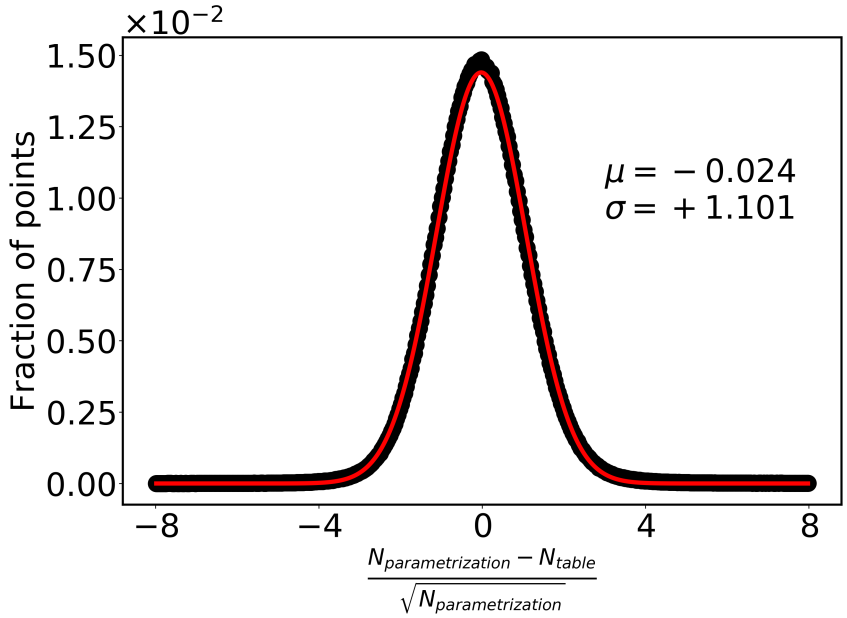

Figure 4.20: *Pull* distribution for all PMTs and all grid points in the NEXT-100 S1 table simulation. The distribution is normal within statistical uncertainties.

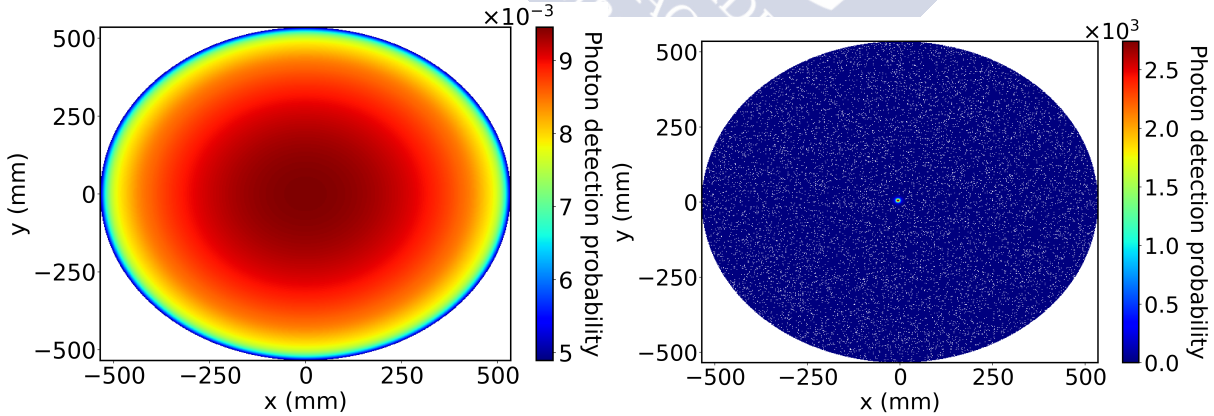

(a) (b)

Figure 4.21: Display of the S2 photon detection probability as a function of the (x, y) coordinate of the emission point for a PMT close to the center (left) and for a SiPM at x = −5 mm, y = +5 mm (right).

In Figure 4.22 the photon detection probability as a function of $r_{emission}$ is shown for four PMTs, one from each ring. The black dots correspond to the simulation data, while the red solid curve is the best fit line of the parametrization. The fit results in a good χ^2/ndof value.

The validation of the model is again performed by analyzing the *pull* distribution. As shown in Figure 4.23, the figure-of-merit is normally distributed. Thus, it is concluded that the parametrization of the PMT model is robust.

The SiPM model is parametrized using the relative transverse distance between the SiPM and the emission point. The dependende of the probability with dr is equivalent to that of the NEXT-White detector. Due to this similarity, the same functions used for NEW can be employed for this detector.

In Figure 4.24 the photon detection probability for all SiPMs in the NEXT-100 detector is represented as a function of dr for the first (left) and the second (right) time bins. The curves found are statistically equivalent to that found for the NEXT-White detector. Therefore, the data (black dots) are well modeled using a 9th-degree polynomial (red line). The fit results in a good χ^2/ndof value.

Finally, the SiPM parametrization is validated. The *pull* distribution is shown for both time bins in Figure 4.25. In both cases, a mean zero, unit sigma gaussian shape is observed, which demonstrates the robustness of the parametrization.

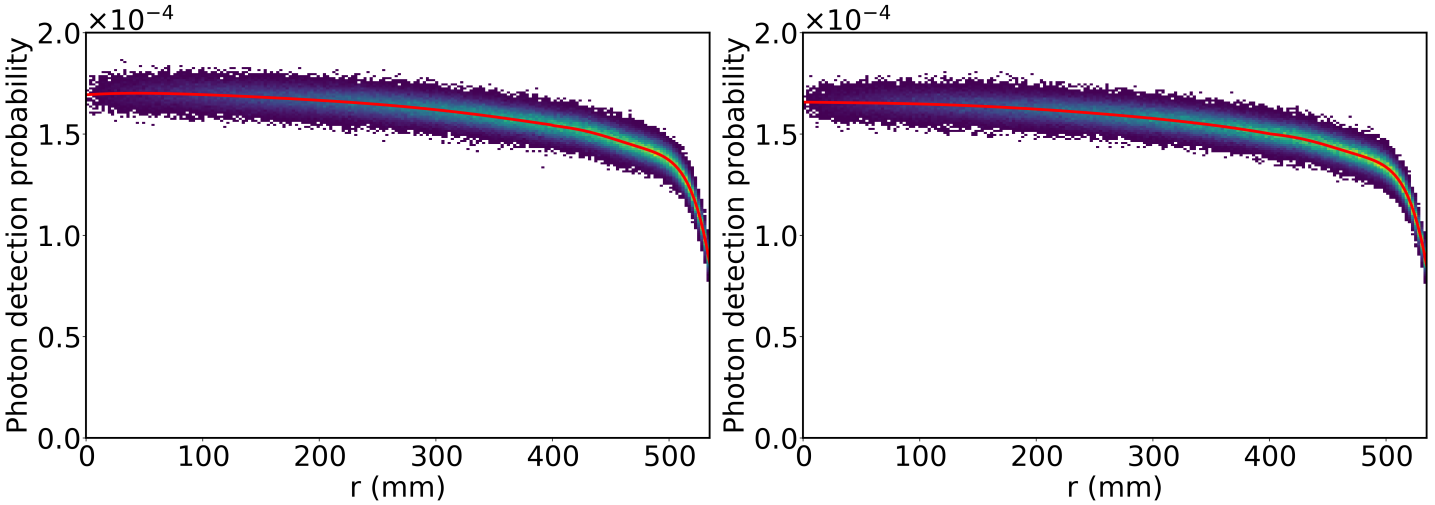

(a) Ring 0

(b) Ring 1

(c) Ring 2

(d) Ring 3

Figure 4.22: Photon detection probability as a function of r (black dots) and best fit line (red) for a PMT in the first (top left), second (top right), third (bottom left) and fourth (bottom right) rings.

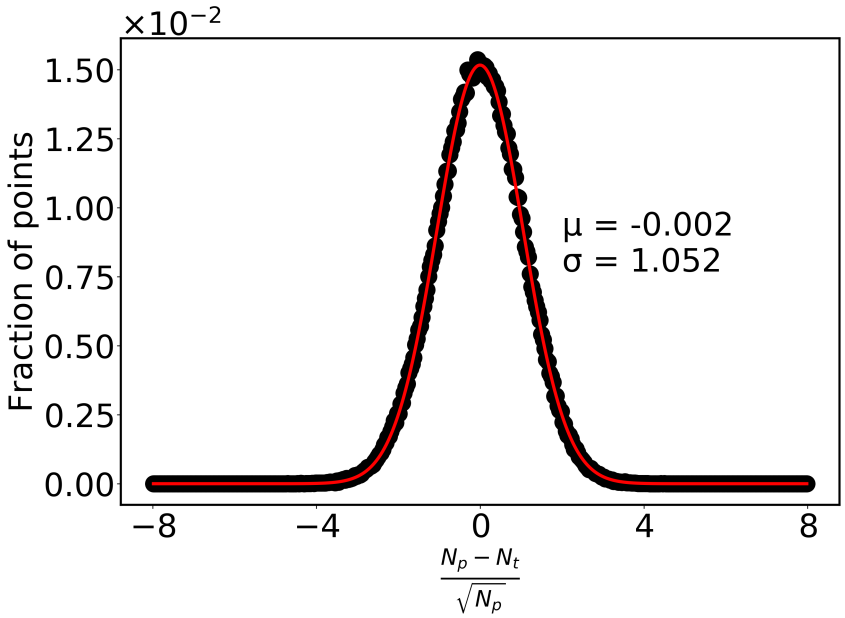

Figure 4.23: *Pull* distribution for all PMTs and all grid points in the NEXT-100 S2 table simulation using a combination of a 5th- and a 6th-degree polynomial parametrization for each PMT. A normal distribution is observed, proving that the parametrization of the S2 PMT model is robust.

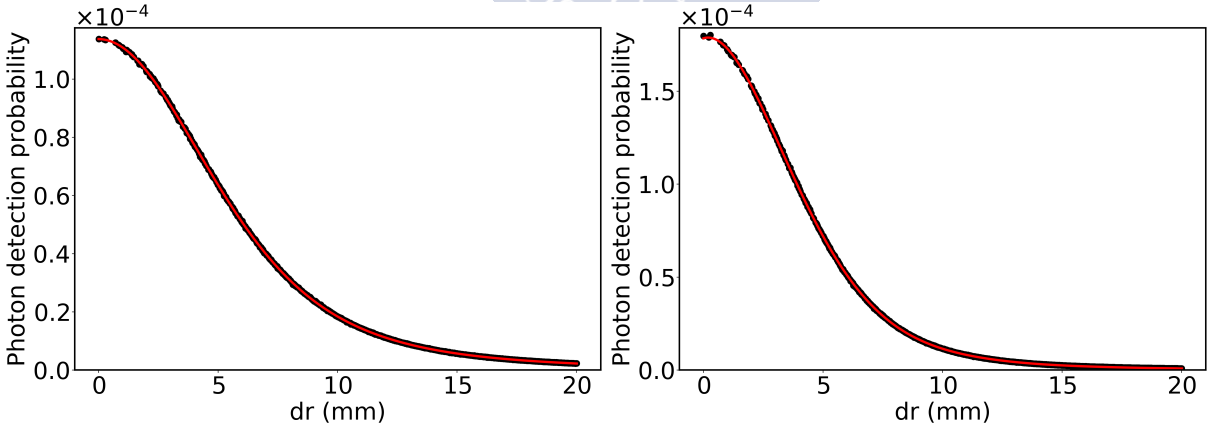

Figure 4.24: S2 photon detection probability for all SiPMs in the NEXT-100 detector as a function of dr (black dots) and best fit (red line) for the first (left) and second (right) time bins.

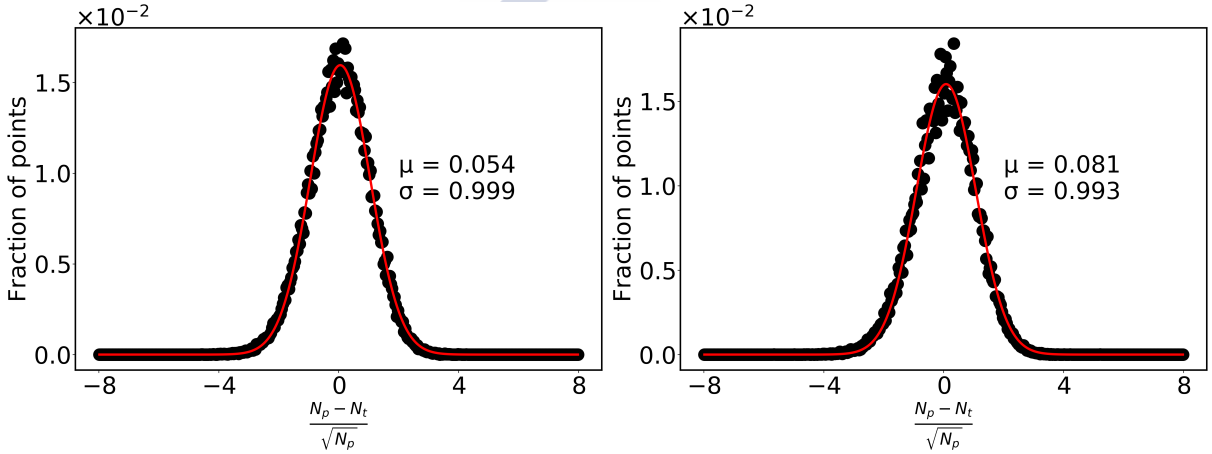

Figure 4.25: *Pull* distributions for the parametrizations of the first time bin (left) and the second time bin (right) data. A mean zero, unit sigma gaussian distribution is obtained, proving the robustness of the parametrization.

5 The NEXT reconstruction software

The output of the detector consists of a collection of electric signals. These signals are digitized by ADC cards and formatted by FPGA modules to produce the so-called *raw data*. These data have very low entropy and need to be processed to produce meaningful information. This task is performed by reconstruction algorithms: a collection of functions that transform data into more ellaborate structures, easily understandable by humans. These structures are ultimately used for data analysis and the production of physics results.

In this chapter, we describe the data reconstruction software used in the NEXT experiment. The following sections provide a detailed explanation of the algorithms and data structures used to process the data produced by the NEXT-White detector.

In the first stage of the data processing, the detector raw data or the Monte Carlo data are transformed into *Raw Waveforms* (Section 5.1), the collection of sensor waveforms corresponding to the same event.

These waveforms need to be further processed to account for different features. Firstly, the PMT waveforms contain an effect introduced by the energy plane electronics, which needs to be deconvoluted. Secondly, all waveforms need to be baseline-subtracted and calibrated, as different sensors produce different signals for a common input. Finally, since the signal is distributed over a few relatively short time intervals, the waveforms are sliced to select those regions and reduce the data size. This constitutes the `PMap` object (Section 5.2).

The final stage of the processing is split depending on the type of the event. Short, point-like events are processed by an algorithm that reduces the sensors' information to a single point in space with an associated energy (Section 5.3). On the other hand, long tracks are processed by a different algorithm that produces a collection of *hits* that form a discretized representation of a track (Section 5.4).

The chapter concludes with a description of the software framework used in NEXT (Section 5.5). This structure follows an innovative approach in the particle physics community. It is entirely written in python and makes use of software tools developed by a broader community.

The main feature of this framework is the so-called *dataflow* scheme (Section 5.6). The similarity between the schematic representation of the workflow and its actual implementation is the most remarkable benefit introduced by this structure.

5.1 Production of raw waveforms

This data structure is identical to both the data coming from the detector and Monte Carlo data, but they need to be produced from different data structures. Thus, the generation of Raw Waveforms is explained separately

5.1.1 From the detector binary data

The binary data stored by the FPGAs is reorganized in order to produce the so-called *Raw Waveforms* (RWFs). A RWF is the time-ordered signal amplitude of each sensor measured in adc counts (ADC). The RWFs are characterized by two properties: the data acquisition window (DAQW) and the sampling time. The former specifies the length of the waveform and the latter the size of the time interval used to measure the amplitude[1]. The time interval depends on the type of the sensor: 25 ns for PMTs and 1 μs for SiPMs. On the one hand, the finer sampling of the PMTs translates in a more accurate description of the PMT waveform, crutial to achieve an optimal energy resolution. On the other hand, it allows to decouple the effect of the energy plane electronics from the true sensor signal, as described in Section 5.2.1.

The data from the detector comes in a specific binary format defined by the collaboration. In order to produce the raw waveforms for each sensor the binary data needs to be decoded. This task is performed by a C++ programme that is semi-automatically launched when the detector is taken data.

The waveforms are stored in an *hdf5*[2] [173] file. The PMT and SiPM waveforms are stored in independent nodes within the file using the *pytables* [174] module. Each node consists of a homogeneous extensible array (*EArray*) of type `int`[3] with dimensions (number of events, number of sensors, waveform length). A fast and memory-efficient processing of the data can be achieved due to the homogeneous structure and the clever file management provided by *pytables*.

5.1.2 From Monte Carlo true waveforms

As detailed in Section 4.1, the Monte Carlo hits (*mchits*) are a collection of energy depositions produced by charged particles interacting in the gas. These energy depositions are translated into ionization electrons and propagated under the effect of an electric drift field towards the EL region to finally replicate the light emission process with the parametrized probability models. This process is carried out by the DETSIM C++ programme and results in a collection of *true waveforms*.

[1] Within each time interval the charge in the sensor is integrated.
[2] **H**ierarchical **D**ata **F**ormat
[3] At this point integers is the natural representation of the data, as they come in ADC.

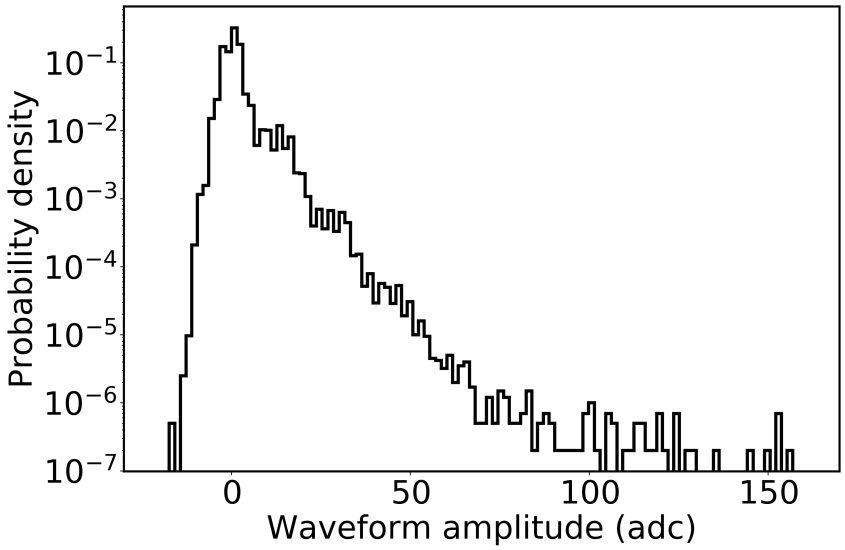

Figure 5.1: Dark noise spectrum for SiPM 5028 of the NEXT-White detector after baseline subtraction. The spectrum is composed of a *pedestal* and a sequence of peaks. The pedestal corresponds to low charge processes occurring within the sensor and the peaks to thermal creation of photoelectrons in the active region of the SiPM.

A true waveform represents the signal amplitude of a given sensor without any type of distortion or effect. It is a perfect description of the exact number of photons detected by the sensor in a certain time interval, given by the sensor sampling time.

The electronics of the detector introduces a number of distortions to the sensors' waveforms. For the Monte Carlo data to be truly representative of that of the detector, these distortions must be simulated. Each PMT waveform starts with a baseline number of ADC, measured from the detector waveforms. The noise of the PMTs is known to be gaussianly distributed with a certain standard deviation. This distribution is randomly sampled for each entry in the waveform and added to the baseline. On the other hand, the true waveform is transformed from photoelectrons (*pes*) to ADC using the experimentally-measured PMT gain (g). This transformation requires the replication of charge fluctuations in the PMT response. Due to the multiplication mechanism used in PMTs, the signal produced by a given input can be described by a gaussian distribution. The conversion from *pes* to ADC is then accomplished by sampling a gaussian distribution with $\mu = n_{pe} \cdot g$ and $\sigma = \sqrt{n_{pe} \cdot g} \cdot \sigma_{1pe}$, where n_{pe} is the number of photoelectrons in a given sample of the true waveform and σ_{1pe} is the measured standard deviation in 1-photoelectron signals. Finally, this waveform is passed through an algorithm that emulates the effect of the Front End electronics and added to the previous noisy waveform.

The procedure is similar for the SiPMs. Each SiPM starts with a baseline number of ADC measured from the detector waveforms. The noise is added to the waveform by sampling the SiPM dark noise PDF. These PDFs are extracted from some dedicated runs, where the detector drift voltages are lowered while keeping the SiPMs are biased. The waveforms produced by the SiPMs in this scenario contain only spurious counts comming from the solid-state nature of the detector. The waveform amplitudes are histogrammed, to produce a *dark noise spectrum* as the one shown in Figure 5.1. Finally, The true waveform is converted to ADC following the same technique as for PMTs and added to the former noisy waveform.

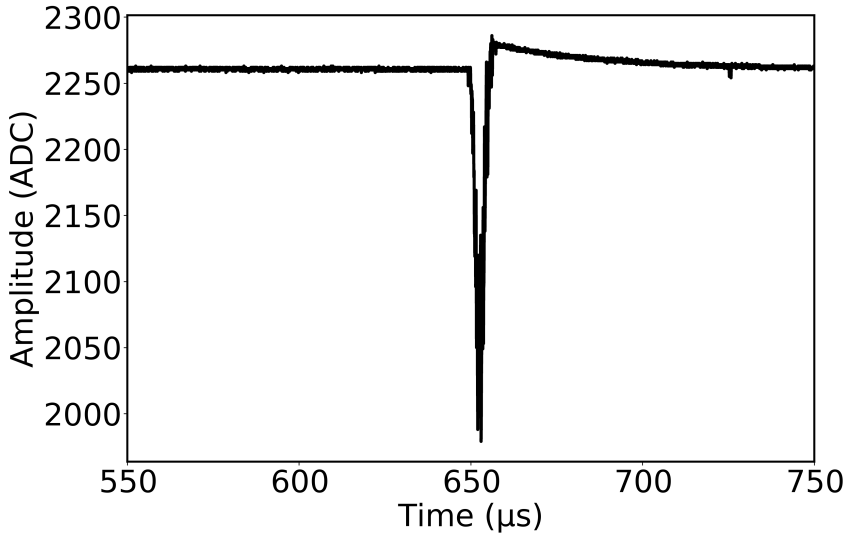

Figure 5.2: Section of a PMT raw waveform containing the S2 signal of a $^{83}Kr^{m}$ event in the NEXT-White detector. The effect of the electronics produces a swing in the response of the PMT.

5.2 Production of `PMaps`

The information in a waveform is localized in the time intervals corresponding to the S1 and S2 signals. The majority of any waveform produced by the detector does not contain any useful information. For this reason, the RWF is sliced to selectively choose the sections defined by a peak-finding algorithm that contain signal (peaks). Besides, the PMT and SiPM peaks need to be matched and combined into a single structure that provides all the usable information of the event. The collection of all the peaks in the set of waveforms of a given event is called Peak-map or `PMap`.

5.2.1 `PMap` building algorithm

The creation of `PMaps` can be divided in the three main tasks described in the following sections.

Baseline subtraction and deconvolution of the PMT waveforms

Due to the configuration of the PMTs bias (see Section 3.3.7), the PMT waveform does not represent the actual signal produced by the PMT, but its derivative [164]. This is shown in Figure 5.2, where a section of a PMT RWF is shown for a $^{83}Kr^{m}$ event. Before receiving any signal, the PMT output current is stable around the sensor baseline, producing a constant number of ADC. When the PMT receives light, the PMT output current increases as it converts photons into electrons, creating a decrease in output voltage which in turn decreases the ADC amplitude. However, when the light received begins to faint and the PMT produces a smaller amount of electrons, the current decreases, which produces the opposite effect and the ADC amplitude increases.

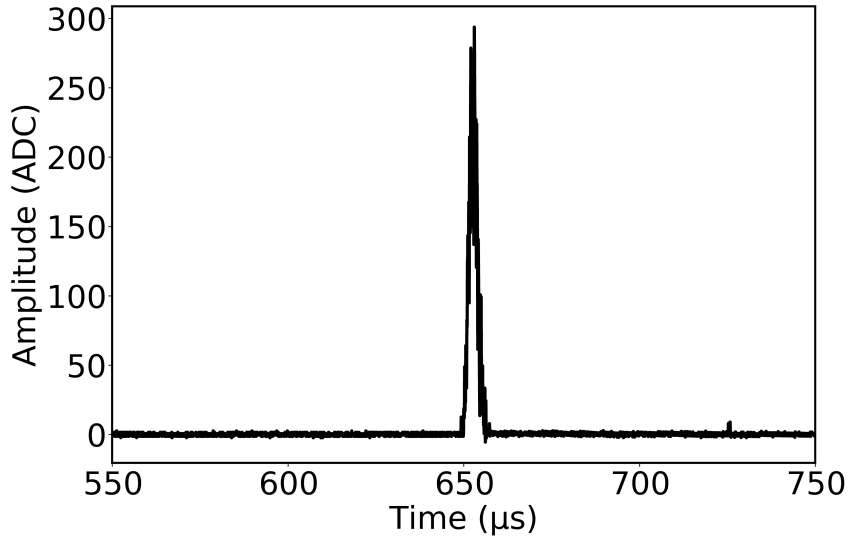

Figure 5.3: Deconvoluted version of the PMT waveform shown in Figure 5.2. After removing the effect of the electronics, the waveform has zero baseline and is positively-defined.

The signal in the PMT RWFs is characterized by a null area. Due to this feature, the integral of the signal above and below the baseline are equal. The baseline of each PMT is calculated as the average of the amplitude of the entire waveform and subtracted. Because of the aforementioned feature, the deviations from the baseline produced by any signal is cancelled out. Besides, the intrinsic noise of the PMT is gaussianly distributed and therefore does not bias the measurement in any direction. The resulting signal is inverted to counteract the fact that the PMT signals are negative.

The event energy is proportional to the area of the signal and therefore it is crucial to recover the originating signal. This is achieved by means of a deconvolution algorithm (BLR) that reverses the effect of the electronics. The algorithm is based on an accumulator and is described in detail in [164], but it can be summarized as follows.

The algorithm is inactive until a signal above certain threshold is found. At this point, the waveform samples are accumulated until this value falls below some predefined threshold. The rise of the accumulator is controled by some precomputed channel-specific coefficients. Then, the accumulator goes into a controlled discharge state. A smooth curve is enforced to ensure the reconstructed signal is continuous. The parameters of the discharge state of the algorithm are common to all channels.

Due to its connection to the energy resolution capabilities of the detector, an excellent accuracy in the BLR algorithm is required. Indeed, applying the deconvolution algorithm to Monte Carlo-simulated signals results in a contribution to the energy resolution smaller than 0.3%FWHM for long signals. This contribution is smaller than that of the Fano Factor in xenon, satisfying the accuracy requirement.

This BLR algorithm is applied to each PMT independently to produce the so-called Corrected Waveforms (CWFs). Figure 5.3 shows the result of the deconvolution process applied to the waveform in Figure 5.2.

The SiPMs waveforms, on the other hand, lack of this feature. The signal in a SiPM

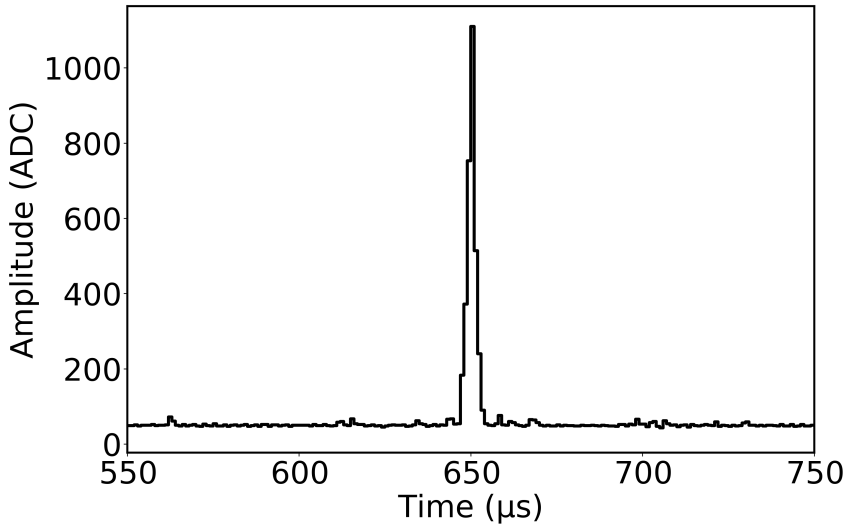

Figure 5.4: Section of a SiPM waveform containing the S2 signal of a $^{83}\mathrm{Kr}^{m}$ event in the NEXT-White detector. The waveforms are positively defined and have a non-null baseline.

waveform is positive with respect to a generally non-null baseline, as shown in Figure 5.4. Thus, the baseline cannot be computed using the average of the waveform as it would be biased to a higher value. In this case, the baseline is measured using the mode of the waveform, which results in an unbiased measurement for all realistic SiPM signals. The baseline is computed and then subtracted on an event-by-event basis and for each SiPM independently.

Waveform calibration

The production and manufacturing of the sensors and other electronic components does not guarantee a homogeneous response among all sensors. Thus, the waveforms are calibrated to equalize their response. The calibration consists of a constant for each sensor indicating the number of ADC corresponding a photoelectron, which is a physical quantity common to all of them. The calibration technique is similar for PMTs and SiPMs.

Using LEDs installed both in the energy and in the tracking plane[4], the single photoelectron spectrum (SPE) is measuremed for each sensor. The LEDs are configured to emit short pulses ($\mathcal{O}$(100 ns)) of VUV photons in regular intervals. The resulting waveforms are divided into fixed-width sections and integrated to produce the SPE. The distance between peaks corresponds to the ADC-to-*pes* conversion factor (calibration constant).

Each sensor waveform (of both PMTs and SiPMs) is scaled according to its calibration constant to produce a set of Calibrated Corrected Waveforms (CCWFs).

[4]The PMTs are calibrated with the LEDs installed in the tracking plane and the SiPMs with the LEDs placed in the energy plane

Peak finding and waveform slicing

The peak finding and waveform slicing is arguably the most complex part of the RWF processing. The algorithm must be able to find two very different types of signals (S1 and S2), while accurately establishing the limits on those peaks to maintain the energy resolution capabilities of the detector. In order to satisfy the latter condition, the PMT CCWFs are used as they are sampled each 25 ns. Besides, these waveforms are summed to increase the signal-over-noise ratio[5].

Each type of signal (S1 and S2) is independently searched. The summed waveform is searched for samples above a certain threshold (`thr_sum`), which may depend on the signal and event types. Nonetheless, fluctuations in the PMT signal near the threshold can lead to a split in an otherwise single peak. This is particularly relevant for S1 signals due to their small amplitude. To minimize this effect, signal regions separated by some configurable short time (*stride*) are joined back together. This *stride* may also depend on the signal and event types. In order to reduce the amount of spurious or unphysical peaks, the search can be restricted to certain buffer times in the waveform and the resulting peaks are then filtered based on their width, which is another parameter of the algorithm, improving the efficiency of finding peaks corresponding to a true signal. The beginning and end of the signal region is kept for each peak. This information is then used to slice each sensor waveform.

For S1 peaks, only the PMTs are taken into account as the signal is too weak to be detected in the SiPMs. Thus, each PMT waveform is sliced in the region defined the previous algorithm and stored.

For S2 peaks, on the other hand, both the PMTs and SiPMs waveforms contain information. Due to the different sampling time of these sensors, the PMT waveforms need to be resampled to 1 μs. Besides, as detailed in Chapter 4, the tracking plane response is highly focused around the emission point. Thus, most of the SiPMs lack of a real signal. In order to reduce the amount of data stored, those SiPMs with less signal than a given configurable amount (`thr_sipm`) in a given peak are discarded. This reduces the data size by roughly a factor 100. After the resampling and the SiPM selection, the PMTs and the remaining SiPMs peaks are matched and stored.

Figure 5.5 shows how the algorithm performs on a S1 and a S2 peak of a $^{83}\mathrm{Kr}^{m}$ event. In Figure 5.5a the section of a PMT-summed waveform around a S1-like signal is shown in black. The algorithm was configured to search for short peaks (between 50 ns and 400 ns long) in the first 600 μs of the buffer[6] with *stride* = 100ns and `thr_sum` = 0.5 *pes*. The result, shown in red, matches the expected region of the waveform. Figure 5.5b shows the section of a resampled PMT-summed waveform around a S2-like signal (black line). The algorithm was configured to search for moderately long peaks (between 2 μs and 40 μs long) in the $[600, 1300)\mu$s window of the buffer with a *stride* of 1 μs, `thr_sum` = 1 *pes* and `thr_sipm` = 5 *pes*. The result, shown in red, matches the expected region of the waveform. The waveform (black) for SiPM 9058 for the same time window is shown in Figure 5.5c with the red line indicating the selected SiPM peak.

[5]The noise in the PMT waveforms is gaussianly distributed around the baseline with a standard deviation σ_{pmt}. Assuming similar values of σ_{pmt}, the addition of the PMT waveforms results in a waveform with a standard deviation $\sqrt{n_{\mathrm{pmt}}}\sigma_{\mathrm{pmt}}$ of the noise. However, the signal increases linearly with the number of sensors and therefore the signal-to-noise ratio improves with $\sqrt{n_{\mathrm{pmt}}}$

[6]Notice that the S2 of the event is set by the trigger algorithm at the center of the buffer window. This corresponds to 650 μs.

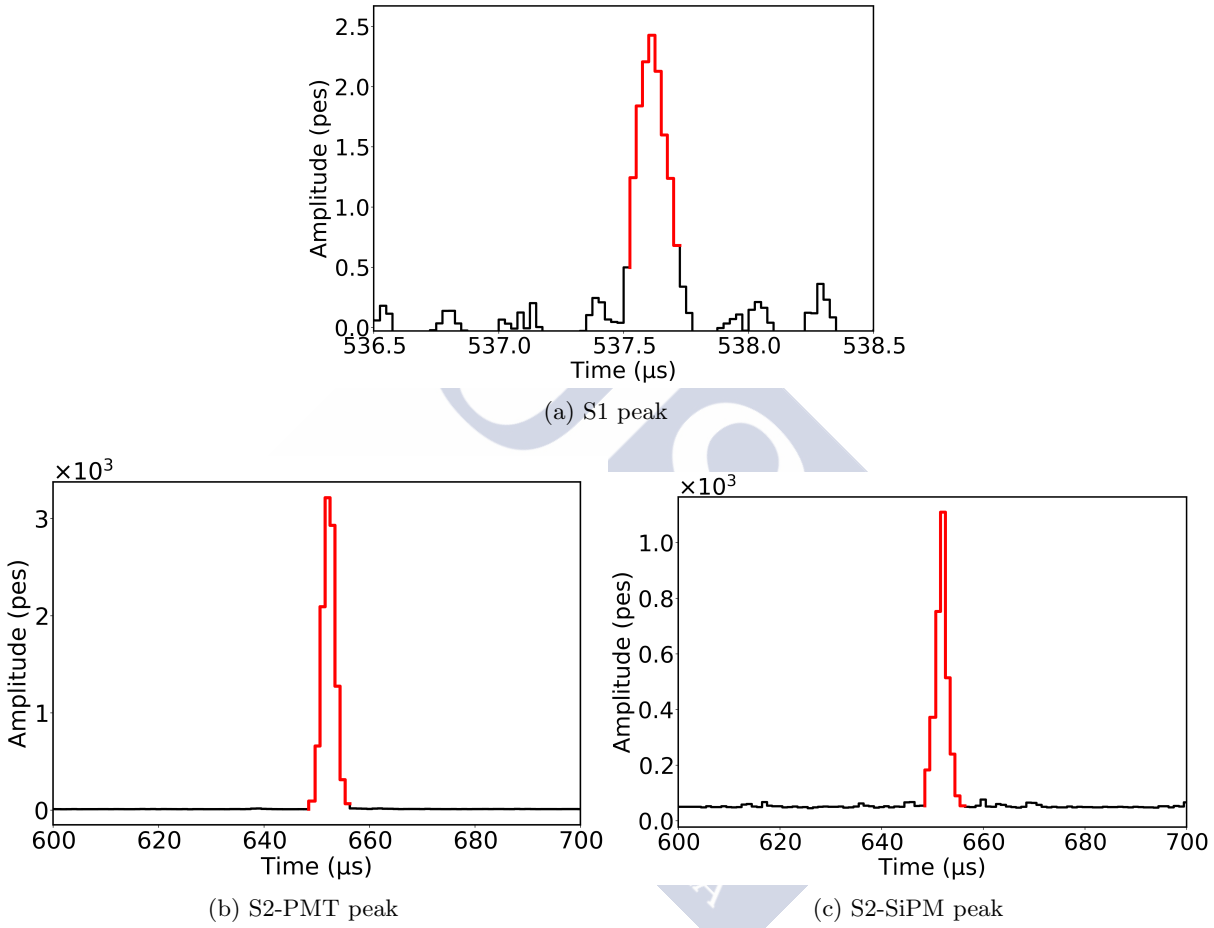

(a) S1 peak

(b) S2-PMT peak

(c) S2-SiPM peak

Figure 5.5: Demonstration of the performance of the peak-finding algorithm. On the top panel, the algorithm is configured to search for short signals in the PMT-summed waveform. On the bottom-left panel, the algorithm is configured to search for moderately long signals in the PMT-summed waveform. The time window defined by the algorithm is used to define the peak in the SiPM waveform as shown in the bottom-right panel

5.2.2 `PMap` representations

The `PMap` structure is fairly inhomogeneous and calls for a particular data structure in order to store them efficiently (persistent representation). However, at user level, the persistent representation is not manageable. Thus, in order to perform operation on `PMaps`, a more suitable transient representation is built.

Persistent representation

As metioned above, the S1 signals can only be measured in the PMTs and therefore that is the only information saved. Each file will contain multiple events and each event may contain a number of peaks. Since the sections of the waveform without any signal have been removed, the time information is no longer implicit. Besides, since the PMTs are considered signal integrators, the individual PMT signals are usually used only for debugging purposes. This leads to a table structure were with four fields: the event number, the peak number, the sample time and the PMT-summed signal amplitude at that time.

In case the individual PMT signals are needed a second table is written. Since the time information is already stored in the PMT-summed table, it is assumed that the information in this table will be stored in the same order. However, now there is a need to specify the PMT to which a certain sample corresponds. The final result is a table with four fields: the event number, the peak number, the PMT number and the signal amplitude of the PMT at a given time. Notice that the time of each sample is implicit in the order they are stored.

The PMT section of the S2 signals is stored in a similar fashion to that of the S1 signal. The SiPM component is stored separately in a different table. Following the same strategy as for the individual PMT tables, the SiPM information is stored assuming the time information is kept on the PMT-summed table. A similar table is used to store the SiPM data. It contains four fields: the event number, the peak number, the SiPM number and the signal amplitude of the SiPM at a given time. As mentioned in Section 5.2.1, not all SiPMs are stored in disk. This reduces considerably the size of this particular table.

Listing 5.1 displays the persistent representation of a `PMap`, as stored in a file. A more explicit output can be found in Listing B.1 of Appendix B.

```
/ (RootGroup) ''
/PMAPS (Group) ''
/PMAPS/S1 (Table(2068,), shuffle, zlib(4)) 'S1 Table'
/PMAPS/S1Pmt (Table(22748,), shuffle, zlib(4)) 'S1Pmt Table'
/PMAPS/S2 (Table(2308,), shuffle, zlib(4)) 'S2 Table'
/PMAPS/S2Pmt (Table(25388,), shuffle, zlib(4)) 'S2Pmt Table'
/PMAPS/S2Si (Table(206874,), shuffle, zlib(4)) 'S2Si Table'
```

Listing 5.1: `PMap` persistent representation. The `PMAPS/S1` and `PMAPS/S2` nodes contain the table for the PMT-summed information for the S1 and S2 peaks, respectively. Similarly, the `PMAPS/S1pmt` and `PMAPS/S2pmt` nodes contain the individual PMT amplitudes for the S1 and S2 peaks, respectively. In `PMAPS/S2SiPM` the SiPM amplitudes for the S2 peaks are stored.

Transient representation

The transient representation of the `PMap` is more human-readable than the persistent one. It is structured in three layers of information resembling the natural structure of the event. Figure 5.6 displays a diagram of this representation. On the top layer, the `PMap` contains a collection of S1 `Peak`s and a collection of S2 `Peak`s. The `Peak` object constitutes the second layer and is formed of an array of times and two instances of a `SensorResponse` object: one for PMTs and one for SiPMs. The time array represents the sampling times of the peak, common to all sensors. The third layer of the structure is the `SensorResponse` object, which is in essence a collection of waveforms. It contains an array of ID numbers of the sensors within the structure and a 2-dimensional array of amplitudes. The time information is implicit and it is assumed that each amplitude can be assigned a time when matching its index in the array with the time array in the `Peak` instance.

5.3 Production of `kDST`s

Low-energy electrons produce an extremely short ionization track. In this case, the event can be considered a point-like energy deposition and use a single (x, y, z) coordinate to describe its position. This type of events are used to equalize the response of the detector across the whole chamber as described in Section 6.2.

At this point, it is useful to construct a structure that summarizes all relevant data in the event. This includes both energy and tracking information and combines the S1 and S2 information to produce a fully-reconstructed event. Despite being optimized for small events, this structure is also useful to make some rough estimations on the data, such as the event distribution and the energy spetrum. The structure must be compact and flexible, as it will be used directly in the data analysis stage. Thus, a *DST* scheme is chosen, as it has many advantages: its persistent and transient representations are analogous, it can hold an extremely large number of events without a major overhead and allows for a fast, intuitive and flexible event selection based on their properties.

5.3.1 `kDST` building procedure

Regardless of its energy, any event will occupy some volume in the space. In order to reduce it to a single point of the space, the data must be combined. Since a given event may contain an arbitrary number of S1 and S2 signals, the following procedure is carried out for all possible combinations of S1-S2 pairs.

The S1 and S2 signals are composed of 25-ns and 1-μs time slices, respectively. Each peak is summarized in four quantities based on the PMT data:

- The width, defined as time of the signal over a predefined threshold.
- The height, defined as the maximum amplitude of the peak.
- The time, defined as the average of the time slices in the peak weighted by the amplitude of the PMT-summed waveform at each time.

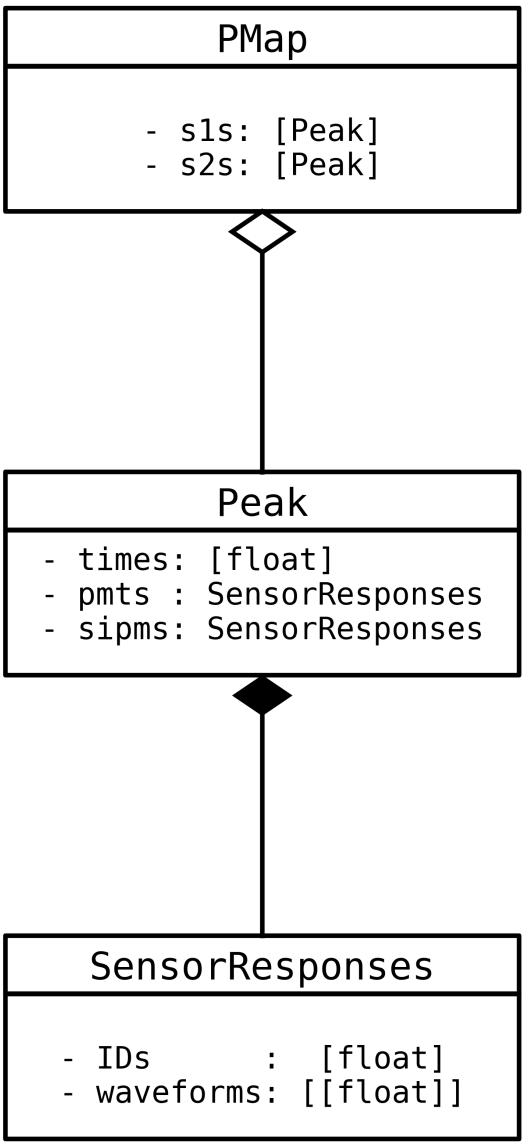

Figure 5.6: Structure of the `PMap` transient representation.

- The energy, defined as the time-integral of the PMT-summed waveform.

In order to reduce the z coordinate to a single value, the signal in each sensor is summed over time. The drift time of a certain S2 is computed as the difference between the S2 and S1 signals[7]. The z coordinate is calculated by dividing the drift time by the drift velocity of the electrons in the detector[8]. The standard deviation of the signal along the z coordinate is also computed using $z_{std} = \sum_k (t_k - t_{peak})^2 q_k / \sum_k q_k$

For the tracking information, only those SiPMs with an integrated signal above a predefined threshold are considered. The number of SiPMs reflects the number of sensors surviving this cut. The total charge of the S2 signal is computed by summing the signal of the time-collapsed SiPM waveforms. The x and y coordinates and their standard deviations are computed using a barycenter algorithm. This method uses the relative charges of the triggered SiPMs to compute the weighted average of the sensor positions. Despite its simplicity, the barycenter algorithm has shown remarkable accuracy. A more detailed description and a study of the performance of this algorithm can be found in Appendix A.

5.3.2 `kDST` representations

The persistent representation of the `kDST` consists of a *hdf5* table with 25 fields. The data are stored in a single node, as shown in Listing 5.2. An explicit display of this representation can be found in Listing B.2 of Appendix B. The table fields can be gathered into four groups depending on what they describe:

- The fields describing the event as a whole: the event number, the time stamp of the event, the number of S1 peaks and the number of S2 peaks
- The fields describing the PMT-component of the peaks: the S1 (S2) peak number, the time within buffer, the width, the maximum amplitude or height and the integrated PMT signal.
- The fields describing the tracking information of the S2 peak: the total charge measured in the tracking plane, the number of SiPMs with signal above a certain threshold, the reconstructed x, y, r and ϕ positions and the standard deviation of the signal along the x and y coordinates.
- The fields describing the drift information: the drift time, the reconstructed z position and the standard deviation of the signal along the z coordinate.

```
/ (RootGroup) ''
/DST (Group) ''
/DST/Events (Table(4,), shuffle, zlib(4)) 'KDST Events'
```

Listing 5.2: `kDST` persistent representation. A unique node `Events` within a group `DST` holds all the data. This node contains the column descriptors described in the text.

[7]Notice that for any physical and related signals, the S1 *always* comes first. Thus, any negative drift time must come from an unphysical event or from a combination of the signals of two different events.

[8]The drift velocity can be estimated from the value of the voltages at the cathode and the gate and the pressure, but it can also be measured from the data themselves.

Each event may contain multiple S1 and S2 signals. This can be caused by an event pile-up in the buffer, a missidentification of S1 signals[9], or a single event producing multiple interactions in different regions of the chamber. Hence, each row in the table refers to a certain pair of S1 and S2 signals, and all possible combinations are stored.

As mentioned above, the persistent and transient representations are analogous. The latter is built by directly reading the persistent one in a *pandas* [175, 176] `DataFrame`. This two-dimensional tabular data structure is specifically designed to perform data analysis on large amounts of data. It contains labeled axes and allows for a vast number of operations, such as selecting, grouping, aggregating or slicing data based on their by properties. Besides, it contains a large number of built-in utilities to perform statistical analysis on the data.

For a display of the first rows of a `kDST` created with reconstructed $^{83}\mathrm{Kr}^{m}$ events, see Listing B.3.

5.4 Production of `hDSTs`

Unlike $^{83}\mathrm{Kr}^{m}$ events, high-energy electrons produce long, twisty ionization tracks along their path. For instance, a 2.5 MeV electron at 15 bar produces a 15-cm-long track [152]. The background rejection capabilities of the detector rely on the ability to recreate the path of the electron in the gas. Thus, the reconstruction is carried out in term of *track hits*.

5.4.1 `hDST` building procedure

In this methodology, the S2 peaks are divided into z sections or *slices*. Usually, the default 1-μs slicing is used, but the peaks can be rebinned to produce peaks sampled in any multiple of 1 μs. For each z *slice*, the data are combined to produce a finite number of reconstructed points. The reconstruction of the z coordinate is identical to that described in Section 5.3.1. The reconstruction of the x and y coordinates, on the other hand, follows a more complex procedure: the *corona* algorithm. This algorithm can find multiple energy depositions in the same z *slice*, provided they are suffiently separated.

The data stored in this reconstruction step is a collection of *hits*. A *hit* is defined as a set of three-dimensional coordinates, with their respective standard deviations and associated values of energy and charge. Contrary to the `kDST`, the S1 information is not stored. The higher efficiency of true S1 identification at higher energies allows for a single S1 to be reconstructed. The S1 characteristics are therefore not as useful in this scenario and thus ignored.

The corona algorithm

This method is designed to be able to recognize separate energy depositions in the same *slice* and reconstruct them as distinct *hits*. The process starts by finding the SiPM with the highest signal. Next, the SiPMs within a certain range, `lm_radius`, are selected to produce a local maximum $(\mathrm{x},\ \mathrm{y})_L$ position usign the barycenter algorithm. Then, the previous step is repeated

[9] S2 signals are too strong to be confused with a fluctuation in the waveforms.

taking $(x,\ y)_L$ as the reference and selecting the SiPMs within the range of another parameter `new_lm_radius` to produce a reconstructed *hit*. If the number of SiPMs in the *hit* is at least `min_sipm`, the *hit* is considered valid and kept, otherwise it is discarded. The SiPMs considered for the *hit* are discarded and the whole process is repeated until there are no SiPMs left of until the greatest signal is below `Q_min_hottest`. The algorithm returns a collection of reconstructed *hits*.

In Figure 5.7 an example of the application of the algorithm is shown. The images display the sipm positions colored according to their measured charge. Each image corresponds to one iteration of the algorithm. In Figure 5.7a the input to the algorithm is shown. The data corresponds to a section of a ^{208}Tl track coincident with an X-ray emission. In Figure 5.7b, the first iteration reconstructs a *hit* from the main track (red cross) using the SiPMs enclosed in the black line. In Figure 5.7c, the SiPMs from the previous iteration have been removed and the algorithm finds another local maximum with the remaining SiPMs around the separate energy deposition. The process is repeated and the main track produces another local maximum in Figure 5.7d. Finally, in Figure 5.7e the tracking the remaining SiPMs are shown. Since there is not a sensor with the minimum amount of charge required to produce a *hit*, the algorithm stops.

5.4.2 `hDST` representations

The persistent representation of the `hDST` consists of a *hdf5* table with 11 fields. As shown in Listing 5.3, the data are stored in a single node. An explicit display of this representation can be found in Listing B.4 of Appendix B. Each row in the table correspond to a single hit. The table fields are: the event number, the event time stamp, the peak number[10], the energy and charge of the *hit*, the number of affected SiPMs and the three-dimensional coordinates and the standard deviations of the transverse coordinates. The standard deviation in the longitudinal coordinate is not well defined in this case, as each *slice* is treated separately.

```
/ (RootGroup) ''
/RECO (Group) ''
/RECO/Events (Table(23,), shuffle, zlib(4)) 'Hits'
```

Listing 5.3: `hDST` persistent representation. A unique node `Events` within a group `RECO` holds all the data. This node contains the column descriptors described in the text.

Two transient representations are available for this data format. A *pandas* `DataFrame` is used for generic data transformations on the hits, such as energy or charge corrections. This representation is analogous to the persistent one. A display of this format can be found in Listing B.5 of Appendix B.

A second representation uses a *HitCollection* object. As it name indicates, each event is formed of a collection of reconstructed *hits*. This representation is more suitable for further stages of the reconstruction, were the hits are ordered and the extremes found. A diagram of this structure is shown in Figure 5.8.

[10]Since there may be multiple S2 signals in the event, it is useful to be able to associate a hit to a given S2 signal

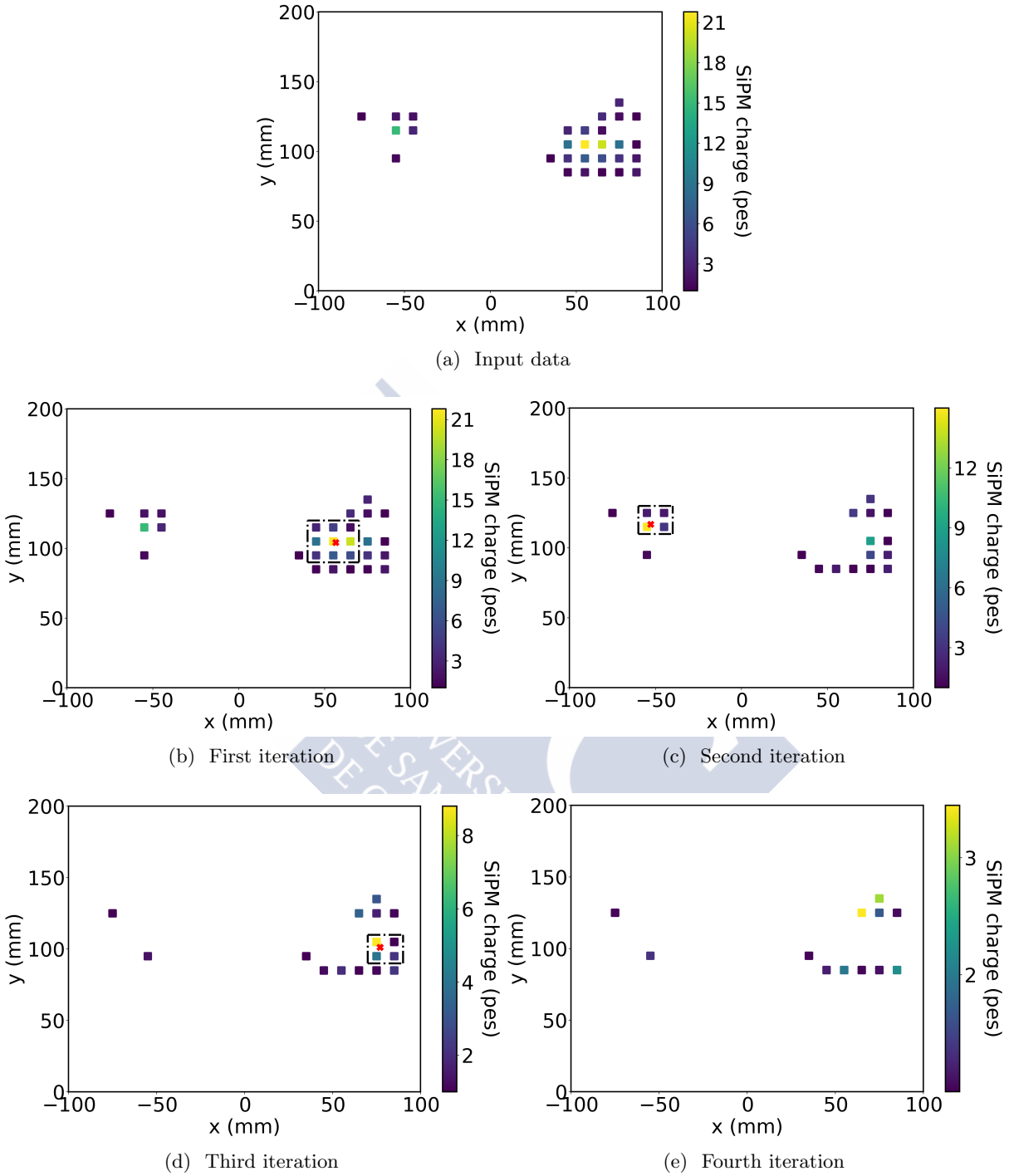

(a) Input data

(b) First iteration

(c) Second iteration

(d) Third iteration

(e) Fourth iteration

Figure 5.7: Performance of the corona algorithm on the tracking data corresponding to a section of a ^{208}Tl event were an X-ray emission is caugth in the same *slice* as the main track. The triggered SiPMs (squares) are shown in their positions with the color scale representing the measured charge. The black dash-dotted line and the red cross are shown to illustrate the functionality of the corona algorithm (see text for details). Each panel corresponds to an iteration of the algorithm.

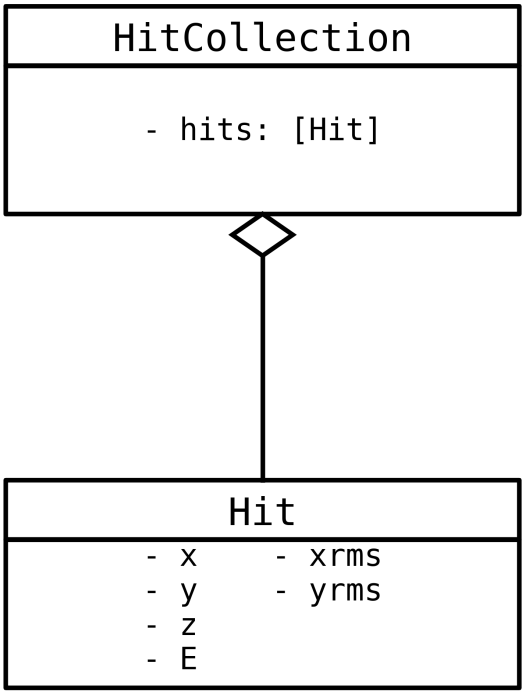

Figure 5.8: Transient representation of the `hDST` data format in the form of a *HitCollection*.

5.5 Software framework

Most of the official reconstruction chain of the experiment is implemented in what is known as the *IC*[11] framework. The only exceptions are the decoder programme described in Section 5.1.1 and Detsim (Section 4.1.2). IC is organized in a *git* repository and publicly available at [177]. The most remarkable characteristic of this framework is the innovative *dataflow* scheme, detailed in Section 5.6. This structure provides a one-for-one correspondence between the schematic representation of the workflow with its implementation. This is achieved by means of a modular structure, with pluggable components, that builds sequences of meaningful data transformations. The implementation of this scheme, despite not being yet released, has been proven to increase the understanding of the data reconstruction process among the collaborators.

5.5.1 Features

The IC framework is written almost entirely in Python[12] [178, 179]. It is built around the anaconda [180] ecosystem with just a few exceptions not yet available in the environment. The software does not include any C++ code or any interaction with ROOT [181]. ROOT has been frequently critisized for its lack of compatibility with other software tools and for its memory management model. Besides, it is developed, designed for and used by a small community, which difficults the interaction outside the particle physics community. Thus, whenever possible, the software relies on the widely-used solutions available in the standard libraries. Development efficiency, code reliability, readability and speed performance are some of the benefits provided by this approach.

The main argument for using a lower-level language such as C++ is usually the increased execution speed. However, when using the stardard scientific libraries (such as *scipy* [182]), which are usually composed of python interfaces to compiled languages, the speed penalty is minimal and the performance is close to that of C++. On top of that, the moderaly large volume of data produced by an experiment like NEXT, does not require highly-optimized execution times. Whenever neccesary, a speed improvement can be obtained by using compiled extensions of the python language, such as *cython* [183] or *numba* [184]. Notwithstanding, the use of these extensions has been found to be expendable.

Furthermore, python is an easy-to-learn, comprehensible language, that greatly increases the readability of the code. This, combined with the interactivity of the language, allows for a much faster software development and data analysis.

The framework is supported by an extensive test suite. Each function in the code has at least one dedicated test function that ensure it produces the correct result. Test are performed using two different techniques:

- With particular cases. Simple cases are used to test easily predictable results. In general, this technique verifies exact outputs.

[11] IC stands for book ***I**nvisible **C**ities* and for **I**talo **C**alvino, its author.

[12] At the time of this work, IC supports Python 3.6 and 3.7. When new python versions become available, the repository is rapidly upgraded to avoid tedious software migrations in the future.

- With exhaustive input screening. The function is called repeatedly varying its arguments. By using some heuristic methods, the values of the function arguments are drawn from the domain in which they are defined. This method is used predominantly to certify statistical properties or to assert a proper execution and realistic output of the function for all conceivable scenarios.

This philosophy improves the robustness of the sofware, not only by ensuring the correct functioning at the time of implementation, but also protecting it against errors in future modifications. Since the tests exercise their corresponding functions, they can also be used as a documentation of the code, therefore increasing the comprehension of the code.

The repository is based on a continuous release scheme. This implies that the latest version of the code with the newest features is always available for all users. The robustness of this method is guaranteed by a continuous integration system such as *Travis CI* [185]. *Travis CI* is a software tool that can be connected to git repositories to execute the aforementioned test suite to ensure the code is working properly. Until *Travis CI* does not certify the correctness of a new piece of code, it cannot be introduced in the official repository.

On top of that, the code is subject to an external revision. Any change to the code must be reviewed by one collaborator that did not contribute to its development. This philosophy favors the learning and overall comprehension of the software among the developers, impeding that a piece of code is understood by a single person. It also advocates good coding practices and reinforces the testing routine, which is examined by the reviewer.

5.5.2 Structure

The framework is composed of of six major modules:

- *core*: contains generic functions not specific to the experiment, such as those used for statistical analysis.
- *reco*: contains the experiment-specific functions, such as the functionality described in this chapter.
- *database*: contains all the tools to interface the sensor database.
- *event model & IO*: defines the event model in both the persistent and transient representations. It also contains the IO operations to read and write data.
- *dataflow*: contains the definition and implementation of the *dataflow* scheme described in Section 5.6.
- *cities*: contains the implementation of each step in the reconstruction chain and other data processing operations.

Cities

There are currently seven *cities*[13] constituting the framework. Four of them are dedicated to implement the reconstruction chain and the remaining three are devoted to extract the sensor calibration data.

diomira transforms the Monte Carlo true waveforms into RWFs following the procedure described in Section 5.1.2. *irene* produces `PMaps` from RWF as detailed in Section 5.2.1. The cities *dorothea* and *penthesilea* process `PMaps` to build `kDST`s and `hDST`s, respectively. The PMT calibration data are obtained with *phyllis*. On the other hand, *zemrude* produces the SiPM dark noise spectrum, whilst *moriana* generates the calibration data for these sensors.

5.6 *Dataflow*

Each *city* in the framework is implemented following a coroutine-based scheme known as *dataflow*. Following the functional programming paradigm, this formula implements a pipeline structure that generates a semantically-obvious workflow. It is composed of three main components:

- Sources: feed data into the pipeline.
- Pipelines: transform or filter data.
- Sinks: terminate pipelines.

Sources are usually readers for a specific data format, while sinks are generally used to summarize data or to write them to disk. Each pipeline may be composed of multiple pipes in sequence creating a pluggable architecture. The flexibility added by this design is strengthened by the ability to easily test each component separately, which facilitates the development.

Pipelines may be split using *forks* and *branches*. The difference between *forks* and *branches* is purely a matter of interpretation. The graph generated by both elements are equivalent. *branches* are thought as secondary pipelines, with lower priority[14]. They are usually expressed in minimalistic terms so their presence does not disturb the visualization of the main workflow, as shown in Figure 5.9b. *forks*, on the other hand, are very explicit split points in the workflow, as shown in Figure 5.9a. Each subsequent pipeline is thought as having the same priority. Both *forks* and *branches* replicate the input stream in multiple pipelines, allowing for a more visual workflow and facilitating the paralellization of tasks.

Running variables are stored using *futures*[15]. An interesting application of *futures* are the so-called *spies*. These are minimalistic branches used for data monitoring. They can *spy* some information from the data and store it during the execution of the program. The product of

[13]The *city* nomenclature is a reference to the book, where the narrator describes the cities it passes by. Indeed, the name of the programmes are the actual names of the cities in the book.

[14]There is not an actual priority ordering.

[15]In computer sciente, *futures* are variables the behave as proxies for an initially unknown result. The value of the *future* variable is expected to be set during the execution of the programme. This allows the reference to the variable in other sections of the code, that may be executed concurrently.

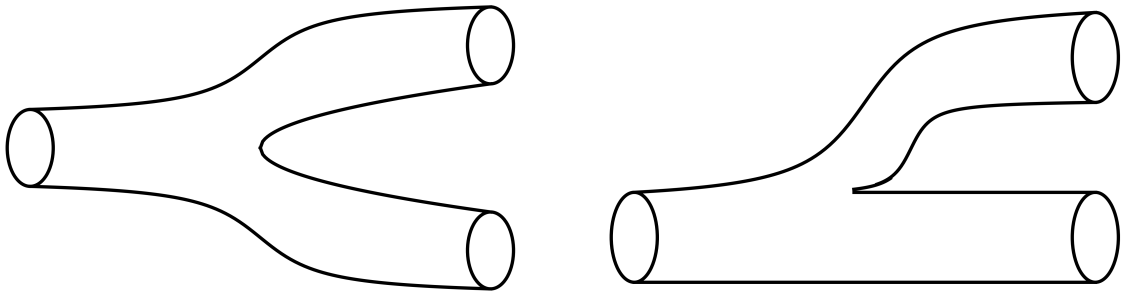

(a) Fork (b) Branch

Figure 5.9: Graphical representation of a *fork* and a *branch*. Both elements generate the same graph and are therefore equivalent. Notwithstanding, the *fork* scheme breaks the workflow explicitly into two equal streams, whilst in the *branch* design one of the pipelines is perceived as a side stream.

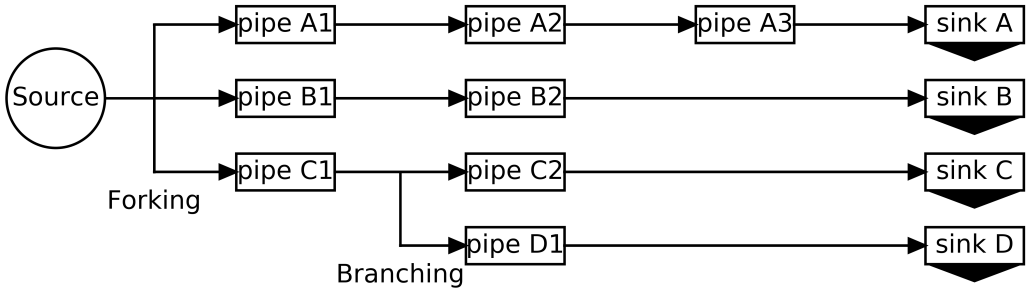

Figure 5.10: Generic workflow of a data processing stage. Each operation is marked with its *dataflow* equivalent.

the *spy* is stored as a *future* variable. *spies* are tremendously helpful for debugging, as they can essentially detect an unexpected result at any stage of the programme.

One of the best design features of the *dataflow* architecture is the similarity between the implementation and the corresponding workflow graph. This is illustrated in Figure 5.10, where a generic workflow is presented along with its *dataflow* equivalent operation.

5.6.1 The *dataflow* implementation of *diomira*

Tha worflow for *diomira* is shown in Figure 5.11. As detailed in the scheme, Monte Carlo data are read from a file to then perform four different tasks:

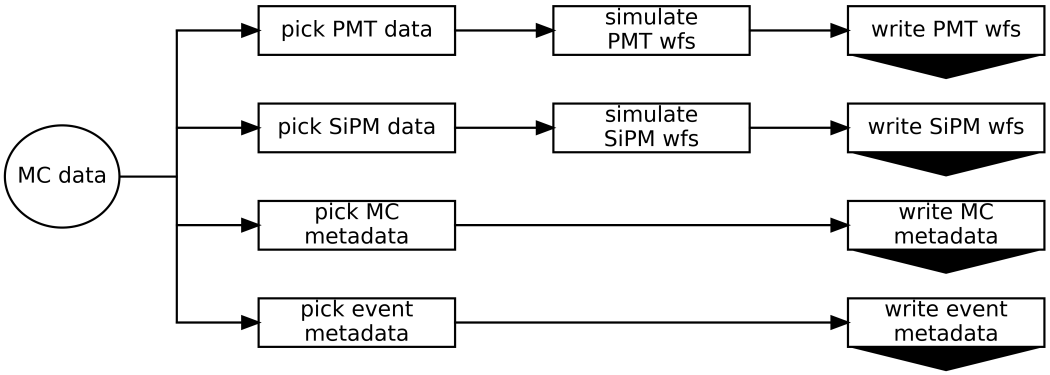

Figure 5.11: Worflow of the *diomira* programme. Monte Carlo data are read from a file and four independent tasks are performed: simulation and storage of PMT waveforms, simulation and storage of SiPM waveforms, storage of Monte Carlo metadata and storage of the event metadata.

- Select the PMT data, simulate the PMT waveforms and store them.
- Select the SiPM data, simulate the SiPM waveforms and store them.
- Select the Monte Carlo metadata and store them.
- Select the Event metadata and store them.

The implementation, shown in Listing 5.4, uses some functions defined beforehand. The source is defined as `mc_data_reader`, which reads the Monte Carlo data from the file. The pipeline is built from a number of components. The first element, `event_count_in.spy`, introduces a *spy* instance to count the number of events entering the pipeline. Next, the data stream is forked into four different ones. The first stream simulates and writes the PMT waveforms, the second one, does the same for SiPMs and the last two write the Monte Carlo and event metadata. `simulate_pmt_waveforms` and `simulate_sipm_waveforms` implement the procedure described in Section 5.1.2 to simulate waveforms. Finally, the result of the programme execution is stored in a dictionary, holding the aforementioned future variables. Clearly, the implementation layout resembles the workflow graph in Figure 5.11.

```
dataflow.push(source = mc_data_reader(files_in),

              pipe   = dataflow.pipe(event_count_in.spy,
                                     dataflow.fork((  "pmt", simulate_pmt_response  , write_pmt        ),
                                                   ( "sipm", simulate_sipm_response, write_sipm       ),
                                                   (   "mc",                       write_mc         ),
                                                   ("event",                       write_event_info))),

              result = dict(events_in = event_count_in.future))
```

Listing 5.4: *Dataflow* implementation of *diomira*.

6 Low-energy calibration of the NEXT-White detector

The response of the detector depends on the three-dimensional position of the event. In particular, small concentration of impurities in the gaseous xenon capture a fraction of the drifting electrons[1], reducing the amount of signal produced. On top of that, as described in Chapter 4, the light-collection efficiency of S2 signals depends on the (x, y) position of the event[2]. Both of these effects result in an uneven response across the active volume that deteriorate the energy resolution of the detector. As described in Section 3.1.2, energy resolution is of the utmost importance for a $\beta\beta$ decay experiment. Any physics data analysis performed with the detector relies ultimately on the accuracy of the energy measurement. Thus, the response of the detector must be equalized over the active volume.

In this chapter, we describe the calibration of the NEXT-White detector using $^{83}\mathrm{Kr}^{m}$ decays. $^{83}\mathrm{Kr}^{m}$ atoms are introduced in the active volume through the gas system. They eventually decay, producing extremely short signals, that can be considered point-like, over the whole active volume. The events produced by $^{83}\mathrm{Kr}^{m}$ decays are used to correct for both the attachment process and the light-collection efficiency variations across the detector. The attachment effect introduces an exponential dependence of the signal with the z coordinate. This dependende is characterized by the electron lifetime, τ. We correct this dependence by measuring τ as a function of (x, y, z). Furthermore, light-collection efficiency variations are also accounted for by measuring the lifetime-corrected signal across the (x, y) plane. The event energy is normalized to the average value at the center of the chamber, where the light-collection efficiency is optimal. The effectiveness of this method is assessed by measuring the energy resolution achieved for this decays. A comparison of the results with theoretical and Monte-Carlo-simulated predictions is provided to demonstrate the near-intrinsic energy resolution achieved. Finally, the application of the method to a number of physics analysis is presented to illustrate the indispensability of signal corrections.

[1] This process is known as attachment

[2] The same is true for the S1 signals, where the light collection efficiency depends on the (x, y, z) position of the event.

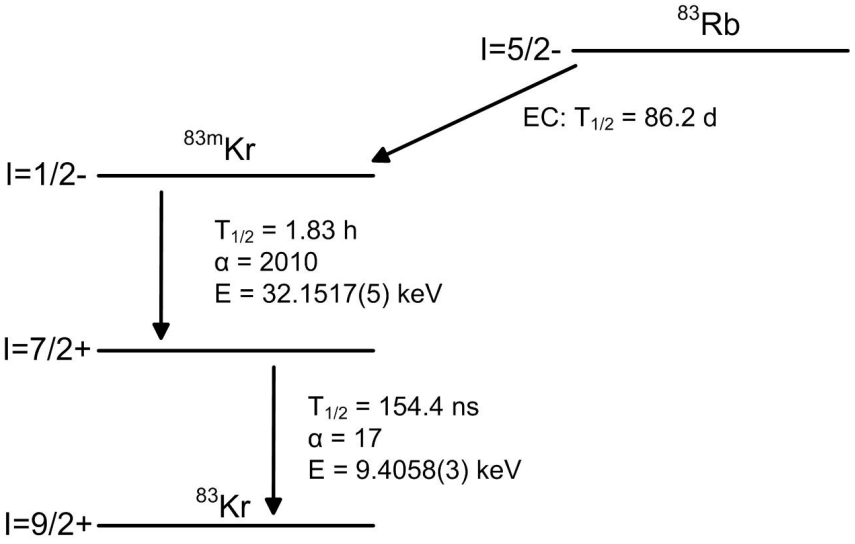

Figure 6.1: ^{83}Kr decay scheme [187].

6.1 Production of $^{83}\mathrm{Kr}^{m}$ events

Figure 6.1 shows the decay scheme of a ^{83}Kr nucleus. The exotic rubidium isotope decays to $^{83}\mathrm{Kr}^{m}$ via electron capture with a half-life of 86.2 days. The krypton then decays to the ground state via two consecutive electron conversions. The decay rate is dominated by the first conversion with a half-life of 1.83 h, while the second has a very short half-life of 154.4 ns. The total released energy sums to 41.5 keV and the ground state of ^{83}Kr is stable. The rubidium source is formed by a number of small (1-mm-diameter) zeolite balls stored in a dedicated section of the gas system. $^{83}\mathrm{Kr}^{m}$ nuclei produced after the electron capture of ^{83}Kr emanate from the zeolite and flow with the gas inside the chamber. A significant contribution to radon emanation from this section of the gas sytem is not expected [186]. The ^{83}Kr source has an intensity of 1 kBq which results, after $^{83}\mathrm{Kr}^{m}$ decays in the gas system, in a rate of ∼100 Hz in the active volume. The rate of $^{83}\mathrm{Kr}^{m}$ decay read-out is limited by the data acquisition system to a rate of about 10 Hz to avoid DAQ crashes.

A $^{83}\mathrm{Kr}^{m}$ decay in the NEXT-White detector results in a point-like energy deposition. The time elapsed between detection of S1 and detection of S2 is the drift time and its measurement, together with the known value of the drift velocity [170], determines the z-coordinate at which the ionization was produced in the active region. The x and y coordinates are obtained using the barycenter algorithm described in Appendix A. The combination of the PMT and SiPM sensor responses yields a full 3D event reconstruction.

6.1.1 Datasets

The data used in this analysis were collected with NEXT-White in Fall 2017. Two Runs are considered. Run 4734 started in October 10, 2017 and collected 2 687 860 events at a trigger rate of 10.5 Hz. The pressure was 7.2 bar, the cathode was held at 28 kV and the gate at 7.0 kV. Run 4841 started in November 16, 2017 and collected 2 993 867 events at a trigger rate of 8.2 Hz. The pressure was 9.1 bar, the cathode was held at 30 kV and the gate at 8.5 kV.

6.2 Method description

To properly measure the energy of an event in NEXT-White it is necessary to correct for two instrumental effects: a) the finite electron lifetime, due to attachment of ionization electrons drifting towards the cathode to residual impurities in the gas, and b) the dependence of the light detected by the energy plane on the (x, y) position of the event. Krypton calibrations provide a powerful tool to measure and correct both effects.

The effect of electron attachment is described using an exponential relation:

$$\mathrm{q(t)} = \mathrm{q_0} e^{-\mathrm{t}/\tau} \tag{6.1}$$

where $\mathrm{q_0}$ is the charge produced by the $^{83}\mathrm{Kr}^m$ decay, t is the drift time, and τ is the electron lifetime. Ideally, attachment can be corrected by measuring a single number. However, in a high pressure detector the lifetime may depend on the position (x, y, z) due to the presence of non-homogenous recirculation of the gas, or concentrations of impurities due to virtual leaks. As discussed in Section 6.4, the dependence of τ with the longitudinal coordinate z in the NEXT-White detector can be neglected, while the dependence of τ with the transverse (x, y) coordinates must be taken into account. This is done using krypton calibrations to produce a *lifetime map* that records the lifetime as a function of (x, y).

Furthermore, $^{83}\mathrm{Kr}^m$ decays can be used to produce a map of energy corrections. This map is needed to properly equalize the energy of events occurring in different locations in the chamber as the light detected by the photomultipliers depends on the (x, y) coordinates of the event even after the lifetime correction. Such dependence comes from the variation of the solid angle covered by the PMTs for direct light and expected acceptance for reflected light as well as from losses in events close to the detector edges. The map cannot be computed analytically due to the multiple reflections of the light inside the light tube and on other internal surfaces of the chamber.

6.3 Data processing and event selection

The detector triggers on S2 signals produced by $^{83}\mathrm{Kr}^m$-like events. The uncorrected energy of the S2 signals depends quite strongly on (x, y, z) given the sizable effect of both the spatial (x, y) corrections and the lifetime. However, as illustrated in Figure 6.2, the range of the total signal detected in photoelectrons[3] (pes) in the sum of the photomultipliers is well defined between $5 \cdot 10^3$ pes and $15 \cdot 10^3$ pes. Events are triggered on the signal of two PMTs located at small radius. Each PMT accounts for roughly 1/12 of the total light recorded. For this reason, the trigger requires that the two central PMTs record a signal in the range 200 to 1500 photoelectrons.

The data are processed up to `kDST` level. Since the S2 signal that triggered the event is centered in the DAQ window (650 μs in this case), S1 signals are searched for between 0 and 620 μs. Shorter drift lengths are discarded to avoid the introduction of biases due to misidentified S1 signals. As shown in Figure 6.3, a single S1 is identified in roughly 70 % of the cases, while two or more S1 candidates are identified in near 10 % of the events and 20 % lack a S1 signal.

[3] An electron emitted from an atom by interaction with a photon. In this case, it refers specifically to an electron produce in the active surface of a photosensor.

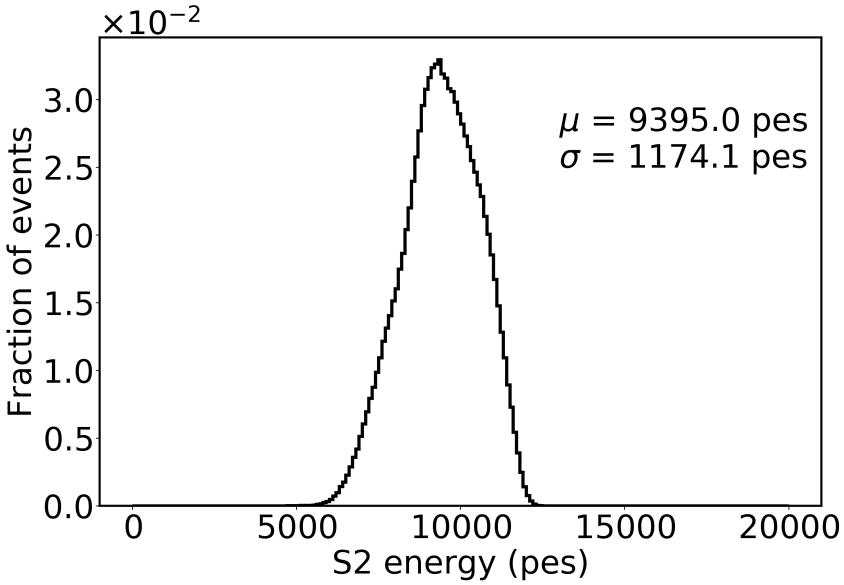

Figure 6.2

The one-S1 sample is dominated by genuine S1 signals, while the sample with two or more S1 include fake signals associated with krypton events happening in the field-cage buffer, or small scintillation signals. Buffer times greater than 620 μs are searched for S2 signals. Most of the time a single S2 candidate is found. Notwithstanding, only events with exactly one S1 and one S2 are accepted for the analysis.

The reconstruction is performed using the barycenter algorithm described in Appendix A. The z coordinated is measured using the ellapsed time between S1 and S2 detection and the drift velocity[4] as detailed in Section 5.3.1. The reconstruction algorithm is tuned by requiring a minimum charge of 10 *pes* in the triggered SiPMs.

Figure 6.4 shows the distribution of events for Run 4734 in the (x, y) plane, which is roughly uniform. The low-statistics pixels (dark blue color) correspond to inoperative or defective SiPMs or to defects in the EL region.

6.4 Lifetime and energy maps

As stated in Section 6.1, under certain conditions (non homogenous recirculation of the gas combined with concentrations of impurities due to virtual leaks), the drift lifetime, τ, may depend on the (x, y, z) position.

In NEXT-White, the dependence of τ with z is found to be negligible. This is illustrated by Figure 6.5, where the dependence of the average residuals, $R_z = \frac{\sum_{xy} r_z}{n_{xy}}$ is plotted as a function of z. R_z is computed by dividing the chamber into n_{xy} bins in the transverse coordinates (x, y) and fitting the function $f(\mathrm{t}) = \mathrm{e}_0 \exp \mathrm{t}/\tau$ to the detected signal versus drift time (the raw z coordinate) in each (x, y) bin. The pull in each bin for each fit is then calculated as $r_z = \frac{e_\mathrm{t} f(\mathrm{t})}{\sigma}$.

[4]The drift velocity is measured using also $^{83}\mathrm{Kr}^m$ data, as shown in [170].

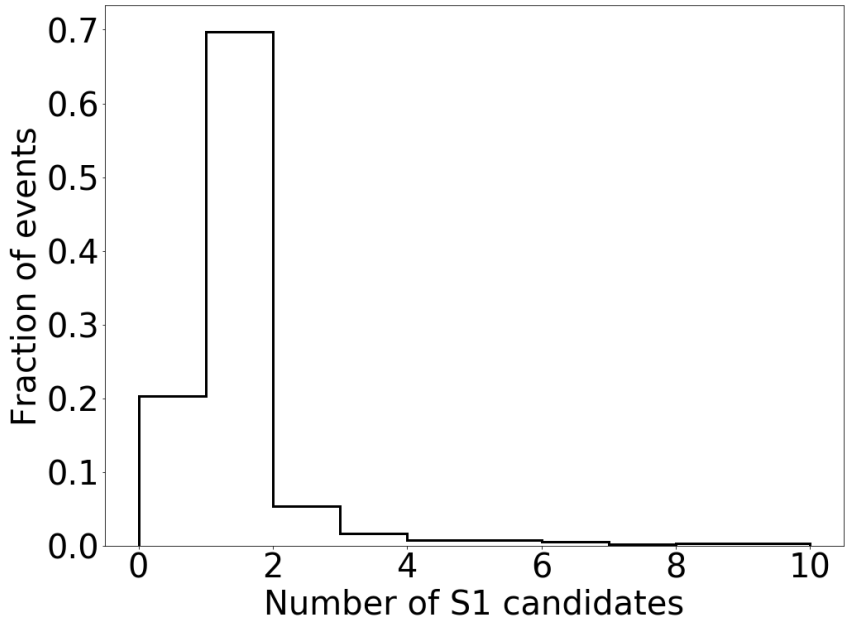

Figure 6.3: Distribution of the number of S1 candidates found in Run 4734 of the NEXT-White detector. The peak finding algorithm was tuned to search for S1 signals in the [0, 620] μs time range with a *stride* of 100 ns. The width of these signals was required to be between 125 ns and 500 ns.

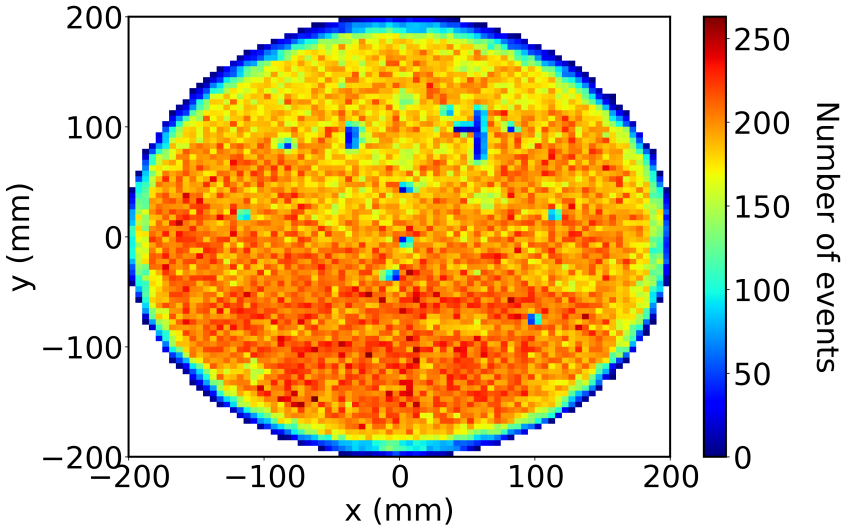

Figure 6.4: Distribution of events in the (x, y) plane for Run 4734 of the NEX-White detector. A similar homogeneous distribution is found in Run 4841.

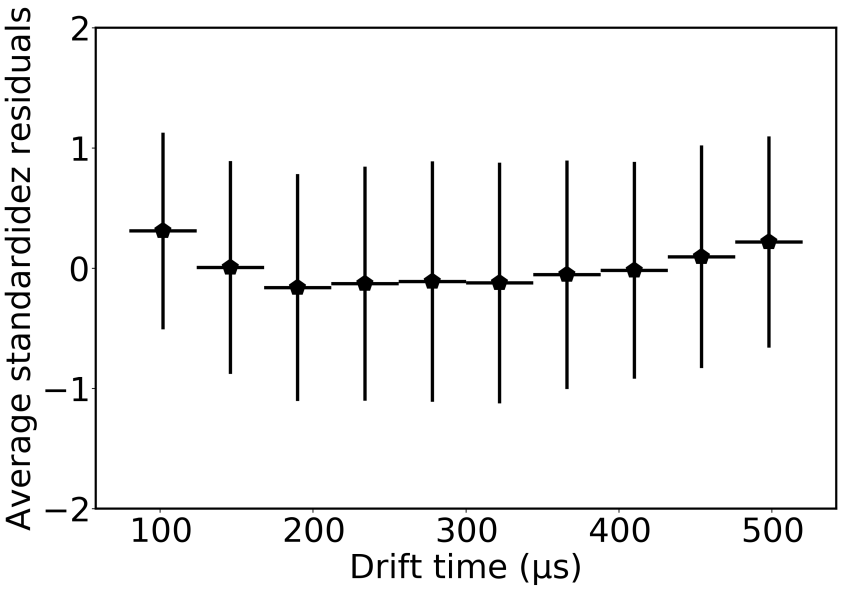

Figure 6.5: Average electron-lifetime (τ) residuals (R_z) as a function of z for Run 4734 of the NEXT-White detector. The small deviations of R_z from 0 indicate that τ is practically constant along the longitudinal coordinate.

The distribution of these values over the (x, y) plane for each z bin is then fitted with a Gaussian and the mean value taken as R_z. As can be seen in Figure 6.5 the dependence of this value with z is very small, justifying the hypothesis that the τ does not depend on z. The data correspond to Run 4734, but Run 4841 shows the same behavior.

On the other hand, the lifetime is found to depend on (x, y) for Run 4734. This effect is illustrated in Figure 6.6 where lifetime fits for two regions are shown. The left panel corresponds to a region near the center, defined by x = [0, 50]mm, y = [0, 50]mm and the right panel to one in the upper edge, defined by x = [120, 150]mm, y = [120, 150]mm. Both fits yield a good χ^2/ndof (0.9 for the first fit, 1.0 for the second), but considerably different lifetimes of $(1789 \pm 4)\mu$s (near the center of the chamber) and $(2049 \pm 44)\mu$s (near the top of the chamber).

This dependence can be taken into account and corrected for using large-statistics $^{83}\mathrm{Kr}^m$ runs to produce a *lifetime map*. The map is built by dividing the chamber in 60×60 (x, y) bins, each of edge 6.7 mm, and fitting for the lifetime in each bin. The number of bins is chosen to maximize granularity while still keeping enough data in each bin so that the statistical uncertainties of the fits are small. The resulting maps are shown in Figure 6.7 for Run 4734. The fits result in a lifetime parameter and a prediction of e_0 for each bin and the corresponding uncertainties. Thus, the map displayed in the top-left panel is essentially a signal map, where the effect of the lifetime has been factored out, showing the dependence of the event energy on (x, y). The map is rather uniform in the central region, with the exception of a *crater* centered around (x, y) $\simeq (50, 50)$ mm whose origin we attribute to a few SiPM boards with degraded reflectance, and fall abruptly at large radius, as the solid angle covered by the PMTs falls to zero. The lifetime map is shown in the bottom-left panel. A region of longer lifetime (close to 2 ms) appears at large positive y, near the top of the chamber (the average lifetime in the center of the chamber is around 300 μs smaller). While this feature is unexpected, study has shown that the flow of the gas through the detector active volume can be turbulent causing regions to have different concentrations of impurities. As can be seen in Figure 6.8, which shows the same

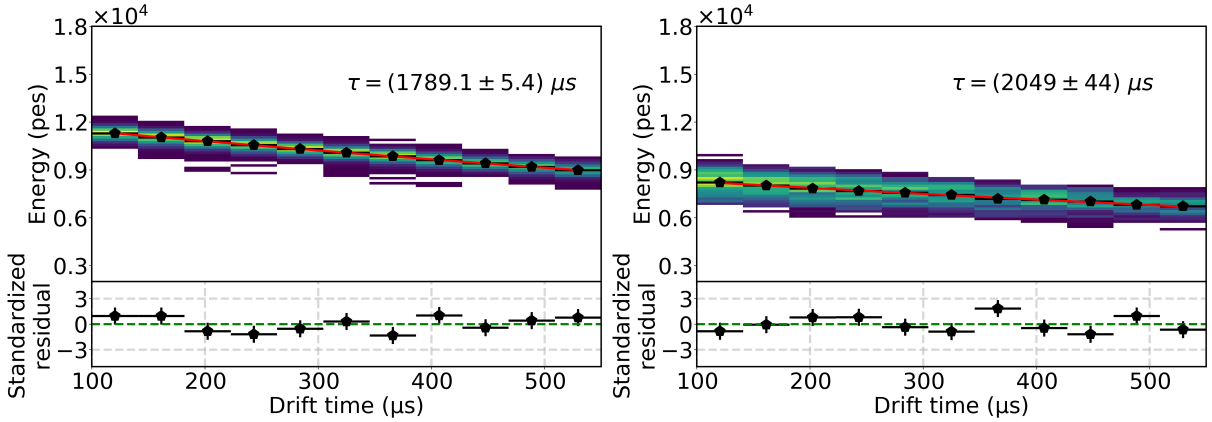

Figure 6.6: Exponential fits to the distribution of $^{83}Kr^{m}$ integrated signal as a function of the drift time in two different regions of the NEXT-White chamber. In the region defined by x = [0, 50] mm, y = [0, 50] mm (left panel) the lifetime is (1789 ± 5) μs, whilst in the region defined by x = [120, 150] mm, y = [120, 150] mm (right panel) the lifetime is (2049 ± 44) μs. Color indicates number of events, black lines averages and the red line the best fit line.

maps for Run 4841, taken at 9.1 bar the signal map still shows the *crater* in the same position, but the lifetime map is uniform, indicating that, as the gas is recirculated and cleaned, these inhomogeneities are gradually removed.

The quality of the fits used to extract the lifetime maps as well as the success of their application (see Figure 6.9 and the clear Gaussian form of the corrected spectra) indicates that the effect is physical and the correction method valid. The crucial point is that, while it is difficult to understand the complex physics that may lead to variable lifetime maps, $^{83}Kr^{m}$ calibrations permit a correction for those effects.

6.5 Refined energy map

Correcting event by event for the fitted lifetimes extracted using the method described in Section 6.4 yields a signal map with the residual variations not related to attachment. The map can be further refined by dividing the (x, y) plane into smaller bins and computing for each bin the sum of the PMT energies corrected by lifetime. The energy in each bin can then be fitted to a Gaussian distribution. An example is shown in Figure 6.9. The signal correction factor f(x, y) is simply the inverse of the mean of the gaussian distribution in each (x, y) bin, normalized to a constant factor which can be chosen as the maximum energy bin or the average at the center of the chamber.

Figure 6.10a and Figure 6.10b show the signal map for Run 4734 and Run 4841, respectively. As stated above, both maps are statistically compatible. These maps are compared with the signal map computed using Monte Carlo data in Figure 6.10c. Notice that the behavior of the map at large radius, largely due to solid angle effects and edge effects is well predicted by the Monte Carlo, but not the presence of the *crater*, which can only be corrected using calibration data. The uncertainties, as shown in Figure 6.11, are very small (of the order of 0.3 %) introducing a small residual error in the energy correction, which is negligible compared with

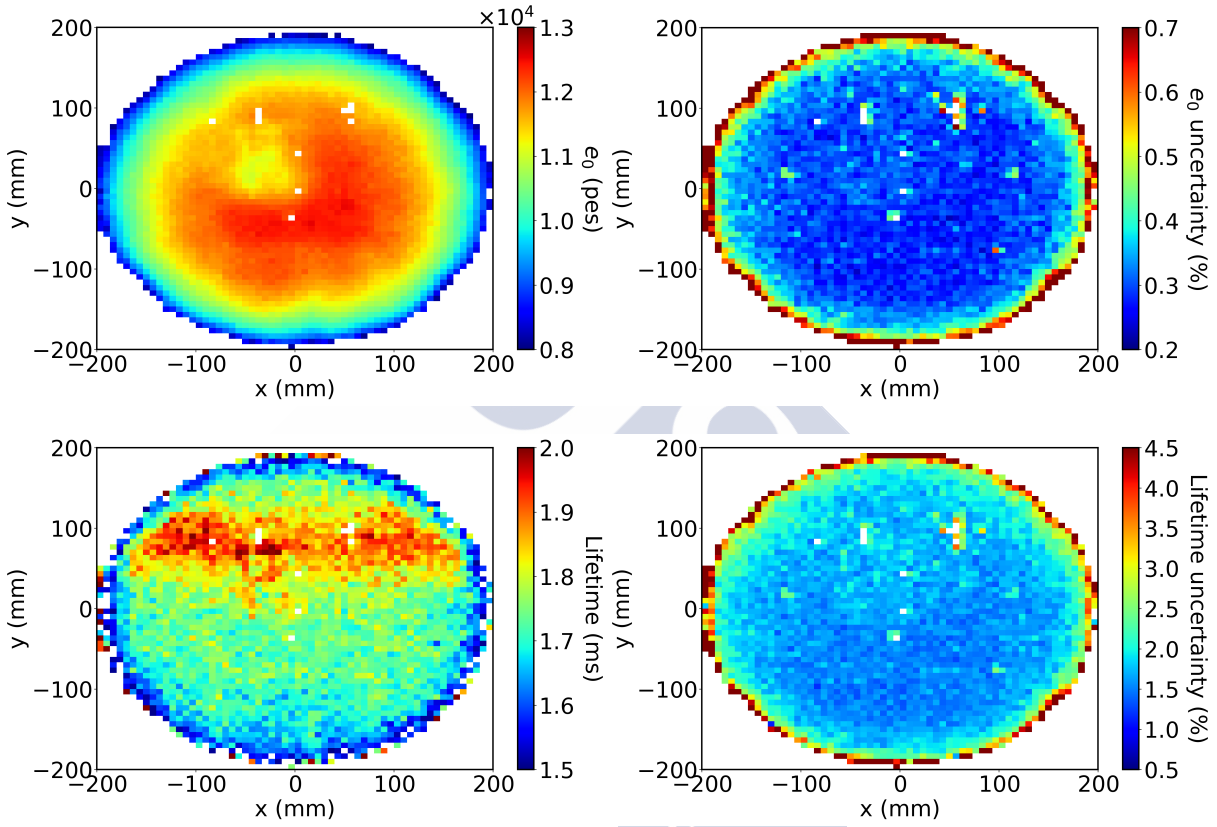

Figure 6.7: Maps obtained by fitting the lifetime as a function of (x, y) for Run 4734. The predicted signals for z = 0 (left panel) and their uncertainties (right panel) are displayed in the top row, while the lifetimes (left panel) and their uncertainties (right panel) are shown in the bottom row. A clear dependence of the lifetime on (x, y) is observed. The uncertainty in the energy scale is of the order of 0.2 %, making a sub-dominant contribution to the energy resolution at 41.5 keV. On the other hand, the uncertainty in the lifetime value is of the order of the 1 % and cannot be neglected for the interpretation of the final value of the energy resolution.

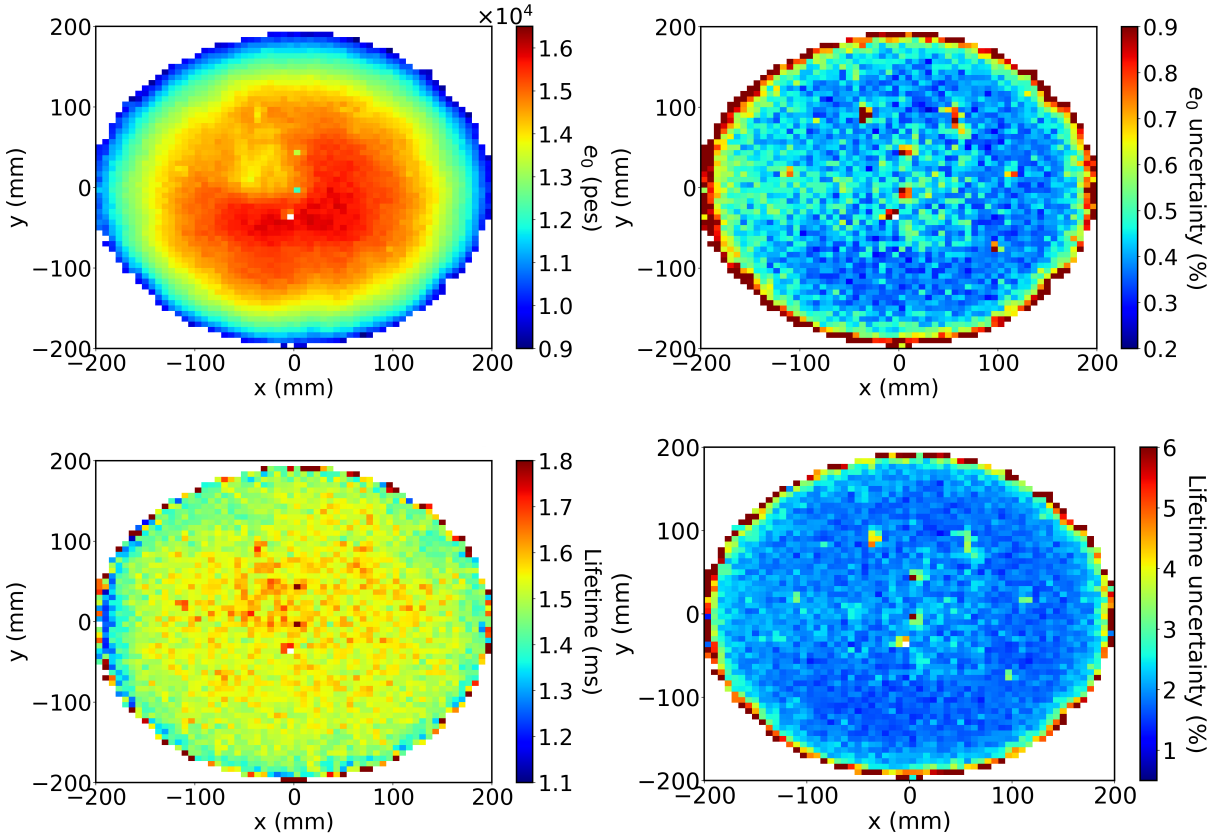

Figure 6.8: Maps obtained by fitting the lifetime as a function of (x, y) for Run 4841. The signal map is statistically compatible with the one obtained with Run 4734, while the lifetime map has become homogeneous.

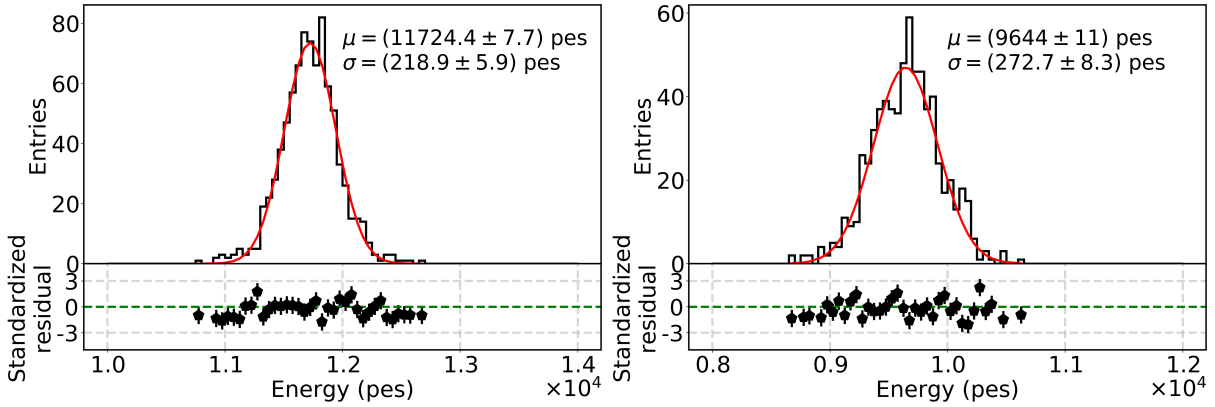

Figure 6.9: Gaussian fits to the lifetime-corrected energy for Run 4734 in two opposite regions of the NEXT-White chamber. In the region defined by x = [0, 10] mm, y = [0, 10] mm (left panel), the fit yields a mean value for the energy of (11724 ± 8) *pes*, with $\chi^2/\text{ndof} = 0.94$, whilst in the region defined by x = [120, 130] mm, y = [120, 130] mm (right panel), the fit yields a mean value for the energy of (9652 ± 11) *pes*, with $\chi^2/\text{ndof} = 1.03$.

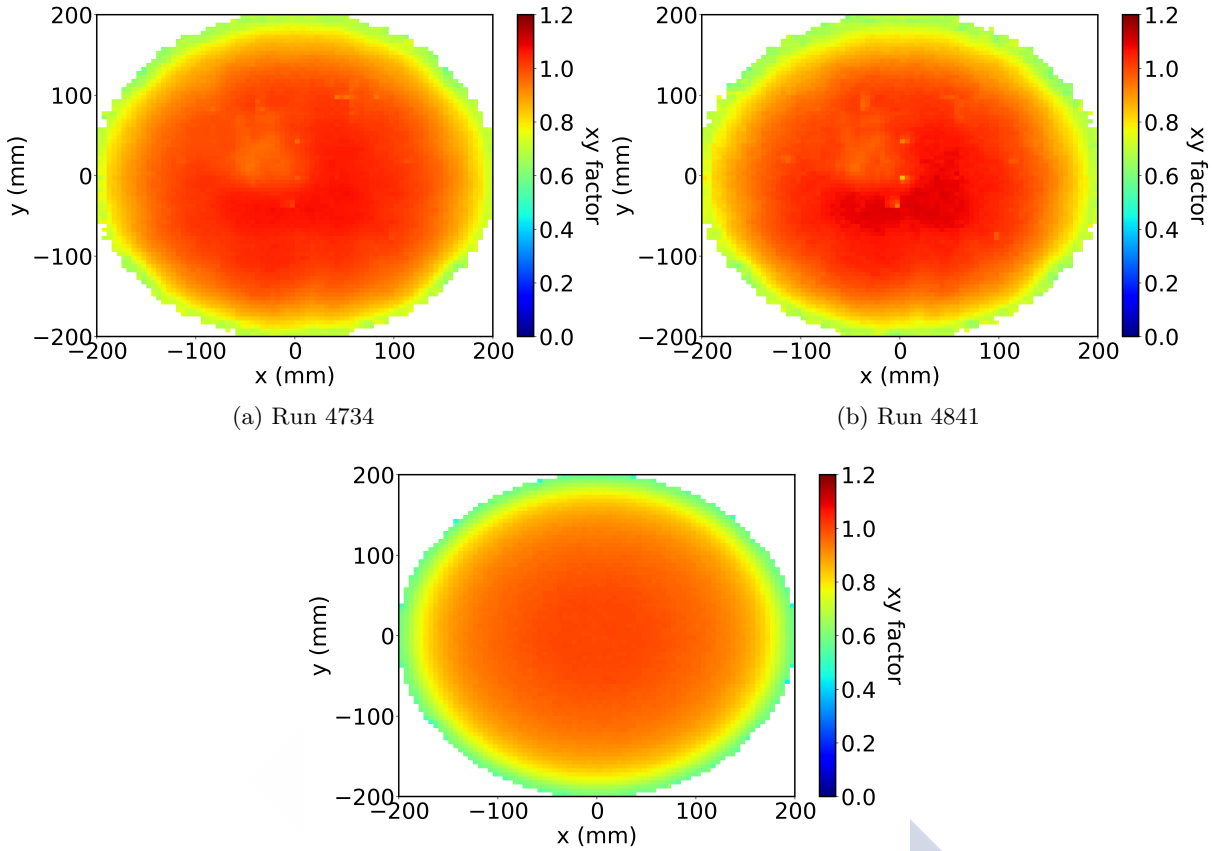

(a) Run 4734

(b) Run 4841

(c) Monte Carlo

Figure 6.10: Normalized signal map for Run 4734 (top left panel), for Run 4841 (top right panel) and for Monte Carlo data (bottom panel).

the residual error introduced by the lifetime correction, except at large radius where the angular coverage of the PMTs falls steeply.

6.6 Energy resolution

In order to estimate the energy resolution for point-like energy deposits in NEXT-White, the $^{83}\mathrm{Kr}^{m}$ data are divided in two samples. The *correction* sample is used to compute the lifetime and geometry correction maps, which are then applied to the data in the *measurement* sample. The corrected signal of the PMT sum is then fitted to estimate the energy resolution.

Even after corrections, the energy resolution is expected to depend on both the radial and the longitudinal coordinates. The dependence with the radius is related with the decreasing solid angle coverage, which means that PMTs record less light (thus larger fluctuations) for events happening at larger r. The dependence with z is related with the loss of secondary electrons caused by attachment. A smaller number of electrons is associated with larger fluctuations and correction factors, which worsens the energy resolution as described in Section 3.1.2.

Figure 6.12a shows the dependence of the energy resolution as a function of r for events

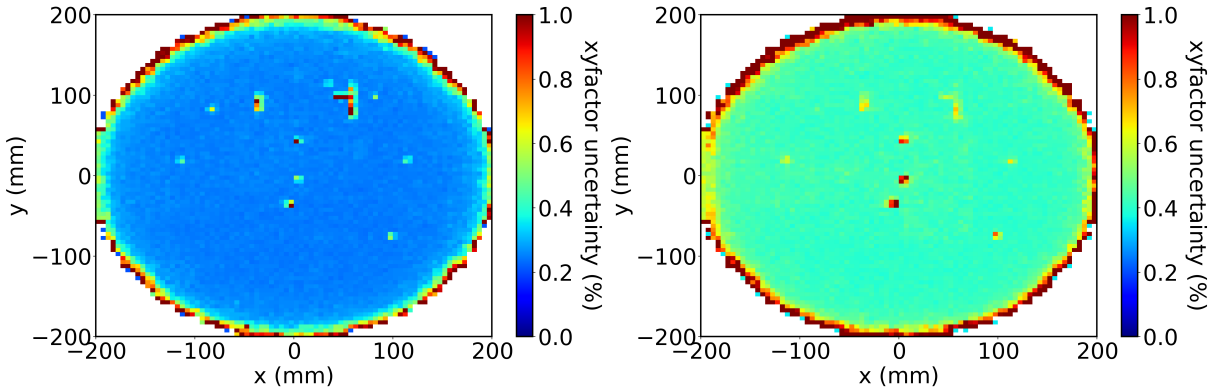

Figure 6.11: (x, y) map of the relative uncertainty in the correction factor for Runs 4734 (left) and 4841 (right). The uncertainties are of the order of 0.3 % and 0.4 %, respectively, and therefore introduce a sub-dominant contribution to the energy resolution measurement.

with z < 200mm (black squares data, red circles Monte Carlo), where it is possible to define 3 regions. A fiducial region up to r < 150mm, where the resolution is roughly flat, at around 4 % FWHM. The resolution stays below 4.5 % FWHM, for r < 175mm, and degrades rapidly for larger radial values. Since the total radial coverage of the chamber is 200 mm, this implies that an extended fiducial region of acceptable resolution extending up to 175 mm can be defined for physics analysis. The PMT coverage improves as detector radial dimensions increases, since the region of low solid angle coverage corresponds essentially to the last PMT ring. Taking this into consideration, a considerably smaller reduction in fiducial volume is expected for NEXT-100 since only the last 10 mm to 15 mm of the total radius need to be removed.

Figure 6.12b shows the dependence of the energy resolution as a function of z for events with r < 100mm (black squares), which degrades with increased drift, although it stays always below 5 % FWHM. The obvious implication is that long lifetimes are a must for TPC detectors striving to achieve excellent energy resolution. Figure 6.12b also shows the energy resolution for Monte Carlo events (red circles). The effect of the lifetime dependence with (x, y), as measured in data, has been also simulated. The agreement between data and Monte Carlo results is good, indicating that the main dependencies of the resolution are the geometrical effects (lower coverage at a larger radius) and the finite electron lifetime (worse resolution at longer drift times). The data corresponds to Run 4734, but the same conclusions are extracted from Run 4841.

Figure 6.13a illustrates the energy resolution measured with Run 4734 (at a pressure of 7.2 bar). The data are fitted to a gaussian plus a 2nd-degree polynomial to take into account tails due to residual background events[5]. The fit yields an energy resolution of (4.55 ± 0.01) % FWHM in the full NEXT-White volume. A naive $E^{-1/2}$ extrapolation to $Q_{\beta\beta}$ yields (0.592 ± 0.001) %. Figure 6.13b corresponds to the data contained in a fiducial region defined by a radius smaller than 150 mm and z smaller than 150 mm. The radial cut ensures optimal geometrical coverage and the z cut minimizes the residual errors due to lifetime fluctuations, which increase with z. The fit yields (3.88 ± 0.04) %, extrapolating to (0.504 ± 0.005) % at $Q_{\beta\beta}$. This value is reasonably close to the best resolution expected in NEXT-White (Section 3.1.2), confirming the excellent capabilities of the technology and the good working conditions of the chamber.

[5]Here the term background is used very broadly. It covers small energy deposits, $^{83}Kr^{m}$ decays with wrong S1 identification and poorly reconstructed events.

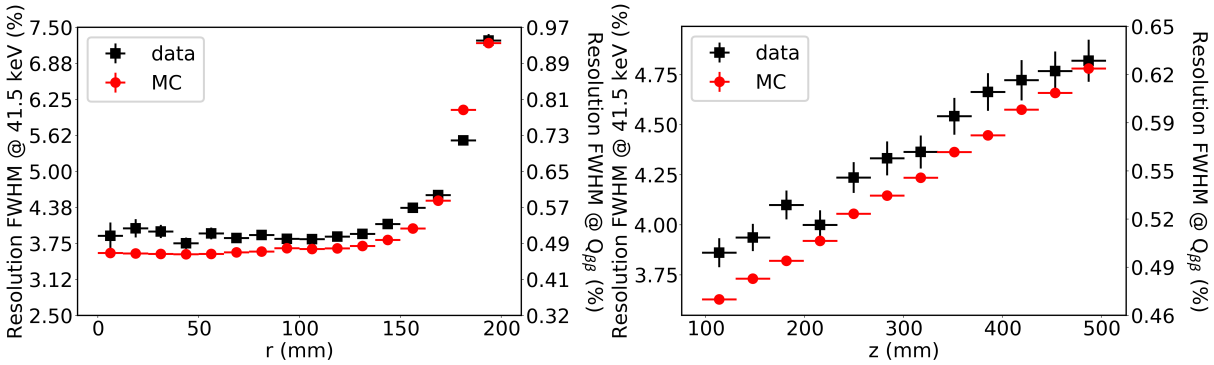

(a) (b)

Figure 6.12: Left panel: dependence of the resolution with r for events at short drift time (z < 200mm). Right panel: dependence of the resolution with z for events near the center (r < 100mm). The data correspond to Run 4734, but similar results are obtained for Run 4841.

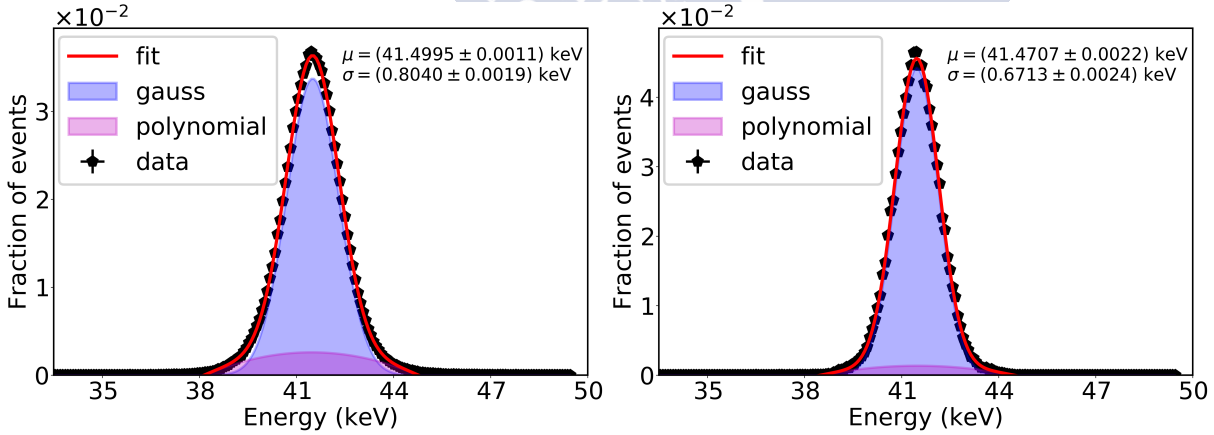

(a) Full volume (b) Fiducial volume

Figure 6.13: Corrected energy distribution for $^{83}Kr^{m}$ events in the full volume of the NEXT-White TPC (left), and in a restricted fiducial volume (right) defined by r < 150 mm and z < 150 mm, for Run 4734. The fits yield energy resolutions of (4.55 ± 0.01) % FWHM and (3.88 ± 0.04) %, respectively.

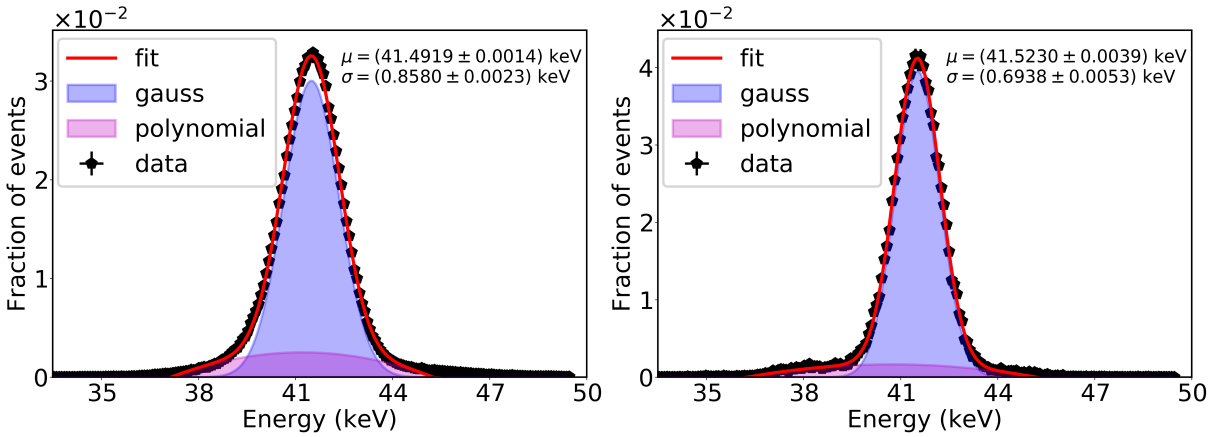

(a) Full volume

(b) Fiducial volume

Figure 6.14: Corrected energy distribution for $^{83}\mathrm{Kr}^{m}$ events in the full volume of the NEXT-White TPC (left), and in a restricted fiducial volume (right), defined by r $<$ 150 mm and z $<$ 150 mm, for Run 4841. The fits yield energy resolutions of (4.86 ± 0.01) % FWHM and (3.93 ± 0.03) %, respectively.

The same procedure is applied to Run 4841 (at a pressure of 9.1 bar) in Figure 6.14. The fit yields an energy resolution of (4.86 ± 0.01) % FWHM in the full NEXT-White volume (left panel). A naive $E^{-1/2}$ extrapolation to $Q_{\beta\beta}$ yields (0.631 ± 0.002) % FWHM. The fit in the right panel corresponds to the data contained in the fiducial region defined above. The fit yields (3.93 ± 0.03) % FWHM ((0.510 ± 0.004) % FWHM at $Q_{\beta\beta}$), similar to the values obtained for Run 4734, and confirming that resolution for point-like energy deposits scales well with pressure.

6.6.1 Systematic uncertainties

The systematic uncertainties in the energy resolution have also been estimated. The main sources of uncertainty are the lifetime and geometrical corrections, the fit range and the model used to describe the tails of the energy spectrum.

The systematic uncertainties of the lifetime and geometrical corrections have been estimated by measuring the variation of the energy resolution when those factors are shifted by $\pm n\ \sigma$ around their optimal value. The variation of the energy resolution when fluctuating the lifetime map is shown in Figure 6.15 for both Runs. The effect is well described by a second-degree polynomial. The value of the polynomial at $\pm 1\sigma$ is taken as the contribution to the systematic uncertainty of the lifetime map.

An analogous method is used to measure contribution of the geometry map to the energy resolution. The data and the fit to a second-degree-polynomial is shown in Figure 6.16.

The systematic uncertainty associated to the bin size has been estimated as the maximum difference of the resolution when varying the bin size, within a sensible range, of the energy spectrum histogram. This contribution has been found to be minimal, as shown in Figure 6.17.

The measurement of the energy resolution depends also on the range chosen to perform the fit. Figure 6.18 displays this dependence for both Runs. The contribution to the sytemetic

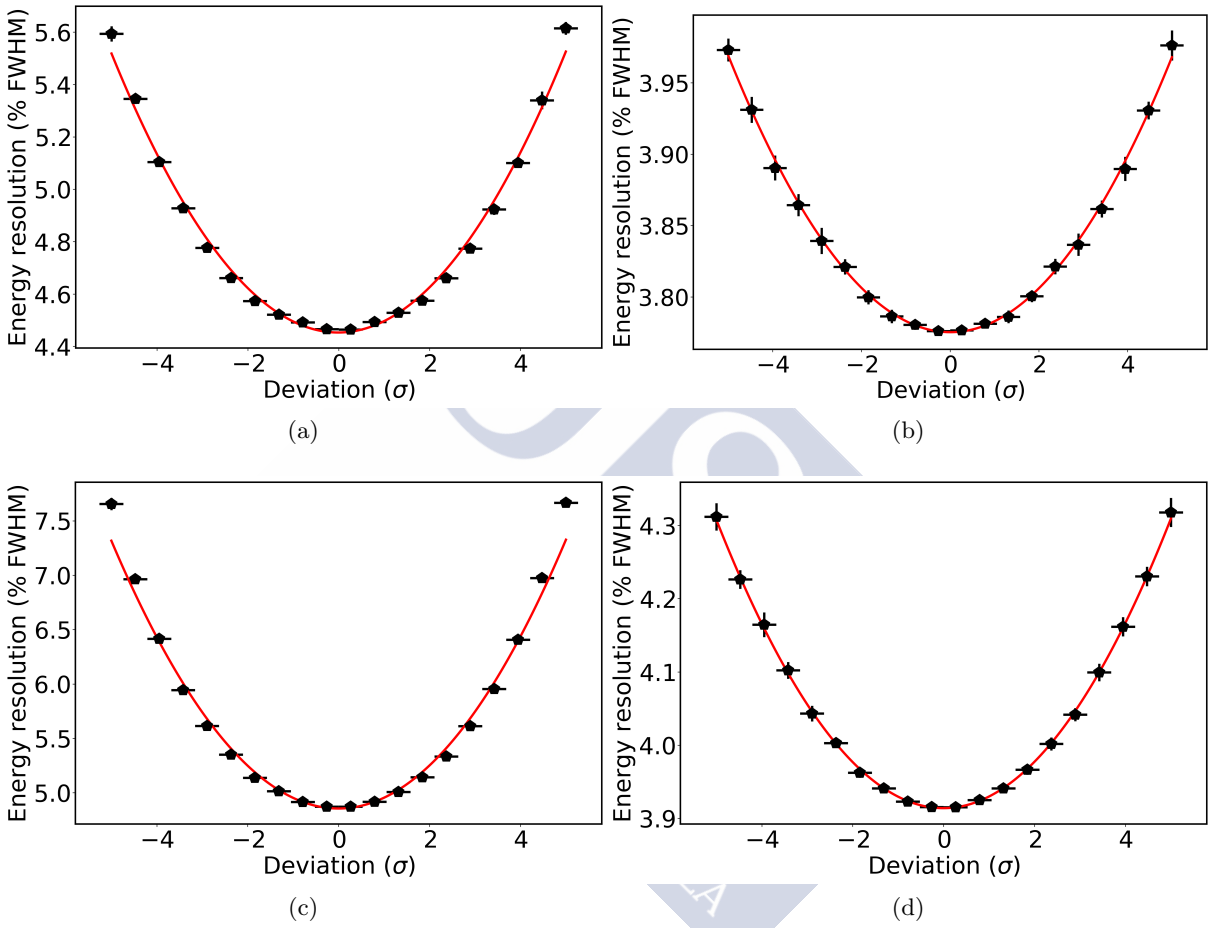

Figure 6.15: Contribution of the lifetime map to the systematic uncertainty of the energy resolution measurement. The values in the lifetime map are randomly shifted by $\pm n$ σ. The uncertainty is taken as the difference between the resolution at ± 1 σ and the optimal value. The top row corresponds to Run 4734 and the bottom row to Run 4841. The left column shows the analysis performed on the full volume and the right column on the fiducial volume defined by r $<$ 150 mm and z $<$ 150 mm.

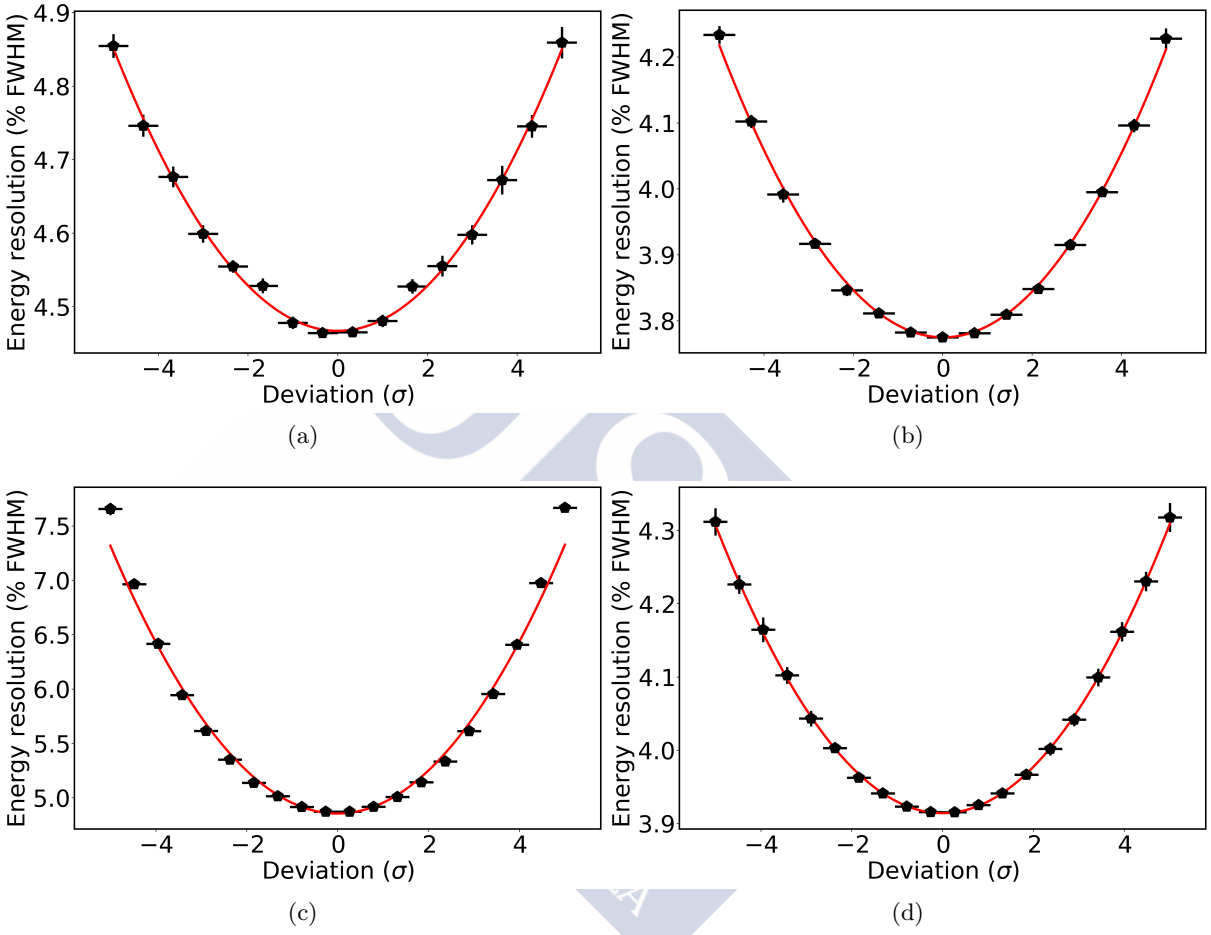

Figure 6.16: Contribution of the geometry map to the systematic uncertainty of the energy resolution measurement. The values in the geometry map are randomly shifted by $\pm n\ \sigma$. The uncertainty is taken as the difference between the resolution at $\pm 1\ \sigma$ and the optimal value. The top row corresponds to Run 4734 and the bottom row to Run 4841. The left column shows the analysis performed on the full volume and the right column on the fiducial volume defined by r $<$ 150 mm and z $<$ 150 mm.

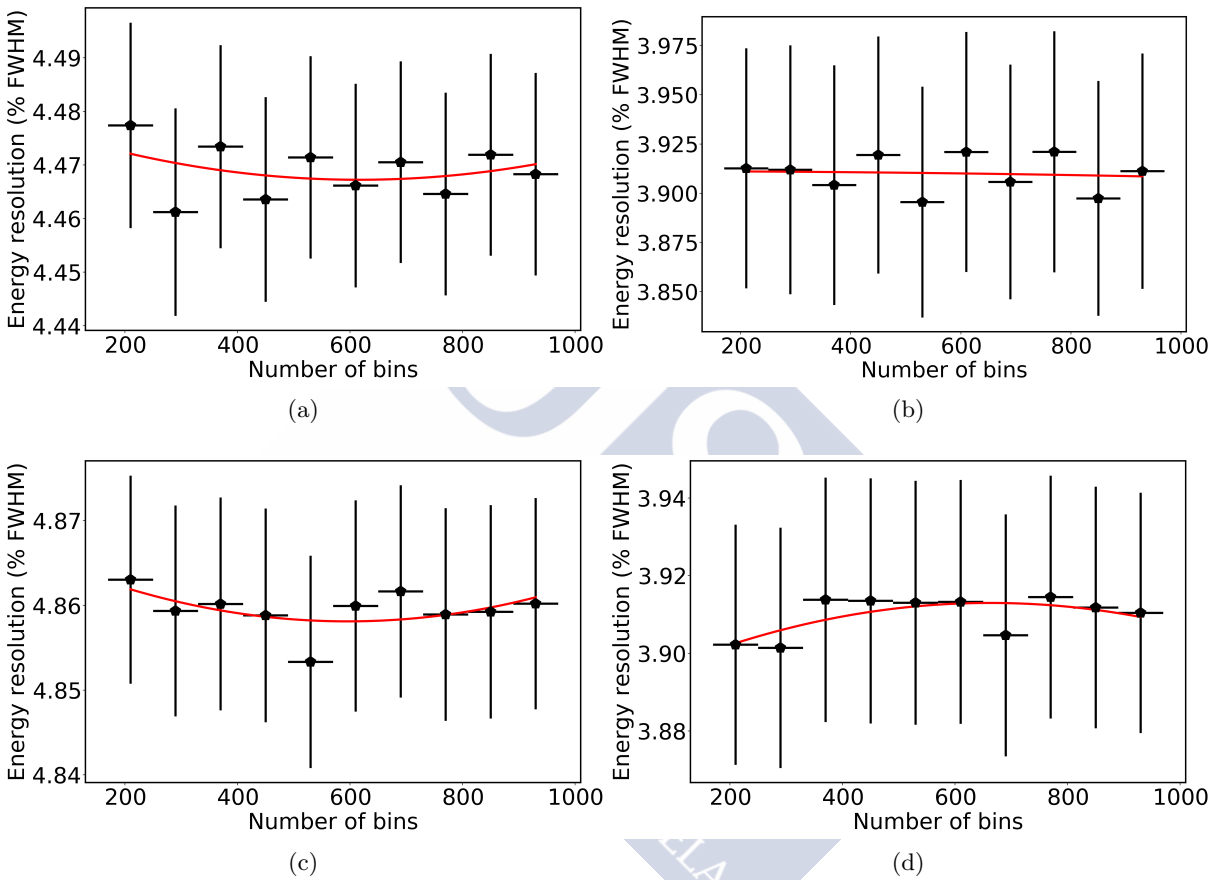

Figure 6.17: Contribution of the binning of the energy spectrum to the systematic uncertainty of the energy resolution measurement. The number of bins in a fixed-range histogram has been studied for different values. The uncertainty is taken as the maximum difference between the resolution of the fits with an acceptable goodness of the fit. The top row corresponds to Run 4734 and the bottom row to Run 4841. The left column shows the analysis performed on the full volume and the right column on the fiducial volume defined by r $<$ 150 mm and z $<$ 150 mm.

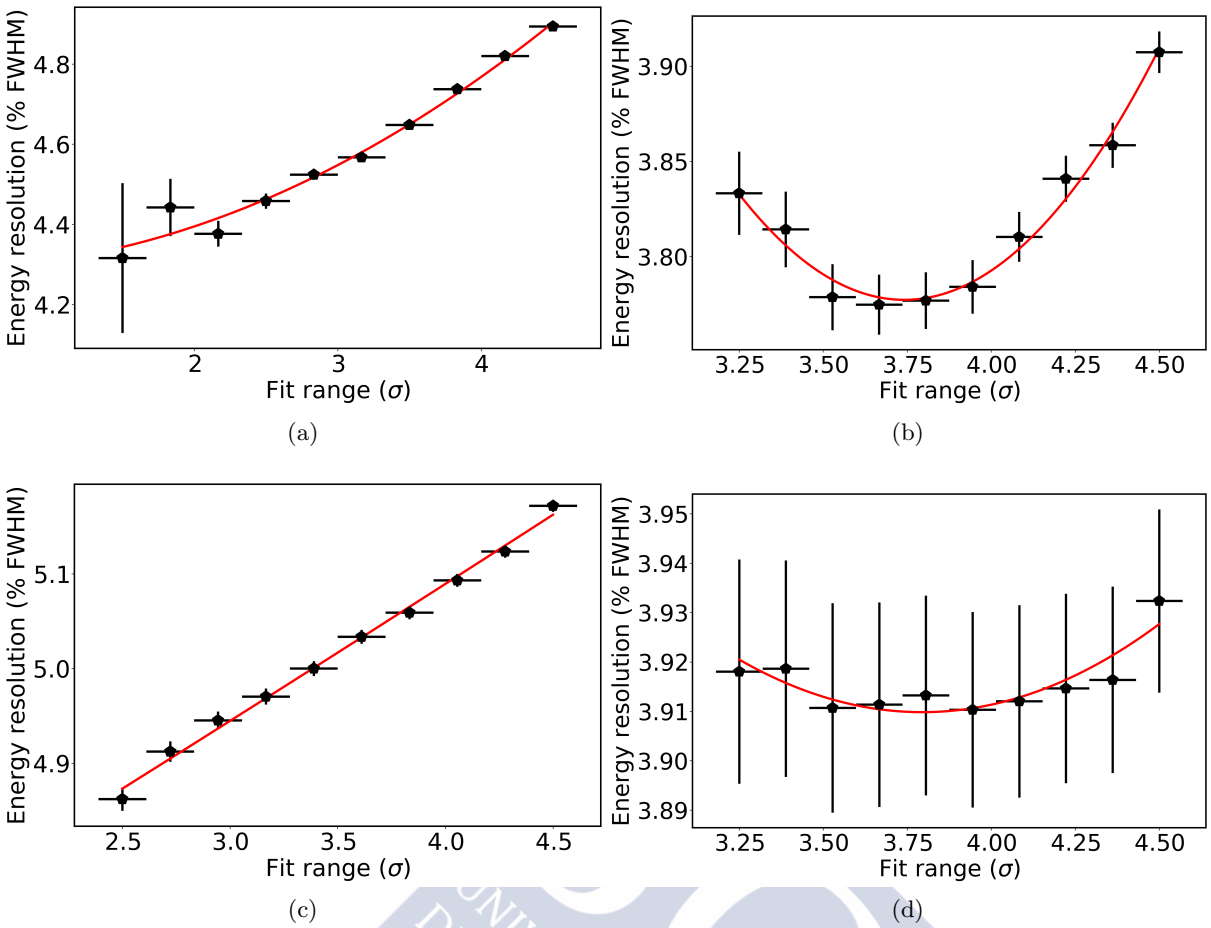

Figure 6.18: Contribution of the fit range of the energy spectrum to the systematic uncertainty of the energy resolution measurement. The fit has been performed for different energy ranges with respect to the peak value. The uncertainty is taken as the maximum difference between the resolution of the fits with an acceptable goodness of the fit. The top row corresponds to Run 4734 and the bottom row to Run 4841. The left column shows the analysis performed on the full volume and the right column on the fiducial volume defined by r $<$ 150 mm and z $<$ 150 mm.

uncertainty is defined as the maximum variation among the fits that yield an acceptable fit.

In order to estimate the uncertainties related to the fit model, different functions have been considered to describe the tails of the energy distribution. The energy resolution measurements for the different models are shown in Figure 6.19. The maximum difference of the resolution among those models and fits that resulted in an acceptable goodness of the fit defined the contribution to the energy resolution systematic uncertainty.

Table 6.1 summarizes the contributions to the systematic uncertainty of the energy resolution considering the full and fiducial volumes for both Run 4734 and Run 4841. The total systematic uncertainty, adding the different contributions in quadrature, is 0.324 % (0.112 %) for Run 4734 and 0.246 % (0.148 %) for Run 4841 for the full (fiducial) volume.

For the 7.2 bar Run, we get a final estimate of the energy resolution of (4.553$\pm$0.010 (stat.)$\pm$ 0.324 (sys.)) % FWHM in the full volume and (3.804 $\pm$ 0.013 (stat.) $\pm$ 0.112 (sys.)) % FWHM

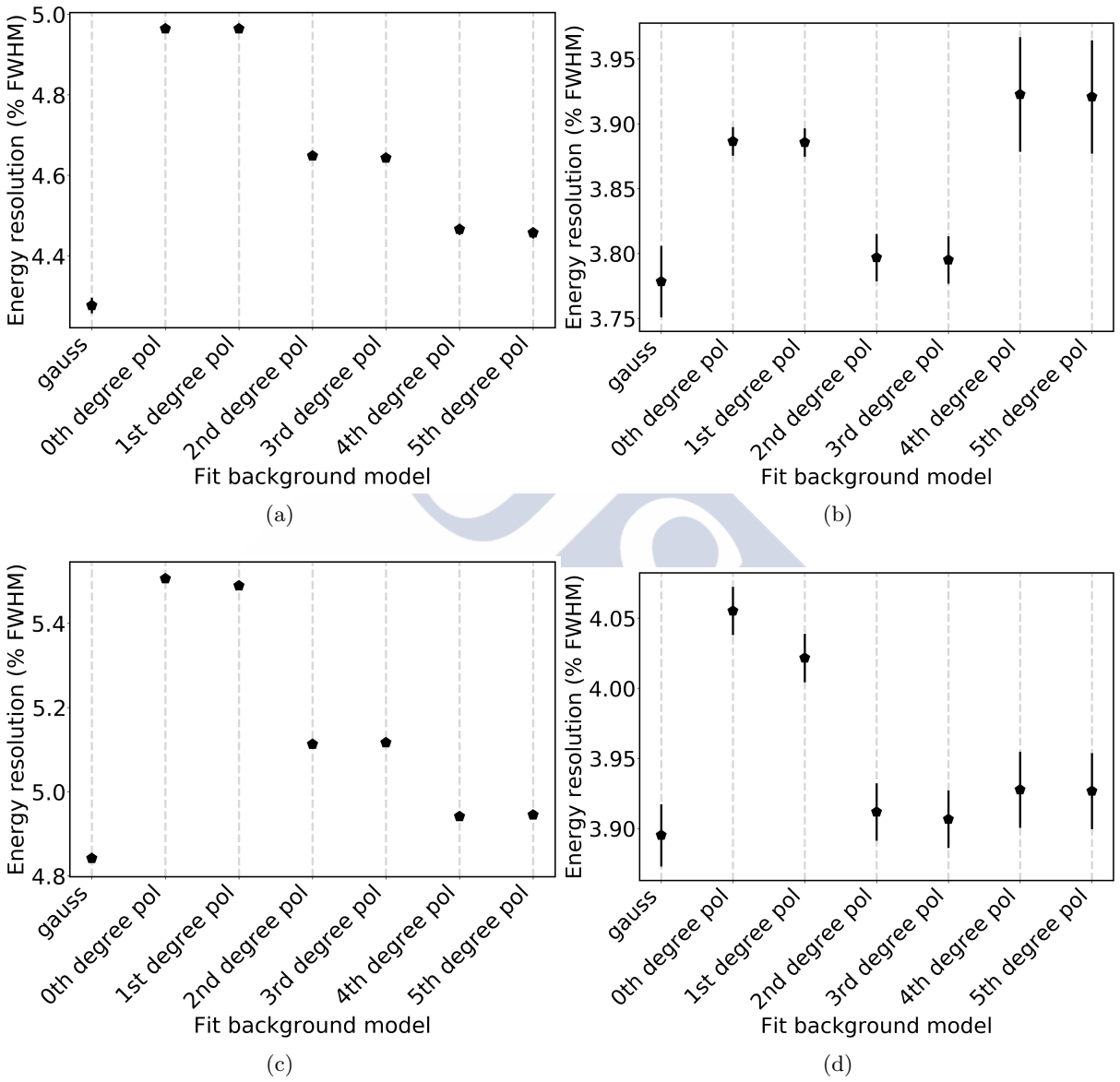

Figure 6.19: Contribution of the fit model to the systematic uncertainty of the energy resolution measurement. The fit has been performed using different functions to model the tails of the energy spectrum. The uncertainty is taken as the maximum difference between the resolution of the fits with an acceptable goodness of the fit. The top row corresponds to Run 4734 and the bottom row to Run 4841. The left column shows the analysis performed on the full volume and the right column on the fiducial volume defined by r $<$ 150 mm and z $<$ 150 mm.

	Run 4734		Run 4841	
	Full	Fiducial	Full	Fiducial
Lifetime map	0.044 %	0.008 %	0.100 %	0.016 %
Geometry map	0.015 %	0.018 %	0.030 %	0.031 %
Fit range	0.265 %	0.064 %	0.143 %	0.011 %
Histogram binning	0.002 %	0.003 %	0.002 %	0.011 %
Background model	0.182 %	0.090 %	0.172 %	0.143 %
Total	0.324 %	0.112 %	0.246 %	0.148 %

Table 6.1: Main contributions to the systematic uncertainty in the measurement of the energy resolution at 41.5 keV of the NEXT-White detector.

in the fiducial volume. For the 9.1 bar Run, on the other hand, an energy resolution of $(4.860 \pm 0.013\ (\text{stat.}) \pm 0.246\ (\text{sys.}))$ % FWHM is achieved in the full volume and improved to $(3.93 \pm 0.03\ (\text{stat.}) \pm 0.148\ (\text{sys.}))$ % FWHM in the fiducial volume.

A $E^{-1/2}$ extrapolation yields energy resolutions at $Q_{\beta\beta}$ in the full volume of $(0.5916 \pm 0.0014\ (\text{stat.}) \pm 0.0421\ (\text{sys.})))$ % FWHM and $(0.6314 \pm 0.0017\ (\text{stat.}) \pm 0.0320\ (\text{sys.}))$ % FWHM for the 7.2 bar and 9.1 bar Runs, respectively. Similarly, for the fiducial volume we get $(0.4943 \pm 0.0017\ (\text{stat.}) \pm 0.0146\ (\text{sys.}))$ % FWHM for the 7.2 bar Run and $(0.510 \pm 0.004\ (\text{stat.}) \pm 0.019\ (\text{sys.}))$ % FWHM for the 9.1 bar Run.

6.7 Application of the method to high energy electrons

As stated in Section 2.5, energy resolution is an indispensable feature of a detector for $\beta\beta$ decay. Signal fluctuations introduce contributions to the energy resolution as described in (Equation 3.12). On top of that, signal losses deteriorate the energy resolution by introducing non-gaussian, assymetric *tails* to the energy spectrum. The geometrical and lifetime effects described in previous sections introduce large signal losses and, hence, they need to be corrected.

Figure 6.20 shows the comparison between the uncorrected, the lifetime-corrected, the geometry-corrected and the fully-corrected energy spectra for Run 4734. The mono-energetic underlying nature of the data can only be recognized in the fully-corrected spectrum. This emphasizes the necessity for this method, as any physics analysis performed with uncorrected would be highly compromised.

The main physics analysis performed with the NEXT-White detetor rely on the accuracy and robustness of the calibration method described in this chapter. The background contributions from ^{222}Rn emmanation have been studied in [186]. In this paper, the energy of α particles interacting in the gas are corrected using the geometrical map from a previous $^{83}\text{Kr}^m$ Run. The lifetime was extracted in this case from the same α interactions[6] without an (x, y) dependence. The corrected S2 energy is combined with the independently-corrected S1 signal to produce the energy spectrum shown in Figure 6.21. The yields of the different α-emitting isotopes are measured by fitting to a multiple-gaussian model which are ultimately used to determine the identity of the background sources.

[6] α particles produce also short signals and can be considered point-like and therefore can be used to measure the chamber properties accurately.

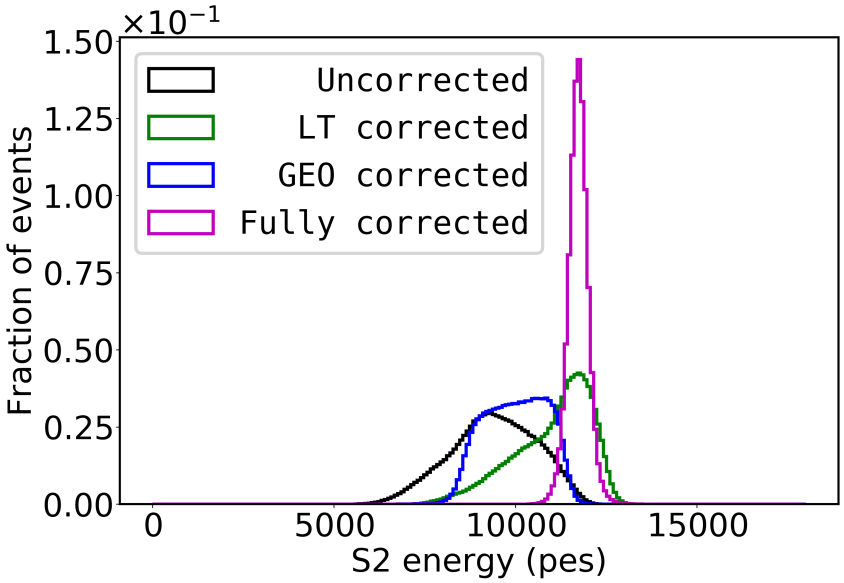

Figure 6.20: Comparison between the energy spectrum for Run 4734 obtained with uncorrected, lifetime-corrected, geometry-corrected and fully-corrected data. This figure evidences the importance of applying full, accurate corrections to perform physics analyses.

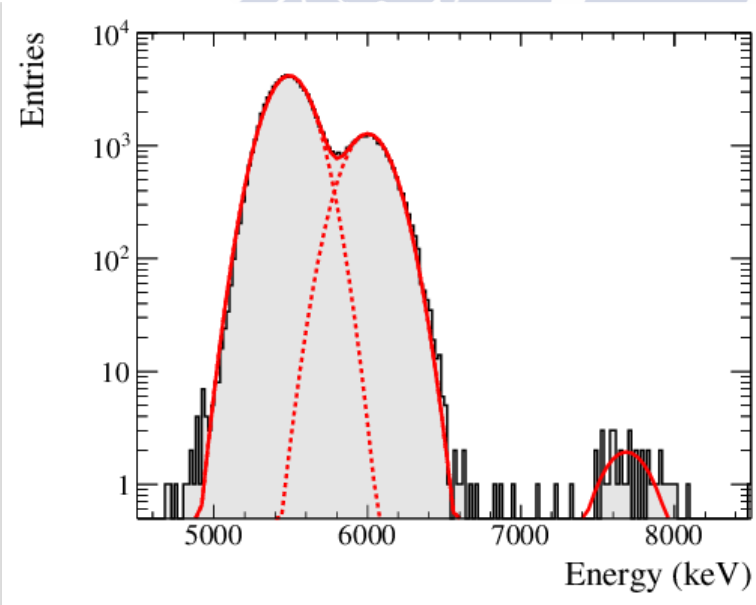

Figure 6.21: Energy distribution for fiducial α candidate events in the NEXT-White detector during a high α activity Run. A triple gaussian fit is superimposed to describe the ^{222}Rn (5590 keV), ^{218}Po (6115 keV) and ^{214}Po (7834 keV) populations [186].

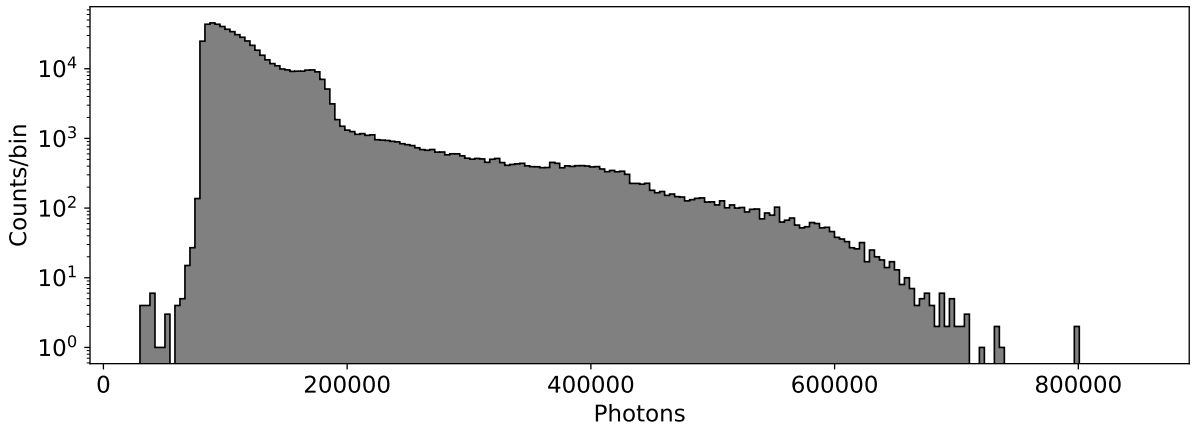

(a)

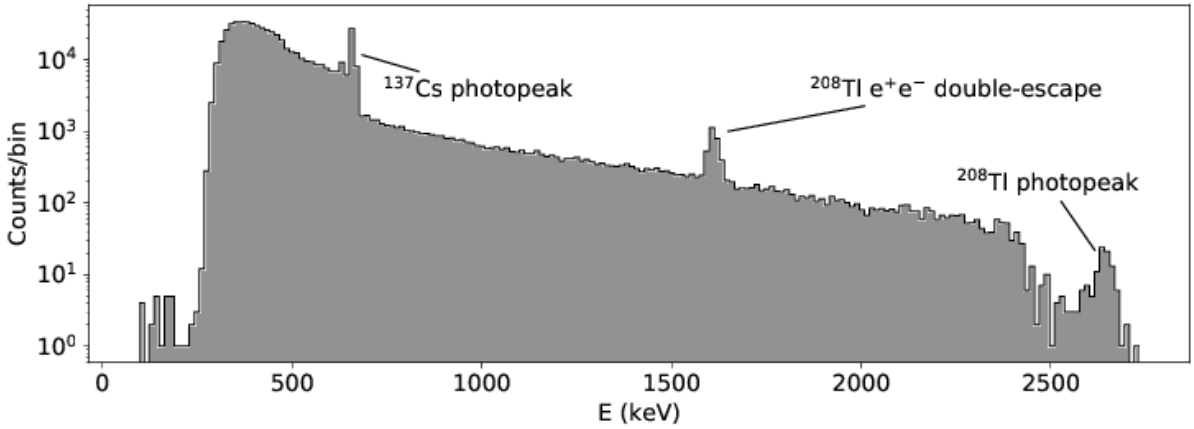

(b)

Figure 6.22: Uncorrected (left) and corrected (right) energy spectra for a ^{137}Cs + ^{208}Tl Run taken to measure the energy resolution of the NEXT-White detector at high energies.

The energy resoluton for higher energy depositions and a more complete study of the extrapolation to $Q_{\beta\beta}$ is made in another analysis [188]. High energy electrons are reconstructed up to the `hDST` level and the track hits are fully corrected using the maps produced with ^{83}Kr^{m} Runs taken shortly before the analyzed data. Figure 6.22 shows a comparison between the uncorrected and fully-corrected spectra of a ^{137}Cs + ^{208}Tl Run. In Figure 6.22b the photopeaks of both the ^{137}Cs and ^{208}Tl photon interactions and the double-escape peak of ^{208}Tl are clearly visible in the spectrum over a compton background. However, in the uncorrected specturm (Figure 6.22a), these peaks are diluted over a wider energy range and are therefore barely noticeable.

These two cases demonstrate how without correcting for both the geometrical and lifetime effects, the physics analysis with the detector would be extremely compromised.

USC
UNIVERSIDADE
DE SANTIAGO
DE COMPOSTELA

7 Summary and conclusions

Neutrinos are, arguably, the less understood particles in the Standard Model of particle physics. In the past decades, it has been discovered through neutrino oscillation experiments that they are massive, contradicting the assumptions of the theory. Their nature, whether they are Dirac or Majorana particles, is still to be determined. The possible Majorana nature of neutrinos could explain not only their seemly arbitrary low mass, but also the matter-antimatter asymmetry of the universe. Thus, the research in neutrino physics has been recently focused in the search for the neutrinoless double beta decay, a hypothetical nuclear process that would prove the Majorana nature of neutrinos.

The standard mode of the double beta decay, with two-neutrino emission and allowed within the Standard Model, has already been observed in a number of isotopes. The neutrinoless mode, on the other hand, can only occur if neutrinos are Majorana particles. There are a number of experiments already in the hunt for the decay. EXO, KamLAND-Zen and GERDA are the three experiments leading the field, but there are multiple projects implementing different techniques to search for the decay, such as CUORE, SNO+, SuperNEMO and NEXT.

NEXT will search for the neutrinoless double beta decay in ^{136}Xe with a High-Pressure Xenon TPC. For the NEXT-100 detector, the collaboration plans to use $\mathcal{O}(100$ kg) of xenon enriched to 91 % in ^{136}Xe at 15 bar. The design of the detector implements the SOFT concept and is based on the observations of the R & D phase. It consists of an electroluminiscent TPC instrumented with two sensor planes. A plane filled with PMTs, on the cathode side, measures the energy of the event and a plane instrumented with an array of SiPMs is used for tracking purposes. The technique is focused on achieving an excellent energy resolution (< 1 % FWHM at $Q_{\beta\beta}$) with significant background rejection using topological information.

The NEXT collaboration started in 2009 with an R & D phase to demonstrate the detector concept and the capabilities of the technology. Two main prototypes were built (NEXT-DEMO and NEXT-DBDM) and operated from 2009 to 2014. These detectors were used to demonstrate the excellent energy resolution and tracking capabilities of the technique. The project is currently in its first phase, with the operation of the NEXT-White (NEW) detector. Built in 2015-2016,

NEW is a ∼1:2 scale model of the NEXT-100 detector and uses the same materials and practically the same technology. The purposes of this apparatus are the validation of the technological solutions for NEXT-100 in a large-scale detector and the assesment of the background model. A measurement of the $\beta\beta^{2\nu}$ half life with NEXT-White will certify the technology and shed some light on the prospects for the future generation of experiments.

This work has been focused on three aspects of the NEXT-White detector: its optical simulation, the reconstruction software used to process data and the low-energy calibration with data.

In Chapter 4, the optical simulation of NEXT-White was described. It consisted in the production of a photon detection probability models (light tables) for the detector and its parametrization. The probability models (one for S1 and one for S2 signals) describe the fraction of light received by a certain sensor as a function of the light emission coordintes. Its use reduces significatively the computation time of Monte Carlo simulations. Notwithstanding, a fine description of the detector requires enormous tables, which need to be stored in RAM during the execution of the programme. This caveat leads to the parametrization of the probability model, where data are replaced by functions. The parametrized model of the detector is also less affected by statistical fluctuations and, unlike the light tables, provides a continuous probability model for the entire region of simulation. Furthermore, the technique was propagated to the simulation of the NEXT-100 detector, building and parametrizing its probability models.

The second part of this thesis (Chapter 5) contains the depiction of the reconstruction software of the NEXT experiment. Each stage of the reconstruction chain has been described in depth along with the software structures created to hold the information. Both the transient and persistent representations of such structures were also discussed. Furthermore, the software framework, IC, was analyzed in Section 5.5, where the repository structure and software philosophy were commented in detail. The main feature of this framework, the *dataflow* structure, was described in detail in Section 5.6, and the implementation of *diomira* within this structure was shown for illustration purposes.

The low-energy calibration methology was studied in the final section of this work (Chapter 6). The method consisted on measuring the detector response as a function of the spatial coordinates using $^{83}\mathrm{Kr}^{m}$ events. $^{83}\mathrm{Kr}^{m}$ decays produce an extremely short track, which can be treated as a point-like event. Using two $^{83}\mathrm{Kr}^{m}$ datasets taken in Fall 2017, the electron lifetime was measured and a dependence on the (x, y) coordinate was found in the first dataset. In order to correct the lifetime effect, a *lifetime map* was created. This map contains the measured lifetime in different (x, y) bins. The lifetime effect is then corrected using the lifetime measurement closest to the event reconstructed position. Noticiably, the (x, y)-dependence of the lifetime vanishes is no longer present the second dataset. This procedure yields also the information of the lifetime-corrected event energy as a function of (x, y): the *energy map*. However, the energy map can be further refined by measuring the lifetime-corrected energy as a function of (x, y). A more accurate map is achieved with this method.

Finally, both the lifetime and the energy maps were used to correct the $^{83}\mathrm{Kr}^{m}$ datasets and measure the energy resolution. Even after these corrections, the resolution is found to depend on z and r, as expected. The dependences matches the predictions from Monte Carlo simulations. The dependence with r is fairly constant up to 150 mm, while the dependence with z is approximately linear. Thus, a fiducial region of $r < 150$ mm and $z < 150$ mm is chosen to compare the performance of the detector with that of a bigger detector with a better lifetime.

Besides, the systematic uncertainties of the meassurement were studied.

A final estimate of the energy resolution for 41.5 keV point-like deposits of $(4.553 \pm 0.010(\text{stat.}) \pm 0.324(\text{sys.}))$ % FWHM in the full volume and $(3.804 \pm 0.013(\text{stat.}) \pm 0.112(\text{sys.}))$ % FWHM in a restricted fiducial volume is obtained for the 7.2 bar Run. A naive $E^{-1/2}$ extrapolation yields energy resolutions at $Q_{\beta\beta}$ of $(0.5916 \pm 0.0014(\text{stat.}) \pm 0.0421(\text{sys.}))$ % FWHM in the full volume and $(0.4943 \pm 0.0017(\text{stat.}) \pm 0.0146(\text{sys.}))$ % FWHM in the fiducial volume. Similar results were obtained for a 9.1 bar Run. The comparison of the results with theoretical and Monte-Carlo-simulated predictions demonstrate the near-intrinsic energy resolution achieved.

USC
UNIVERSIDADE
DE SANTIAGO
DE COMPOSTELA

A The barycenter algorithm

A.1 Definition

The barycenter algorithm is used to reconstruct the (x, y) position of some signal. Given a set of k triggered sensors with coordinates (x_k, y_k) and charge q_k, the reconstructed (x, y) position is defined as the charge-weighted average of the sensor positions. For the x coordinate, we have:

$$x_B = \frac{\sum_k q_k x_k}{\sum_k q_k}. \tag{A.1}$$

Similarly, the standard deviation of the signal along x is:

$$(x_{rms})_B = \frac{\sum_k q_k (x_k - x_B)^2}{\sum_k q_k}. \tag{A.2}$$

An analogous definition is used for the y coordinate and its standard deviation.

A.2 Performance

In order to study the performance of the algorithm, a moderately-large dataset of $^{83}Kr^m$ events was simulated. The events were produced homogeneously in the active volume and reconstructed up to the `PMaps` level.

The true position (x_T, y_T) of the event is defined as the energy-weighted average position of the *mchits*. The average number of *mchits* in an event is 7 with small fluctuations around this value. These events are contained in a cube of 0.2 mm side and therefore can be considered pointlike.

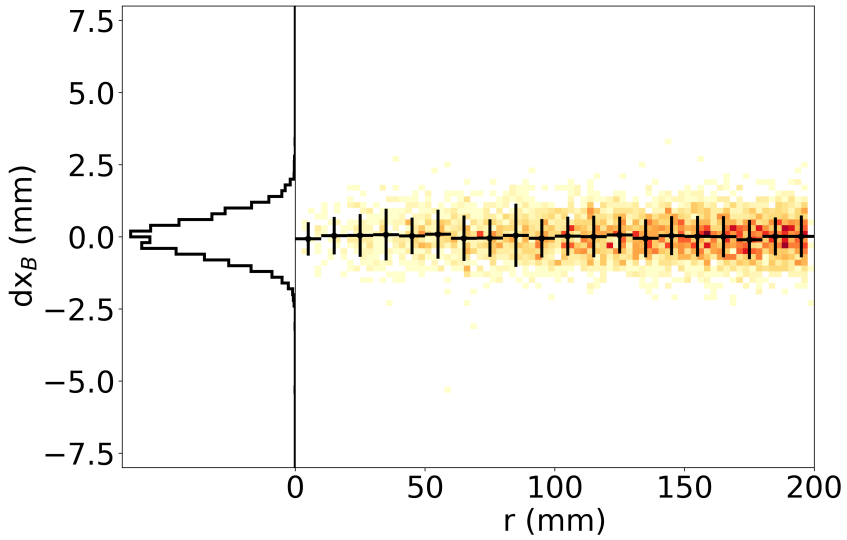

Figure A.1: Main panel: distribution of dx_B as a function of the radial position of the event. The color scale represents number of events and the errorbars indicate the mean and standard deviation in different r bins. The algorithm shows no significant biases in the whole plane. Left subpanel: r-integrated distribution of dx_B. A gaussian distribution with a standard deviation of 0.68 mm is found, which is constant along r. A similar distribution is found for the y coordinate.

The performance of the algorithm is assessed measuring the transverse distance between the reconstructed and true positions. Thus, we define:

$$dx_B = x_B - x_T \tag{A.3}$$

for the x coordinate, with an analogous definition for the y coordinate. Moreover, for the spatial resolution of the detector we define

$$dr_B = \sqrt{dx_B^2 + dy_B^2} \tag{A.4}$$

The main panel in Figure A.1, shows the distribution of dx_B as a function of the radial position of the event. The color scale represents number of events and the errorbars indicate the mean and standard deviation in different r bins. The algorithm shows no significant biases in the whole plane. The left subpanel in Figure A.1 shows the r-integrated distribution, which is gaussianly distributed with a standard deviation of 0.68 mm. As shown in the main panel, this standard deviation is constant along r. A similar distribution is found for the y coordinate.

In Figure A.2 the distribution of the dr_B variable is shown. It is characterized by an average deviation from the true position of 0.87 mm. 95.45 % of the distribution is contained below 1.75 mm, giving an indication of the good spatial resolution of the detector.

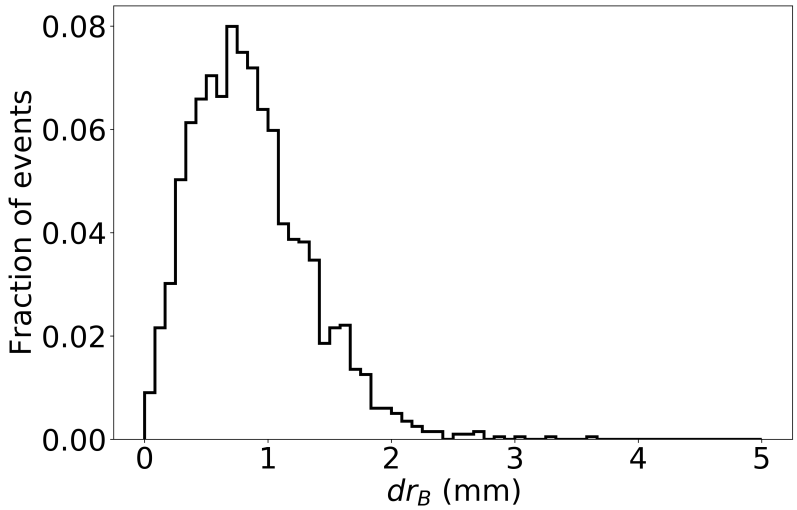

Figure A.2: Distribution of the dr_B variable. 95.45 % of it is contained below 1.75 mm with an average of 0.87 mm, which constitutes a demonstration of the good spatial resolution of the detector.

USC
UNIVERSIDADE
DE SANTIAGO
DE COMPOSTELA

Data structures representations

B

The different representations of the data structures presented in Chapter 5 can be complex. Here, we present the lengthy versions of some of them.

```
/ (RootGroup) ''
/PMAPS (Group) ''
/PMAPS/S1 (Table(2068,), shuffle, zlib(4)) 'S1 Table'
  description := {
  "event": Int32Col(shape=(), dflt=0, pos=0),
  "peak": UInt8Col(shape=(), dflt=0, pos=1),
  "time": Float32Col(shape=(), dflt=0.0, pos=2),
  "ene": Float32Col(shape=(), dflt=0.0, pos=3)}
  byteorder := 'little'
  chunkshape := (5041,)
  autoindex := True
  colindexes := {
    "event": Index(6, medium, shuffle, zlib(1)).is_csi=False}
/PMAPS/S1Pmt (Table(22748,), shuffle, zlib(4)) 'S1Pmt Table'
  description := {
  "event": Int32Col(shape=(), dflt=0, pos=0),
  "peak": UInt8Col(shape=(), dflt=0, pos=1),
  "npmt": UInt8Col(shape=(), dflt=0, pos=2),
  "ene": Float32Col(shape=(), dflt=0.0, pos=3)}
  byteorder := 'little'
  chunkshape := (6553,)
  autoindex := True
  colindexes := {
    "event": Index(6, medium, shuffle, zlib(1)).is_csi=False}
/PMAPS/S2 (Table(2308,), shuffle, zlib(4)) 'S2 Table'
  description := {
  "event": Int32Col(shape=(), dflt=0, pos=0),
  "peak": UInt8Col(shape=(), dflt=0, pos=1),
  "time": Float32Col(shape=(), dflt=0.0, pos=2),
  "ene": Float32Col(shape=(), dflt=0.0, pos=3)}
  byteorder := 'little'
  chunkshape := (5041,)
  autoindex := True
  colindexes := {
    "event": Index(6, medium, shuffle, zlib(1)).is_csi=False}
/PMAPS/S2Pmt (Table(25388,), shuffle, zlib(4)) 'S2Pmt Table'
  description := {
  "event": Int32Col(shape=(), dflt=0, pos=0),
  "peak": UInt8Col(shape=(), dflt=0, pos=1),
  "npmt": UInt8Col(shape=(), dflt=0, pos=2),
  "ene": Float32Col(shape=(), dflt=0.0, pos=3)}
  byteorder := 'little'
  chunkshape := (6553,)
  autoindex := True
  colindexes := {
    "event": Index(6, medium, shuffle, zlib(1)).is_csi=False}
/PMAPS/S2Si (Table(206874,), shuffle, zlib(4)) 'S2Si Table'
  description := {
  "event": Int32Col(shape=(), dflt=0, pos=0),
  "peak": UInt8Col(shape=(), dflt=0, pos=1),
  "nsipm": Int16Col(shape=(), dflt=0, pos=2),
  "ene": Float32Col(shape=(), dflt=0.0, pos=3)}
  byteorder := 'little'
  chunkshape := (5957,)
  autoindex := True
  colindexes := {
    "event": Index(6, medium, shuffle, zlib(1)).is_csi=False}
```

Listing B.1: `PMap` persistent representation. The `PMAPS/S1` and `PMAPS/S2` nodes contain the table for the PMT-summed information for the S1 and S2 peaks, respectively. Similarly, the `PMAPS/S1pmt` and `PMAPS/S2pmt` nodes contain the individual PMT amplitudes for the S1 and S2 peaks, respectively. In `PMAPS/S2SiPM` the SiPM amplitudes for the S2 peaks are stored.

```
/ (RootGroup) ''
/DST (Group) ''
/DST/Events (Table(4,), shuffle, zlib(4)) 'KDST Events'
  description := {
  "event": Int32Col(shape=(), dflt=0, pos=0),
  "time": Float64Col(shape=(), dflt=0.0, pos=1),
  "s1_peak": UInt16Col(shape=(), dflt=0, pos=2),
  "s2_peak": UInt16Col(shape=(), dflt=0, pos=3),
  "nS1": UInt16Col(shape=(), dflt=0, pos=4),
  "nS2": UInt16Col(shape=(), dflt=0, pos=5),
  "S1w": Float64Col(shape=(), dflt=0.0, pos=6),
  "S1h": Float64Col(shape=(), dflt=0.0, pos=7),
  "S1e": Float64Col(shape=(), dflt=0.0, pos=8),
  "S1t": Float64Col(shape=(), dflt=0.0, pos=9),
  "S2w": Float64Col(shape=(), dflt=0.0, pos=10),
  "S2h": Float64Col(shape=(), dflt=0.0, pos=11),
  "S2e": Float64Col(shape=(), dflt=0.0, pos=12),
  "S2q": Float64Col(shape=(), dflt=0.0, pos=13),
  "S2t": Float64Col(shape=(), dflt=0.0, pos=14),
  "Nsipm": UInt16Col(shape=(), dflt=0, pos=15),
  "DT": Float64Col(shape=(), dflt=0.0, pos=16),
  "Z": Float64Col(shape=(), dflt=0.0, pos=17),
  "Zrms": Float64Col(shape=(), dflt=0.0, pos=18),
  "X": Float64Col(shape=(), dflt=0.0, pos=19),
  "Y": Float64Col(shape=(), dflt=0.0, pos=20),
  "R": Float64Col(shape=(), dflt=0.0, pos=21),
  "Phi": Float64Col(shape=(), dflt=0.0, pos=22),
  "Xrms": Float64Col(shape=(), dflt=0.0, pos=23),
  "Yrms": Float64Col(shape=(), dflt=0.0, pos=24)}
  byteorder := 'little'
  chunkshape := (394,)
  autoindex := True
  colindexes := {
    "event": Index(6, medium, shuffle, zlib(1)).is_csi=False}
```

Listing B.2: `kDST` persistent representation. A unique node `Events` within a group `DST` holds all the data. This node contains the column descriptors described in the Section 5.3.2.

```
   event   time   s1_peak   s2_peak   nS1   nS2     S1w       S1h        S1e  \
0      3    0.0         0         0     1     1   175.0  1.258654   6.622321
1      4    0.0         0         0     1     1   125.0  1.406974   5.844857
2      5    0.0         0         0     1     1   150.0  1.921667  10.123529
3      9    0.0         0         0     1     1   125.0  0.906976   4.907313

         S1t        S2w         S2h          S2e         S2q          S2t  \
0  100150.0   6.447969  650.964783  2720.479004  586.347412  392470.50000
1  100125.0   9.440062  646.592285  2865.423340  562.968018  277481.62500
2  100175.0   6.450062  677.497070  2736.497070  535.010254  373514.59375
3  100200.0   4.659234  892.476440  3156.472168  616.893250  263485.46875

   Nsipm          DT           Z      Zrms          X           Y  \
0     13  292.320526  584.641052  1.491539  45.594534 -136.065685
1     11  177.356628  354.713257  2.393880 -55.716592  -91.441193
2     12  273.339600  546.679199  1.418878 110.427065   56.718705
3     13  163.285477  326.570953  1.162399 111.867225  -43.214848

             R       Phi      Xrms      Yrms
0  143.501681 -1.247464  7.330917  7.237720
1  107.078618 -2.118038  6.305316  6.966430
2  124.141645  0.474492  7.406061  7.606368
3  119.924139 -0.368645  7.249234  6.468532
```

Listing B.3: `kDST` transient representation. A *pandas* `DataFrame` holds the relevant data attributes for point-like events. Each row in the structure is a S1-S2 pair of a certain event, and all possible S1-S2 combinations are stored. See text for details of details on the fields.

```
/ (RootGroup) ''
/RECO (Group) ''
/RECO/Events (Table(23,), shuffle, zlib(4)) 'Hits'
  description := {
  "event": Int32Col(shape=(), dflt=0, pos=0),
  "time": Float64Col(shape=(), dflt=0.0, pos=1),
  "npeak": UInt16Col(shape=(), dflt=0, pos=2),
  "Xpeak": Float64Col(shape=(), dflt=0.0, pos=3),
  "Ypeak": Float64Col(shape=(), dflt=0.0, pos=4),
  "nsipm": UInt16Col(shape=(), dflt=0, pos=5),
  "X": Float64Col(shape=(), dflt=0.0, pos=6),
  "Y": Float64Col(shape=(), dflt=0.0, pos=7),
  "Xrms": Float64Col(shape=(), dflt=0.0, pos=8),
  "Yrms": Float64Col(shape=(), dflt=0.0, pos=9),
  "Z": Float64Col(shape=(), dflt=0.0, pos=10),
  "Q": Float64Col(shape=(), dflt=0.0, pos=11),
  "E": Float64Col(shape=(), dflt=0.0, pos=12)}
  byteorder := 'little'
  chunkshape := (744,)
  autoindex := True
  colindexes := {
    "event": Index(6, medium, shuffle, zlib(1)).is_csi=False}
```

Listing B.4: `hDST` persistent representation. A unique node `Events` within a group `RECO` holds all the data. This node contains the column descriptors described in the Section 5.4.2.

```
   event  time  npeak  nsipm          X         Y      Xrms      Yrms  \
0     15   0.0      0      0        NaN       NaN       NaN       NaN
1     15   0.0      0      6 -179.940785  4.861519  4.999649  6.991795
2     15   0.0      0      7 -177.493026  5.643189  6.162855  7.167120
3     15   0.0      0      7 -176.512358  4.571614  6.397761  6.579099
4     15   0.0      0      4 -175.334056  0.834642  4.731667  4.929845

       Z          Q           E
0 847.85   0.000000    64.084826
1 851.60  46.248235   454.434708
2 855.60  91.702595  1472.345154
3 859.60  91.381085  1584.528442
4 863.60  30.761120   791.471527
```

Listing B.5: `hDST` transient representation in the for of a *pandas* `DataFrame`.

Bibliography

[1] MissMJ, *Standard model of elementary particles*, 2018. [Online; accessed ¡citation¿24-August-2018¡/citation¿].

[2] **SLD Electroweak Group, DELPHI, ALEPH, SLD, SLD Heavy Flavour Group, OPAL, LEP Electroweak Working Group, L3** Collaboration, S. Schael et al., *Precision electroweak measurements on the Z resonance*, *Phys. Rept.* **427** (2006) 257–454, [hep-ex/0509008].

[3] **Super-Kamiokande** Collaboration, Y. Fukuda et al., *Evidence for oscillation of atmospheric neutrinos*, *Phys. Rev. Lett.* **81** (1998) 1562–1567, [hep-ex/9807003].

[4] B. T. Cleveland, T. Daily, R. Davis, Jr., J. R. Distel, K. Lande, C. K. Lee, P. S. Wildenhain, and J. Ullman, *Measurement of the solar electron neutrino flux with the Homestake chlorine detector*, *Astrophys. J.* **496** (1998) 505–526.

[5] **SNO** Collaboration, Q. R. Ahmad et al., *Direct evidence for neutrino flavor transformation from neutral current interactions in the Sudbury Neutrino Observatory*, *Phys. Rev. Lett.* **89** (2002) 011301, [nucl-ex/0204008].

[6] **KamLAND** Collaboration, K. Eguchi et al., *First results from KamLAND: Evidence for reactor anti-neutrino disappearance*, *Phys. Rev. Lett.* **90** (2003) 021802, [hep-ex/0212021].

[7] **KamLAND** Collaboration, T. Araki et al., *Measurement of neutrino oscillation with KamLAND: Evidence of spectral distortion*, *Phys. Rev. Lett.* **94** (2005) 081801, [hep-ex/0406035].

[8] **K2K** Collaboration, M. H. Ahn et al., *Indications of neutrino oscillation in a 250 km long baseline experiment*, *Phys. Rev. Lett.* **90** (2003) 041801, [hep-ex/0212007].

[9] **MINOS** Collaboration, D. G. Michael et al., *Observation of muon neutrino disappearance with the MINOS detectors and the NuMI neutrino beam*, *Phys. Rev. Lett.* **97** (2006) 191801, [hep-ex/0607088].

[10] B. Pontecorvo, *Neutrino Experiments and the Problem of Conservation of Leptonic Charge*, *Sov. Phys. JETP* **26** (1968) 984–988. [Zh. Eksp. Teor. Fiz.53,1717(1967)].

[11] V. N. Gribov and B. Pontecorvo, *Neutrino astronomy and lepton charge*, *Phys. Lett.* **28B** (1969) 493.

[12] S. Eliezer and D. A. Ross, *A 'Cabibbo' Theory for Leptons and the Neutrino Masses*, *Phys. Rev.* **D10** (1974) 3088.

[13] H. Fritzsch and P. Minkowski, *Vector-Like Weak Currents, Massive Neutrinos, and Neutrino Beam Oscillations*, *Phys. Lett.* **62B** (1976) 72–76.

[14] S. M. Bilenky and B. Pontecorvo, *Lepton Mixing and Neutrino Oscillations*, *Phys. Rept.* **41** (1978) 225–261.

[15] F. Capozzi, E. Di Valentino, E. Lisi, A. Marrone, A. Melchiorri, and A. Palazzo, *Global constraints on absolute neutrino masses and their ordering*, *Phys. Rev. D* **95** (May, 2017) 096014.

[16] S. Bilenky, J. Hoek, and S. Petcov, *On the oscillations of neutrinos with dirac and majorana masses*, *Physics Letters B* **94** (1980), no. 4 495 – 498.

[17] N. Cabibbo, *Time reversal violation in neutrino oscillation*, *Physics Letters B* **72** (1978), no. 3 333 – 335.

[18] V. Barger, K. Whisnant, and R. J. N. Phillips, CP *nonconservation in three-neutrino oscillations*, *Phys. Rev. Lett.* **45** (Dec, 1980) 2084–2088.

[19] M. Tanabashi et al., *Review of Particle Physics*, *Phys. Rev.* **D98** (2018), no. 3 030001.

[20] **Planck** Collaboration, P. A. R. Ade et al., *Planck 2013 results. XVI. Cosmological parameters*, *Astron. Astrophys.* **571** (2014) A16, [arXiv:1303.5076].

[21] **Planck** Collaboration, P. A. R. Ade et al., *Planck 2015 results. XIII. Cosmological parameters*, *Astron. Astrophys.* **594** (2016) A13, [arXiv:1502.01589].

[22] **Planck** Collaboration, N. Aghanim et al., *Planck 2018 results. VI. Cosmological parameters*, arXiv:1807.06209.

[23] E. Fermi, *Trends to a Theory of beta Radiation. (In Italian)*, *Nuovo Cim.* **11** (1934) 1–19. [,535(1934)].

[24] V. Lobashev, *The search for the neutrino mass by direct method in the tritium beta-decay and perspectives of study it in the project katrin*, *Nuclear Physics A* **719** (2003) C153 – C160.

[25] C. Kraus et al., *Final results from phase II of the Mainz neutrino mass search in tritium beta decay*, *Eur. Phys. J.* **C40** (2005) 447–468, [hep-ex/0412056].

[26] K. Eitel, *Direct neutrino mass experiments*, *Nucl. Phys. Proc. Suppl.* **143** (2005) 197–204. [,587(2005)].

[27] V. N. Aseev, A. I. Belesev, A. I. Berlev, E. V. Geraskin, A. A. Golubev, N. A. Likhovid, V. M. Lobashev, A. A. Nozik, V. S. Pantuev, V. I. Parfenov, A. K. Skasyrskaya, F. V. Tkachov, and S. V. Zadorozhny, *Upper limit on the electron antineutrino mass from the troitsk experiment*, *Phys. Rev. D* **84** (Dec, 2011) 112003.

[28] L. Wolfenstein, *Neutrino Oscillations in Matter*, *Phys. Rev.* **D17** (1978) 2369–2374. [,294(1977)].

[29] V. D. Barger, K. Whisnant, S. Pakvasa, and R. J. N. Phillips, *Matter Effects on Three-Neutrino Oscillations*, *Phys. Rev.* **D22** (1980) 2718. [,300(1980)].

[30] S. P. Mikheyev and A. Yu. Smirnov, *Resonance Amplification of Oscillations in Matter and Spectroscopy of Solar Neutrinos*, *Sov. J. Nucl. Phys.* **42** (1985) 913–917. [,305(1986)].

[31] Y.-F. Li, J. Cao, Y. Wang, and L. Zhan, *Unambiguous Determination of the Neutrino Mass Hierarchy Using Reactor Neutrinos*, *Phys. Rev.* **D88** (2013) 013008, [arXiv:1303.6733].

[32] C. Giunti and C. W. Kim, *Fundamentals of Neutrino Physics and Astrophysics*. 2007.

[33] M. C. Gonzalez-Garcia and M. Maltoni, *Phenomenology with Massive Neutrinos*, *Phys. Rept.* **460** (2008) 1–129, [arXiv:0704.1800].

[34] B. Kayser, *Neutrino mass, mixing, and flavor change*, hep-ph/0211134.

[35] P. Hernandez, *Neutrino physics*, in *High-energy physics. Proceedings, 5th CERN-Latin-American School, Recinto Quirama, Colombia, March 15-28, 2009*, 2010. arXiv:1010.4131.

[36] E. Majorana, *Teoria simmetrica dell'elettrone e del positrone*, *Nuovo Cim.* **14** (1937) 171–184.

[37] S. Davidson, E. Nardi, and Y. Nir, *Leptogenesis*, *Phys. Rept.* **466** (2008) 105–177, [arXiv:0802.2962].

[38] J. M. Cline, *Baryogenesis*, in *Les Houches Summer School - Session 86: Particle Physics and Cosmology: The Fabric of Spacetime Les Houches, France, July 31-August 25, 2006*, 2006. hep-ph/0609145.

[39] A. D. Sakharov, *Violation of CP Invariance, C asymmetry, and baryon asymmetry of the universe*, *Pisma Zh. Eksp. Teor. Fiz.* **5** (1967) 32–35. [Usp. Fiz. Nauk161,no.5,61(1991)].

[40] A. Riotto and M. Trodden, *Recent progress in baryogenesis*, *Ann. Rev. Nucl. Part. Sci.* **49** (1999) 35–75, [hep-ph/9901362].

[41] M. Fukugita and T. Yanagida, *Baryogenesis Without Grand Unification*, *Phys. Lett.* **B174** (1986) 45–47.

[42] C. S. Fong, E. Nardi, and A. Riotto, *Leptogenesis in the Universe*, *Adv. High Energy Phys.* **2012** (2012) 158303, [arXiv:1301.3062].

[43] **ATLAS** Collaboration, G. Aad et al., *Search for heavy Majorana neutrinos with the ATLAS detector in pp collisions at $\sqrt{s} = 8$ TeV*, *JHEP* **07** (2015) 162, [arXiv:1506.06020].

[44] A. Das, N. Okada, and D. Raut, *Enhanced pair production of heavy Majorana neutrinos at the LHC*, *Phys. Rev.* **D97** (2018), no. 11 115023, [arXiv:1710.03377].

[45] **LHCb** Collaboration, X. Cid Vidal, *Searches for Majorana Neutrinos and Direct Searches for Exotics at LHCb*, in *International School on High Energy Physics: Session C: Workshop in HEP (LISHEP 2015) Manaus, Amazonas, Brazil, August 2-9, 2015*, 2015. arXiv:1510.05483.

[46] A. Das, P. Konar, and A. Thalapillil, *Jet substructure shedding light on heavy Majorana neutrinos at the LHC*, *JHEP* **02** (2018) 083, [arXiv:1709.09712].

[47] A. Atre, V. Barger, and T. Han, *Upper bounds on lepton-number violating processes*, *Phys. Rev.* **D71** (2005) 113014, [hep-ph/0502163].

[48] M. Goeppert-Mayer, *Double beta-disintegration*, *Phys. Rev.* **48** (Sep, 1935) 512–516.

[49] A. H. Williams and M. L. Wiedenbeck, *Correlation in the direction and polarization of two successive quanta for* rh^{106}*,* co^{60}*, and* cs^{134}, *Phys. Rev.* **78** (Jun, 1950) 822–822.

[50] S. R. Elliott, A. A. Hahn, and M. K. Moe, *Direct evidence for two-neutrino double-beta decay in* ^{82}Se, *Phys. Rev. Lett.* **59** (Nov, 1987) 2020–2023.

[51] **NEMO-3** Collaboration, R. Arnold et al., *Measurement of the double-beta decay half-life and search for the neutrinoless double-beta decay of* ^{48}Ca *with the NEMO-3 detector*, *Phys. Rev.* **D93** (2016), no. 11 112008, [arXiv:1604.01710].

[52] M. Agostini et al., *Results on* $\beta\beta$ *decay with emission of two neutrinos or Majorons in*^{76} *Ge from GERDA Phase I*, *Eur. Phys. J.* **C75** (2015), no. 9 416, [arXiv:1501.02345].

[53] Y. M. Gavrilyuk, A. M. Gangapshev, V. V. Kazalov, V. V. Kuzminov, S. I. Panasenko, and S. S. Ratkevich, *Indications of* $2\nu2k$ *capture in* ^{78}kr, *Phys. Rev. C* **87** (Mar, 2013) 035501.

[54] **NEMO** Collaboration, R. Arnold et al., *First results of the search of neutrinoless double beta decay with the NEMO 3 detector*, *Phys. Rev. Lett.* **95** (2005) 182302, [hep-ex/0507083].

[55] **NEMO-3** Collaboration, J. Argyriades et al., *Measurement of the two neutrino double beta decay half-life of Zr-96 with the NEMO-3 detector*, *Nucl. Phys.* **A847** (2010) 168–179, [arXiv:0906.2694].

[56] E. Armengaud et al., *Development of* ^{100}*Mo-containing scintillating bolometers for a high-sensitivity neutrinoless double-beta decay search*, *Eur. Phys. J.* **C77** (2017), no. 11 785, [arXiv:1704.01758].

[57] **NEMO-3** Collaboration, R. Arnold et al., *Results of the search for neutrinoless double-decay in* ^{100}*Mo with the NEMO-3 experiment*, *Phys. Rev.* **D92** (2015), no. 7 072011, [arXiv:1506.05825].

[58] P. Belli et al., *New observation of 2beta 2nu decay of Mo-100 to the 0+(1) level of Ru-100 in the ARMONIA 1 experiment*, *J. Phys. Conf. Ser.* **203** (2010) 012142.

[59] **NEMO** Collaboration, R. Arnold et al., *Measurement of double beta decay of Mo-100 to excited states in the NEMO 3 experiment*, *Nucl. Phys.* **A781** (2007) 209–226, [hep-ex/0609058].

[60] **NEMO-3** Collaboration, R. Arnold et al., *Measurement of the* $2\nu\beta\beta$ *Decay Half-Life and Search for the* $0\nu\beta\beta$ *Decay of* ^{116}*Cd with the NEMO-3 Detector*, *Phys. Rev.* **D95** (2017), no. 1 012007, [arXiv:1610.03226].

[61] F. A. Danevich et al., *Search for 2 beta decay of cadmium and tungsten isotopes: Final results of the Solotvina experiment*, *Phys. Rev.* **C68** (2003) 035501.

[62] **CUORE** Collaboration, C. Alduino et al., *Measurement of the two-neutrino double-beta decay half-life of*^{130} *Te with the CUORE-0 experiment*, *Eur. Phys. J.* **C77** (2017), no. 1 13, [arXiv:1609.01666].

[63] **NEMO-3** Collaboration, R. Arnold et al., *Measurement of the Double Beta Decay Half-life of* ^{130}Te *with the NEMO-3 Detector*, *Phys. Rev. Lett.* **107** (2011) 062504, [arXiv:1104.3716].

[64] **EXO-200** Collaboration, J. B. Albert et al., *Improved measurement of the $2\nu\beta\beta$ half-life of ^{136}Xe with the EXO-200 detector*, *Phys. Rev.* **C89** (2014), no. 1 015502, [arXiv:1306.6106].

[65] **KamLAND-Zen** Collaboration, A. Gando et al., *Measurement of the double-β decay half-life of ^{136}Xe with the KamLAND-Zen experiment*, *Phys. Rev.* **C85** (2012) 045504, [arXiv:1201.4664].

[66] **NEMO** Collaboration, J. Argyriades et al., *Measurement of the Double Beta Decay Half-life of Nd-150 and Search for Neutrinoless Decay Modes with the NEMO-3 Detector*, *Phys. Rev.* **C80** (2009) 032501, [arXiv:0810.0248].

[67] W. H. Furry, *On transition probabilities in double beta-disintegration*, *Phys. Rev.* **56** (Dec, 1939) 1184–1193.

[68] J. Kotila and F. Iachello, *Phase space factors for $\beta^+\beta^+$ decay and competing modes of double-β decay*, *Phys. Rev. C* **87** (Feb, 2013) 024313.

[69] J. Barea, J. Kotila, and F. Iachello, *Neutrinoless double-positron decay and positron-emitting electron capture in the interacting boson model*, *Phys. Rev. C* **87** (May, 2013) 057301.

[70] J. Kotila, J. Barea, and F. Iachello, *Neutrinoless double-electron capture*, *Phys. Rev. C* **89** (Jun, 2014) 064319.

[71] J. Schechter and J. W. F. Valle, *Neutrinoless double-β decay in su(2)$\times$u(1) theories*, *Phys. Rev. D* **25** (Jun, 1982) 2951–2954.

[72] W. Rodejohann, *Neutrino-less Double Beta Decay and Particle Physics*, *Int. J. Mod. Phys.* **E20** (2011) 1833–1930, [arXiv:1106.1334].

[73] M. Duerr, M. Lindner, and A. Merle, *On the Quantitative Impact of the Schechter-Valle Theorem*, *JHEP* **06** (2011) 091, [arXiv:1105.0901].

[74] M. Doi, T. Kotani, and E. Takasugi, *Double beta Decay and Majorana Neutrino*, *Prog. Theor. Phys. Suppl.* **83** (1985) 1.

[75] F. Vissani, *Signal of neutrinoless double beta decay, neutrino spectrum and oscillation scenarios*, *JHEP* **06** (1999) 022, [hep-ph/9906525]. [,700(1999)].

[76] **KamLAND-Zen** Collaboration, A. Gando et al., *Search for Majorana Neutrinos near the Inverted Mass Hierarchy Region with KamLAND-Zen*, *Phys. Rev. Lett.* **117** (2016), no. 8 082503, [arXiv:1605.02889]. [Addendum: Phys. Rev. Lett.117,no.10,109903(2016)].

[77] **GERDA** Collaboration, M. Agostini et al., *Improved Limit on Neutrinoless Double-β Decay of ^{76}Ge from GERDA Phase II*, *Phys. Rev. Lett.* **120** (2018), no. 13 132503, [arXiv:1803.11100].

[78] **CUORE** Collaboration, K. Alfonso et al., *Search for Neutrinoless Double-Beta Decay of ^{130}Te with CUORE-0*, *Phys. Rev. Lett.* **115** (2015), no. 10 102502, [arXiv:1504.02454].

[79] P. F. de Salas, D. V. Forero, C. A. Ternes, M. Tortola, and J. W. F. Valle, *Status of neutrino oscillations 2018: 3σ hint for normal mass ordering and improved CP sensitivity*, *Phys. Lett.* **B782** (2018) 633–640, [arXiv:1708.01186].

[80] A. F. Heavens and E. Sellentin, *Objective Bayesian analysis of neutrino masses and hierarchy*, *JCAP* **1804** (2018), no. 04 047, [arXiv:1802.09450].

[81] F. T. Avignone, III, S. R. Elliott, and J. Engel, *Double Beta Decay, Majorana Neutrinos, and Neutrino Mass*, *Rev. Mod. Phys.* **80** (2008) 481–516, [arXiv:0708.1033].

[82] R. N. Mohapatra, *Limits on the mass of the right-handed majorana neutrino*, *Phys. Rev. D* **34** (Aug, 1986) 909–910.

[83] R. N. Mohapatra, *New contributions to neutrinoless double-beta decay in supersymmetric theories*, *Phys. Rev. D* **34** (Dec, 1986) 3457–3461.

[84] H. M. Georgi, S. L. Glashow, and S. Nussinov, *Unconventional Model of Neutrino Masses*, *Nucl. Phys.* **B193** (1981) 297–316.

[85] J. Menendez, A. Poves, E. Caurier, and F. Nowacki, *Disassembling the Nuclear Matrix Elements of the Neutrinoless beta beta Decay*, *Nucl. Phys.* **A818** (2009) 139–151, [arXiv:0801.3760].

[86] J. Suhonen and O. Civitarese, *Review of the properties of the 0 nu beta- beta- nuclear matrix elements*, *J. Phys.* **G39** (2012) 124005.

[87] F. Šimkovic, V. Rodin, A. Faessler, and P. Vogel, $0\nu\beta\beta$ *and* $2\nu\beta\beta$ *nuclear matrix elements, quasiparticle random-phase approximation, and isospin symmetry restoration*, *Phys. Rev. C* **87** (Apr, 2013) 045501.

[88] J. Barea, J. Kotila, and F. Iachello, *Nuclear matrix elements for double-β decay*, *Phys. Rev. C* **87** (Jan, 2013) 014315.

[89] N. L. Vaquero, T. R. Rodríguez, and J. L. Egido, *Shape and pairing fluctuation effects on neutrinoless double beta decay nuclear matrix elements*, *Phys. Rev. Lett.* **111** (Sep, 2013) 142501.

[90] M. Redshaw, B. J. Mount, E. G. Myers, and F. T. Avignone, III, *Masses of Te-130 and Xe-130 and Double-beta-Decay Q Value of Te-130*, *Phys. Rev. Lett.* **102** (2009) 212502, [arXiv:0902.2139].

[91] B. J. Mount, M. Redshaw, and E. G. Myers, *Double-β-decay Q values of ˆ{74}Se and ˆ{76}Ge*, *Physical Review C* **81** (Mar., 2010) 032501.

[92] S. Rahaman, V.-V. Elomaa, T. Eronen, J. Hakala, A. Jokinen, A. Kankainen, J. Rissanen, J. Suhonen, C. Weber, and J. yst, *Double-beta decay q values of 116cd and 130te*, *Physics Letters B* **703** (2011), no. 4 412 – 416.

[93] D. Fink et al., *Q-Value and Half-Lives for the Double-Beta-Decay Nuclide 110Pd*, *Phys. Rev. Lett.* **108** (2012) 062502, [arXiv:1112.5786].

[94] M. Redshaw, G. Bollen, M. Brodeur, S. Bustabad, D. L. Lincoln, S. J. Novario, R. Ringle, and S. Schwarz, *Atomic mass and double-beta-decay Q value of Ca-48*, *Phys. Rev.* **C86** (2012) 041306.

[95] D. L. Lincoln, J. D. Holt, G. Bollen, M. Brodeur, S. Bustabad, J. Engel, S. J. Novario, M. Redshaw, R. Ringle, and S. Schwarz, *First direct double- decay Q-Value measurement of^{82} Se in support of understanding the nature of the Neutrino*, *Phys. Rev. Lett.* **110** (2013), no. 1 012501, [arXiv:1211.5659].

[96] J. J. Gómez-Cadenas and J. Martín-Albo, *Phenomenology of neutrinoless double beta decay*, *PoS* **GSSI14** (2015) 004, [arXiv:1502.00581].

[97] J. Barea, J. Kotila, and F. Iachello, *Nuclear matrix elements for double-β decay*, *Phys. Rev.* **C87** (2013), no. 1 014315, [arXiv:1301.4203].

[98] M. K. Moe, *New approach to the detection of neutrinoless double beta decay*, *Phys. Rev.* **C44** (1991) 931–934. [,1019(1991)].

[99] A. D. McDonald et al., *Demonstration of Single Barium Ion Sensitivity for Neutrinoless Double Beta Decay using Single Molecule Fluorescence Imaging*, *Phys. Rev. Lett.* **120** (2018), no. 13 132504, [arXiv:1711.04782].

[100] S. Umehara et al., *Neutrino-less double-beta decay of Ca-48 studied by Ca F(2)(Eu) scintillators*, *Phys. Rev.* **C78** (2008) 058501, [arXiv:0810.4746].

[101] **NEMO** Collaboration, A. S. Barabash and V. B. Brudanin, *Investigation of double beta decay with the NEMO-3 detector*, *Phys. Atom. Nucl.* **74** (2011) 312–317, [arXiv:1002.2862].

[102] **CUORE** Collaboration, C. Alduino et al., *First Results from CUORE: A Search for Lepton Number Violation via $0\nu\beta\beta$ Decay of ^{130}Te*, *Phys. Rev. Lett.* **120** (2018), no. 13 132501, [arXiv:1710.07988].

[103] **CUORICINO** Collaboration, E. Andreotti et al., *Double-beta decay of ^{130}Te to the first 0^+ excited state of ^{130}Xe with CUORICINO*, *Phys. Rev.* **C85** (2012) 045503, [arXiv:1108.4313].

[104] **EXO-200** Collaboration, J. B. Albert et al., *Searches for double beta decay of ^{134}Xe with EXO-200*, *Phys. Rev.* **D96** (2017), no. 9 092001, [arXiv:1704.05042].

[105] **KamLAND-Zen** Collaboration, K. Asakura et al., *Search for double-beta decay of ^{136}Xe to excited states of ^{136}Ba with the KamLAND-Zen experiment*, *Nucl. Phys.* **A946** (2016) 171–181, [arXiv:1509.03724].

[106] H. V. Klapdor-Kleingrothaus et al., *Latest results from the Heidelberg-Moscow double beta decay experiment*, *Eur. Phys. J.* **A12** (2001) 147–154, [hep-ph/0103062].

[107] H. V. Klapdor-Kleingrothaus and I. V. Krivosheina, *The evidence for the observation of 0nu beta beta decay: The identification of 0nu beta beta events from the full spectra*, *Mod. Phys. Lett.* **A21** (2006) 1547–1566.

[108] **GERDA** Collaboration, M. Agostini et al., *Searching for neutrinoless double beta decay with GERDA*, in *15th International Conference on Topics in Astroparticle and Underground Physics (TAUP 2017) Sudbury, Ontario, Canada, July 24-28, 2017*, 2017. arXiv:1710.07776.

[109] M. Agostini et al., *Background-free search for neutrinoless double-β decay of ^{76}Ge with GERDA*, arXiv:1703.00570. [Nature544,47(2017)].

[110] **KamLAND-Zen** Collaboration, A. Gando et al., *Limit on Neutrinoless $\beta\beta$ Decay of ^{136}Xe from the First Phase of KamLAND-Zen and Comparison with the Positive Claim in ^{76}Ge*, *Phys. Rev. Lett.* **110** (2013), no. 6 062502, [arXiv:1211.3863].

[111] E. Andreotti et al., *130Te Neutrinoless Double-Beta Decay with CUORICINO*, *Astropart. Phys.* **34** (2011) 822–831, [arXiv:1012.3266].

[112] R. S. Raghavan, *New approach to the search for neutrinoless double beta decay*, *Phys. Rev. Lett.* **72** (Mar, 1994) 1411–1414.

[113] S. Dell'Oro, S. Marcocci, M. Viel, and F. Vissani, *Neutrinoless double beta decay: 2015 review*, *Adv. High Energy Phys.* **2016** (2016) 2162659, [arXiv:1601.07512].

[114] **KamLAND-Zen** Collaboration, K. Asakura et al., *Results from KamLAND-Zen*, *AIP Conf. Proc.* **1666** (2015) 170003, [arXiv:1409.0077].

[115] **EXO-200** Collaboration, J. B. Albert et al., *Search for Majorana neutrinos with the first two years of EXO-200 data*, *Nature* **510** (2014) 229–234, [arXiv:1402.6956].

[116] **EXO-200** Collaboration, M. Auger et al., *Search for Neutrinoless Double-Beta Decay in ^{136}Xe with EXO-200*, *Phys. Rev. Lett.* **109** (2012) 032505, [arXiv:1205.5608].

[117] **EXO-200** Collaboration, E. Conti et al., *Correlated fluctuations between luminescence and ionization in liquid xenon*, *Phys. Rev.* **B68** (2003) 054201, [hep-ex/0303008].

[118] M. Auger et al., *The EXO-200 detector, part I: Detector design and construction*, *JINST* **7** (2012) P05010, [arXiv:1202.2192].

[119] **GERDA** Collaboration, K. H. Ackermann et al., *The GERDA experiment for the search of $0\nu\beta\beta$ decay in ^{76}Ge*, *Eur. Phys. J.* **C73** (2013), no. 3 2330, [arXiv:1212.4067].

[120] H. V. Klapdor-Kleingrothaus, L. Baudis, A. Dietz, G. Heusser, B. Majorovits, and H. Strecker, *GENIUS-TF: A Test facility for the GENIUS project*, *Nucl. Instrum. Meth.* **A481** (2002) 149–159, [hep-ex/0012022].

[121] **GERDA** Collaboration, M. Agostini et al., *Results on Neutrinoless Double-β Decay of ^{76}Ge from Phase I of the GERDA Experiment*, *Phys. Rev. Lett.* **111** (2013), no. 12 122503, [arXiv:1307.4720].

[122] R. Ardito et al., *CUORE: A Cryogenic underground observatory for rare events*, hep-ex/0501010.

[123] C. Arnaboldi et al., *A Calorimetric search on double beta decay of Te-130*, *Phys. Lett.* **B557** (2003) 167–175, [hep-ex/0211071].

[124] **CUORE** Collaboration, D. R. Artusa et al., *Searching for neutrinoless double-beta decay of ^{130}Te with CUORE*, *Adv. High Energy Phys.* **2015** (2015) 879871, [arXiv:1402.6072].

[125] **CUORE** Collaboration, C. Alduino et al., *Analysis techniques for the evaluation of the neutrinoless double-β decay lifetime in ^{130}Te with the CUORE-0 detector*, *Phys. Rev.* **C93** (2016), no. 4 045503, [arXiv:1601.01334].

[126] **CUORE** Collaboration, D. Chiesa, *The CUORE experiment at LNGS*, in *18th Lomonosov Conference on Elementary Particle Physics Moscow, Russia, August 24-30, 2017*, 2017. arXiv:1712.07995.

[127] **SNO** Collaboration, J. Boger et al., *The Sudbury neutrino observatory*, *Nucl. Instrum. Meth.* **A449** (2000) 172–207, [nucl-ex/9910016].

[128] **SNO+** Collaboration, S. Biller, *SNO+ with Tellurium*, *Phys. Procedia* **61** (2015) 205–210, [arXiv:1405.3401].

[129] **SNO+** Collaboration, E. Caden, *Status of the SNO+ Experiment*, in *15th International Conference on Topics in Astroparticle and Underground Physics (TAUP 2017) Sudbury, Ontario, Canada, July 24-28, 2017*, 2017. arXiv:1711.11094.

[130] **CUPID** Collaboration, G. Wang et al., *CUPID: CUORE (Cryogenic Underground Observatory for Rare Events) Upgrade with Particle IDentification*, arXiv:1504.03599.

[131] A. Bettini, *The Canfranc Underground Laboratory (LSC)*, *Eur. Phys. J. Plus* **127** (2012) 112.

[132] R. Luscher et al., *Search for beta beta decay in xe-136: New results from the gotthard experiment*, *Phys. Lett.* **B434** (1998) 407–414.

[133] D. R. Nygren, *High-pressure xenon gas electroluminescent TPC for 0nu beta beta-decay search*, *Nucl. Instrum. Meth.* **A603** (2009) 337–348.

[134] **NEXT** Collaboration, V. Alvarez et al., *The NEXT-100 experiment for neutrinoless double beta decay searches (Conceptual Design Report)*, arXiv:1106.3630.

[135] **NEXT** Collaboration, L. Serra, D. Lorca, J. Martin-Albo, M. Sorel, and J. J. Gomez-Cadenas, *Latest results of NEXT-DEMO, the prototype of the NEXT 100 double beta decay experiment*, in *Proceedings, 37th International Conference on High Energy Physics (ICHEP 2014): Valencia, Spain, July 2-9, 2014*, 2014. arXiv:1410.6700.

[136] U. Fano, *Ionization Yield of Radiations. 2. The Fluctuations of the Number of Ions*, *Phys. Rev.* **72** (1947) 26–29.

[137] A. Policarpo, M. Alves, M. Salete, S. Leite, and M. dos Santos, *Detection of soft x-rays with a xenon proportional scintillation counter*, *Nuclear Instruments and Methods* **118** (1974), no. 1 221 – 226.

[138] H. Sipil, *Energy resolution of the proportional counter*, *Nuclear Instruments and Methods* **133** (1976), no. 2 251 – 252.

[139] D. Anderson, T. Hamilton, W.-M. Ku, and R. Novick, *A large area, gas scintillation proportional counter*, *Nuclear Instruments and Methods* **163** (1979), no. 1 125 – 134.

[140] T. H. V. T. Dias, J. M. F. dos Santos, P. J. B. M. Rachinhas, F. P. Santos, C. A. N. Conde, and A. D. Stauffer, *Full-energy absorption of x-ray energies near the xe l- and k-photoionization thresholds in xenon gas detectors: Simulation and experimental results*, *Journal of Applied Physics* **82** (1997), no. 6 2742–2753, [https://doi.org/10.1063/1.366105].

[141] E. Aprile, C. E. Dahl, L. DeViveiros, R. Gaitskell, K. L. Giboni, J. Kwong, P. Majewski, K. Ni, T. Shutt, and M. Yamashita, *Simultaneous measurement of ionization and scintillation from nuclear recoils in liquid xenon as target for a dark matter experiment*, *Phys. Rev. Lett.* **97** (2006) 081302, [astro-ph/0601552].

[142] E. Aprile, A. E. Bolotnikov, A. L. Bolozdynya, and T. Doke, *Noble Gas Detectors*. Wiley, 2008.

[143] E. Aprile and T. Doke, *Liquid Xenon Detectors for Particle Physics and Astrophysics*, *Rev. Mod. Phys.* **82** (2010) 2053–2097, [arXiv:0910.4956].

[144] A. Bolotnikov and B. Ramsey, *The spectroscopic properties of high-pressure xenon*, *Nuclear Instruments and Methods in Physics Research A* **396** (Feb., 1997) 360–370.

[145] L. M. P. Fernandes, E. D. C. Freitas, M. Ball, J. J. Gomez-Cadenas, C. M. B. Monteiro, N. Yahlali, D. Nygren, and J. M. F. d. Santos, *Primary and secondary scintillation measurements in a xenon Gas Proportional Scintillation Counter*, *JINST* **5** (2010) P09006, [arXiv:1009.2719]. [Erratum: JINST5,A12001(2010)].

[146] T. H. V. T. Dias, F. P. Santos, A. D. Stauffer, and C. A. N. Conde, *Monte carlo simulation of x-ray absorption and electron drift in gaseous xenon*, *Phys. Rev. A* **48** (Oct, 1993) 2887–2902.

[147] C. A. N. Conde, *Gas Proportional Scintillation Counters for x-ray spectrometry.* John Wiley & sons, 2004. Chapter 4.2 in *X-ray Spectrometry: Recent Technical Advances*, K. Tsuji, J. Injuk and R. van Greiken, eds.

[148] J. Miyamoto and G. Knoll, *The statistics of avalanche electrons in micro-strip and micro-gap gas chambers*, *Nuclear Instruments and Methods in Physics Research Section A: Accelerators, Spectrometers, Detectors and Associated Equipment* **399** (1997), no. 1 85 – 93.

[149] P. J. B. M. Rachinhas, T. H. V. T. Dias, A. D. Stauffer, F. P. Santos, and C. A. N. Conde, *Energy resolution of xenon proportional counters: Monte carlo simulation and experimental results*, *IEEE Transactions on Nuclear Science* **43** (Aug, 1996) 2399–2405.

[150] C. A. B. Oliveira, M. Sorel, J. Martin-Albo, J. J. Gomez-Cadenas, A. L. Ferreira, and J. F. C. A. Veloso, *Energy Resolution studies for NEXT*, *JINST* **6** (2011) P05007, [arXiv:1105.2954].

[151] **NEXT** Collaboration, G. Martínez-Lema et al., *Calibration of the NEXT-White detector using* ^{83m}Kr *decays*, arXiv:1804.01780.

[152] **NEXT** Collaboration, P. Ferrario et al., *First proof of topological signature in the high pressure xenon gas TPC with electroluminescence amplification for the NEXT experiment*, *JHEP* **01** (2016) 104, [arXiv:1507.05902].

[153] **NEXT** Collaboration, J. J. Gomez-Cadenas et al., *Present status and future perspectives of the NEXT experiment*, *Adv. High Energy Phys.* **2014** (2014) 907067, [arXiv:1307.3914].

[154] **NEXT** Collaboration, V. Alvarez et al., *Initial results of NEXT-DEMO, a large-scale prototype of the NEXT-100 experiment*, *JINST* **8** (2013) P04002, [arXiv:1211.4838].

[155] **NEXT** Collaboration, V. Alvarez et al., *Operation and first results of the NEXT-DEMO prototype using a silicon photomultiplier tracking array*, *JINST* **8** (2013) P09011, [arXiv:1306.0471].

[156] **NEXT** Collaboration, D. Lorca et al., *Characterisation of NEXT-DEMO using xenon* K_α *X-rays*, *JINST* **9** (2014), no. 10 P10007, [arXiv:1407.3966].

[157] **NEXT** Collaboration, V. Alvarez et al., *Near-Intrinsic Energy Resolution for 30 to 662 keV Gamma Rays in a High Pressure Xenon Electroluminescent TPC*, *Nucl. Instrum. Meth.* **A708** (2013) 101–114, [arXiv:1211.4474].

[158] **NEXT** Collaboration, V. Alvarez et al., *NEXT-100 Technical Design Report (TDR): Executive Summary*, *JINST* **7** (2012) T06001, [arXiv:1202.0721].

[159] W. Maneschg, M. Laubenstein, D. Budjáš, W. Hampel, G. Heusser, K. Knpfle, B. Schwingenheuer, and H. Simgen, *Measurements of extremely low radioactivity levels in stainless steel for gerda*, *Nuclear Instruments and Methods in Physics Research Section A: Accelerators, Spectrometers, Detectors and Associated Equipment* **593** (2008), no. 3 448 – 453.

[160] E. A. et al., *Material screening and selection for {XENON100}*, *Astroparticle Physics* **35** (2011), no. 2 43 – 49.

[161] B. Rebel et al., *High Voltage in Noble Liquids for High Energy Physics*, *JINST* **9** (2014) T08004, [arXiv:1403.3613].

[162] **DarkSide project** Collaboration, P. Agnes et al., *The DarkSide project*, *JINST* **11** (2016), no. 02 C02051.

[163] K. Lung, K. Arisaka, A. Bargetzi, P. Beltrame, A. Cahill, T. Genma, C. Ghag, D. Gordon, J. Sainz, A. Teymourian, and Y. Yoshizawa, *Characterization of the hamamatsu r11410-10 3-in. photomultiplier tube for liquid xenon dark matter direct detection experiments*, *Nuclear Instruments and Methods in Physics Research Section A: Accelerators, Spectrometers, Detectors and Associated Equipment* **696** (2012) 32 – 39.

[164] V. Álvarez, V. Herrero, R. Esteve, A. Laing, J. Rodríguez, M. Querol, F. Monrabal, J. F. Toledo, and J. J. Gómez-Cadenas, *The electronics of the energy plane of the NEXT-White detector*, arXiv:1805.08636.

[165] J. Toledo, H. Muller, R. Esteve, J. M. Monzo, A. Tarazona, and S. Martoiu, *The Front-End Concentrator card for the RD51 Scalable Readout System*, *JINST* **6** (2011) C11028.

[166] A. Tarazona, K. Gnanvo, S. Martoiu, H. Muller, and J. Toledo, *A point-to-point link for data, trigger, clock and control over copper or fibre*, *J. Instrum.* **9** (2014) T06004. 13 p.

[167] **NEXT** Collaboration, F. Granena et al., *NEXT, a HPGXe TPC for neutrinoless double beta decay searches*, arXiv:0907.4054.

[168] S. Agostinelli et al., *Geant4 simulation toolkit*, *Nuclear Instruments and Methods in Physics Research Section A: Accelerators, Spectrometers, Detectors and Associated Equipment* **506** (2003), no. 3 250 – 303.

[169] J. Martín-Albo, *The NEXT experiment for neutrinoless double beta decay searches*. PhD thesis, Valencia U., IFIC, 2015.

[170] **NEXT** Collaboration, A. Simón et al., *Electron drift properties in high pressure gaseous xenon*, *JINST* **13** (2018), no. 07 P07013, [arXiv:1804.01680].

[171] I. Murayama and S. Nakamura, *Time profile of the scintillation from liquid and gaseous xenon*, *Nuclear Instruments and Methods in Physics Research Section A: Accelerators, Spectrometers, Detectors and Associated Equipment* **763** (2014) 533 – 537.

[172] **NEXT** Collaboration, J. Martín-Albo et al., *Sensitivity of NEXT-100 to Neutrinoless Double Beta Decay*, *JHEP* **05** (2016) 159, [arXiv:1511.09246].

[173] The HDF Group, *Hierarchical Data Format, version 5*, 1997-2018. http://www.hdfgroup.org/HDF5/.

[174] P. D. Team, *PyTables: Hierarchical datasets in Python*, 2002–.

[175] W. McKinney, *Data structures for statistical computing in python*, in *Proceedings of the 9th Python in Science Conference* (S. van der Walt and J. Millman, eds.), pp. 51 – 56, 2010.

[176] W. McKinney, *pandas: a foundational python library for data analysis and statistics*, .

[177] J. Gómez-Cadenas and J. Generowicz, *IC: Invisible Cities* *https://github.com/nextic/IC*, 2016-.

[178] "www.python.org."

[179] G. Rossum and J. Boer, *Interactively testing remote servers using the python programming language*, 12, 1991. Volume 4, Issue 4, Amsterdam, pp 283303.

[180] *Anaconda software distribution. computer software. vers. 2-2.4.0*, 11, 2016.

[181] R. Brun and F. Rademakers, *Root an object oriented data analysis framework*, *Nuclear Instruments and Methods in Physics Research Section A: Accelerators, Spectrometers, Detectors and Associated Equipment* **389** (1997), no. 1 81 – 86. New Computing Techniques in Physics Research V.

[182] E. Jones, T. Oliphant, P. Peterson, et al., *SciPy: Open source scientific tools for Python*, 2001–.

[183] S. Behnel, R. Bradshaw, C. Citro, L. Dalcin, D. S. Seljebotn, and K. Smith, *Cython: The best of both worlds*, *Computing in Science Engineering* **13** (March, 2011) 31–39.

[184] S. K. Lam, A. Pitrou, and S. Seibert, *Numba: A llvm-based python jit compiler*, in *Proceedings of the Second Workshop on the LLVM Compiler Infrastructure in HPC*, LLVM '15, (New York, NY, USA), pp. 7:1–7:6, ACM, 2015.

[185] "www.travis-ci.org."

[186] **NEXT** Collaboration, P. Novella et al., *Measurement of radon-induced backgrounds in the NEXT double beta decay experiment*, arXiv:1804.00471.

[187] S. Rosendahl et al., *A novel ^{83m}Kr tracer method for characterizing xenon gas and cryogenic distillation systems*, *JINST* **9** (2014), no. 10 P10010, [arXiv:1407.3981].

[188] **NEXT** Collaboration, J. Renner et al., *Initial results on energy resolution of the NEXT-White detector*, arXiv:1808.01804.